

**University of Nottingham**

**School of Chemical, Environmental and Mining Engineering**

**Gas-liquid Flows in  
Inclined Pipes and Venturis**

**By Giorgio Geraci, Laurea**

**Thesis submitted to the University of Nottingham**

**for the degree of Doctor of Philosophy**

**September 2005**

Cd missing from  
original thesis

**To my Grandfather**

**Nicola**

**Now he is wandering in  
places he could not visit**

**before.**

## ABSTRACT

In oil industrial applications, the modern practice in the drilling of oil wells, deviated drilling, results in inclinations from the vertical to the horizontal being present in such wells. Their design requires an accurate knowledge of the pressure drop/flowrates/physical-properties relationships. The measurement of wet-gas streams can be improved significantly by the use of a Venturi flow meter with an “overreading” correction. Moreover, at high gas mass fractions, knowledge of the liquid distribution about the well tubing cross section is required to inform policy on the use of inhibitors to protect the tubing from corrosion.

Therefore, the aims of this study are to address aspects of two-phase gas/liquid flow in the pipe upstream the Venturi and in the Venturi. The main thrust of the project is to examine the effects of stratification that occur in annular flow when the pipe inclination is from horizontal to much higher inclinations. The study of annular flow includes the prediction of the three principal dependent variables – film flowrate, film thickness and pressure drop – as a function of position along the channel. All experiments were carried out with air and water in an inclinable rig. It consisted of a 5 m long stainless steel pipe of 38 mm internal diameter. The pipe could be positioned at any angle between horizontal and vertical in intervals of 5 degrees. The Venturi, located downstream the pipe, had a 19 mm i.d. throat and angles of convergent and diffuser respectively of 32° and 4°. Measurements on liquid film flowrate and liquid film thickness were carried on with two conductance probe techniques and sintered porous wall units. Measurements on pressure drop were conducted with the use of two differential pressure cells. In all experiments described, gas and liquid flowrates and pipe orientation were varied.

Another aim of the study was to develop computer modelling for the prediction of air-water pressure gradient and liquid film thickness along the Venturi. The models of Azzopardi *et al.* (1991) regarding pressure drop and the models of Fukano and

Ousaka (1988) for film thickness circumferential variations have been analysed and modified according to the characteristics of the system.

## ACKNOWLEDGEMENTS

In the first place, I would like to express my gratitude to Prof. Barry Azzopardi. His guidance and his trust also outside of the supervision of this work have given me uncommon opportunities. I thank him for leading me with the strength of his example rather than by plain authority. Special thanks also to my internal assessor, Dr G. Li Puma for his friendship and precious help during these years.

I would like to express my gratitude to Dr. van Maanen for his invaluable help. Although far from the School, he has been indispensable for the achievement of many important results. I also thank Shell Global Solution International for funding my project.

I would also like to thank the technical staff of SChEME. In particular, I thank the technicians of the workshop in laboratory 3 (Mick, Andy, Fred, Phil, Bill, Marion, Reg and Jim). They have been patient and understanding, as well as excellent professionals. They provided much support in the experimental part of this work.

Many thanks to all my colleagues of Research Rooms 6 that have finished and started the experience of a PhD during my permanence at Nottingham University (Liz, Glen, Richard, Limin, Sun Hong, Jamie, Vas, Karl, Ryu, Valente and Paisa). They have been giving me friendship, encouragement, understanding and much help in Academia. I wish them a successful career in their future.

I thank all my friends that I have met during my long permanence in Nottingham. In particular, thanks to all my friends of Broadgate Park with whom I have spent an extraordinary time during my first year. *Merci à mes amies françaises*, in particular Celine, Maggy, Helene among others. *Grazie ai miei amici italiani* but mainly Sardinians, in particular my dear “brothers” Alessandro, Davide and Daniele. With them I have sheared moments that I will never forget. Thanks to

all my other friends from England and the rest of the world, in particular to my unique friend Tej.

I would also like to thank Rosanna for being so close to me and for her formidable support and patience, especially during the last period. I would like to express all my love to her. She is the most sensitive person I have ever met. Grazie Rosanna.

I thank my family in the persons of my mother Rosa Alba, my father Gianfranco and my grandmother Olga. Without their example, understanding and encouragement from home this would have never been possible. Also thanks to my grandfather Nicola who is now elsewhere looking upon my life. I will never forget his jokes, teachings and passion.

Finally, I would like to express all my attachment to the city of Nottingham and belief that one day I will come back. Here I have had the most beautiful time of my life and I will always feel at home.

# Table of Contents

## Abstract

## Acknowledgements

## Table of contents

### Chapter 1: Introduction

1.1. Two-phase flow	1
1.2. Two-phase flow in oil & gas industrial applications	2
1.2.1. Corrosion and inhibition of pipelines in oil wells	3
1.2.2. Venturi for metering	4
1.2.2.1. The Venturi overreading correlation	5
1.2.2.2. Tracer dilution technique	7
1.3. Aims of study	9
1.4. Structure of the thesis	11

### Chapter 2: Literature review

2.1. Flow patterns	12
2.1.1. Vertical upward flow	12
2.1.2. Horizontal flow	14
2.1.3. Annular flow	16
2.2. Flow pattern maps	17
2.2.1. Taitel & Dukler flow pattern map for horizontal-slightly inclined flow	19
2.3. Entrainment and deposition	22
2.3.1. Rate of entrainment and rate of deposition	23
2.3.2. Interfacial waves	29
2.3.3. Deposition mechanism	30

2.3.4. Entrainment mechanism	30
2.3.5. Critical film flowrate	32
2.3.6. Entrainment and deposition in Venturi	34
2.4. Pressure gradient	37
2.4.1. Basic equations	37
2.4.2. Homogeneous and separated models	38
2.4.3. Frictional pressure gradient	39
2.4.4. Gravitational pressure gradient	41
2.4.5. Acceleration pressure gradient	41
2.4.6. Pressure drop in Venturi	42
2.5. Liquid film thickness	50
2.5.1. Vertical upward flow	51
2.5.2. Horizontal flow	51
2.5.3. Inclined flow	55
2.5.4. Experimental techniques for liquid film thickness measurements	56
2.5.4.1. Typology and design of conductance probes	56
2.5.4.2. Needle probes	57
2.5.4.3. Wire probes	58
2.5.4.4. Flush-mounted probes	58
2.6. Recommendation for data processing and analysis	59
2.6.1. Sampling frequency	60
2.6.2. Fourier transform and power spectrum density	61
2.6.3. Methods for correlating wave frequencies	63

### **Chapter 3: Experimental arrangements**

3.1. Description of the inclinable rig	67
3.2. Pressure drop arrangement	71
3.3. Film thickness arrangement	72
3.3.1. Flush-mounted probe sections and their calibrations	72
3.3.2. Wire probe test section and its calibration	78
3.3.3. Data acquisition procedure	81
3.4. Liquid film flowrate arrangement	82

<b>Chapter 4: Liquid film flowrate and entrainment results</b>	
4.1. Results in the pipe upstream of the Venturi	91
4.2. Results in the throat of the Venturi	107
<b>Chapter 5: Liquid film thickness results</b>	
5.1. Results in the pipe upstream of the Venturi	120
5.2. Results in the throat of the Venturi	171
5.2.1. Results in slightly inclined Venturi	208
5.3. Modelling of liquid film thickness	212
<b>Chapter 6: Pressure drop results</b>	
6.1. Pressure drop in the Venturi	217
6.2. Modelling of pressure drop	229
<b>Chapter 7: Final conclusion and future work</b>	
7.1. Introduction	235
7.2. Conclusion for liquid film mass flowrate and entrainment determination	236
7.3. Conclusion for film thickness measurements	237
7.4. Conclusions for pressure profile and pressure drop studies	238
7.5. Recommendations for future experimental work	239
7.6. Recommendations for future developments of models	241
<b>Appendix A: Venturi scrubbers</b>	242
<b>Appendix B1: Theoretical details on separated flow</b>	245
<b>Appendix B2: Methods for calculation of frictional pressure gradient</b>	248
<b>Appendix C: Error analysis</b>	250
<b>Appendix D: Signal processing</b>	254
<b>List of figure</b>	285
<b>List of table</b>	300

<b>Nomenclature</b>	301
---------------------	-----

<b>References</b>	305
-------------------	-----

# CHAPTER 1

## Introduction

### 1.1 Two-phase flow

Central to this thesis is an understanding of two-phase flow and how it behaves. The term two-phase flow covers the interaction of two different phases such as gas-liquid, liquid-liquid, solid-liquid or solid-gas travelling together within a pipeline. These flows are extremely important in industrial applications such as oil and gas pipelines, water-cooled nuclear reactors, boilers, steam generators, heat exchangers, distillation columns, reboilers and condensers, fluidised beds and pneumatic conveying to oil and gas wells and pipelines. Knowledge of the fluid dynamics and heat transfer processes occurring in two-phase flow is needed for the design and construction of such equipment.

On examination of many pieces of equipment within the chemical, power generation and hydrocarbon production industries, it can be observed that gas-liquid flow occurs in pipelines which carry a mixture of oil and gas and in boiling and condensation operations such as in condensers and vapour generators. Liquid-liquid flow, containing two immiscible layers, occurs in liquid-liquid extraction processes. Gas-solid flow

occurs in fluidised bed and in pneumatic conveying of solid particles. Solid-liquid flow occurs in hydraulic conveying, in flows of suspension such as coal-water slurries, crystallizers and river bed sediments. This work is concerned only with gas-liquid flows with particular interest towards oil industry applications.

The majority of these studies have been performed either in vertical or horizontal flow. However, there is increasing interest in the oil industry in the use of directional wells for economic reasons. These are drilled at angles, which deviate continuously from the vertical to reach out to a larger part of the reservoir from a central platform. Flows in inclined pipes have been less extensively studied and, therefore, one of the main aims of the present study is to provide new data on pressure gradient, liquid film thickness and liquid flowrate in inclined pipes and particularly in a Venturi with the same axis as the pipe.

In this chapter, the main oil & gas industrial applications of two-phase gas/liquid flow will be discussed as well as the aims of the study, and then the structure of this thesis will be outlined.

## **1.2 Two-phase flow in oil & gas industrial applications**

Natural gas is rapidly growing as an energy source for the world. There are several reasons such as: relatively low carbon dioxide emission, low emissions of solids and nitrogen oxides, large sources available.

Therefore the number of fields in operation is continuously increasing with consequent significant investments involved. However, the number of reservoirs which produce only (dry) gas is negligible. All reservoirs contain higher hydrocarbons and water vapour, which condense once the temperature and pressure drop down when the fluids reach the surface. It is essential to measure these flows for allocation and production &

reservoir management although a mixture of different phases is more complicated to measure than a single-phase fluid. These reservoirs where condensation of hydrocarbons takes place (gas-condensate reservoirs) require high management for two reasons:

- Avoid large amounts of valuable condensate left behind in the reservoir.
- Avoid increase of pressure drop due to the "condensate banking" around the bore hole.
- Maintain the gas flow in the bore hole.

Therefore, monitoring is an important key in the optimisation and ultimate recovery of the heavier hydrocarbons and reduction of the operational costs.

### **1.2.1 Corrosion and inhibition of pipelines in oil wells**

In oil industrial applications, the modern practice in the drilling of oil wells, deviated drilling, results in inclinations from the vertical to the horizontal being present in such wells. Their design requires an accurate knowledge of the pressure drop/flow rates/physical property relationships. Moreover, at high gas mass fractions, knowledge of the liquid distribution about the well tubing cross section is required to inform policy on the use of inhibitors to protect the tubing from corrosion. On those parts of the walls not wetted by the hydrocarbon liquid, water could condense out of the gas phase. Any carbon dioxide present in the gas could dissolve forming highly corrosive carbonic acid. Protection is normally provided by an inhibitor. There are two main ways of introducing this. In some cases the appropriate chemicals, dissolved in diesel are pumped to the bottom of the well and sprayed into the production flow. Obviously, the flow rate should be as low as possible for cost reasons. An alternative strategy is to pump a large quantity of the inhibitor solution down the well against the gas flow. This should coat the entire internal surfaces of the well tubing as it goes down and as it is forced back up by the gas. Here, the period between dosing needs to be optimised to

minimise the interruption to production. A third item of interest is the size of drops produced in the well as this parameter would affect erosion of flow control devices such as chokes placed at the top of the well. All these motivations require a detailed and accurate knowledge of the two-phase flow. In particular, knowledge is required of annular flow for gas/condensate production wells.

### 1.2.2 Venturi for metering

The fluids of most gas fields contain heavier components as well as water vapour. Due to the drop in both pressure and temperature that occurs when fluids reach the surface, liquids (condensate and water) will form in the well fluid. In many cases water from an aquifer is produced as well. As a result, the well fluid, as it arrives at the surface, contains both gas and liquids and can thus be regarded as “wet-gas”. The definition of “wet-gas” as used by many petroleum industries is that the Lockhart-Martinelli parameter (eq. 3) is  $\leq 0.35$ .

In oil industrial applications, wet-gas metering is conventionally done using a test-separator. Such an approach has several disadvantages, both from an operational point of view (24 hours to stabilise, significant volume and small range-ability) and from the costs involved (high cost of equipment, requirement of platform space for off-shore applications, additional investments).

De Leeuw (1994, 1997 and 1999) and van Maanen (1999) have been working on the development of wet-gas flow metering without test-separators for years. The study has been focused on two major issues: the influence of liquids on the readings of pressure drop flow meters like Venturis and the independent determination of the water and condensate flow rates. In fact, the Venturi being a relatively cheap, robust and reliable pressure drop flow meter can be used to measure wet-gas flows in each well. Unfortunately, pressure drop flow meters react in a complicated manner to the liquids

in the gas flow. This behaviour is only partly understood and, therefore, a further study on the applications of pressure drop flow meters in wet-gas is necessary. So far, an approach with empirical correlations has been proposed, which describe the so-called "overreading" as a function of the flow parameters. The expression "overreading" is used to indicate the higher reading of differential pressure when liquid flowing in the gas stream is present, so the "overreading" can be determined by the equation:

$$\text{Overreading} = \sqrt{\frac{\Delta P_p}{\Delta P_g}}$$

where  $\Delta P_p$  is the two-phase pressure drop and  $\Delta P_g$  is the single gas-phase pressure drop. This means that when the differential pressure between the Venturi inlet and the Venturi throat is measured and the liquid flowrate is obtained by executing a tracer test (Section 1.2.2.2), the gas flowrate can be calculated by making use of the Venturi "overreading" correlations.

### 1.2.2.1 The Venturi "overreading" correlation

It has been known for a long time that differential pressure meters ( $\Delta p$ -meters) like the orifice plates and the Venturis, can be used in wet-gas conditions, provided corrections are applied. In general the pressure drop in wet-gas conditions is higher than that of the gas alone (Murdock, 1962), which can be easily understood: as the average density of the fluid is higher than that of the gas alone, the  $\Delta p$  should be higher as well. However, the amount by which it is higher cannot be explained by the increase in average density alone. Experimental data have been used to find correlations, which describe this so-called "overreading" of orifices and Venturis for practical applications. Although these correlations lack insight into the physical phenomena, they describe the "overreading" with sufficient accuracy to determine the gas flow rate using  $\Delta p$  meters, Murdock

(1962), Chisholm (1977), de Leeuw (1997) and van Maanen (1999). Essential in all these correlations is an expression for the "wetness" of the gas, which is commonly obtained using the Lockhart-Martinelli parameter, LM or X. This X parameter is the ratio of the liquid and gas Froude numbers, which themselves also occur more explicitly in the newer correlations. To obtain the Froude number and the Lockhart-Martinelli parameter, the liquid flowrate(s) need to be known:

$$Fr_g = \frac{U_{sg}}{\sqrt{gD}} \cdot \sqrt{\frac{\rho_g}{\rho_l - \rho_g}} \quad (1)$$

$$Fr_l = \frac{U_{sl}}{\sqrt{gD}} \cdot \sqrt{\frac{\rho_l}{\rho_l - \rho_g}} \quad (3)$$

$$X = \frac{Fr_l}{Fr_g} = \frac{U_{sl}}{U_{sg}} \cdot \sqrt{\frac{\rho_l}{\rho_g}} = \frac{Q_l}{Q_g} \cdot \sqrt{\frac{\rho_l}{\rho_g}} \quad (3)$$

The "overreading" of Venturis is predicted by several different correlations, the most well-known are those of Murdock (1962) and Chisholm (1977). These are, however, based on air-water systems of relatively low pressures and are thus not really representative for the conditions encountered in gas production. De Leeuw (1997) has measured the "overreading" of a Venturi at different pressures and has shown that the "overreading" is also dependent on the pressure. He has subsequently extended Chisholm's correlation in order to get a more accurate prediction of the "overreading" under more realistic conditions. His correlation is:

$$Overreading = \sqrt{\frac{\Delta p_{ip}}{\Delta p_g}} = \sqrt{1 + C \cdot X + X^2} \quad (4)$$

in which

$$C = \left( \frac{\rho_l}{\rho_g} \right)^n + \left( \frac{\rho_g}{\rho_l} \right)^n \quad (5)$$

in which

$$\left. \begin{aligned} n &= 0.606 \cdot (1 - e^{-0.746 \cdot Fr_g}) & Fr_g > 1.5 \\ n &= 0.41 & 0.5 \leq Fr_g \leq 1.5 \end{aligned} \right\} \quad (6)$$

The results of Leeuw (1997) also showed that the pressure recovery of the Venturi is dependent on the Lockhart-Martinelli parameter, so by monitoring the pressure recovery, a change in liquid loading can be discerned. This enables the continuous measurement of the gas flow rate once the liquid flow rates are known.

As this correlation uses the gas and liquid Froude numbers and the Lockhart-Martinelli parameter, it is essential to determine the liquid flow rate(s) in one or other way to find the “overreading” in order to measure the correct gas flow rate. This can be done using the tracer dilution technique.

### 1.2.2.2 Tracer dilution technique

Tracer dilution technique was investigated by van Maanen (1999). He assumed that only one type of liquid is present in the pipeline. When a tracer, dissolved in a liquid, is injected into the flow line with a constant flow rate, the tracer will mix with the liquid in the pipeline and it will be diluted as is illustrated in figure 1.2.1. When the

injected and produced liquids are completely mixed<sup>1</sup> and provided that the tracer solution flow rate is far smaller than the liquid flow rate in the pipeline, the concentration of the tracer in the pipeline is equal to:

$$c_p = \frac{Q_i}{Q_p} \cdot c_i \quad (1)$$

where  $c_i$  and  $Q_i$  are the tracer concentration and flowrate of the injected solution and  $c_p$  is the tracer concentration in the pipeline.

It is simple to derive the liquid flow rate in the pipeline from this relation:

$$Q_p = \frac{c_i}{c_p} \cdot Q_i \quad (2)$$

Thus, by determining the concentrations of the tracer in the injected solution and from a sample from the pipeline, the liquid flow rate in the pipeline can be determined. Fluorescent tracers are suitable for this task and both hydrophobic and hydrophilic tracers are available. In this way the water and condensate flow rates can be determined. Fluorescent tracers have the advantage that they do not require special licences (compare to radio-active tracers), because they are harmless to the environment. Also, the small amounts ending up in the product is not a problem for the processing of the hydrocarbons. This technique cannot be applied subsea mainly because of logistics and also cannot be applied continuously, so the liquid flow rate determination remains a "spot" measurement.

Despite these limitations, the tracer dilution technique offers an option for the determination of the liquid flow rates without the use of a test-separator.

---

<sup>1</sup> The tracer is homogeneously dissolved in the mixture of the injected and produced liquids.

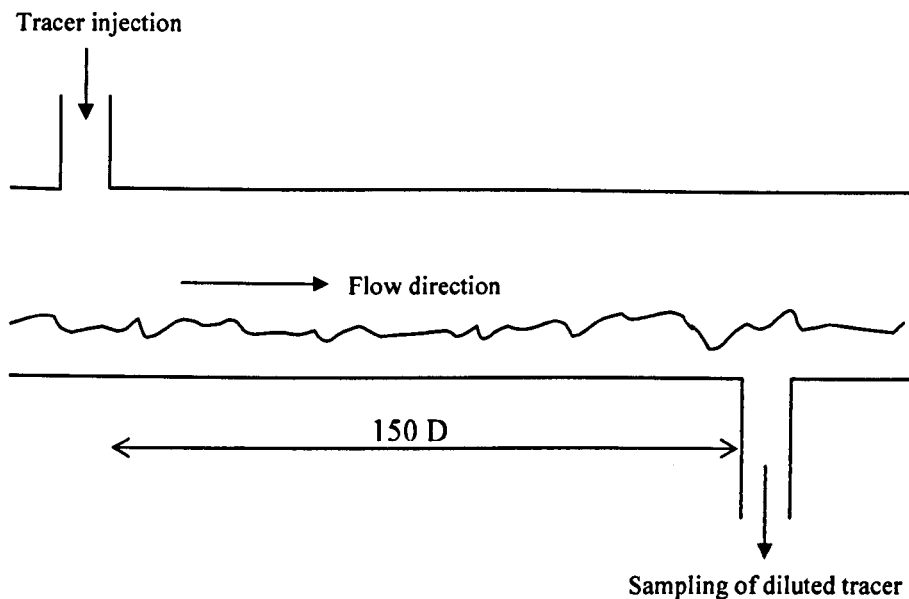


**Figure 1.2.1:** Principle of the tracer technique

### 1.3 Aims of study

This study is aimed at attempting to reduce the problems and complications discussed above. It involves research on straight pipes and Venturis.

The aims of this study are to address aspects of two-phase gas/liquid flow in the Venturi, in particular, the case of annular flow. The main thrust of the project is to examine the effects of the stratification that occur when the pipe inclination is from vertical to horizontal. The study of annular flow includes the prediction of three principal dependent variables – liquid film flowrate, liquid film thickness and pressure gradient – as a function of position along the channel.

The experimental study was carried out on the Inclinable Flow Facility shown and described in Chapter 3. This rig was built in the School of Chemical, Environmental and Mining Engineering at the University of Nottingham. The fluid pairing used in this

rig was air-water. The essential components of the rig were a 5 m long and 38 mm internal diameter pipe, an orifice plate/difference pressure cell for the measurements of air flow rate, rotameters for water metering, a water pump, a tank for the storage of water and a recycling tank for water. The 5 meter long pipe could be positioned at any angle between the vertical and the horizontal. The Venturi was connected between two flanges of the main pipe. Its geometrical characteristics are shown in Chapter 3.

The reason for using a 38 mm tube and 19 mm Venturi are to be found in the industrial applications discussed in Chapter 3, section 2.4.6. The distance to achieve a fully developed flow is quoted to be approximately 200 times the pipe diameter, Whalley & Hewitt (1978). In the present work, the length of the pipe was 5 m to approach fully developed hydrodynamic conditions.

In the literature the majority of information on two-phase flow is for vertical and horizontal pipes. There is a moderate amount on pipes inclined a few degrees from the horizontal and data for large inclinations are much more sparse. Therefore the aim of the current experiments is an attempt at filling the gaps encountered in the literature.

Papers on flow patterns in steeply inclined flow have been published by Spedding & Nguyen (1980), Barnea *et al.* (1985) and Mukerjee & Brill (1985). Most of the data involved is from air-water experiments. Pressure drop data has been published by Beggs & Brill (1973) and Spedding *et al.* (1982). The last two sources also provided void fraction (1 - liquid holdup) data. The majority of the data are for air-water. More detailed information may be found in Paz & Shoham (1994) who measured the circumferential variation of film thickness for vertical pipes and those inclined at 15°, 30° and 45° from the vertical. They found that significant asymmetry in film thickness occurs very quickly once the tube deviates from the vertical.

Hence, the work here, as regards to the air-water system, is aimed at providing some new data concerning, liquid film flow rate, film thickness, and pressure drop in air-water phase flow in inclined Venturi.

Another aim of the study is to develop computer modelling for the prediction of air-water pressure gradient and liquid film thickness along the Venturi. The model of Azzopardi *et al.* (1991) regarding pressure drop and the model of Fukano & Ousaka (1989) for film thickness variations have been analysed and modified according to the characteristics of the system.

#### **1.4 Structure of the thesis**

Chapter 1 provides an introduction of the thesis, defining the problems and aims of the study. Chapter 2 reviews the relevant literature and previous studies on two-phase flows. The descriptions of the experimental apparatus and measurements of liquid film flowrate, film thickness and pressure drop are discussed in Chapter 3. Experimental results on these three dependent variables are presented in Chapter 4, 5, and 6 along with data analysis and modelling. Chapter 7 presents the conclusions and recommendations for experimental and theoretical future work.

## CHAPTER 2

### Literature review

#### 2.1 Flow patterns

When a gas-liquid mixture flows in a pipe, it has been observed that the interface between the two phases can assume different properties depending on variables such as inlet flowrates, fluid properties, pipe geometry and orientation of the flow. The various configurations of interfacial distributions can be classified into “flow patterns”. Many flow patterns have been named in vertical, horizontal and inclined gas/liquid phase flow in pipes.

##### 2.1.1 Vertical upward flow

Figure 2.1.1 shows a sequence of flow patterns in the case of a vertical pipe with co-current upward flow. The ratio between gas and liquid flowrate is increasing from left to right.

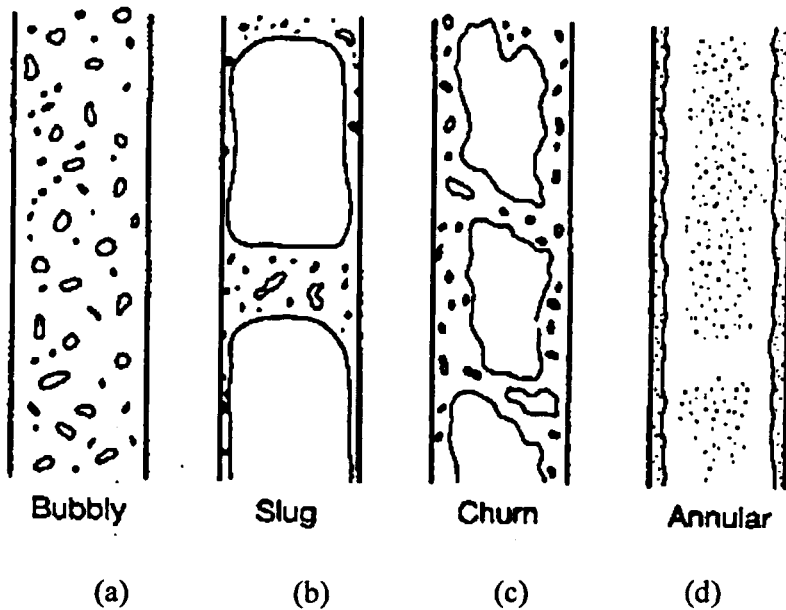


**Figure 2.1.1:** Flow patterns in vertical upward flow

For low values of this ratio *bubbly flow* (figure 2.1.1a) is observed. The main feature is the stability of such a flow in which bubbles of approximately uniform diameter are carried throughout the liquid.

As the ratio is increased, the flow pattern switches from bubbly to slug flow (figure 2.1.1b). *In slug flow*, the bubbles are separated from the wall by a thin liquid film and between two gas bubbles it is possible to observe a liquid slug entraining gas from the gas bubble's wake. It should be pointed out that no gas entrainment is observed in the liquid slugs, for small diameter pipes.

From slug flow, a tendency is initiated for the gas and the liquid to travel separately and this leads to the *annular flow* (figure 2.1.1d) passing through a chaotic behaviour known as *churn flow* (2.1.1c). In the latter a churning motion of irregularly shaped portions of both fluids is observed, in the former two well defined zones are identifiable:

- 1) Liquid film adjacent to the wall possibly entraining gas bubbles
- 2) Gas core flowing in the remaining part of the tube entraining liquid droplets.

Those droplets are caused by break-up of waves on the surface of the film. Some authors (Taitel *et al.* 1980) regard churn flow as a zone of adjustment of the two phases to create the slug flow pattern. In this sense churn flow would not be regarded as a real flow-pattern although it can develop for a considerable number of pipe diameters. Recent studies on the churn flow transition have been carried out by Watson & Hewitt (1999).

Furthermore, if starting from annular flow conditions the gas flowrate is decreased, for a certain gas flowrate the liquid film starts flooding the pipe in some sections in a chaotic fashion: the churn flow pattern appears. This description as a flooding condition rather than an entrance effect for the slug flow pattern shows that the churn flow pattern must be considered a flow pattern in addition to the others described above.

### **2.1.2 Horizontal flow**

For co-current flow in a horizontal pipe, the situation changes because the main direction of motion is no longer coincident with that of gravity. Alves (1954) classified the types of patterns, figure 2.1.2. Reasoning again in terms of growing gas flowrate, the following sequence can be observed.

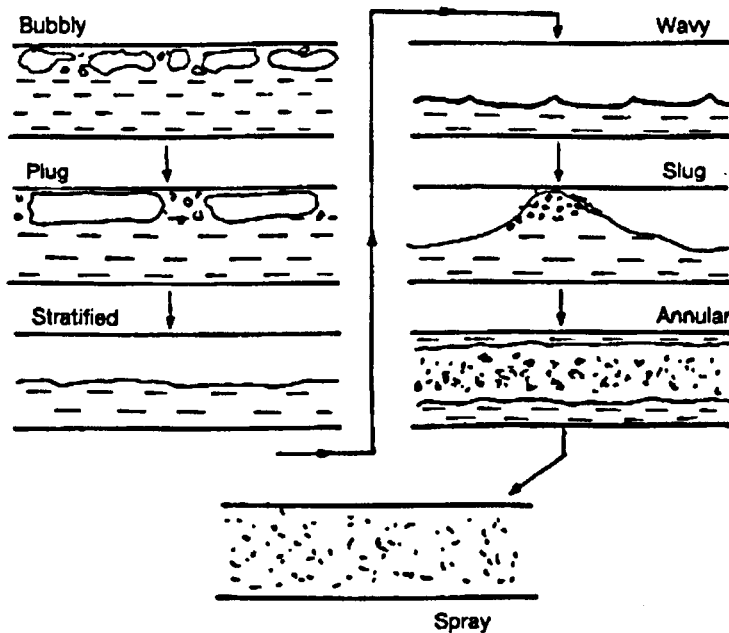


**Figure 2.1.2:** Flow Patterns in horizontal two-phase flow

For low gas flowrates the flow is defined as *bubbly* but in this case the bubbles are confined to a zone near the top of the pipe. As the gas flowrate increases, the bubbles become bigger and their coalescence leads to a flow pattern known as *plug flow*. The next qualitative change occurs when a continuous gas layer is formed in the upper part of the pipe as consequence of the plugs joining and we can speak of *stratified flow*.

A further increase in the gas flowrate leads to the formation of waves on the liquid surface due to the shear stress exerted by the gas phase on the liquid. This is *wavy stratified flow*. As the waves become high enough to touch the top of the pipe, the *slug flow* is reached. For higher gas flowrates, *annular flow* takes place, basically with the same feature described in the case of vertical pipe with the only difference that the liquid film will be thicker at the bottom than at the top because of the effect of gravity. If the gas flowrate is very high, and the pipe is heated, the thickness of the

film becomes negligible and the liquid travels only in the gas core occupying the entire pipe. This is the flow known as *spray* or *mist flow*.

### 2.1.3 Annular flow

Annular flow is the configuration of gas/liquid flow in which some of the liquid travels as a film on the channel walls and the rest is carried as drops by the gas in the centre of the channel, figure 2.1.3. The fraction of liquid travelling as drops (entrained fraction) varies from zero to close to one. It occurs at high gas and low to medium liquid flowrate and at all pipe orientations. The high velocity gas phase exerts a considerable drag on the liquid surface, introducing various types of waves on the liquid film and causing the surface to be rough. Droplets are created because of the shearing action of the gas on the waves called disturbance waves (shown in figure 2.1.3 and discussed in Section 2.3.2) and the process is called atomisation or entrainment. The droplets are called entrained droplets and are carried into the turbulent gas phase where they interact with the gas and deposit back onto the liquid film. It is possible that they could undergo collision and coalescence. In sufficiently long tubes, equilibrium is achieved whereby the liquid is divided between the film and the droplets with continuous interchange between them. In vertical flow the film is fairly uniform about the pipe circumference but for inclined and horizontal pipes, gravity causes a significant asymmetry of the film, much higher flowrates and film thicknesses at the bottom than at the top. For downwards flows there are wide ranges of conditions where the liquid flows entirely as a film.

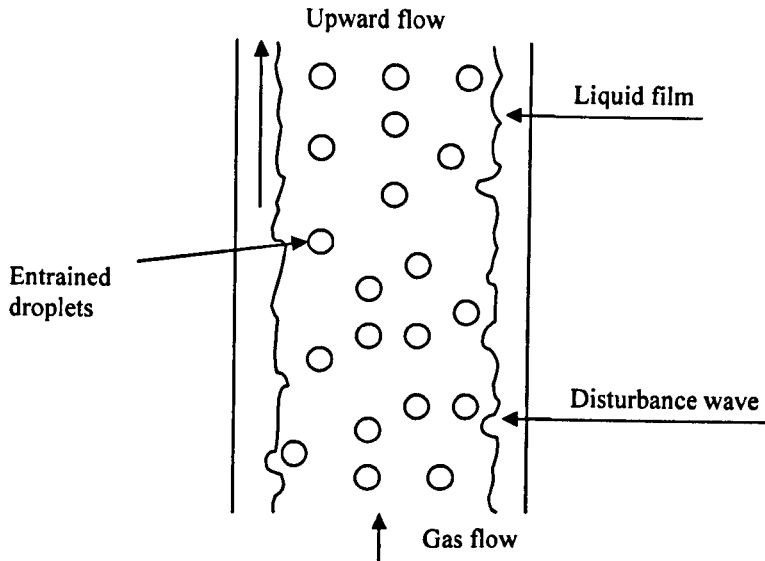


Figure 2.1.3: Vertical annular flow

Researchers such as Hewitt & Hall Taylor (1970) and Hawkes (1996) defined another flow pattern, which is termed *wispy annular flow*. This occurs at very high liquid flowrates, which result in high liquid concentrations in the gas core. Such that “wisps” are observed instead of droplets, and there is also a significant amount of gas entrapped within the liquid film.

## 2.2 Flow pattern maps

The prediction of flow pattern in gas-liquid flow in pipes is one of the most important problems in two-phase flow. Traditionally, the approach that has been used to treat this problem was to correlate the data and to plot the results on a “flow pattern map”. A wide variety of maps with different coordinate systems have been published.

Recently, efforts were directed towards the development of physical models that allow the analytical prediction of the flow patterns and the transition boundaries. Such an approach was used by Taitel & Dukler (1976) for horizontal and slightly

inclined flow, Taitel *et al.* (1980) and Mishima & Ishii (1984) for the case of vertical upward flow and Barnea *et al.* (1982a) for vertical downward flow.

Physical models for flow-pattern transition in inclined pipes were presented by Barnea *et al.* (1982b) for downward inclinations and Barnea *et al.* (1985) for upward inclinations. The approach taken was to extend and modify the vertical models to include steep inclinations, while the shallow inclinations were treated via an extension of the horizontal case.

In the development of predictive models for flow-pattern transition boundaries the objective should be to propose models that will apply to all angles of inclination, i.e. that the effect of inclination will be incorporated in the model in such a way that the same model will apply for horizontal, vertical upward, vertical downward and all angles of inclination.

So far this aim has not been fully achieved in the model presented by Barnea *et al.* (1982b, 1985). The main disadvantage in these models arises when dealing with the transition from annular to intermittent flow and the transition from the dispersed bubble flow. These two transition boundaries exist in the whole range of inclinations (although not necessarily at the same location on the flow-pattern map), but different mechanisms were suggested for these boundaries in the horizontal (Taitel & Dukler, 1976) and vertical (Taitel *et al.*, 1980; Barnea *et al.*, 1982a) cases.

Transition to annular flow according to the “horizontal” model of Taitel & Dukler (1976), requires that stratified flow becomes unstable while the liquid level is low enough to form an annular film rather than a complete bridge that leads to slug flow. For the upward vertical case, Taitel *et al.* (1980), suggested a totally different mechanism for the transition to annular flow. In this case the gas velocity must be large enough to lift the largest stable drop in order to maintain annular flow. The “downwards vertical” model, presented by Barnea *et al.* (1982a), adopted the same

idea as the “horizontal” model and suggests that the transition from annular to intermittent flow occurs when the liquid holdup is large enough to cause a blockage of the gas core. The transition to dispersed bubble flow was determined from a balance between breakage due to turbulence and coalescence forces due to gravity in the “horizontal” model and due to surface tension in the “vertical” models.

The effect of shallow inclination from the horizontal on the transition to dispersed bubble and annular flows has already been incorporated in the “horizontal” model by Taitel & Dukler (1976). In a similar way, the mechanisms presented in the “vertical” models were modified for slight changes from the vertical (Barnea *et al*, 1982b, 1985). Since the transition mechanism for the horizontal and shallow inclinations differs from those of vertical and steep inclinations, it is necessary to choose the appropriate mechanism in intermediate angle of inclination, and thus to determine the applicability of the shallow and steep-inclinations models.

The terms shallow and steep inclination may thus apply to different inclination angles for each transition boundary. In addition the “switch” between the two mechanisms was based on experimental results in an air-water system.

### **2.2.1 Taitel & Dukler flow pattern map for horizontal and slightly inclined flow**

Collecting the work of several authors it was possible to draw flow pattern maps in which the boundaries between different flow patterns are drawn in the  $U_{sg} - U_{sl}$  plane.

The difficulty in doing this consists in the gradual transition from one flow pattern to another and in the subjectivity of the interpretation of a flow pattern as belonging to one class or to the other on the boundary between two of them. Furthermore, flow pattern maps are dependent on the pair of fluids being considered as well as on the pipe diameter and operating pressure.

Apart from visual observation, some authors propose more objective criteria. For instance, Barnea *et al.* (1980) and Costigan & Whalley (1997) use a conductance probe technique to measure void fraction and support visual observations.

A Semi-theoretical prediction of the boundaries between flow patterns was developed by Taitel *et al.* (1980) for vertical pipes and Taitel & Dukler (1976) for horizontal and near horizontal pipes.

The Taitel & Dukler (1976) model has the objective of presenting a mean for unambiguous analytical prediction of the transition between flow patterns. The patterns considered are intermittent (slug and plug), stratified smooth, stratified wavy, dispersed bubble, and annular-annular dispersed liquid flow. The theory predicts the effect on transition boundaries of pipe size, fluid properties, gas and liquid mass flowrates, and angle of inclination from the horizontal.

The theory can be solved using the following dimensionless groups:

$$X = \left[ \frac{|(dP/dx)_l|}{|(dP/dx)_g|} \right]^{1/2} \quad (2.1)$$

$$T = \left[ \frac{|(dP/dx)_l|}{(\rho_l - \rho_g) \cdot g \cdot \cos \alpha} \right]^{1/2} \quad (2.2)$$

$$Y = \frac{(\rho_l - \rho_g) \cdot g \cdot \sin \alpha}{|(dP/dx)_g|} \quad (2.3)$$

$$F = \sqrt{\frac{\rho_g}{\rho_l - \rho_g}} \cdot \frac{U_{sg}}{\sqrt{D \cdot g \cdot \cos \alpha}} \tag{2.4}$$

$$K = F \cdot \left[ \frac{D \cdot U_{sl}}{\nu_l} \right]^{1/2} = F \cdot [\text{Re}_l]^{1/2} \tag{2.5}$$

All of these quantities can be determined from operating conditions, since velocities and pressure gradients are calculated from superficial conditions.

The particular transitions are shown to be controlled by the following groups:

Stratified to annular	X, F, Y
Stratified to intermittent	X, F, Y
Intermittent to dispersed bubble	X, T, Y
Stratified smooth to stratified wavy	X, K, Y
Annular to intermittent and to dispersed bubble	X, Y

Figure 2.2.1 shows the theoretically located transition boundaries for Y=0 (horizontal tube) as a generalized two-dimensional map.

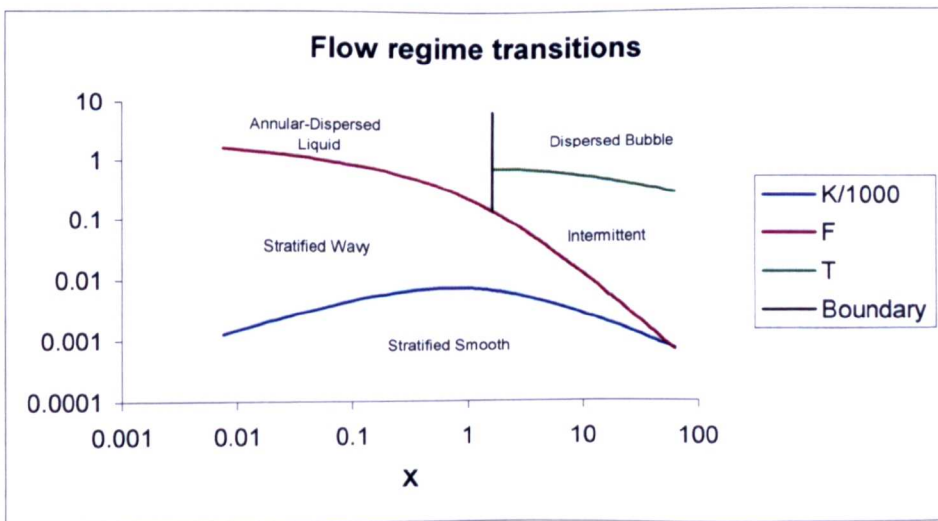


Figure 2.2.1: Two-phase flow pattern transitions, Y=0

Similar maps can be developed for any other value of  $Y$  by using the equations.

Each curve in the figure 2.2.1 represents a transition boundary between two different flow patterns. The parameter  $X$  is recognized as the parameter introduced by Lockhart & Martinelli (1949) and can be calculated unambiguously with the knowledge of flowrates, fluid properties, and tube diameter.  $Y$  is zero for horizontal tubes and represents the relative forces acting on the liquid in the flow direction due to gravity and pressure drop.

### **2.3 Entrainment and deposition**

In annular flow, the majority of drops are created from the wall film by the action of the gas flowing over it.

The surface of the film is not smooth but covered with small-wavelength waves (usually termed ripples). In addition, for a wide range of conditions, there are longer-wavelength, larger-amplitude waves (usually termed disturbance or roll waves). These waves have a height several times the average film thickness and travel at a velocity greater than that of the film. A close examination of the process of drop creation indicates that drops are not created from the entire film interface, but very specifically they arise from these disturbance waves (Arnold & Hewitt 1967; Cousins & Hewitt 1968; and Woodmansee & Hanratty 1969). The most conclusive proof that waves are the source of drops was provided by Azzopardi & Whalley (1980). They noticed that, if the film flowrate was set at a flowrate just below that required for disturbance wave creation and a small volume of liquid was suddenly injected into the film, a small number of waves were created. The flow at the top of the pipe was observed by means of a high speed cine camera used in conjunction with a special axial viewing device. Before the waves were created no drops were present. Subsequent to injection, drops were seen; the number of drops increased as the waves

approached the end of the pipe. Once the waves had passed out of the pipe, no drops were seen. An additional type of waves has been identified by Sekoguchi & Takeishi (1989). These were named huge waves and were characterized by larger amplitudes, wavelengths and velocities than disturbance waves.

### 2.3.1 Rate of entrainment and rate of deposition

Rate of entrainment (or atomisation),  $R_A$ , is defined as the mass flux of liquid droplets transferring from the film to the gas core. Rate of deposition,  $R_D$ , is the rate at which droplets in the gas core deposit onto the liquid film.  $R_A$  and  $R_D$  are based on the film surface area.

Entrainment can easily alter the mechanisms of interfacial mass, momentum and energy transfer between phases. Knowledge of the physical phenomena leading to entrainment of liquid droplets is of considerable importance for the modelling of fluid-dynamic and heat transfer processes in two-phase system especially under transient conditions. These are needed for oil industrial applications and for reactor safety analysis.

Papers available in open literature mainly consider the equilibrium entrained droplet fraction. This is obtained from an integral balance between the rate of deposition,  $R_D$ , and droplet entrainment rate,  $R_A$ , due to experimental difficulties in measuring rate of entrainment,  $R_A$ . To understand the fluid dynamics of two-phase flow, it is a usual practise to study equilibrium annular flows assuming the rate of entrainment and deposition to be equal to each other. This is often achieved in tubes with long enough development lengths, usually approximately 600 tube diameters although after about 200 diameters, the changes in entrained fraction were quite small (Brown,

1975 and Whalley & Hewitt, 1978). At these lengths, most of the entrance effects had been eliminated.

By assuming equilibrium flow and a thin liquid film, a mass balance on a small section annular liquid film will produce the following relationship:

$$\frac{dM_{LF}}{dx} = \pi \cdot D \cdot (R_D - R_A) \quad (2.6)$$

Azzopardi (1997) gave a comprehensive review of the measurement of rate of entrainment and concluded that it was difficult to remove the drops from the core without being intrusive. Artificial techniques to initiate waves in order to create entrainment were suggested by Azzopardi & Whalley (1980). As the wave approached the measuring station, high speed cine films were taken through an axial viewer. The entrainment liquid flowrate could be determined through analysis of the individual frames. However, the technique was time consuming, tedious and inaccurate. Azzopardi (1997) suggested that the best technique to determine rates of entrainment would be the tracer technique originally proposed by Quandt (1965).

The rate of deposition can be considered to follow a mass transfer process and be described by  $R_D = k_D \cdot C$  where  $k_D$  is the deposition coefficient and  $C$  is the droplet concentration. Hence, at equilibrium conditions, the rate of entrainment is given by  $R_A = R_D = k_D \cdot C$ . Hewitt & Govan (1990) produced complex forms for the deposition coefficient:

$$k_D \cdot \sqrt{\frac{\rho_g \cdot D}{\sigma}} = 0.18 \quad \text{for } C/\rho_g < 0.3; \text{ and} \quad (2.7)$$

$$k_D \cdot \sqrt{\frac{\rho_g \cdot D}{\sigma}} = 0.083 \cdot \left(\frac{C}{\rho_g}\right)^{-0.65} \quad \text{for } C/\rho_g > 0.3 \quad (2.8)$$

In directional deposition experiments, the expression for  $k_D$ , shown in equation (2.9), can be formed by performing a mass balance over a small increment of length and then, by an integration between then limits  $M_{LE1}$  (at  $x=x_0$ ) and  $M_{LE2}$  (at  $x=x_1$ ).

$$k_D = \frac{M_g}{2\pi \cdot r \cdot x \cdot \rho_g} \ln\left(\frac{M_{LE1}}{M_{LE2}}\right) \quad (2.9)$$

$M_g$  and  $M_{LE}$  are the mass flowrates (kg/s) for the gas and the entrained liquid respectively;  $r$  is the tube radius,  $D$  is the tube diameter, and  $x$ , the deposition length.

Most entrainment models are strongly dependent on dimensionless groups. These have been indicated in the works of Hutchinson & Whalley (1973), Kataoka & Ishii (1982), Schadel *et al.* (1990), Hewitt & Govan (1990) and Nigmatulin *et al.* (1996) among others. The method proposed by Hutchinson & Whalley (1973) suggested that the droplet concentration in  $R_A$  should be characterized in terms of the following dimensionless group

$$S = \frac{\tau_i \cdot s}{\sigma} \quad (2.10)$$

where  $\tau_i$  is the interfacial stress and  $s$  is the film thickness.

---

<sup>1</sup> The dimensionless group  $S$  is a form of the Weber number  $We = \frac{\rho \cdot U^2 \cdot l}{\sigma}$  where  $l$  is a characteristic length.

The expression proposed by Kataoka & Ishii (1982) includes a surface tension dependence and it was based on a force balance at the gas-liquid wavy interface.

For the fully developed region:

$$\frac{R_A D}{\mu_l} = 6.67 \cdot 10^{-7} (\text{Re}_l \text{We}_l)^{0.925} \times \left( \frac{\mu_g}{\mu_l} \right)^{0.26} (1-E)^{0.185} \quad (2.11)$$

$$\text{where } \text{We}_l = \frac{\rho_g U_g^2 D}{\sigma} \left( \frac{\Delta \rho}{\rho_g} \right)^{1/3} \quad (2.12)$$

Schadel *et al.* (1990) suggested that the rate of deposition and hence the rate of entrainment is given by:

$$R_D = \frac{0.034}{D^{0.6}} \frac{M_{LE}}{Q_g} \quad \text{for } \frac{M_{LE}}{Q_g} \leq \frac{0.078}{D^{0.6}}; \quad \text{and} \quad (2.13)$$

$$R_D = \frac{0.021}{D^{0.6}} \quad \text{for } \frac{M_{LE}}{Q_g} > \frac{0.078}{D^{0.6}} \quad (2.14)$$

Hewitt & Govan (1990) made further improvements by noting that there was a film rate below which there was not entrainment. They related the film flowrate to the excess film flowrate above this minimum value. They developed an empirical deposition rate equation using a large databank. This has the form:

$$\frac{R_D}{m_g} = 5.75 \cdot 10^{-5} \left[ (m_{LF} - m_{LFC})^2 \frac{D \rho_l}{\sigma \rho_g^2} \right]^{0.316} \quad (2.15)$$

Many researchers also agreed that there is an interfacial instability phenomena affecting entrainment. Models of this sort have been published by Bertodano *et al.* (1997) and Holowach *et al.* (2002) although the former did not directly account for this effect. Bertodano *et al.* (1997) modified the  $R_A$  correlation of Kataoka & Ishii (1982) based on new data of higher gas and liquid flows and higher pressures, and a Kelvin-Helmholtz model for ripple growth. They suggested the following correlation:

$$\frac{R_A D}{\mu_l} = 4.47 \cdot 10^{-7} \left[ (\text{Re}_l - \text{Re}_{LF}) \text{We}_g \left( \frac{\Delta \rho}{\rho_g} \right)^{1/2} \right]^{0.925} \left( \frac{\mu_g}{\mu_l} \right)^{0.26} \quad (2.16)$$

It is noted that for  $R_A D / \mu_l > 1$ , the data calculated from the dimensionless correlation deviates from the linear trend.

The complex nature of the interface has made it more convenient to consider correlations utilizing dimensionless groups such as Reynolds and Weber numbers in computer modelling compared to physically based models. Reasonable results have been obtained over a limit range of conditions and fluids but are not satisfactory when extrapolated outside the conditions to which they were derived.

Okawa *et al.* (2000) developed a mechanistic correlation for predicting the entrainment fraction in quasi-equilibrium annular flow. In quasi-equilibrium region of annular two-phase flow, the rate of liquid droplet entrainment  $M_{LE}$  is considered to be almost the same as that of liquid droplet deposition  $M_{LD}$ :

$$M_{LE} = M_{LD}$$

Hence, if  $M_{LE}$  and  $M_{LD}$  are expressed in terms of E, the equation about E is obtained:

$$\frac{E}{1-E} = \frac{1}{4} \cdot \frac{k_E}{k_D} \cdot \frac{\sqrt{f_i f_w} \sqrt{\rho_g \rho_l U_g^2 D}}{\sigma} \cdot \left( \frac{\rho_l}{\rho_g} \right)^n \equiv R \quad (2.17)$$

where  $f_i$  and  $f_w$  are the interfacial friction factor and the wall friction factor,  $n$  is a constant and  $R$  is a dimensionless number. The following correlation proposed by Wallis (1969) is adopted for estimating  $f_i$  and  $f_w$ :

$$f_i = 0.005 \cdot \left( 1 + 300 \cdot \frac{s}{D} \right) \quad (2.18)$$

$$f_w = \max \left( \frac{16}{\text{Re}_f}, 0.005 \right) \quad (2.19)$$

where  $\text{Re}_{LF}$  is the liquid film Reynolds number defined by:

$$\text{Re}_{LF} = \frac{\rho_l \cdot U_{LF} \cdot D}{\mu_{LF}} \quad (2.20)$$

Govan *et al.* (1998) pointed out that the mass transfer coefficient of droplet deposition decreases with increasing droplet concentration in gas core. Using their result,  $k_D$  is correlated by:

$$k_D \cdot \sqrt{\frac{\rho_g D}{\sigma}} = 0.0632 \cdot \left( \frac{C}{\rho_g} \right)^{-0.5} \quad (2.21)$$

There are not available correlations of  $k_E$  in literature. By giving tentative value of 1 m/s to  $k_E$  (eq. 2.17) and setting the value of  $n$  at 0.2, the relation between  $R$  and the entrainment fraction is obtained:

$$\frac{E}{1-E} = 1.85 \cdot 10^{-4} \cdot R^{1.06} \quad (2.22)$$

The following correlation of  $k_E$  is obtained for the entrained fractions measured in a wide range of flow conditions:

$$k_E = 1.85 \cdot 10^{-4} \cdot R^{0.06} \quad (2.23)$$

### 2.3.2 Interfacial waves

The understanding of annular flow is complicated by the highly disturbed nature of the liquid surface. There are two main types of waves on the surface. They are the ‘ripple’ and ‘disturbance’ waves. Ripples are small capillary type waves with small amplitudes and a relatively high frequency. They do not maintain their identity over any considerable distance (Owen (1986)).

It is now agreed that entrainment occurs when disturbance waves, needed for droplet creation, are present. Proof of this is provided by Azzopardi & Whalley (1980) and Hills (1997). Hewitt & Hall-Taylor (1970) noted that entrainment was caused by “undercutting” and “rolling” of the disturbance waves. This only happens when a critical film flowrate,  $m_{LFC}$ , is exceeded. These waves, shown in figure 2.1.3 are frothy two-dimensional flow surges with high amplitudes. They maintain their identity over considerable distances and travel at higher velocities compared to that of the liquid film. Disturbance waves have a uniform velocity which increases with increasing gas velocity and are circumferentially coherent (Hawkes (1996)).

### 2.3.3 Deposition mechanism

Initially, it was assumed that the deposition process is caused by droplets interacting with turbulent eddies. Eventually, the droplets are deposited onto the liquid film in a random diffusion-like manner. This concept that all drops are deposited by a diffusion-like mechanism was questioned by James *et al.* (1980) who employed the shadowgraphy technique of Hewitt & Whalley (1980) to observe drop behaviour. They reported that the (larger) drops that were visible did not move in a random manner but travelled across the cross section in straight lines. This was caused by the initial impetus given to the drop by the entrainment process. They divided the depositing drops into two classes, those which landed by 'direct impaction' and those which arrived by a diffusion-like process, Azzopardi (1997). Jepson (1992) considered a larger data set and showed that the direct impaction component is more prevalent at low gas velocities, smaller tube diameters, lower gas densities and higher surface tension. To determine which of the two components was more dominant, Azzopardi (1997) proposed the following equation where the fraction of droplets deposited by diffusion,  $F_D$ , can be determined.

$$F_D = 1 - e^{-\left[2.217 \frac{We_g^{1.42}}{Re_g^{0.98}} + 0.27\right]} \quad (2.24)$$

Azzopardi (1997) suggested that this concept of deposition by diffusion and by direct impaction might be linked with the increase of entrained fraction with decreasing gas velocity found in the churn flow pattern.

### 2.3.4 Entrainment mechanism

The break-up of disturbance waves at the surface of the liquid film will result in entrainment. Two mechanisms by which the droplets in motion relative to the gas

phase in annular flows may break-up are bag break-up and ligament break-up. The details of these processes can be found in Owen (1986) and Azzopardi (1997). ‘Bag break-up’ process is initiated by ‘under-cutting’, which occurs at lower gas and liquid flowrates. At high flowrates, ‘ligament break-up’ is initiated by ‘rolling’ of the wave. These mechanisms of droplets entrainment are shown in figure 2.3.1.

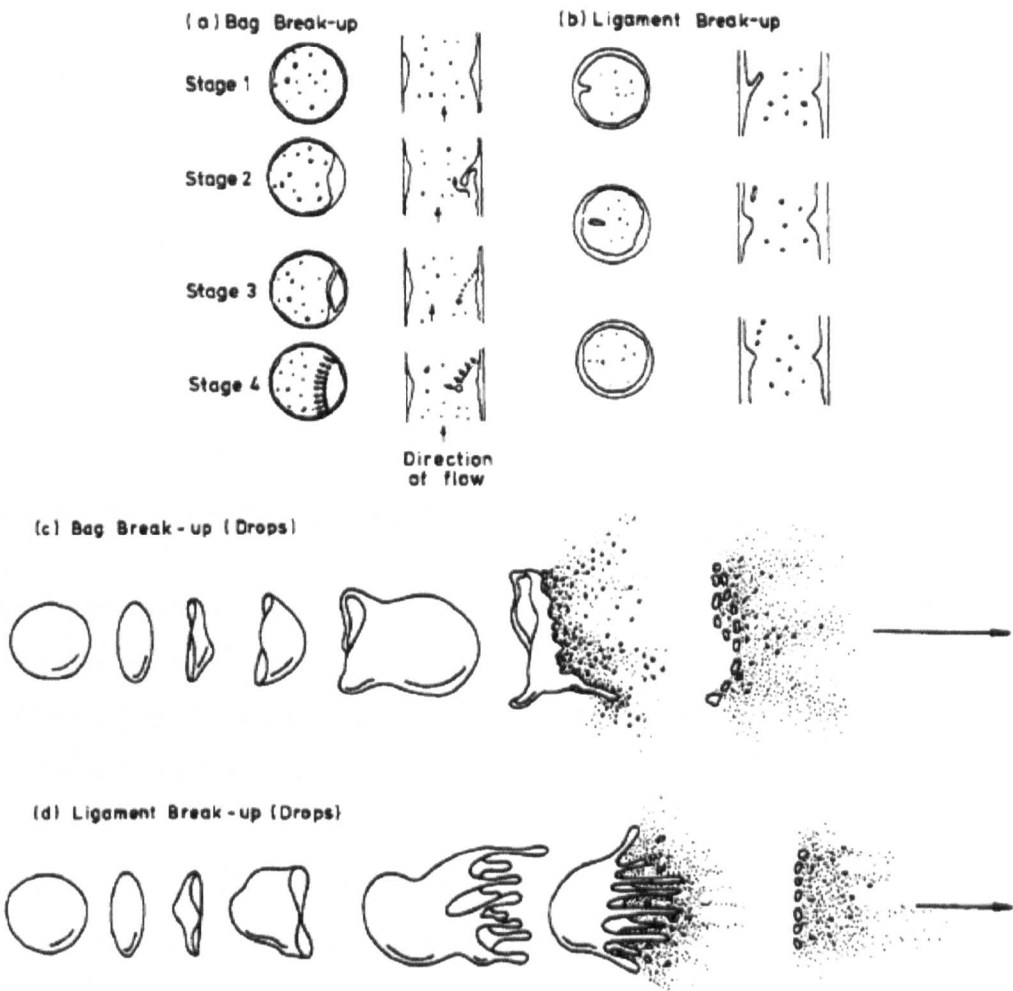


**Figure 2.3.1:** Mechanism of droplet entrainment. Figure taken from Azzopardi (1997)

### 2.3.5 Critical film flowrate

It is now known that entrainment occurs if the liquid film flowrate exceeds what is known as the critical film flowrate,  $m_{LFC}$ . According to Owen (1986),  $m_{LFC}$  can be applied in two ways:

- $m_{LFC}$  represents the minimum liquid film flow for the onset entrainment at low flows;
- At high flows,  $m_{LFC}$  is the minimum achievable film flowrate irrespective of gas velocity, often called “the fully-entrained limit”.

Azzopardi *et al.* (1983) who employed dimensional analysis produced a graphical form for inception of entrainment based on the dimensionless groups,  $Re, \sqrt{On}$  (liquid Reynolds number and the Onhenzoge number,  $\left( On = \frac{\mu_l}{\sqrt{\sigma \rho_l D}} \right)$ ), and a dimensionless gas velocity, the ratio of the Weber number and the gas Reynolds number ( $We/Re_g = \mu_g U_{sg} / \sigma$ ). Based on available experimental data, Abolfadl (1984) specified the start of entrainment as  $Re = 368$ . He ascribed the phenomenon to the onset of turbulence in the film.

Some of the recent correlations developed for  $m_{LFC}$  are by Ishii & Grolmes (1975), Asali *et al.* (1985), Owen (1987), Schadel (1990) and Hills (1997):

Ishii & Grolmes (1975):

$$Re_{LFC} = \left( \frac{y^+}{0.347} \right)^{1.5} \left( \frac{\rho_l}{\rho_g} \right)^{0.75} \left( \frac{\mu_g}{\mu_l} \right)^{1.5} \quad (2.25)$$

$y^+$  is the non-dimensional distance from the wall = 10.

Asali *et al.* (1985):

$$\text{Re}_{LFC} = \exp(5.3050 + 0.6570(\mu_g / \mu_l)(\rho_l / \rho_g)^{0.5}) \quad (2.26)$$

Owen (1986):

$$\text{Re}_{LFC} = \exp(5.8405 + 0.4249(\mu_g / \mu_l)(\rho_l / \rho_g)^{0.5}) \quad (2.27)$$

The method of Hills (1997) is in an adaptation of that of Schadel:

$$m_l = m_{LFC} + k' m_{LE} \quad (2.28)$$

$$k' = a U_g^\alpha \rho_g^\beta \quad (2.29)$$

Ishii & Grolmes (1975) ascribed the critical film flow limit as the penetration of the boundary layer of the gas. Asali *et al.* (1985) analysed the stability of the disturbance waves on the interface to develop a graphical correlation relating the critical liquid Reynolds number with the group  $(\mu_l / \mu_g) \sqrt{(\rho_l / \rho_g)}$ . Owen modified this relation to account for evaporation of the film due to the humidity. Schadel *et al.* (1990) varied the liquid flow at constant gas rates and plotted  $R_A$  against the total liquid flowrate. By extrapolating back to zero  $R_A$ , they were able to estimate  $m_{LFC}$  as a function of gas rate for air-water systems for tube diameters of 25.4, 42 and 57.2 mm. The method of Hills (1997) is an adaptation of that of Schadel. The  $k'$  values in the equations by Hills (1997) are the gradients of graphs of  $m_l$  against  $m_{LE}$ . By performing a multiple regression on Equation (2.29), the constants  $a$ ,  $\alpha$  and  $\beta$  can be determined. A plot of  $m_l$  against  $k' \cdot m_{LE}$  will give a general  $m_{LFC}$  (y-intercept). The assumptions made by Hills (1997) are that  $m_{LFC}$  are independent from  $U_{sg}$  and  $\rho_g$  and that  $m_{LE} / U_{sg} \leq 0.62 \text{ kg/m}^3$ .

The method by Schadel *et al.* (1990) will only be applied well if there are enough experimental points near the critical flow limit to justify the extrapolation to zero film flowrate. The method by Hills (1997) on the other hand, considers many empirical assumptions and it is too implicit. An explicit analytical equation would be preferred for ease of computation.

### 2.3.6 Entrainment and deposition in Venturi

The geometry of the Venturi and the liquid introduction arrangements (Behie & Beeckmans, 1974, Mayinger & Lehner, 1995) and (Rudnick *et al.*, 1986) can have a strong influence on the performance of Venturis. This is probably due to the effect of hydrodynamics, which results in different pressure drops and liquid film distribution.

Many studies have observed the presence of a wavy film flowing on the walls of Venturis. Boll (1973), Azzopardi & Govan (1984), Koehler *et al.* (1987), Leith *et al.* (1985) and Viswanathan *et al.* (1997) are some of the most significant examples. The disadvantages of the film are evident: for gas cleaning purposes, the film is relatively inefficient in terms of particle collection and acts as a rough surface on the walls, thus increasing the shear stress when compared to a smooth wall. On the other hand, it increases heat transfer through the walls and it protects the equipment from corrosion, abrasion and the deposition of sticky dust.

Although the existence and influence of the liquid film flowing on the walls of Venturi has long been recognised (Azzopardi, 1993) only a few of the models proposed thus far include this parameter (Azzopardi & Govan, 1984, Viswanathan *et al.*, 1985, Leith *et al.*, 1985 and Muir & Kuye, 1986). Unfortunately, the tools for the estimation of the fraction flowing as a film are more limited.

After the liquid is introduced in the pipe, the film can be formed in one of these two ways. When the liquid is introduced as a jet, the water would initially be flowing in the gas core, but a fraction is deposited on the walls of the equipment forming a film. If the liquid is introduced as a film deposition is not necessary for the presence of the film. Once the film is formed, a part of it can be re-entrained into the gas core by a mechanism similar to the entrainment found for straight pipes in annular two-phase flow, figure 2.3.2.

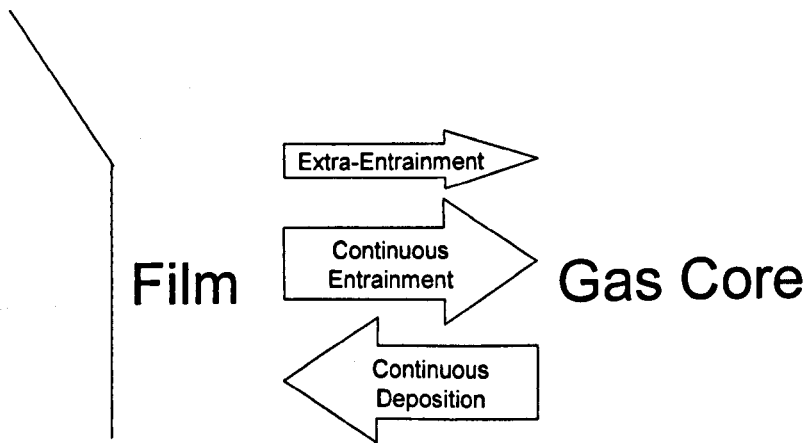


**Figure 2.3.2:** Schematic representation of the variation of film flow

Additionally, in the case of Venturis, the film on the walls has to deal with the corners of the equipment. Due to the sudden change in direction, the film is disturbed. Consequently, a fraction of the film is entrained into the gas core. This type of entrainment is called “extra-entrainment” to differentiate it from the other mechanism. Azzopardi & Govan (1984) proposed a simple equation for the estimation of the extra-entrainment. Their relationship was based on the limited available data. They assumed that the liquid arriving as a film at the corner would be split between film and drops in proportion to the half angle of the convergence. This was corrected in a later work (Azzopardi & Govan, 1985), which considered that no

liquid would be entrained below a certain film flow. The occurrence of “extra-entrainment” at the corner between the throat and the divergence has been suggested by Koehler *et al.* (1987) in order to explain results of drop distribution measurements in experiments where the liquid was introduced through multiple axial jets upstream of the Venturi. It must be noted that there are some large errors in the results of the experiments of Koehler *et al.* (1987). Fractions of entrained water significantly higher than 1 were reported.

Most of the equations and models proposed for Venturis assume complete atomisation of the liquid. Calvert (1970) and Boll (1973) are two of the most significant examples. A general estimation of the film fraction can be made using the model of Azzopardi & Govan (1984), and its later improvements. They based their model on the similarities to a two-phase annular flow. Their model includes the features of continuous deposition, entrainment and the so called “extra-entrainment”. In the rest of the proposed models (Viswanathan *et al.*, 1985, Leith *et al.*, 1985 and Muir and Kuye, 1986) the film fraction is found empirically, and introduced into the model. Only very recently, Viswanathan *et al.* (1997) have proposed a more general semi-empirical correlation based on the equation of Adelberg (1967) for the penetration of a liquid jet.

Following on from above, it can be concluded that a more detailed experimental study of the liquid fraction flowing as a film in Venturi is necessary. In Fernandez (2000), several experiments were carried on varying four main parameters: liquid introduction arrangement, gas velocity, liquid to gas ratio and length of throat. His study gave a more precise insight into the phenomena influencing the entrained fraction in Venturi.

## 2.4 Pressure gradient

One of the major requirements of a two-phase flow model is the prediction of pressure drop. The pressure loss in a system is an essential variable for the determination of the pumping energy for a given flow. The following sections provide details of calculations of pressure gradient.

### 2.4.1 Basic equations

A momentum balance on a section of a two-phase flow (figure 2.4.1) will produce a basic pressure gradient equation as shown below, details of which can be found in Owen (1986). The following equation shows the three major components of the pressure gradient.

$$-\frac{dP}{dx} = -\frac{dP_{fric}}{dx} - \frac{dP_{acc}}{dx} - \frac{dP_{grav}}{dx} \quad (2.30)$$

The resulting two-phase flow integral momentum equation of (2.30) is shown below:

$$\int_A -\frac{dP}{dx} dx dA + \int_P -\tau_o dx dp + \int_A -\rho g dx dA = \int_A \frac{d}{dx} (m_l U_l + m_g U_g) dx dA \quad (2.31)$$

Addition of a void fraction term,  $\varepsilon_g$ , will simplify the above equation:

$$\bar{\rho} = \varepsilon_g \rho_g + (1 - \varepsilon_g) \rho_l \quad (2.32)$$

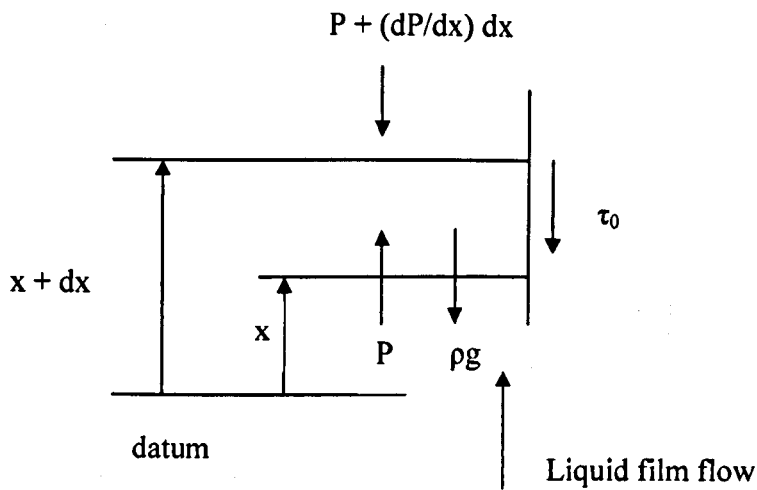


**Figure 2.4.1:** Momentum balance on an element of annular vertical upward flow

## 2.4.2 Homogeneous and separated models

The homogeneous model is the simplest but most inaccurate of the models. This is based on the assumptions that the flow behaves as a single-phase homogeneous mixture and that the velocity and density of this mixture are constant across the channel.

With the assumption of the homogenous model, equation (2.31) simplifies to:

$$-\frac{dP}{dx} = \frac{p}{A} \tau_0 + m_H \frac{dU_H}{dx} + \rho_H g \quad (2.33)$$

where  $p$  is the channel perimeter,  $A$  is the channel cross-sectional area and  $U_H$  is the velocity of the homogeneous mixture.

The separated flow model assumes that there is a negligible interaction between the two phases and that they flow separately in the channel as shown in Appendix B.1.

The resulting equation is shown below and the relative calculations are shown in Appendix B.1.

$$-\frac{dP}{dx} = \frac{4\tau}{D} + (\rho_g \varepsilon_g + \rho_l (1 - \varepsilon_g))g \sin \alpha + m^2 \frac{d}{dx} \left( \frac{x_g^2}{\varepsilon_g \rho_g} + \frac{(1 - x_g)^2}{(1 - \varepsilon_g) \rho_l} \right) \quad (2.34)$$

If liquid entrainment is considered in the determination of pressure gradient, then the only term affected by this variable is the acceleration term. The resulting equation for

$-\frac{dP_{acc}}{dx}$  is shown below:

$$-\frac{dP_{acc}}{dx} = m^2 \frac{d}{dx} \left( \frac{x_g}{\rho_g} [x_g + E(1 + x_g)] \right) \quad (2.35)$$

### 2.4.3 Frictional pressure gradient

For homogeneous flow, the frictional component is as follows:

$$-\frac{dP_{fric}}{dx} = \tau \frac{p}{A} = \tau \frac{4}{D} = \frac{4f}{D} \frac{\rho \bar{U}^2}{2} = \frac{4f}{D} \frac{m^2}{2\rho} \quad (2.36)$$

where the friction factor  $f$  depends on the Reynolds number  $Re = \frac{\rho \cdot U \cdot D}{\mu}$  of the flow and the relative roughness  $e/D$  of the pipe wall:

$$f = \frac{64}{\text{Re}} \quad \text{for } \text{Re} \leq 2100 \quad (2.37)$$

$$f = 0.079 \text{Re}^{-0.25} \quad \text{for } 3000 \leq \text{Re} \leq 10^8 \text{ and } 10^{-6} \leq \frac{e}{D} \leq 10^{-2} \quad (2.38)$$

In separated two-phase flow the following expression is used:

$$\tau \frac{P}{A} = \frac{4 f_{TP} \rho_{TP} \bar{U}^2}{D \cdot 2} = \frac{2 f_{TP} m^2}{D \rho_{TP}} \quad (2.39)$$

It can also be expressed in the form:

$$\tau \frac{P}{A} = \frac{4 f_{TP} \rho_{TP} \bar{U}^2}{D \cdot 2} = \frac{2 f_{SP} m^2}{D \rho_{SP}} \phi^2 \quad (2.40)$$

where  $\phi$  is named two-phase multiplier.

Thus the equation (2.40) leads to the following conclusion:

$$\left( \frac{dP_{fric}}{dx} \right)_{TP} = \left( \frac{dP_{fric}}{dx} \right)_{SP} \cdot \phi^2 \quad (2.41)$$

Hewitt (1983) suggested the following guidelines in calculating the frictional pressure drop:

If  $\mu_l/\mu_g < 1000$ , use Friedel (1979)

If  $\mu_l/\mu_g > 1000$ , use Chisholm (1973)

If  $\mu_l/\mu_g > 1000$  and  $m_{TP} < 100 \text{ kg/m}^2\text{s}$ , use Lockhart and Martinelli (1949).

These three methods are shown in Appendix B.2. Other correlations had been given by Baroczy (1966), Premoli *et al.* (1970), Lombardi and Ceresa (1978) (see Holt (1996)) and Muller-Steinhagen and Heck (1986).

#### 2.4.4 Gravitational pressure gradient

The gravitational component depends on the mean void fraction,  $\varepsilon_g$ . For the case of vertical upward flow, this term will result in a pressure loss.

$$-\frac{dP_{grav}}{dx} = [\varepsilon_g \rho_g + (1 - \varepsilon_g) \rho_l] g \sin \alpha \quad (2.42)$$

#### 2.4.5 Acceleration pressure gradient

This component deals with the loss of momentum flux through the section of a duct. Usually for adiabatic flows, where changes of momentum flux will increase the pressure gradient, this term can be calculated using the homogeneous model<sup>2</sup> ie:

$$-\frac{dP_{acc}}{dx} = \frac{d}{dx} \left[ m^2 \left( \frac{x_g^2}{\varepsilon_g \rho_g} + \frac{(1 - x_g)^2}{(1 - \varepsilon_g) \rho_l} \right) \right]_{x_1}^{x_2} \quad (2.43)$$

---

<sup>2</sup>  $\varepsilon_g = \varepsilon_{gh}$  is recommended for non condensing flows

### 2.4.6 Pressure drop in Venturi

Pressure drop is a key parameter in the performance of Venturis. It is directly linked to the energy cost in terms of pumping gas and liquid. Consequently, its prediction is a very important step in the design process.

The study on pressure drop in Venturi has been carried on for several reasons. The two most important are:

- Metering
- Gas cleaning by using Venturi scrubbers, Appendix A

The metering interest is on the pressure drop  $\Delta p_1$  across the start of the convergence and the throat, figure 2.4.2. On the other hand, the gas cleaning interest is on the pressure drop  $\Delta p_2$  across the start of the convergence and the end of the divergence, figure 2.4.2.

In applications of Venturi as flow meter, the following relation has to be taken into account:

$$\frac{\Delta p_{ii}}{P_i} \leq 0.02 \quad (2.44)$$

In Equation (2.44)  $\Delta p_{ii}$  is the pressure difference between the Venturi inlet and the throat and  $P_i$  is the pressure at the Venturi inlet. The reason behind equation (2.44) is that high pressure losses along a pipeline mean high amount of energy needed to pump the mixture of fluids. The velocity of this mixture is also related to the pressure along the pipeline. In the oil & gas industrial applications a multi-phase flow is constituted by gas, liquid and particles of sand. The presence of sand is one of the main causes of erosion of the pipe walls. Therefore, a high velocity of these

particles can contribute to the deterioration of the pipe and must be avoided. Therefore, the gas velocity in oil and gas applications has to be lower than:

$$U_{sgMax}=30 \text{ m/s}$$

For these two reasons, flow conditions and fluid properties must be always taken into account for the design and building of pipelines and flow meters.

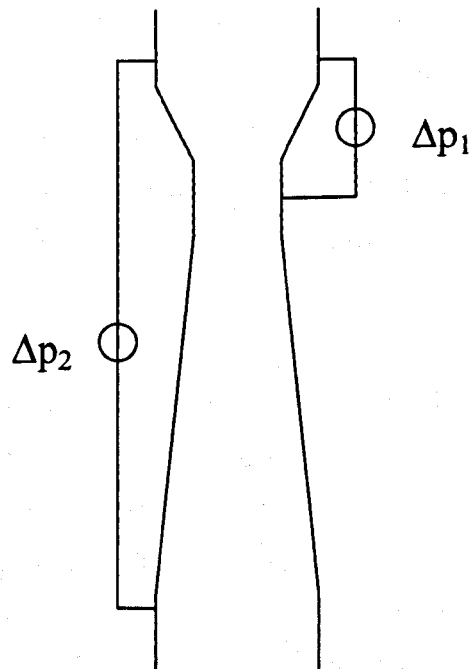


**Figure 2.4.2:** Interests in pressure drop in Venturi

Two kinds of pressure drop model exist in literature: theoretical ones and empirical ones. The theoretical models which are considered having relative significant influence in history are the models of Boll (1973), Yung *et al.* (1977) and Azzopardi & Govan (1984). The third model is used for a comparison with the present experimental data in Chapter 6. Although purely based on experimental data, empirical models can also provide predictions of pressure drop but they are normally

limited to the database from which they were obtained, e.g., Hesketh (1974). Therefore, they are not included in this thesis. Furthermore, there is a tremendous amount of experimental measurements on total pressure drop or pressure drop profile (Baker, 1962; Yung *et al.*, 1981; Yung *et al.*, 1984; Rudnick *et al.*, 1986; Haller *et al.*, 1989; Allen and Van Santen, 1996; Fernandez, 2000; Sun, 2003) available in the research history on Venturi used for gas cleaning or metering purposes.

Early workers considered only acceleration and deceleration of gas and droplets (Calvert, 1970) as the cause of pressure drop in Venturi. Once the liquid is injected and atomised, it is accelerated because of the high relative velocity between the gas and the droplets. In this process, the momentum of the gas is transferred to the liquid, causing an inevitable exchange of energy. Authors such as Calvert (1970) or Yung *et al.* (1977) have considered this mechanism, which influences pressure drop, as the most important, while ignoring other mechanisms that will be described later in this Chapter.

Calvert (1970) proposed a simple description for the prediction of the total pressure drop in Venturi. His relationship is one of the most popular among engineers, probably because of its simplicity. Calvert (1970) assumed that all the liquid is atomised into droplets, and these droplets are accelerated to the velocity of the gas at the end of the throat. He also assumed that there is no pressure recovery in the diffuser due to drop deceleration. He suggested that this would compensate pressure drop due to shear stress between the film or wall and the gas. As a result, he proposed this:

$$\Delta P = \frac{\rho_l}{1000} \frac{L}{G} U_{sg}^2 \quad (2.45)$$

Calvert (1977) observed that in practical cases equation (2.45) predicted values of pressure drop 15% higher than those experimentally found, except at low values of

liquid to gas ratio. It can be observed in equation (2.45) that Calvert (1970) did not provide for any effect derived from the geometry of the Venturi. For example, his equation cannot predict different pressure drops for Venturi with different throat lengths.

Yung *et al.* (1977) also considered that pressure drop in Venturis is simply the result of the acceleration of drops in the throat. Friction and other aspects were ignored in this model, and there was no pressure recovery due to drop deceleration in the diffuser. In contrast to the work of Calvert (1970), drops do not necessarily reach the velocity of the gas at the end of the throat. The model of Yung *et al.* (1977) assumes that all liquid is atomised into uniform drops whose diameter is given by the correlation of Nukiyama & Tanasawa (1938). Yung *et al.* (1977) determined the drop acceleration using the drag coefficient proposed by Hollands & Goel (1975). Their prediction for drop velocity at the end of the throat is given by:

$$U_{drop,f} = U_{sg} \left( 1 - Y^2 + \sqrt{Y^4 - Y^2} \right) \quad (2.46)$$

Y is a dimensionless parameter defined as:

$$Y = \frac{3 l_1 C_D \rho_g}{16 D_{drop} \rho_l} + 1 \quad (2.47)$$

The total pressure drop is then given by:

$$-\Delta P = \rho_l L/G \beta U_{sg}^2 \quad (2.48)$$

Parameter  $\beta$  is given by:

$$\beta = 2 \left( 1 - Y^2 + \sqrt{Y^4 - Y^2} \right) \quad (2.49)$$

Boll (1973) proposed a model including more features than that of Yung *et al.* (1977). In the model of Boll (1973), pressure drop is integrated along the Venturi using equation (2.50). Boll (1973) also assumed that all liquid was atomised to form drops whose diameter was given by the Nukiyama & Tanasawa (1938). In contrast, his model provides details for pressure drop due to friction between the wall and the gas. Boll (1973) proposed that the shear stress produced in the case of Venturi should be higher than that of a smooth pipe due to the presence of a film of liquid on the walls of the equipment. This film has a rough surface, thus increasing friction. Boll (1973) estimated the pressure drop due to this mechanism from his empirical data, and proposed a Moody friction factor in order to calculate the wall-gas stress. Equation (2.50) reproduces the momentum equation of the model of Boll (1973).

$$-\frac{dP}{\rho_g} = U_g dU_g + \frac{L}{G} \frac{\rho_l}{\rho_g} U_g dU_{drop} + \frac{\left( \frac{L}{G} \frac{\rho_l}{\rho_g} + 1 \right) f U_g^2}{D_{eq}} dx \quad (2.50)$$

The model of Azzopardi & Govan (1984) was based on their knowledge in the field of gas/liquid annular flow. Gas/liquid annular flow is characterised by the existence of a film flowing on the walls of the equipment and a gas with droplets flowing in the core. Azzopardi & Govan (1984) observed that the nature of hydrodynamics in Venturi could be described in a similar manner. The main feature in the model of Azzopardi & Govan (1984) was the exchange of liquid between film and gas core. New droplets are continuously stripped off from the film, called entrainment, while other drops are deposited onto the film. Taking this into account they were able to develop mass balances for film and liquid in the core, being able to estimate the liquid split between the film and the gas core at each position along the Venturi. Their mass balance on the film leads to:

$$\frac{dM_{LF}}{dx} = \pi D (m_{dep} - m_{ent}) \quad (2.51)$$

The initial film flow is introduced as a parameter into the model, and it will depend on the liquid injection arrangement. From this point the model is able to calculate the fluxes of entrainment and deposition by equations of this kind:

$$m = k_{mass} C \quad (2.52)$$

Where  $k_{mass}$  is a constant of mass transfer obtained from empirical data in two-phase annular flow. After the calculation of the fluxes of entrainment and deposition, it is possible to evaluate the liquid film flow using equation (2.51). A numerical integration of these equations leads to the estimation of film flow at any point along the Venturi.

Following the ideas of Azzopardi & Govan (1984), Viswanathan *et al.* (1985) tried to describe the flow in a Venturi scrubber in a very similar manner to that of two-phase annular flow. This model also includes the feature of liquid flow, with part of the liquid flowing as droplets in the gas core and the rest as a film on the walls of the equipment. Unfortunately, Viswanathan *et al.* (1985) did not provide any tool for the estimation of the fraction of liquid flowing as a film. In fact, they introduced this parameter in their model using their own empirical data. Consequently, unless the film flow is measured experimentally, or the fraction of water is estimated somehow [e.g. using model of Azzopardi & Govan (1984)] there is a parameter missing in order to implement this model. In any event, it appears quite clearly that the estimation of the fraction of water flowing as a film is necessary if accurate estimations of pressure drop are required.

The velocity of the gas along a Venturi changes due to the effect of geometry. This variation of kinetic energy in the gas is compensated by an equivalent variation in pressure. Boll (1973) showed that pressure drop due to changes of kinetic energy of the gas could be approximately described using the continuity equation of the gas and the equation of Bernoulli. If the density of the gas is approximately constant and the

diameter of the tube at the inlet and outlet are the same, the entire pressure drop caused, as a result of this mechanism, would be recovered in the divergence of the Venturi. In reality, the recovery is not perfect, and some energy is lost. This effect is caused by the negative gradient of pressure in the diffuser, which creates a growth of the boundary layer (Teixeira, 1989). Teixeira (1989) and Azzopardi *et al.* (1991) extended the model of Azzopardi & Govan (1984) in order to include this feature. This model represents the flow in a Venturi quite realistically. On the other hand, it requires many equations and needs more complicated algorithms. A detailed description of this model can be found in the work of Pulley (1997).

The fraction of liquid flowing as a film on the walls of a Venturi could be quite significant. The film can also be accelerated due to the relative velocity between the film and the gas. Azzopardi & Govan (1984) included the acceleration of the film in their model, so the pressure drop due to this acceleration could be calculated, figure 2.4.3. However, they also showed that the pressure drop created by this mechanism is relatively low. Recently, Sun & Azzopardi (2003) showed that the improved model of Azzopardi *et al.* (1991) correctly predicts pressure drop in Venturi scrubbers for high pressure.

The atomisation of the liquid in a Venturi creates a great amount of new surface. Some energy is spent creating the new interface. This energy can be estimated once the drop size is known. In the case of Venturi this energy is only a very small fraction of the total amount of energy spent in other forms. Pressure drop due to the mechanism of surface creation is of the order of 10Pa. This is very small compared to the total pressure drop, which usually is of the order of various kPa. As a consequence, this feature has not been included in any model so far. It can also be concluded that Venturi are very inefficient as atomisers.

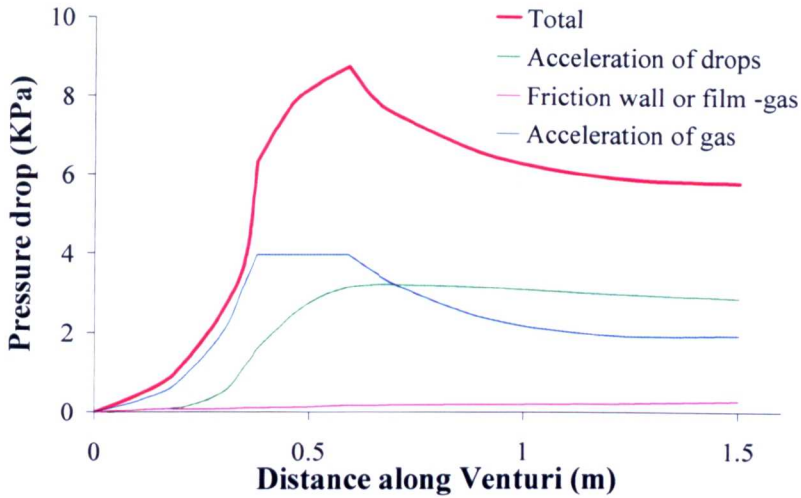


**Figure 2.4.3:** Example of the three main mechanisms of pressure drops in Venturi. Simulation with model of Azzopardi and co-workers, for a Venturi as used by Allen & van Santen (1996),  $D_{\text{throat}} = 0.16$  m,  $U_{\text{GS}} = 89$  m/s,  $L/G = 1.01$  l/m<sup>3</sup>. Figure taken from Fernandez (2000)

The relative importance of each of the mechanisms of pressure drop depends on the operating conditions and also on the scale and geometry of the Venturi. It is important to note that the energy spent accelerating the drops is, as a simple rule of thumb, proportional to the section of the Venturi. In contrast, the energy lost as shear stress between the wall or film and the gas is proportional to the perimeter of the tube. In consequence, the relative importance of these mechanisms is quite different depending on the scale of the Venturi. It can be observed in figure 2.4.3 how the film or wall-gas stress can be as significant as drop acceleration for small scale Venturis at low liquid to gas ratios, even if complete atomisation of the liquid ( $E_f=1$ ) is assumed.

To summarise, numerous models have been proposed for the calculation of pressure drop in Venturi. Some of them are based on simple assumptions (Calvert, 1970 or Yung *et al.*, 1977) and are easy to implement. Others (Azzopardi & Govan, 1984 and its improved versions, or Boll, 1973, among others) include more complicated

algorithms, requiring a more important effort for their implementation. More models for the prediction of pressure drop in Venturi, apart from those described in this section, are available in the literature. Hollands & Goel (1975) can be cited as an illustrative example. The models addressed in this section were chosen because they have been considered the most significant, or they have been compared to the present experimental data. Correlations based on purely empirical data are also available in the literature for the estimation of total pressure drop in Venturi. An illustrative example of this is the correlation proposed by Hesketh (1974).

There is a significant amount of data on pressure drop in Venturi available in the literature. Johnstone *et al.* (1954), Lapple & Kamack (1955) or Brink & Contant (1958) are examples of total pressure drop in a Venturi. Semrau *et al.* (1958), Mayinger & Neumann (1978) and Allen & Van Santen (1996), Van Werwen *et al.* (2001) among others, measured the profiles of pressure drop along their Venturis. All found that pressure drop increased with gas velocity and liquid to gas ratio.

Given the importance of pressure drop in Venturi, the great amount of work dedicated to this subject is well justified. It can be concluded that any improvement or any information that could lead to operations at a lower pressure drop would be very beneficial.

## **2.5 Liquid film thickness**

In the annular flow the liquid flows as a film around the pipe wall, surrounding a high velocity core, which contains entrained liquid droplets. The interface between the gas core and the liquid film is very wavy, and atomization and deposition of liquid droplets occur through this interface. Few experimental and theoretical studies on annular flow have been carried out for inclinations from vertical to horizontal. Changes in the physical phenomena occur as the inclination angle varies from vertical

through off-vertical to horizontal conditions. The effect of the inclination is relevant on liquid hold-up and pressure and must be accounted to enable proper design of pipelines, wellbores and separation facilities. Results on film thickness are presented in Chapter 5.

### 2.5.1 Vertical upward flow

Wallis (1969) and Hewitt & Hall-Taylor (1970) presented general discussion of annular flow. Earlier models for annular flow were developed by Dukler (1960) and Hewitt (1961). More recently, other models have been published by Hasan & Kabir (1988), Yao & Sylvester (1987), Oliemans *et al.* (1986), Caetano (1985), Zabaras *et al.* (1986) and Alves *et al.* (1991).

The physical mechanisms associated with annular flow have also been studied extensively. Turner *et al.* (1969) and Ilobi & Ikoku (1981) studied the minimum gas velocity required for liquid removal from vertical gas wells. Wallis (1969), Henstock & Hanratty (1976), Whalley & Hewitt (1978), and Asali *et al.* (1985) developed interfacial shear stress correlations. The entrainment process was studied by Hanratty & Asali (1983), Shadel *et al.* (1990) and Whalley & Hewitt (1978).

### 2.5.2 Horizontal flow

Measurement of the circumferential film thickness distribution for horizontal flow were reported by McManus (1961), Butterworth (1972), Butterworth & Pulling (1973), Fisher & Pearce (1978), Paras & Karabelas (1991), Paras *et al.* (1994) and Jayanti (1990). Experimental data on film thickness distribution and pressure drop were acquired by Dallman (1978), Laurinat (1982), Nencini & Andreussi (1982) and Laurinat *et al.* (1984). In later studies, Laurinat *et al.* (1985), Lin *et al.* (1985),

Fukano & Ousaka (1989) and Hurlburt & Newell (2000) developed a model for film thickness distribution. Jepson (1988) evaluated a model for large diameter. Recently, Williams (1990) conducted comprehensive studies on the effect of pipe diameter on annular flow in horizontal pipes. Horizontal annular flow in small diameter pipes was studied by Luninski *et al.* (1983). In addition to the acquisition of experimental data for film thickness variation, an analytical model to predict the film thickness at the top and the bottom of the pipe was presented.

Butterworth (1969) presented a model for climbing film flow in an eccentric annular flow. The author has found that the circumferential variations in the liquid film flowrate tend to even out with distance along the channel. This process appears not to be affected by variations in the liquid film thickness or surface shear stress. It was suggested that the process of achieving a uniform liquid film could be described quantitatively by the following equation:

$$\Gamma_{\theta} = -\frac{k \cdot \partial \Gamma_x}{r \cdot \partial \theta} \quad (2.53)$$

where,  $\Gamma_{\theta}$  and  $\Gamma_x$  are the peripheral mass flowrates (flowrates per unit width of surface) in the circumferential and axial directions respectively,  $r$  is the radius of the surface on which the film is flowing,  $\theta$  is the circumferential coordinate angle and  $k$  is the circumferential transport coefficient.

For horizontal annular flow, however, gravitational effects – which tend to stratify the liquid – must be imposed on the effects described by equation (2.53). The correct method of combining these effects is not yet clear since the mechanisms involved in equation (2.53) are unknown. However, Butterworth (1969) assumed that the flow down the walls due to gravity may be given by the equation for laminar flow down an inclined flat plate:

$$\Gamma_{\theta} = \frac{(\rho_l - \rho_g) \cdot \rho_l \cdot g}{3 \cdot \mu_l} s^3 \sin \theta \quad (2.54)$$

where  $\rho_l$  and  $\rho_g$  are the liquid and gas densities respectively,  $\mu_l$  is the liquid viscosity,  $g$  the acceleration due to gravity,  $s$  the film thickness and  $\theta$  the angle of the plane from the horizontal.

Relating equation (2.54) to the flow down the walls of a tube,  $\theta$  becomes the angle which defines the circumferential location around the section of the tube. Also, the effects described by equations (2.53) and (2.54) must be combined. It is assumed here that these effects combine additively although there is a little justification for this assumption. Hence:

$$\Gamma_{\theta} = \frac{(\rho_l - \rho_g) \cdot \rho_l g}{3\mu_l} s^3 \sin \theta - \frac{k \cdot \partial \Gamma_x}{r \cdot \partial \theta} \quad (2.55)$$

Now, for fully developed flow, the film flowrate and film thickness change only with  $\theta$ . The partial derivative in equation (2.55) is therefore replaced by an ordinary derivative. Also, continuity requires that  $\Gamma_{\theta} = 0$  provided that there is not net mass transfer at the interface. Equation (2.55), therefore, becomes:

$$\frac{d\Gamma_x}{d\theta} = \frac{r(\rho_l - \rho_g)\rho_l g}{3\mu_l k} s^3 \sin \theta \quad (2.56)$$

In order to solve equation (2.56), it is necessary to express  $\Gamma_x$  in terms of the film thickness. For thin films, the shear stress in the film may be taken as a constant equal to the interfacial shear stress  $\tau_i$ . Integrating Newton's law of viscosity for constant shear, and integrating the resultant velocity profile over the liquid film gives finally:

$$\Gamma_x = \frac{\rho_l \tau_l}{2\mu_l} s^2 \quad (2.57)$$

Substituting this relationship into equation (2.56) and assuming that  $\tau_l$  is independent of  $\theta$  gives:

$$\frac{ds^2}{d\theta} = 2 \cdot a \cdot s^3 \sin \theta \quad (2.58)$$

where

$$a = \frac{r(\rho_l - \rho_g)g}{3k\tau_l} \quad (2.59)$$

Equation (2.58) may be integrated to give

$$\frac{1}{s} = a \cos \theta + c \quad (2.60)$$

where  $c$  is a constant of integration. The integration constant  $c$  could be evaluated from the following continuity equation for the liquid film:

$$M_{LF} = 2 \int \Gamma_x d\theta \quad (2.61)$$

where  $M_{LF}$  is the liquid film flowrate.

In Chapter 5, experimental data on film thickness will be used to evaluate the constants  $a$  and  $c$ . Once known these two coefficients, the circumferential transport coefficient will be calculated by the following equation:

$$k = \frac{2 \cdot (\rho_l - \rho_g) g}{3 a \tau_l} \quad (2.62)$$

### 2.5.3 Inclined flow

Measurements of the circumferential film thickness distribution for inclined flow were reported by Paz & Shoham (1994). Experimental data acquired for different inclinations, show that the inclination strongly affects the liquid film distribution, figure 2.5.3. Paz & Shoham (1994) also developed a model which has been extended to the entire range of inclination angles, from horizontal to vertical.

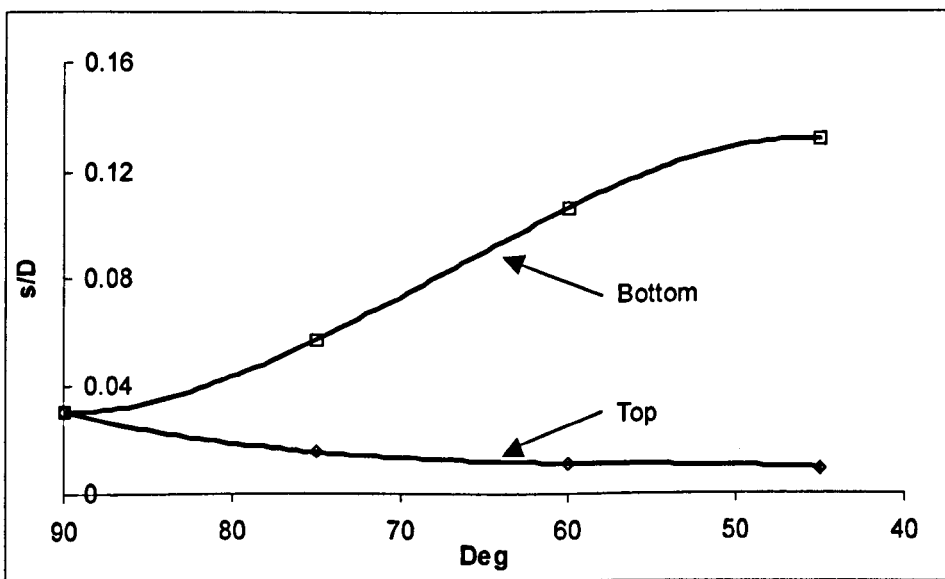


**Figure 2.5.1:** Variation of film thickness with inclination angle. Figure taken from Paz & Shoham (1984)

### 2.5.4 Experimental techniques for liquid film thickness measurements

The most widely used technique for liquid film thickness measurements is based on the different impedance of two media. In particular if the condensed phase is conductive (e.g.: water with dissolved salts), conductance measurements are employed. Capacitance measurements are used in other cases (e.g.: oils). As the conductivity of tap water is several orders of magnitude larger than that of air (virtually 0), the former is employed in the present study. Because the circuit works on alternating current, the total impedance  $Z$  should be considered. Since the water as a resistance and as a capacitor is under the same potential, we should consider it as a capacitor in parallel with a resistance and, therefore, the total impedance is:

$$Z = \sqrt{\frac{1}{R^2} + \frac{1}{X_R^2}} \quad (2.63)$$

where for a frequency  $F$  and capacitance  $c$ , the capacitive reactance is given by  $X_R = 1/(2\pi Fc)$ . For the systems we are dealing with, where  $c \sim 10^{-12}$  F,  $1/X_R$  becomes negligible compared to the resistive component, even when using conventional frequency of the order of 50Hz.

Capacitance probes are used with non-conductive media. In that case, the resistive component is suppressed by the characteristic of the medium.

#### 2.5.4.1 Conductance probe techniques and their design

As evident from the above, by conductance probes we mean the arrangement of two electrodes, extremities of a circuit, which is closed by the liquid film bridging between them. There are several ways to arrange the probes and these result in a large range of response characteristics and hence measured voltage relative to film

thickness. The basic criteria to determine the optimal arrangement of electrodes are listed below:

1. A monotonically growing voltage response with film thickness, with a slope that ensures a good degree of confidence in the measurements.
2. The characteristic dimensions of the probe should be small enough compared with those of the system to ensure locality of measurement.
3. Non-intrusive geometry, probes should not disturb the flow.
4. Probes must work in the expected range of film thickness.

There are three probe configurations, which have been used in the past for film thickness measurement in pipes. These are needle probes, wire probes and flush mounted probes. Barnea *et al.* (1980) used electrical conductance probes to define flow pattern characterization in two-phase flows.

#### 2.5.3.2 Needle probes

This method relies on the contact made between an electrode mounted flush with the pipe surface and the tip of a needle moving across the pipe diameter passing through the fixed electrode. When the tip of the needle is at the gas-liquid interface, the liquid will conduct the signal to the fixed electrode. Because the interface is wavy, it is assumed that the distance between the flush mounted probe and the tip of the needle is equal to the film thickness, when the time of contact with liquid is 50% of the total time of measurement.

The advantage of this method is that it is very precise, it does not require calibration and it is applicable to a wide range of film thickness. Furthermore, the local character of measurement is very good. On the other hand, it can be quite intrusive for thin films and it is particularly laborious to operate.

### 2.5.3.3 Wire probes

In this methodology, the electrodes are constituted of two parallel thin wires stretched along chords of the pipe. As the liquid height varies, the surface of active electrode increases and so the resistance decreases because of the larger area of passage for the electric current. The method relies on calibration depending on geometrical dimensions and conductivity of the medium. The response of this system is fairly linear and can be used for thick films. In fact, the same principle is used in some tank level measurement systems. For thin films it is usually less precise because of its intrusive nature (i.e.: the formation of a meniscus due to surface tension effects). Also, the local character of measurement depends on the distance between the wires.

Hence, this method has been used widely for the measurement of film height in stratified and slug flow.

### 2.5.3.4 Flush mounted probes

This arrangement falls in the general category of flush mounted probes and refers to a particular geometry of the electrodes. The method is used for very thin films, typically up to 2 mm. In this case, each electrode is a pin mounted flush with the pipe surface and coupled to another electrode close to it. If care is taken in the mounting of probes, the method is virtually non-intrusive, but because the active surface of the electrodes does not vary with film thickness, the response is not linear when the thickness exceeds a value depending on diameter and separation between the probes. The electric field is very weak away from the pipe surface and has a negligible contribution to the passage of current. The response is initially linear close to the pipe wall (typically up to 2 mm) and then asymptotically flattens to a uniform value. To enlarge the range of measurements, the diameter and separation of pins can be increased. An optimum balance must be struck between range of operability and

local character of the measurement. Other common flush mounted probes have concentric electrodes or parallel strips.

## **2.6 Recommendations for data processing and analysis**

The computer has proven to be a very powerful tool for control and measurement purposes in experiments and, therefore, has become an essential tool in research. It offers the opportunity for advanced data processing that is superior to analogue counterparts. However, other devices are necessary to collect, analyse and interpret the information gained from experiments, e.g., transducer and data acquisition card. Using transducers the experiments properties are converted into (analogue) electrical signals. The conversion of analogue signals to a digital format plays a crucial role in the process of data acquisition and data processing. The rate of data and the volume of data that must be stored depend on the digitizing system. This conversion is, however, less straightforward than is often thought. As a consequence, the errors introduced in the digitizing process are often neglected or underestimated. The quantization, both in amplitude and time, changes the properties of the signal both in spectral and temporal terms. The latter is very often overlooked.

Bessem & van Maanen (1994) have tried to optimize the digitizing process and to quantify the errors introduced. The data flowrate and the volume of data are reduced as much as possible without sacrificing the accuracy by making use of the properties of the signal itself. These signals are of a stochastic nature, and therefore require long averaging times and a wide spectral bandwidth. But the temporal properties of the signal also contain important information that must be preserved, e.g., if causal relations are to be recognized in the evolution of the signals.

### 2.6.1 Sampling frequency

In order to process the analogue output of a measuring system with a digital computer the signal must be transformed to the digital domain, figure 2.6.1.

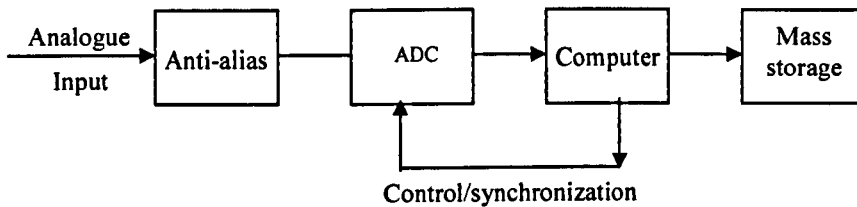


**Figure 2.6.1:** Signal flow diagram

Bessem & van Maanen (1994) restricted their study to systems that sample the signal periodically, the sampling frequency  $F_s = 1/\Delta t$ , in which  $\Delta t$  is the time between two successive samples. If the sampling frequency is chosen too low, information is lost and the digital version of the signal will be a distorted copy of the analogue signal. On the other hand, the amount of data increases proportional to  $F_s$ , thus increasing the data processing requirements. Moreover, if the measurement time  $\Delta t$  is reduced, the statistical reliability of the results at low frequencies is reduced.

The anti-aliasing filter is required in any periodically sampling system if the input signal should be reconstructed from the samples uniquely; the sampling frequency has to be at least twice the highest frequency in the spectrum of the signal (Shannon sampling theorem, see Bessem & van Maanen (1994)). The Nyquist frequency or folding frequency  $F_n (= F_s/2)$  (see Bessem & van Maanen (1994)) is the highest recoverable frequency in the spectrum of the signal. In general, an anti-aliasing filter is required because a guarantee can hardly ever be given that the signal will not contain frequencies above the Nyquist frequency. These components will be aliased into the spectrum of the sampled signal between 0 and  $F_n$ . This can cause a serious reduction in the signal-to-noise ratio in the digital system if the bandwidth is

significantly larger than  $F_n$ , as it will be in the presence of wide band noise. The experimenter must choose the type of filter and the cut-off frequency of the filter.

### 2.6.2 Fourier transform and power spectrum density

In this section some important powerful and straightforward instruments for signal analysis will be introduced. These are important tools that can lead an experimenter to worthless results.

The first important instrument is the Fast Fourier Transform (FFT). According to the main theorem of Fourier, any signal of finite length that contains only a finite number of discontinuities and which can be integrated in its absolute value, can be written as an infinite sum of sine and cosine functions, Appendix D. A plot of the Fourier coefficients as a function of the frequency index, display the signal's spectrum.

Histograms are often used with the analysis of data. They give very useful information about the signal to be analysed. Histograms give the probability  $P(x)$  that an independent variable  $x$  will occur and can therefore be regarded as a projection of the signal on the  $y$ -axis. Figure 2.6.2 illustrates the probability distribution of a film thickness time series.

A property of a probability distribution is:

$$\int_{-\infty}^{\infty} P(x) \cdot dx = 1 \quad (2.64)$$

The average value of the signal is defined as:

$$\int_{-\infty}^{\infty} P(x) \cdot x \cdot dx = \bar{x} \quad (2.65)$$

The Mean Square Value is defined as:

$$\int_{-\infty}^{\infty} P(x) \cdot (x - \bar{x})^2 \cdot dx = x'^2 = \text{variance} \quad (2.66)$$

The standard deviation is defined as:

$$rms = \sqrt{x'^2} \quad (2.67)$$

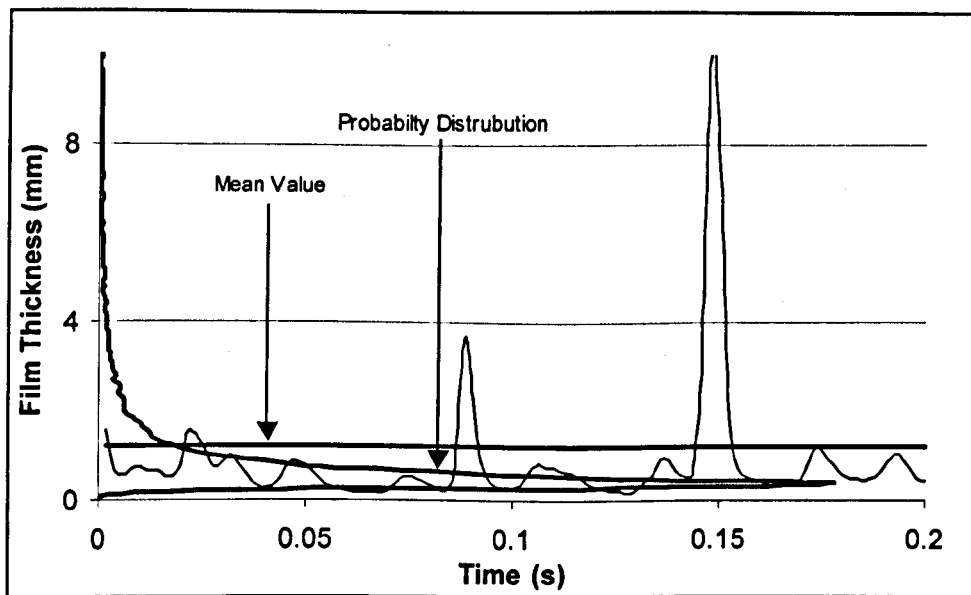


**Figure 2.6.2:** Film thickness trace with average value and probability distribution

Another important feature of a signal is its average power. A signal's instantaneous power is defined as the square of the signal. The average power is the average of instantaneous powers over their time interval. For a periodic signal, the natural time

interval is clearly its period. For a periodic signal, the average power is the mean square value of the signal.

The average power in the frequency domain (power spectrum) is obtained applying the Fourier transform to the average power of the signal. For a given signal, the power spectrum gives a plot of the portion of a signal's power (energy per unit time) falling within given frequency bins. The power spectrum density (PSD) is defined as the power spectrum divided by the sampling frequency.

When a periodic signal with a cycle time is not exactly equal to an integer multiple of the time interval over which the signal is defined, the periodic continuation will create a step at the interval boundaries. In case the signal consists of a pure sinusoidal wave, the spectrum should have only one single peak for a single frequency. However, if the signal does not fit precisely in the time interval, the periodic continuation leads to all kinds of additional components in the spectrum. This phenomenon is called “leakage” because energy leaks from the original input frequency to other frequencies and it is a big nuisance for the interpretation of spectra. As this phenomenon appears in virtually all situations, some improvements can be done by application of so-called “windowing” functions, Appendix D.

Power spectrum density of liquid film thickness traces is essential to analyse the characteristics of the film such as energy distributions among waves and wave frequency.

### **2.6.3. Methods for correlating wave frequencies**

There have not been many methods suggested for correlating frequencies. For disturbance waves Nedderman and Shearer (1963) suggested the use of dimensionless groups, namely, the Strouhal number (frequency times diameter divided by the gas

velocity) and liquid Reynolds number. They defined the diameter as that of the gas between disturbance waves. The gas velocity was that corresponding to the same position. Azzopardi (1997) followed the same approach but proposed that the pipe diameter and the superficial gas velocity should be used in the Strouhal number.

$$St = \frac{F \cdot D}{U_{sg}} \quad (2.68)$$

This simplification was justified by the film thickness being small compared to the pipe diameter. Azzopardi also suggested that the liquid Reynolds number should be based to the liquid film flowrate in excess of that for wave inception. Data from the sources for disturbance waves presented in literature have been correlated in this manner. Such a plot shows that many of the data lie on a straight line and, therefore, are well correlated by the two dimensionless group employed. However, it is only the air/water data that lie on one line. Data for other fluid systems lie above or below the main curve. The deviation is systematic and depends on the liquid/gas density ratio. In an attempt to reconcile that data an alternative correlation method was tried. The original Strouhal number was replaced by one using the superficial liquid velocity instead of that for the gas and this was plotted against the Lockhart-Martinelli parameter. The Lockhart-Martinelli parameter is defined as the square root of the pressure drops for the liquid part of the flow flowing alone in the pipe divided by that for the gas and it is approximately equal to the ratio of liquid and gas superficial velocities times the square root of the liquid to gas density ratio.

$$St = \frac{F \cdot D}{U_{sl}} \quad (2.69)$$

$$X = \sqrt{\frac{\rho_l}{\rho_g} \frac{U_{sl}}{U_{sg}}} \quad (2.70)$$

The Strouhal number/Lockhart-Martinelli parameter combination is independent of the excess liquid film Reynolds number. Figure 5.1.49 of Chapter 5 illustrates the correlation between a liquid based Strouhal number and the Lockhart-Martinelli parameter,  $X$ .

The product of the Strouhal number and the Lockhart-Martinelli parameter is approximately the original Strouhal number times the square root of the liquid to gas density ratio.

$$St \cdot X = \frac{F \cdot D}{U_{sl}} \cdot \sqrt{\frac{\rho_l}{\rho_g}} \frac{U_{sl}}{U_{sg}} = \frac{F \cdot D}{U_{sg}} \sqrt{\frac{\rho_l}{\rho_g}} = K \quad (2.71)$$

where  $K = \text{constant}$ .

Where there is a good correlation, the Strouhal number is approximately inversely proportional to  $X$ . From equation 2.71, the frequency can be obtained:

$$F = K \cdot \sqrt{\frac{\rho_g}{\rho_l}} \cdot U_{sg} \quad (2.72)$$

This implies that the frequency depends to the first order on the gas velocity and that the effect of the liquid flowrate is second order.

## CHAPTER 3

### Experimental Arrangements

The annular two-phase flow experiments were carried out on an inclinable rig in the Chemical Engineering laboratory of the School of Chemical, Environmental and Mining Engineering (SChEME). The Venturi was connected to a 5-meter long pipe to ensure sufficient distance for the flow to fully develop. The distance between the injection point of the liquid and the first test section of the Venturi was 131.58 times the inlet pipe diameter (figure 3.1.1). The film was introduced through a porous wall since the film injection reproduced the annular flow pattern more closely than the jet injection. The work concentrated on a small range of gas mass flowrates, which is of particular interest to the wet-gas metering problem. The gas and liquid mass flowrates ranged respectively from 0.03 to 0.04 kg/s and 0.0079 to 0.0899 kg/s. The inlet pressure of the gas ranged from 1.3 to 1.5 bar absolute.

The first section of this chapter gives a full description of the inclinable rig and the characteristics of the Venturi. Section 3.2, 3.3 and 3.4 give the descriptions of the measurement techniques used for the pressure drop, the liquid film thickness and the liquid film flowrate experiments.

### 3.1 Description of the inclinable rig

All experiments were carried out with air and water in an inclinable rig shown in figures 3.1.2 to 3.1.4. It consists of a 5 m long stainless steel pipe of 0.038 m internal diameter. The pipe was mounted on an inclinable beam so that it could be positioned at any angle between vertical and horizontal in intervals of 5 degrees. The Venturi, made in Unplasticised Polyvinyl Chloride (UPVC), was connected to the main pipe at 4.5 m from the water inlet section to guarantee a well developed two-phase flow. The geometrical characteristics of the Venturi are given in figure 3.1.1.

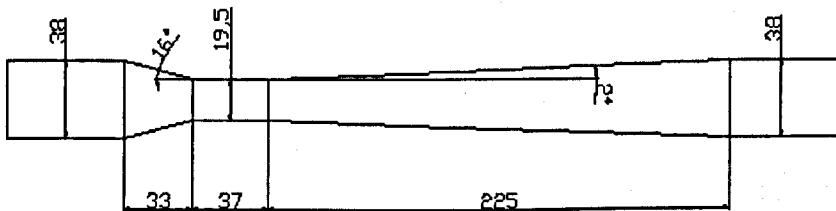


**Figure 3.1.1:** Geometrical characteristic of Venturi. Units in mm

The air was supplied from the laboratory compressed air mains. Its flow was measured by an orifice plate and controlled by valve V1, figure 3.1.4. A pressure gauge indicated the inlet air pressure.

Water was pumped from a 300 l supply tank situated below the rig. Its flow was metered by one of the three calibrated rotameters. After passing down the length of the inclinable beam, the water entered into the main pipe through a porous wall located 0.5 m from the start of it.

A valve on the two-phase exit line upstream of a disengagement tank allowed a constant pressure at the inlet of the Venturi. The mixed air and water were separated in a large vessel. The air was released to the atmosphere and the water was returned to the supply tank.



**Figure 3.1.2:** Inclunable flow facility



**Figure 3.1.3:** Inclinal flow facility

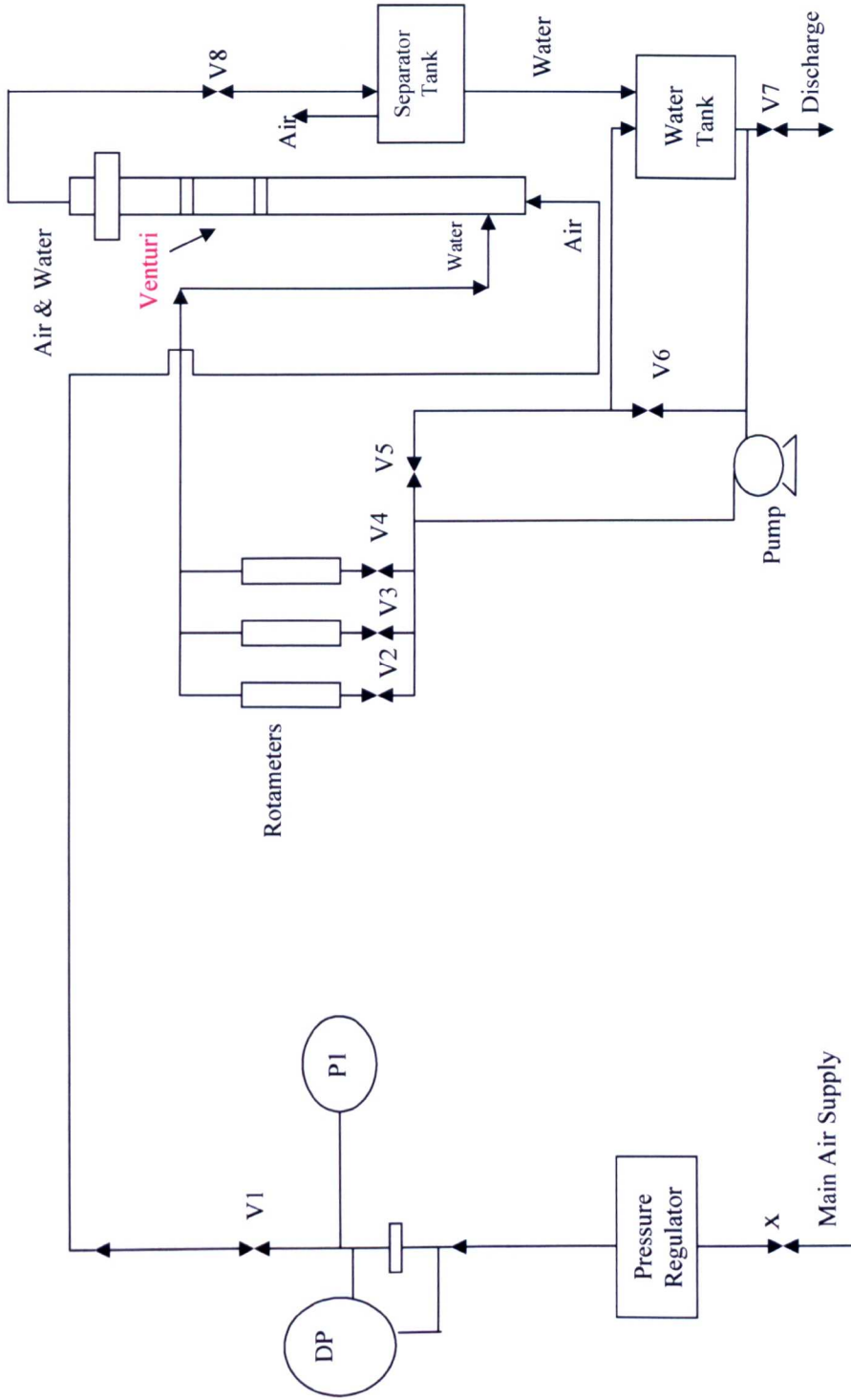


Figure 3.1.4: Schematic arrangement of the inclinable flow facility

## 3.2 Pressure drop arrangement

As discussed in Chapter 1, differential pressure meters ( $\Delta p$  meters) such as the orifice plates and Venturis can be used in wet conditions, provided corrections are applied. However, further experimental data are necessary in order to study the influence of liquid on the readings of the pressure drop.

In the inclinable flow facility the pressure gradient in the Venturi has been determined by using an experimental equipment applied previously by Azzopardi *et al.* (1989) and Altunbas (2001), figure 3.2.1. Two differential pressure cells were used to measure simultaneously the differential pressure along the Venturi. The first D.P. cell had a pressure working range of 0-6 kPa while the second one had a range of 6-60 kPa. The pressure profile along the Venturis was determined by connecting ten pressure tappings in turn to a calibrated differential pressure cell. Each tapping was linked to a separator pot by a horizontal tube. The differential pressure cell was connected to the top of the separator pot via a Scanivalve, which was driven by a computer. This switched automatically from one tapping to another after a certain time, which was long enough to ensure that each subsequent pressure reading was not affected by the previous one. Liquid from the separator pot was drained away through a valve from the bottom. This arrangement was employed for each tapping to ensure that the measurement lines to the pressure cell were always full of gas. The reference pressure was measured just before the start of the convergence.

The complete arrangement for the pressure drop measurements is shown in figure 3.2.1:

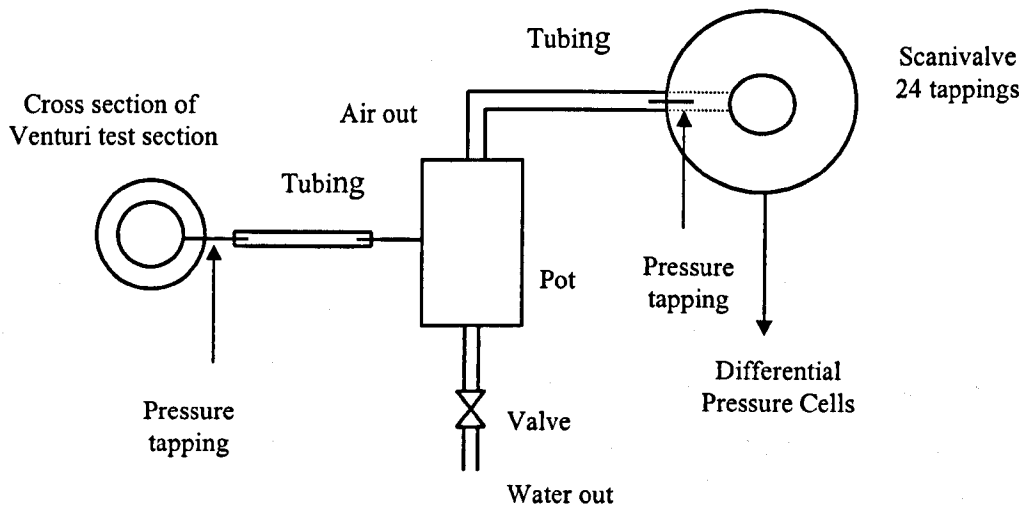


**Figure 3.2.1:** Arrangement for pressure drop measurements

### 3.3 Film thickness arrangement

The types of probe employed in this study were chosen on the basis of their range of operability and previous visual observations of flow patterns in pipes. The liquid film in annular flow was observed to be asymmetrical with a thick film at the pipe bottom, which became abruptly much thinner towards the top. For this reason, the techniques selected for the film thickness measurements were flush mounted probes and wire probes. The first technique was used for the pipe upstream of the Venturi and the throat. The second one, suitable only for higher film thickness, was used only for the main pipe.

#### 3.3.1 Flush-mounted probe test sections and their calibrations

The main advantage of flush mounted probes is their non-intrusivity and accuracy for measurement of small thickness. The range of operability extends typically up to 2 mm but using bigger diameter pins and increasing their separation can widen

the range. However, a limit is imposed as the electrodes have to be sufficiently close to give a good quality local measurement. The measured thickness is assumed to be the value at the mid-point between the centres of the two electrodes.

Two different flush-mounted probes test sections were used for the liquid film thickness measurements, one for the main pipe and another for the throat of the Venturi. The one for the main pipe was a 17 mm long section and it was located just before the convergence of the Venturi. The pins were positioned at one extremity of this pipe, 3 mm from the flange. The linear distance between the pins was 5 mm around the circumference. In the case of the throat, the pins were located in the middle of the throat section. The linear distance between the pins was 5 mm around the circumference. In both sections the pins (1.5 mm diameter welding rods) were made of stainless steel to avoid problems of corrosion. They were glued in precision machined holes and mounted flush to the internal surface of the pipe. However, accuracy of the mounting did not allow the electrodes to be perfectly flush and so machining was needed.

The pairs 3(2) & 5(1) in the test section for the main pipe and the pairs 1(1) & 1(2) and 3(1) & 3(2) in that one for the throat were used by switching the connections so that the intermediate pin could be coupled with two different probes. The sequences of pairs of the two test sections are shown in figures 3.3.1 and 3.3.2. Section 3.3.3 describes the experimental procedure applied.

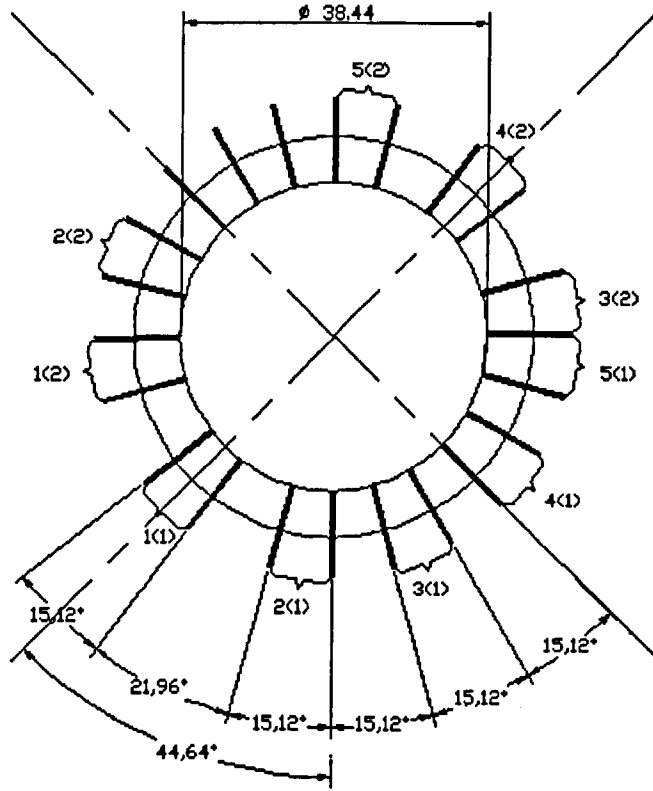


Figure 3.3.1: Main test section with flush-mounted probes

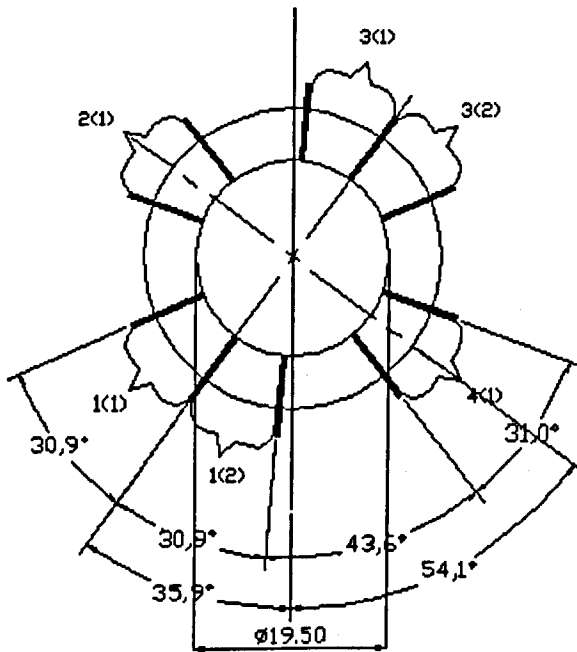
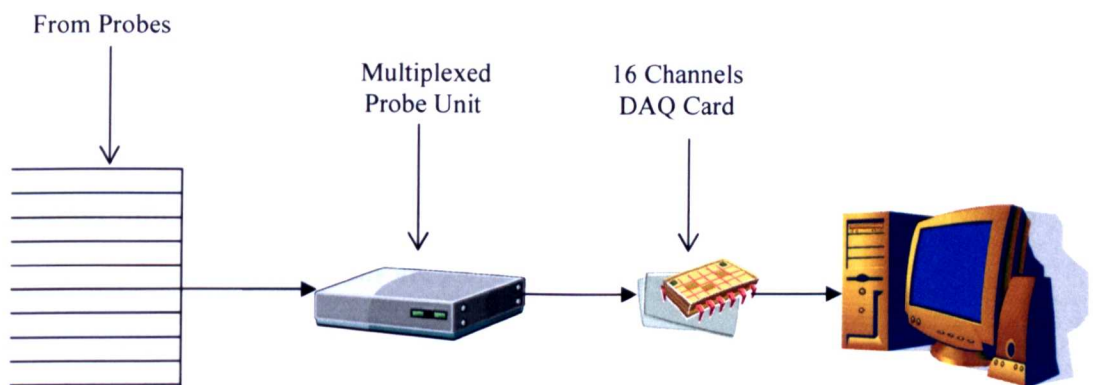


Figure 3.3.2: Throat test section with flush-mounted probes

A schematic diagram of the arrangement used for the data collection is shown in figure 3.3.3. The arrangement was an AC circuit and, therefore, this excluded the formation of ionic “double layers” during the static calibration. The voltage was applied and filtered by a multiplexed unit designed at the Imperial College of London and used also by Conte (2000). The signal from 5 pairs of probes could be obtained simultaneously and, after filtering by the unit, this was fed to a PC equipped with a multi-channel DAQ card. The signal was driven to this DAQ card by a terminal block. Before calibration, the gains were adjusted to obtain optimal operation in the expected range of heights. Data acquisition was carried on using a program assembled in LABVIEW. Microsoft Excel and programs in QuickBasic were used to process and analyse the data.



**Figure 3.3.3:** Sketch of the arrangement for data collection

Calibration of these test sections required the use of two calibration cylinders. These were machined out of a 0.3 m long solid cylinder with the same diameter as the test sections. Starting from one extremity, the diameters of the two cylinders were reduced progressively 4, 3, 2, 1, 0.5 and 0.1 mm. These diameters were 50 mm long, figure 3.3.4 and 3.3.5.

For the calibration each probe test section was located between two 0.3 m long pipes, the three pieces were flanged together and the pipe obtained was closed by a lid on one extremity. The cylinder was inserted in the open cavity and flanged

to it. The gap was filled with water of known conductivity and an external rod, screwed to the cylinder, caused the cylinder to move along the length so that a varying gap of water could be created in front of the probe.

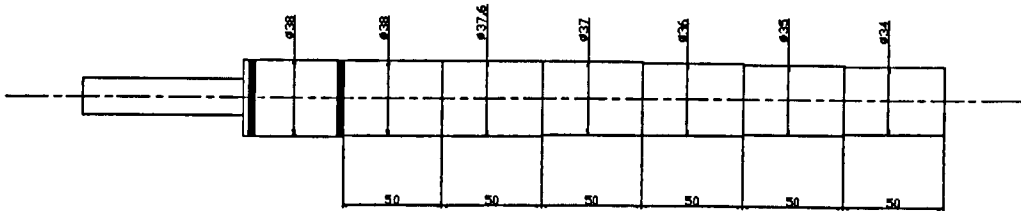


Figure 3.3.4: Main test section cylinder. Unit in mm

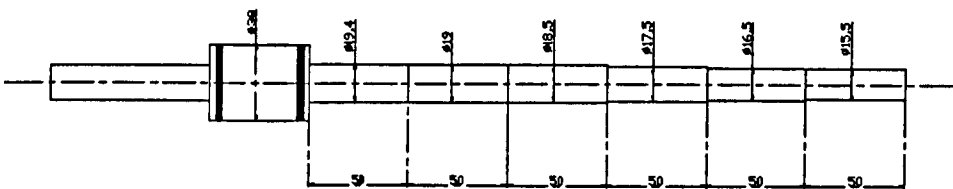


Figure 3.3.5: Throat test section cylinder. Unit in mm

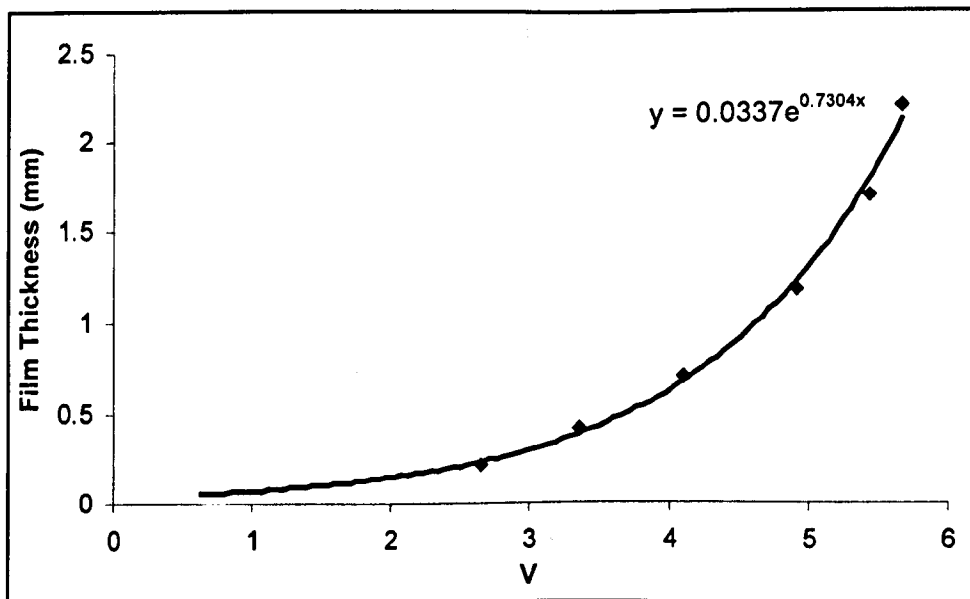
The liquid film thicknesses obtained with the two different solid pipes located into the throat and main test sections are shown in table 3.3.1:

Table 3.3.1: Film thickness obtained with the cylinders into the two test sections

	Liquid film thickness between test section and cylinder
Main test section D=38.44 mm	0.22
	0.42
	0.7
	1.18
	1.7
	2.2
Throat test section D=19.5 mm	0.05
	0.25
	0.5
	1
	1.5
	2

Calibrations as well as measurements were taken in groups of 5 probe pairs as the electronic unit allowed 5 signals to be measured simultaneously. The gains were regulated so that in the main section a signal of 5.7 V was recorded for the maximal liquid thickness of 2.2 mm and in the throat section a signal of 4.3 V was recorded for the maximal liquid thickness of 2 mm. The water conductivity was 612  $\mu\text{S}/\text{cm}$ .

It is known (Williams, 1990) that cross talk among probes can strongly influence the response of such systems. In other words, if measurements from one probe pair are taken simultaneously to adjacent pairs, the response can be affected. For this reason, in the experimental measurements the probes were coupled and connected to the channels with the same configuration considered for the calibration. A calibration curve was built for each pair of probes in the main and throat test sections, figure 3.3.7 and 3.3.8. The calibration curves were fitted with exponential equations. For film thicknesses less than approximately 0.1 mm, the calibration curves should have linear trend to zero. Thus, the present calibration curves were extrapolated up to 0.1 mm and linear calibrations down to 0 were used for lower film thicknesses.



**Figure 3.3.7:** Calibration curve for flush mounted probes in the main test section showing signal plateau. Conductivity = 612  $\mu\text{S}/\text{cm}$

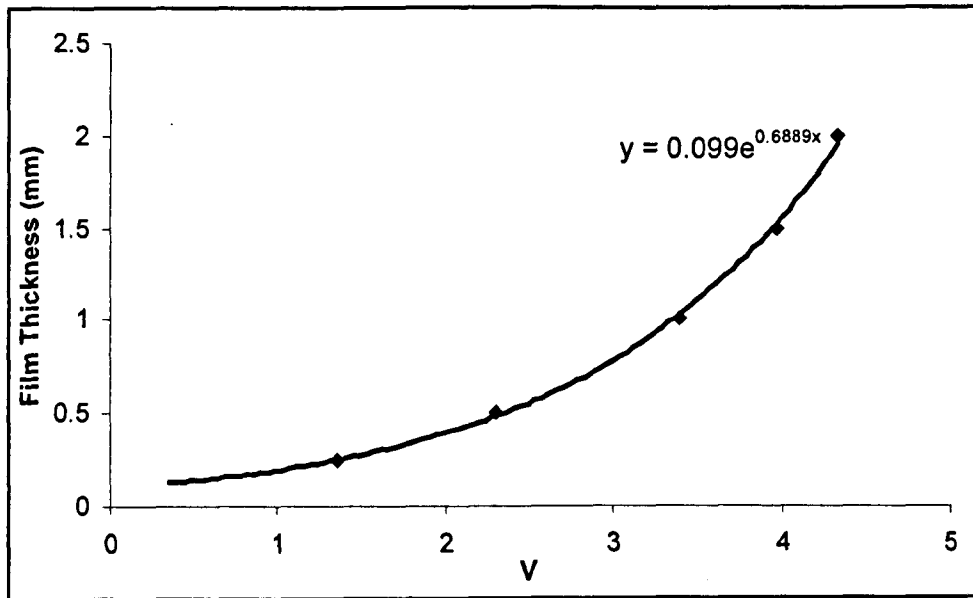


**Figure 3.3.8:** Calibration curve for flush mounted probes in the throat test section showing signal plateau. Conductivity =  $612 \mu\text{S/cm}$

### 3.3.2 Wire probe test section and its calibration

The wire probes test section used for the measurement of film thickness at the bottom of the main pipe was a modification of the facility employed by Rea (1998), figure 3.3.9. Use of the wire probe test section was not necessary for the throat of the Venturi since the range of liquid film thickness was much smaller, see results in Chapter 5. Three pairs of stainless steel wires of 0.5 mm diameter were fixed along chords of the main pipe cross-section. The spacing between two wires of a pair was 3 mm and the distance between two analogous wires of two consecutive pairs was 10 mm, with the central pair symmetrical to the vertical diameter. Because the flow pattern was annular, precaution had to be taken to eliminate the route for current at the top of the main pipe, across the thin film. For this reason, each wire was insulated 5 mm from the upper wall with a synthetic and waterproof coating.

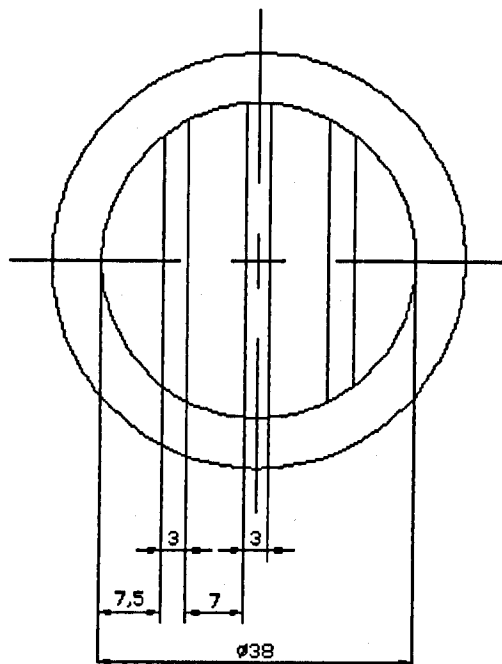


**Figure 3.3.9:** Wire probe test section for film thickness measurement at the bottom of pipe

The same arrangement for data collection described in the previous section was used for the measurements with the wire probe test section, figure 3.3.3. A different unit was used. Before calibration, the gains were adjusted to obtain optimal operation in the expected range of heights. The maximum nominal signal processed by the system was 7.5 V.

The system was calibrated by flanging the test section with fitted probes between two short pieces of acrylic resin. The extremities were closed with transparent lids to form a cylinder and a graded scale in millimetres was placed from the bottom of the pipe (0 mm) up to 7 mm on both lids. Water was added and removed via a small hole. The cylinder so obtained was held horizontally by two V-Blocks and the level of water was checked by using a spirit level. The reading was taken when the level was the same on both lids. The signals of the 3 pairs of wires were recorded simultaneously for steps of 1 mm.

Calibration of the probes at the periphery of the pipe proved to be more difficult. The curvature of the pipe caused a difference in height of  $\sim 2$  mm between the bottoms of the two external pairs of wires (A & C), figures 3.3.9. Furthermore, the shape of the film during calibration was flat as opposed to the annular flow conditions. Therefore, it was assumed that the electrode less wetted by the liquid would give the realistic height of the annular film at those locations of the cross-section. Hence, calibration was made for the liquid height at the external electrode.

For the same reason discussed in section 3.3.1 (Williams, 1990), for the experimental measurements, the wires were coupled and connected to the channels with the same configuration considered for the calibration.

Figure 3.3.10 shows the calibration of the three pairs of probes for a conductivity of  $612 \mu\text{S}/\text{cm}$ . The trendlines indicate that the relationships between liquid depth and voltage are linear.

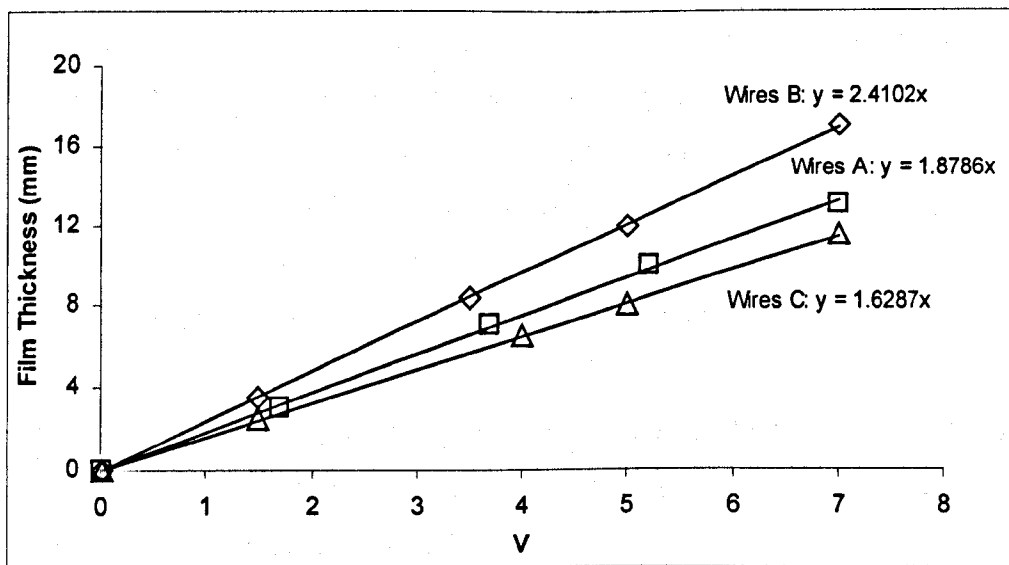


**Figure 3.3.10:** Calibration lines for the three pairs of probes for a conductivity of  $612 \mu\text{S}/\text{cm}$

### 3.3.3 Data acquisition procedure

Particular attention had to be taken in assembling the loop when film thickness measurements were to be made. As the test sections were flanged at some location of the loop, there was concern that irregularities such as gaps and steps could significantly disturb the flow, especially when the film was very thin. Hence, flanges were carefully machined to ensure smooth transition from one section to another one and tightened up to avoid leaks. Moreover, all the electrical connections were checked to make sure of the continuity of the signal from the probes to the terminal block connected to the PC. For every set of flow condition the data acquisition was carried on with a sampling time of 2ms and a recording time of 100s, i.e. samples of 50000 data points.

The measurements of the film thickness in the two sections were carried on separately. For both sections the data acquisition was carried on in two stages: the bottom of the section was measured in the first stage and the top in the second one.

For the main section, the data acquisition was carried on by using both conductance techniques simultaneously. In the first stage, the probes connections used were: 1(1), 2(1), 3(1), 4(1) and 5(1) of the flush mounted test section (figure 3.3.1) and A, B and C of the wire test section, figure 3.3.9. In the second stage, the probes connections used were: 1(2), 2(2), 3(2), 4(2) and 5(2) of the flush mounted test section and A, B and C of the wire test section.

For the throat section, the flush mounted probe test section was use only. The probes connections used in the first stage were 1(1), 2(1), 3(1), 4(1) and 1(2), 2(1), 3(2), 4(1) in the second stage, figure 3.3.2.

Once the data acquisition was carried out, the film thicknesses related to the sample readings were calculated by using the appropriate calibration curves. For every connection, the characteristics of the film thickness were analysed and shown as function of the position around the circumference, see Chapter 5.

### 3.4 Liquid film flowrate arrangement

The film extraction technique using porous sintered wall unit was employed to determine the film flowrates. The facility used for the measurement was the same employed by Butterworth (1972) and Butterworth & Pulling (1973). The idea was to allow a partial section of the liquid film and an amount of gas to be drawn off from the pipe into a cyclone separator. The liquid rate was determined by timing the flow. Two different partial liquid take off devices were built in brass and equipped with a porous sintered wall over a limited sector of the pipe wall. The pipe unit is shown in figures 3.4.1 and 3.4.2 and the throat unit in figures 3.4.3 and 3.4.4. The units were made of two components. The first one was an external cylinder with an exit for the liquid extracted and the second one was an internal cylinder equipped with the porous wall for the liquid film take off. The latter had two fins glued along the two sides of the porous wall to drive the liquid film and to prevent liquid being sucked in from the sides of the porous section. The height of the fins was 9.5 mm in the main unit and 6.5 mm in the throat unit. The internal cylinder of the main pipe unit had a 38 mm internal diameter and that one of the throat unit had a 19 mm internal diameter. The internal cylinder containing the fins was arranged so that it could be rotated without rotating the rest of the tube. Rotation was facilitated by holes made around a small flange of the internal cylinders. A suitable small rod could be inserted into these holes to effect the rotation. A thin smear of silicone grease spread under the small flange guaranteed a better rotation. Leakages were prevented by O-ring seals located above and under the flange. The liquid flow taken off was led by flexible tubing via a control valve to a small cyclone separator.

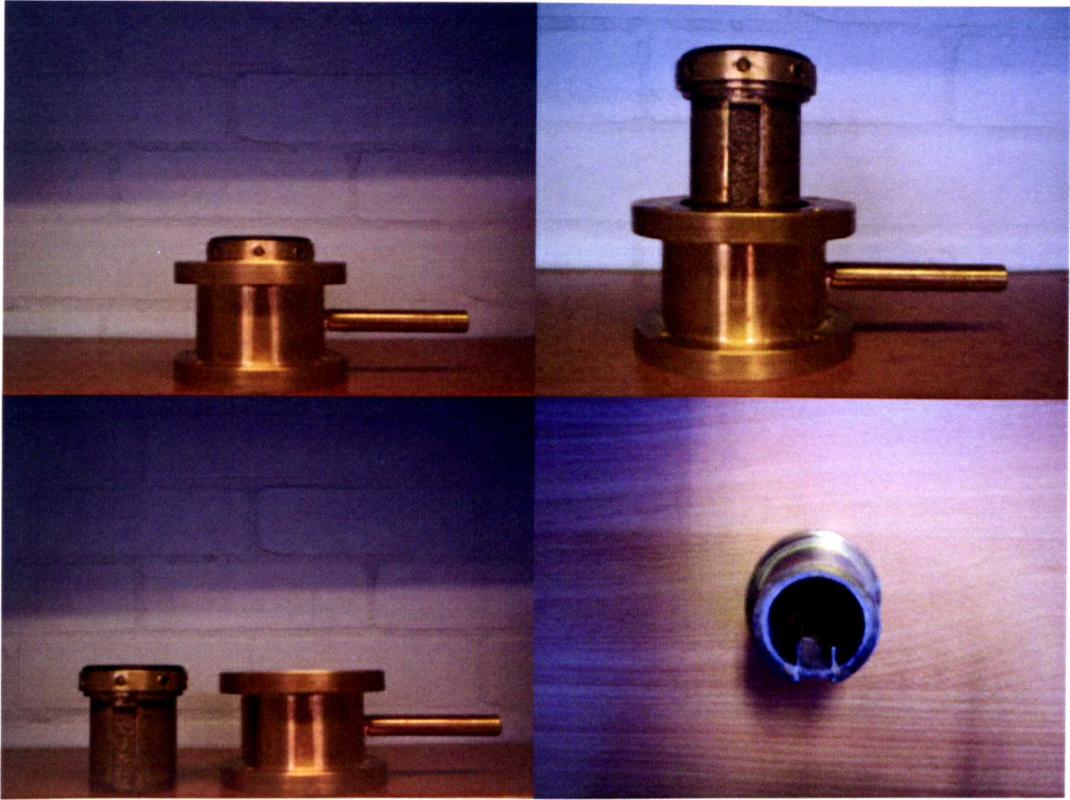


**Figure 3.4.1:** Partial take-off device for the main pipe

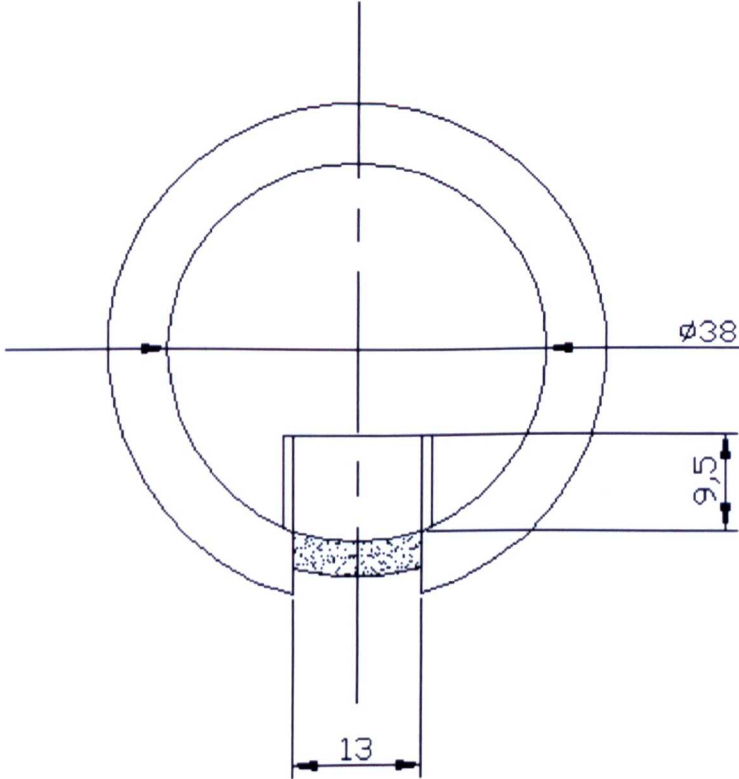


**Figure 3.4.2:** Internal cylinder used for the pipe. Unit in mm

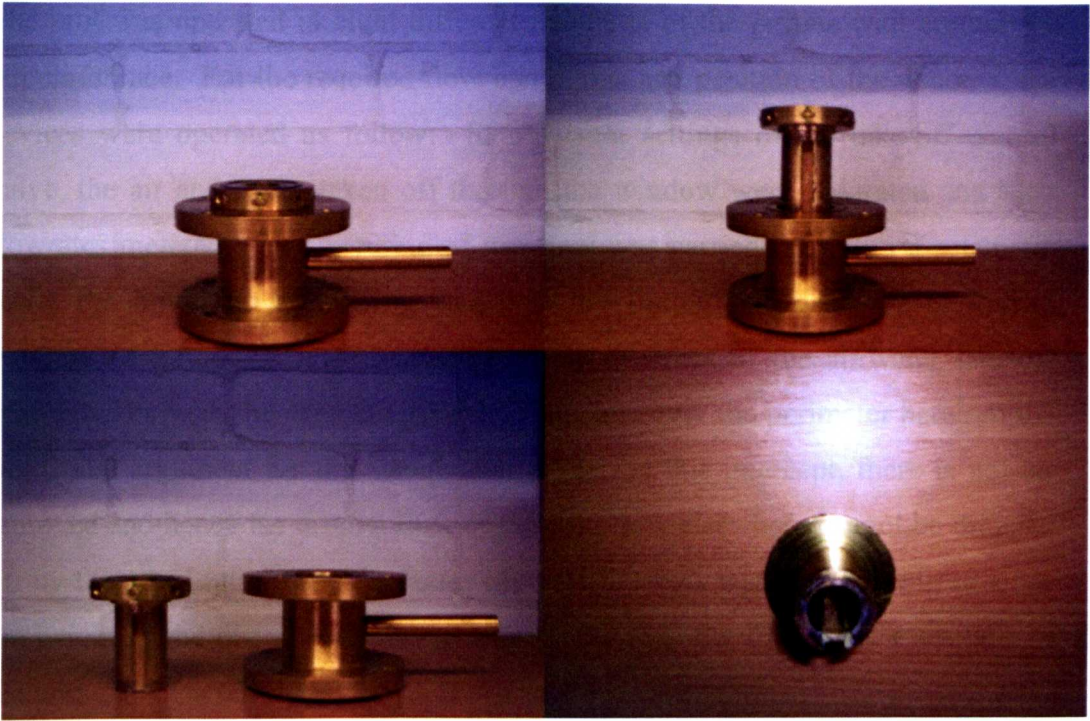


**Figure 3.4.3:** Partial take-off device for the throat

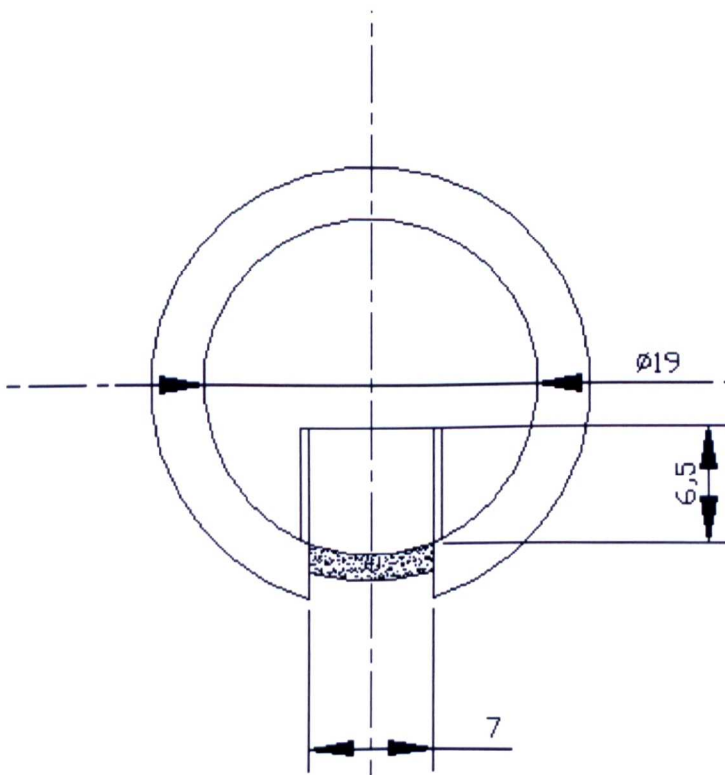


**Figure 3.4.4:** Internal cylinder used for the throat. Unit in mm

The unit was operated at eight different positions of the porous wall around the circumference. For the required flow conditions and position of the window, the devices were operated as follow: for different settings of the take-off control valve, the air and water taken off through the window were separated and their flowrates metered. The metering of gas flow was carried out using a rotameter while the liquid flow metering was done by timing the discharge of known volumes of liquid. It was assumed that the intercept of the air/water take-off characteristic with the ordinate gave the film flow over the perimeter between the fins. The argument for this conclusion is that, at this intercept, there is not air removed and hence the droplet flow or the film flow elsewhere cannot be dragged off by the air. Liquid mass flowrates  $M_l > 0.0131$  kg/s were not considered since the height of the disturbance waves was greater than the fin height, especially at the bottom of the pipe.

With the above assumption, the local film flowrate per unit width of surface, or peripheral film flowrate, is given by:

$$\Gamma'_x = \omega_l / b \quad (3.1)$$

where  $\omega_l$  is the rate of the liquid film taken off at the intercept and  $b$  is the perimeter between the fins. Entrained droplets are also deposited and atomized continuously between the fins. If this is taken into account equation (3.1) becomes:

$$\Gamma_x = \omega_l / b + (R_A - R_D) \cdot a \quad (3.2)$$

where  $R_D$  and  $R_A$  are the droplet deposition and atomization per unit of surface between the two fins and  $a$  is the length of the window.

According to the theory on atomisation and deposition (see Chapter 2), the rates of deposition and entrainment can be described in terms of the coefficients of deposition and entrainment and the droplet concentration  $C$ :

$$R_D = k_D C \quad (3.3)$$

$$R_A = k_A C \quad (3.4)$$

The droplet concentration can be approximately written as:

$$C \cong \frac{M_{LE}}{U_{sg}} \quad (3.5)$$

where  $M_{LE}$  is the entrained liquid mass flowrate and  $U_{sg}$  is the superficial gas velocity.

Considering that entrained fraction as:

$$E = \frac{M_l - M_{LF}}{M_l} = \frac{M_{LE}}{M_l} \quad (3.6)$$

the equation (3.5) can be written as:

$$C \cong \frac{E \cdot M_l}{U_{sg}} \quad (3.7)$$

Considering this last expression of C the equation (3.2) can be written as:

$$\Gamma_x = \omega_l / b + (k_A - k_D) * \frac{E \cdot M_l}{U_{sg}} \cdot a \quad (3.8)$$

It is easy to realize that in equation (3.8) the term considering the deposition and the entrainment is negligible compared to the peripheral film flowrate and, therefore, it can be neglected. Thus, equation (3.8) becomes:

$$\Gamma_x = \omega_l / b \quad (3.9)$$

The value of  $\Gamma_x$  was calculated for eight positions of the window. As the circumferential width of the window was equal to 1/8<sup>th</sup> of the pipe perimeter, the total liquid take-off rate through the cylinder was obtained by summing the eight measurements:

$$\sum_{x=1}^8 \Gamma_x \cdot b \quad (3.10)$$

Once known the total liquid take off, the entrained fraction was calculated from equation (3.6) and compared with other analogue values obtained in previous researches.

## CHAPTER 4

# Liquid Film Flowrate and Entrainment

In this Chapter, results of measurements of the liquid film flowrate in the pipe upstream of the Venturi and in the throat of the Venturi are reported. The film extraction technique using a porous sintered wall unit was employed. This technique was previously used by Butterworth (1972). In the experiments described, the effects of liquid flowrate and of pipe inclination were studied. The pipe upstream of the Venturi was positioned with its axis horizontal and at the inclinations of 20°, 45°, 70°, 85° upwards from the horizontal. However, experiments in the throat were carried out only at horizontal and at the inclinations of 45° and 85°. The gas mass flowrates of 0.03 and 0.04 kg/s were examined. These correspond to a gas superficial velocity of 15 and 21.5 m/s in the pipe upstream of the Venturi and to a gas superficial velocity of 61.8 and 86.3 m/s in the throat. The liquid flowrates of 0.0079 and 0.0131 kg/s were examined. These correspond to a liquid superficial velocity of 0.007 and 0.011 m/s in the pipe upstream of the Venturi and to a liquid superficial velocity of 0.028 and 0.046 in the Venturi throat. For these experiments liquid mass flowrates  $M_l > 0.0131$  kg/s were not taken into consideration since the height of the disturbance

waves was greater than the fin height, especially at the bottom of the pipe. Gas and liquid velocities were reproduced to an uncertainty of 8.62 and 4.1 %. These high values are due to oscillations of the gas pressure gauge and the liquid rotameters. The error analysis conducted with the method of Taylor (1997) is shown in Appendix C.

To check the symmetry about the vertical plane, both sides of the section were studied and one side was distinguished from the other by positive and negative angle,  $\theta$ . Table 4.1 shows the eight circumferential positions of the window examined in the experiments. The zero is assumed at the bottom of the pipe. Tables of results are presented in a DVD enclosed with this thesis.

**Table 4.1:** Positions of the porous sintered wall unit window

Window n°	Angular position $\theta$ (Deg)	Linear position (m)
1	-77	-0.0127
2	-122	-0.0202
3	-167	-0.0276
4	148	0.0245
5	103	0.0170
6	58	0.0096
7	13	0.0021
8	-32	-0.0053

During the measurements, it was essential to ensure that the total liquid was taken out through the porous wall. Thus, the height of the fins had to be higher than the highest waves at the bottom side of the pipe. In order not to have to use excessively high fins, the range of flowrates that could be used was restricted.

A typical take-off result is shown in figure 4.1. In this figure the angle  $\theta$  refers to the circumferential position of the centre of the window, see section 3.4 of Chapter 3. The three points in figure 4.1 are obtained for different settings of the off-take control valve. It is assumed that the intercept of the air/water take-off characteristic with the ordinate gives the film flow over the perimeter between the fins.

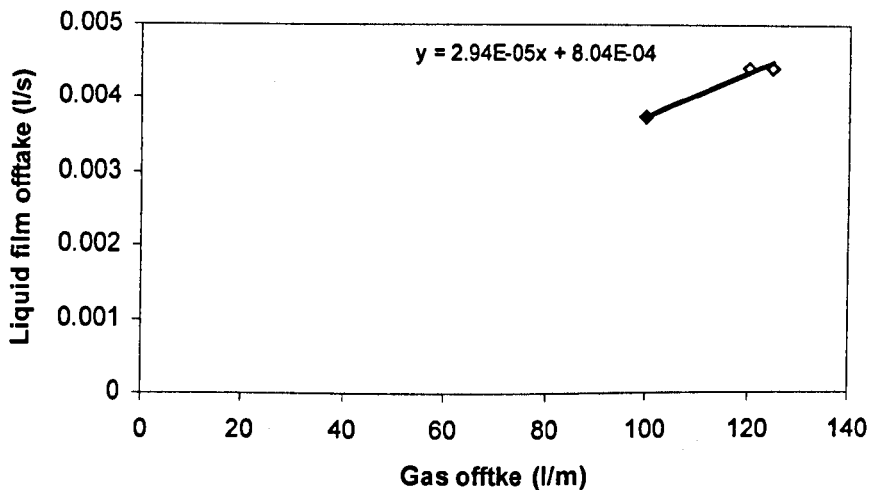


**Figure 4.1:** Take-off characteristic of the porous sinter wall. Gas mass flowrate=0.04 kg/s, liquid mass flowrate=0.0131 kg/s, angle of inclination=85°, circumferential position of the window  $\theta=148^\circ$ .

Considering the effect of deposition and atomization of the entrained droplets on the fins to be negligible, the local film flowrate per unit width of surface, or peripheral film flowrate, is given by:

$$\Gamma_x = \omega_l / b \quad (4.1)$$

where  $\omega_l$  is the liquid film flowrate between the two fins at the intercept with the ordinate,  $b$  is the perimeter between the fins. The value of  $\Gamma_x$  was calculated for eight positions of the window. As the circumferential width of the window was equal

to 1/8<sup>th</sup> of the pipe perimeter, the total flowrate of the liquid film was obtained by summing the eight measurements.

$$\sum_{x=1}^8 \Gamma_x \cdot b \quad (4.2)$$

#### 4.1 Results in the pipe upstream of the Venturi

Figures 4.1.1 and 4.1.2 show the variation of the peripheral film flowrate  $\Gamma_x$  with the inclination from horizontal,  $\alpha$ . The abscissa refers to the linear position of the centre of the window while the ordinate refers to the difference between the partial liquid film mass flowrate divided by the width of the window and the droplet deposition per unit width of surface (eq. 4.1). The peripheral film flowrate  $\Gamma_x$  is not the true local value but it is an average over perimeter  $b$ . Figures 4.1.1 and 4.1.2 show that, for the five inclinations analysed, the peripheral liquid film flowrate has the same trend of the film thickness studied and described in chapter 5. A first analysis indicates that, it is higher around the bottom of the pipe, it is decreasing on the sides and it is lower around the top. Profiles are symmetric about the vertical plane for zero. It is also shown that the inclination of the pipe influences the film flowrate around the section. When the pipe is horizontal, the liquid is entirely distributed around the bottom. Thus, the peripheral film flowrate is above zero only at the lower part of the pipe. For higher inclinations the liquid spreads out and the peripheral film flowrate is above zero also along the sides. When the inclination approaches inclination close to vertical the peripheral film flowrate is above zero also along the top.

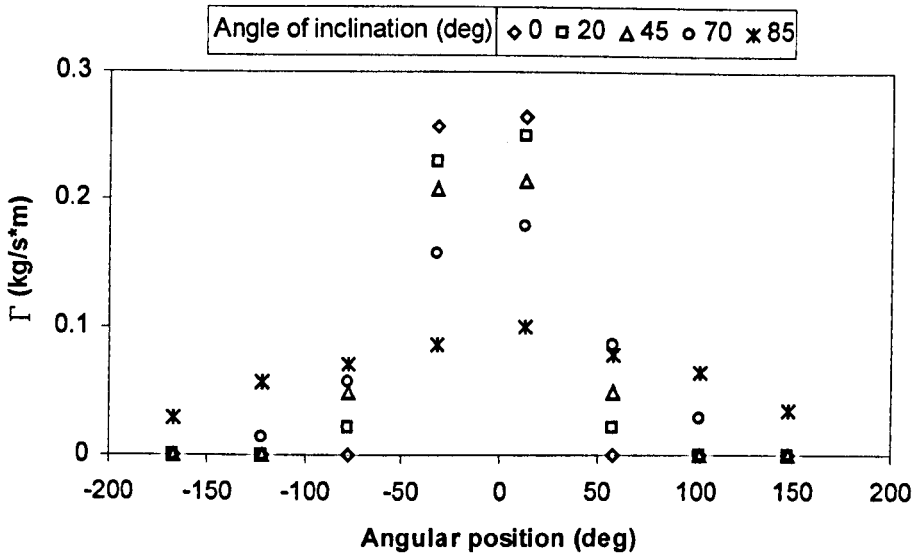


Figure 4.1.1: Liquid flow rate variation with the angle of inclination from horizontal. Gas mass flowrate=0.04 kg/s, liquid mass flowrate=0.0079 kg/s

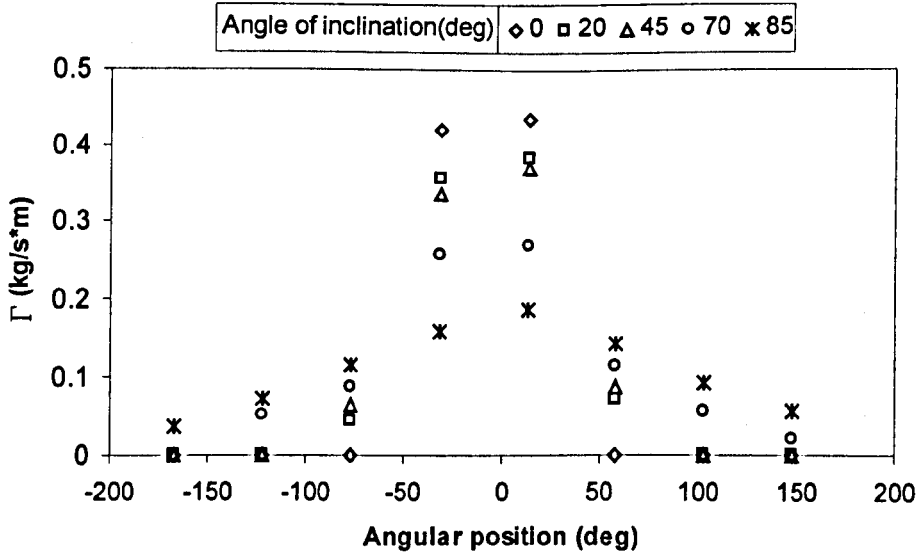


Figure 4.1.2: Liquid flow rate variation with the angle of inclination from horizontal. Gas mass flowrate=0.04 kg/s, liquid mass flowrate=0.0131 kg/s

These results show coherency with the results found for the film thickness distribution presented in Chapter 5. In fact, the profile of the peripheral film flowrate follows the trend of the film thickness profile. This is a logical consequence as the liquid film flowrate between the two fins is given by:

$$\omega_l = \rho_L * A_{LFF} * U_{LFF} = \rho_L * (b * s) * U_{LFF} \quad (4.3)$$

where  $U_{LFF}$  is the peripheral liquid film velocity,  $A_{LFF}$  is the peripheral film area,  $b$  is the width of the window and  $s$  is the film thickness.  $A_{LFF}$  is given by:

$$A_{LFF} = (A_{LF})/8 \quad (4.4)$$

where  $A_{LF}$  is the total liquid film area.

Dividing equation 4.3 by the perimeter  $b$ , the peripheral film flowrate is obtained:

$$\Gamma_x = \omega_l / b = \rho_L * s * U_{LFF} \quad (4.5)$$

The availability of both film thickness and film flowrate data would also enable an interesting comparison of results. Once  $\omega_l$  and  $s$  are determined experimentally, the variation of  $U_{LFF}$  can be analysed by equation 4.3. This study was not carried on because the measurements of the partial film flowrates were taken at circumferential locations different from those considered for the film thickness.

The study of film thickness on Chapter 5 shows that the liquid film thickness decreases with increasing gas mass flowrate, especially at the bottom. Therefore, for a fixed liquid mass flowrate and a fixed inclination, the peripheral film flowrate would be expected to decrease with increasing  $M_g$ , see equation 4.5. In fact, in annular two-phase flow, a higher gas flow results in more liquid entrained and less liquid film. However, figures 4.1.3 and 4.1.7 show that, for the range of total liquid flowrates considered, the peripheral film flow rate  $\Gamma_x$  does not vary considerably with the gas mass flowrate,  $M_g$ . Variations would be more remarkable with higher ranges of liquid mass flowrate.

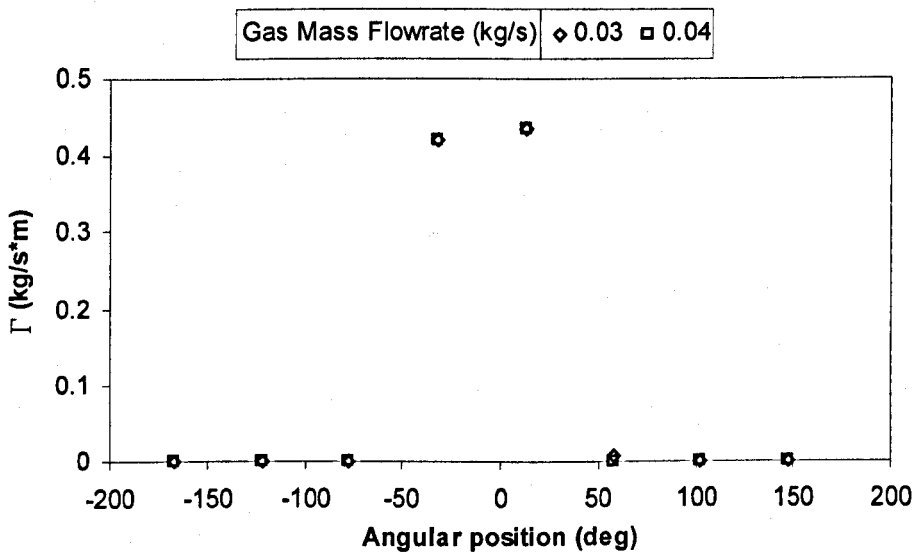


**Figure 4.1.3:** Liquid flow rate variation with gas mass flowrate in the main section. Liquid mass flowrate=0.0131 kg/s, angle of inclination from horizontal= $0^\circ$

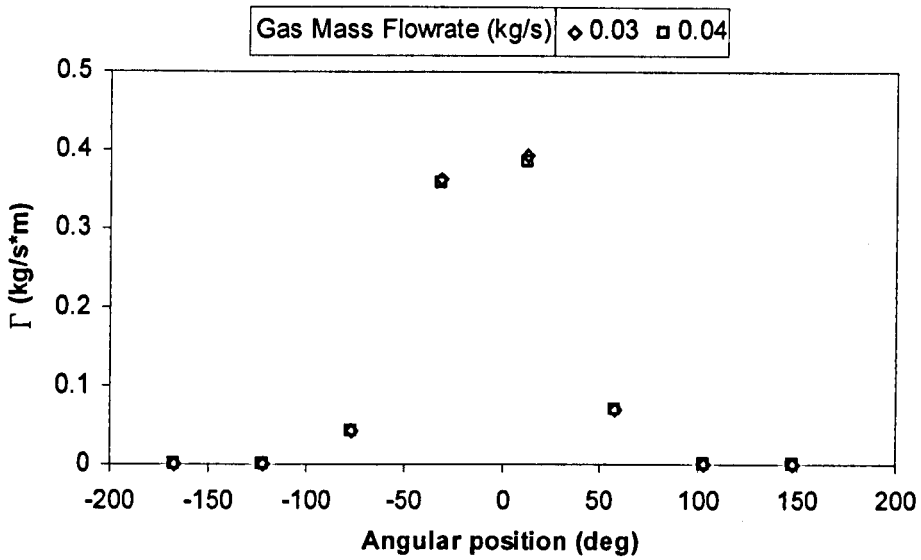


Figure 4.1.4: Liquid flow rate variation with gas mass flowrate in the main section. Liquid mass flowrate=0.0131 kg/s, angle of inclination from horizontal=20°

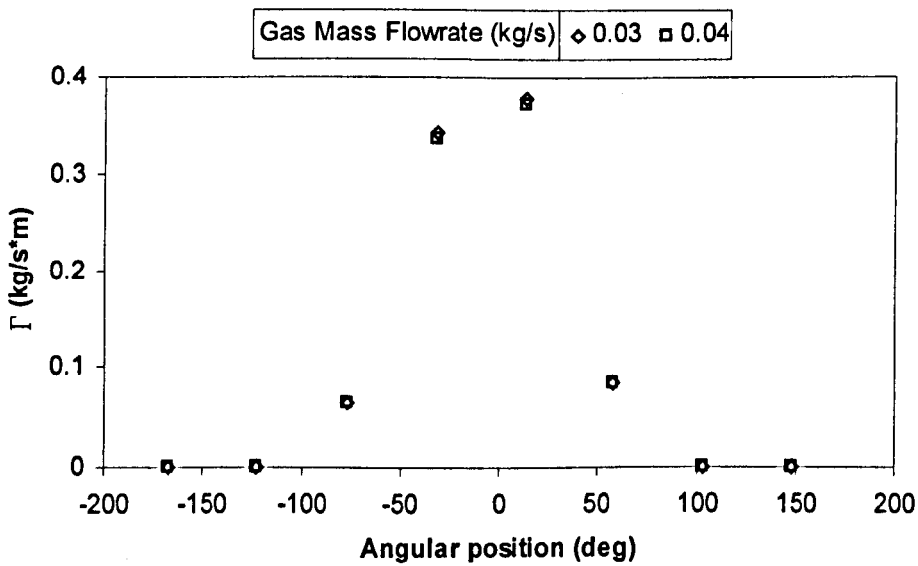
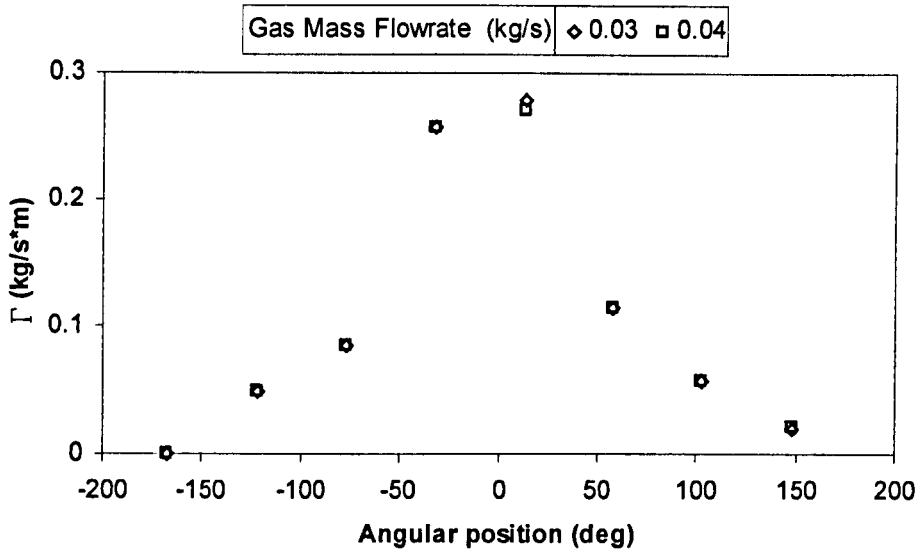
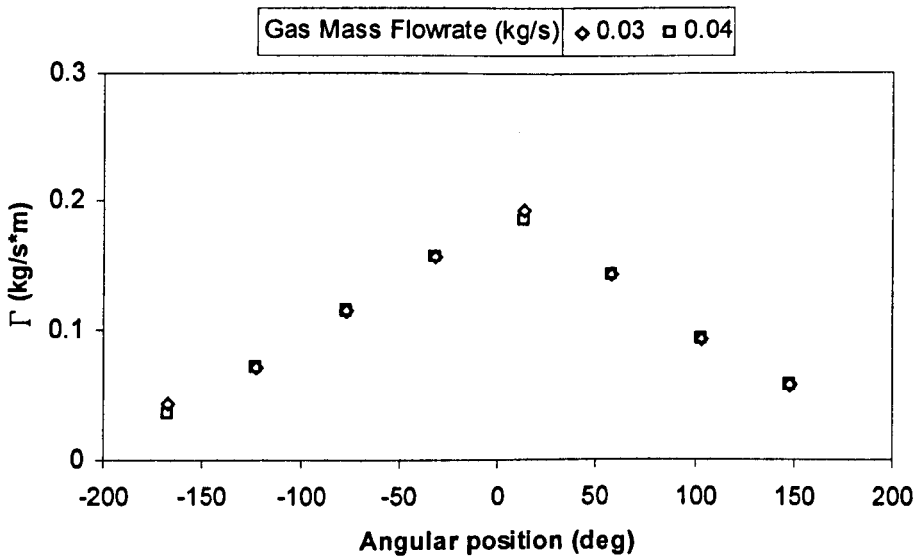


Figure 4.1.5: Liquid flow rate variation with gas mass flowrate in the main section. Liquid mass flowrate=0.0131 kg/s, angle of inclination from horizontal=45°



**Figure 4.1.6:** Liquid flow rate variation with gas mass flowrate in the main section. Liquid mass flowrate=0.0131 kg/s, angle of inclination from horizontal=70°



**Figure 4.1.7:** Liquid flow rate variation with gas mass flowrate in the main section. Liquid mass flowrate=0.0131 kg/s, angle of inclination from horizontal=85°

Figures 4.1.8 to 4.1.12 show that an increasing liquid mass flowrate results in a higher peripheral flowrate,  $\Gamma_x$ . However, at the five inclinations considered, this variation is not uniform around the section. Figures 4.1.8 illustrates that, in horizontal flow, there is a variation of  $\Gamma_x$  only at the bottom of the pipe. Figures 4.1.9 to 4.1.11 show that  $\Gamma_x$  increases with  $M_l$  also along the two sides at higher inclinations. In figure 4.1.12 is illustrated that in  $85^\circ$  inclined flow  $\Gamma_x$  increases around the entire section but the variation is still bigger at the bottom. Moreover, at this inclination the circumferential distribution of  $\Gamma_x$  becomes more uniform.

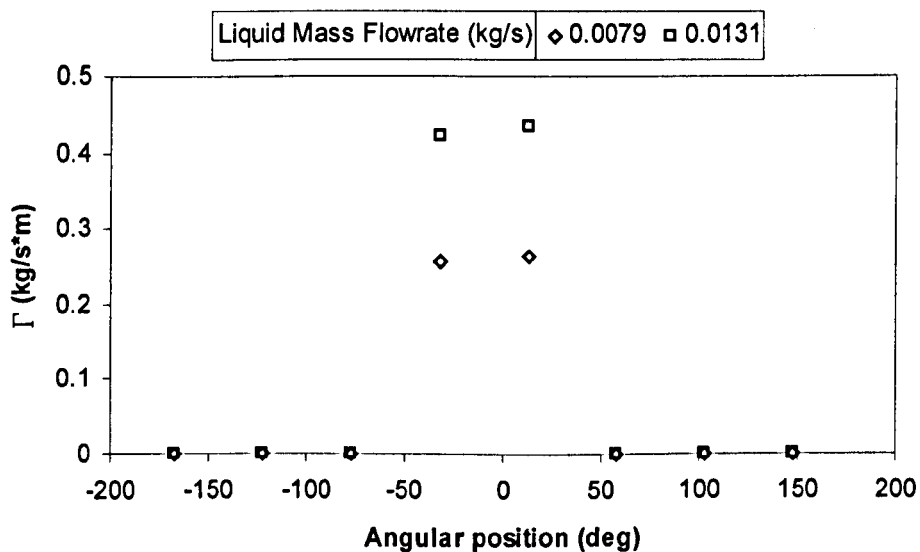


**Figure 4.1.8:** Liquid flow rate variation with liquid mass flowrate in the main section. Gas mass flowrate=0.04 kg/s, angle of inclination from horizontal= $0^\circ$

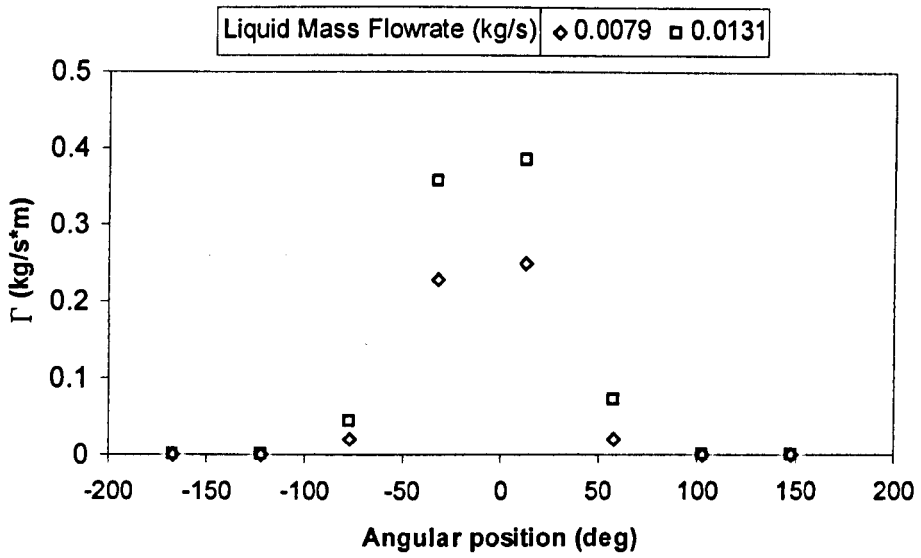


**Figure 4.1.9:** Liquid flow rate variation with liquid mass flowrate in the main section. Gas mass flowrate=0.04 kg/s, angle of inclination from horizontal=20°

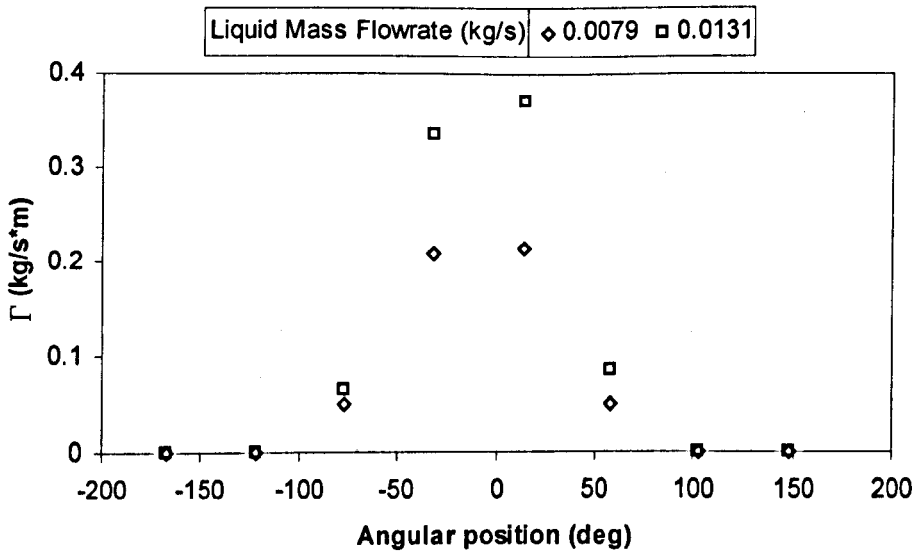


**Figure 4.1.10:** Liquid flow rate variation with liquid mass flowrate in the main section. Gas mass flowrate=0.04 kg/s, angle of inclination from horizontal=45°

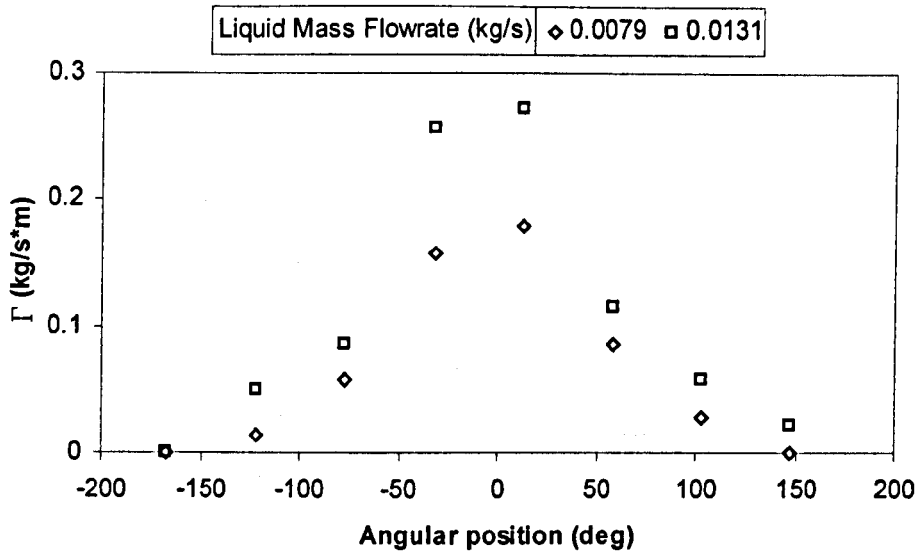


**Figure 4.1.11:** Liquid flow rate variation with liquid mass flowrate in the main section. Gas mass flowrate=0.04 kg/s, angle of inclination from horizontal=70°

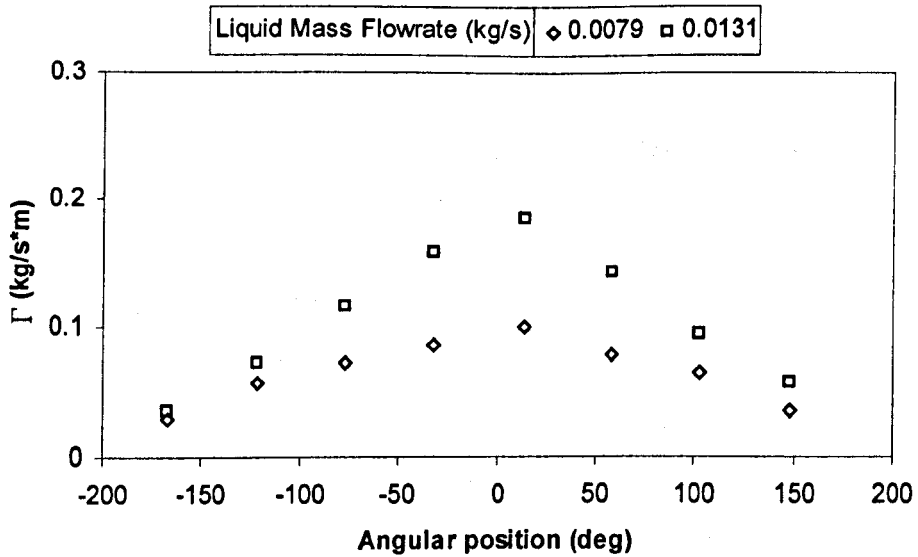


**Figure 4.1.12:** Liquid flow rate variation with liquid mass flowrate in the main section. Gas mass flowrate=0.04 kg/s, angle of inclination from horizontal=85°

Figure 4.1.13 and 4.1.14 show the variation of the entrained fraction with the angle of inclination. It is evident that the orientation of the pipe has a very small effect on the liquid entrainment. To understand the reasons of this, it is essential to examine the process of drop creation. In annular flow, the majority of drops are created from the wall film by the action of gas flowing over it. However, drops are not created from the entire film interface, but very specifically they arise from disturbance waves. The most conclusive proof that waves are the source of drops was provided by Azzopardi & Whalley (1980). They noticed that no drops were created without presence of waves. In Chapter 5, the effect of inclination on the disturbance wave characteristics is investigated. It is noticed that in horizontal flow the film is wetted by large disturbance waves only at the lower half of the pipe and it is flat at the top. When the inclination is increased, the amplitude of waves decreases at the lower side of the pipe and, at the periphery, it is observed the formation of new waves. When the pipe approaches inclination close to vertical, the potential energy of the liquid rises<sup>1</sup> and big waves are present around the entire section. Thus, the interaction between these waves and the gas at the upper half of the pipe balances the lower interface at the bottom. Therefore, although the shear between liquid and gas is higher in 85° inclined pipe, the total friction between waves and gas can be considered the same as in the other inclinations. Also the wave frequency plays an important role in the formation of liquid droplets. In fact, the higher it is the number of the waves passing through the channel in a certain time, the bigger it is the atomization. In Chapter 5, power spectra density of film thickness show that the wave frequency is not influenced by inclination at low liquid mass flowrate ( $M_l < 0.0317$  kg/s). The fact that both friction between waves and gas and wave frequency are not varying considerably with inclination is the reason of the trend of the entrained fraction shown in figure 4.1.13 and 4.1.14. Liquid entrained is not influenced by pipe orientation and shows a horizontal linear profile at the gas and liquid mass flowrates

---

<sup>1</sup> As a result, larger forces are required to move the liquid compared to horizontal flow.

considered. Higher values of liquid velocity could give more significant variations of liquid entrainment. However, the characteristics of the porous sintered wall unit were not suitable for higher liquid mass flowrates.

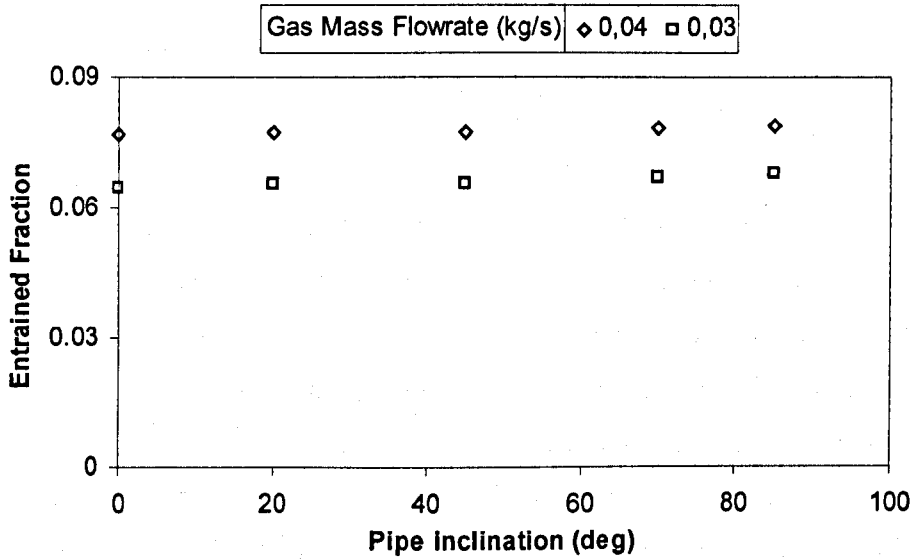


Figure 4.1.13: Entrained fraction variation with angle of inclination from horizontal and gas mass flowrate in the main section. Liquid mass flowrate=0.0079 kg/s

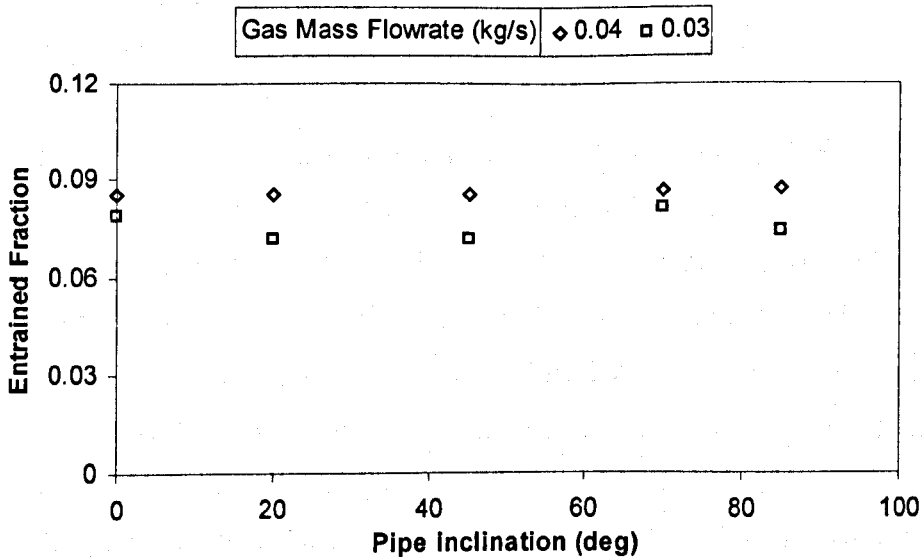


Figure 4.1.14: Entrained fraction variation with angle of inclination from horizontal and gas mass flowrate in the main section. Liquid mass flowrate=0.0131 kg/s

Govan (1990) showed that the entrained fraction is proportional to the liquid film flow  $M_{LF}$  by the following equation:

$$R_A = K \cdot (M_{LF} - M_{LFC})^{0.74} \quad (4.6)$$

where  $R_A$  is the rate of atomization,  $K$  is a coefficient,  $M_{LF}$  is the liquid film flowrate and  $M_{LFC}$  the is the critical film flowrate. Moreover, in inclined pipes the portion of the pipe where the liquid entrainment takes place varies with inclination. In  $85^\circ$  inclined pipe, there is liquid entrainment from the entire pipe circumference. In horizontal flow the liquid entrainment occurs only at the lower half of the pipe. This is a consequence of the film distribution. A more detail analysis can be done considering the local film flowrate,  $M_{LF}(\theta)$  and comparing it with the critical film flowrate,  $M_{LFC}$ . This study gives the portion of pipe where the liquid entrainment occurs,  $R_A > 0$ . The experimental study gives evidence of presence of liquid until  $\theta = 45^\circ$  in horizontal flow. However, more accurate information on the exact portion of pipe cannot be given because of the "spot" measurements of the liquid film flowrate.

Other researchers such as, Paras & Karabelas (1991), Ousaka & Kariyasaki (1992), Ribeiro *et al.* (1995) and Azzopardi *et al.* (1997) studied the entrainment in horizontal and inclined annular flow. Azzopardi *et al.* (1997) have been used light scattering measurements to determine entrained liquid flowrates in annular gas-liquid flow. Data have been obtained for vertical upwards flow and horizontal as well as inclined flow at  $10^\circ$  intervals in between. Their data showed that the entrained liquid flux increases with increasing liquid mass flux. Figure 4.2.19 illustrates a comparison between the present data and those of Azzopardi *et al.* (1991). Both results show that the entrained liquid flux has a remarkably little variation with the inclination.

In chapter 5, the study on the film thickness shows that the area  $A_{LF}$  of the liquid film does not vary considerably with inclination. In horizontal flow, a higher annular area  $A_{LF}$  would be expected since the liquid is more easily moved than in other inclinations. On the other hand, a higher area  $A_{LF}$  means a higher liquid entrained. This two opposing effects result in a non-remarkable variation of  $A_{LF}$  with the inclination,  $\alpha$ . The fact that both entrained fraction and liquid film area do not change with the pipe orientation leads to the conclusion that the effect of inclination on the film mass flowrate and consequently on the film velocity<sup>2</sup> is not significant. However, further studies on the liquid film velocity are required. The variation of  $M_{LF}$  with  $\alpha$  can also be indicated by superimposing graphics which show  $\Gamma_x$  for different inclinations and analysing them using light.

In gas-liquid phase flow, an increment of gas mass flowrate results in a stronger action of the gas on the liquid film. In fact, a higher value of  $M_g$  has the effect to increase the number of droplets stripped off the film. Figures 4.1.15 and 4.1.16 show that the entrained fraction  $E$  increases with the gas mass flowrate,  $M_g$ . It is also shown that, at the five inclinations analysed,  $E$  increases with  $M_g$  with the same trend. This means that the variation of  $E$  with the gas flowrate does not change considerably with the angle of inclination. In figure 4.1.15 the points lie on the same line. This is because the liquid entrainment does not vary with the inclination.

---

<sup>2</sup> The liquid film velocity is related to the liquid mass flowrate and to the liquid film area by the mass flowrate equation of the liquid film:  $M_{LF} = \rho_l \cdot A_{LF} \cdot U_{LF}$

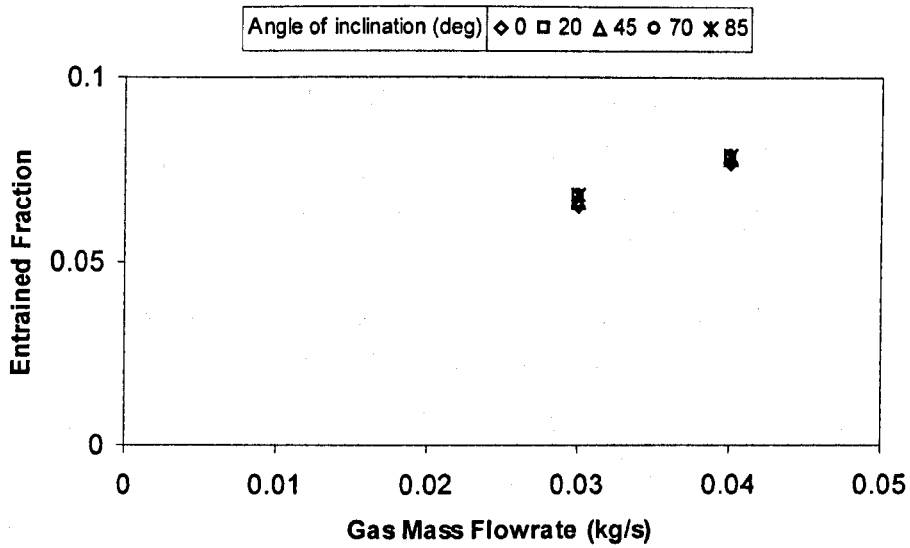


Figure 4.1.15: Entrained fraction variation with gas mass flowrate and pipe inclination in the main section. Liquid mass flowrate=0.0079 kg/s

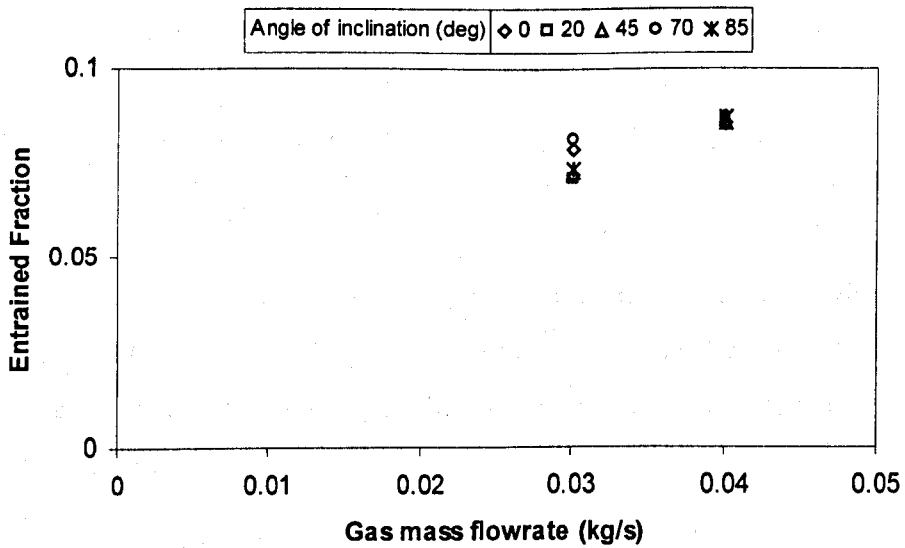


Figure 4.1.16: Entrained fraction variation with gas mass flowrate and pipe inclination in the main section. Liquid mass flowrate=0.0131 kg/s

Azzopardi *et al.* (1997) found that, at gas mass flowrates higher than those considered in this work, the liquid entrained increases with  $M_g$ . It was also found that, for higher liquid mass flowrates, the liquid entrained increases also at lower gas mass flowrates.

Figure 4.2.17 shows the comparison between the present data in horizontal flow and the data of Ribeiro *et al.* (1995). The results show that the entrained fraction  $E$  increases with the gas mass flux. It is also evident that, at higher liquid mass flux, the entrained fraction increases more rapidly with the mass gas flux. This trend is less marked in the throat.

Figures 4.1.17 and 4.1.18 show that the entrained fraction increases with the liquid mass flowrate,  $M_l$ . This means that when the value of  $M_l$  is increased the liquid entrained into the gas core increases consequently. A higher value of  $M_l$  results in more liquid moved along the channel and this has the effect to produce a higher annular area  $A_{LF}$  and a higher liquid entrainment. Figures 4.1.17 and 4.1.18 show that the trend of  $E$  with  $M_l$  does not change considerably with the inclination,  $\alpha$ . Moreover, the entrained fraction  $E$  does not vary considerably with  $\alpha$ , figure 4.1.13 and 4.1.14.

Figure 4.2.18 show the comparison between the present data in the horizontal flow and the data of Ribeiro *et al.* (1995). The results show that the entrained fraction  $E$  initially increases with the liquid gas flux and after tends to remain constant with increasing liquid mass flux.

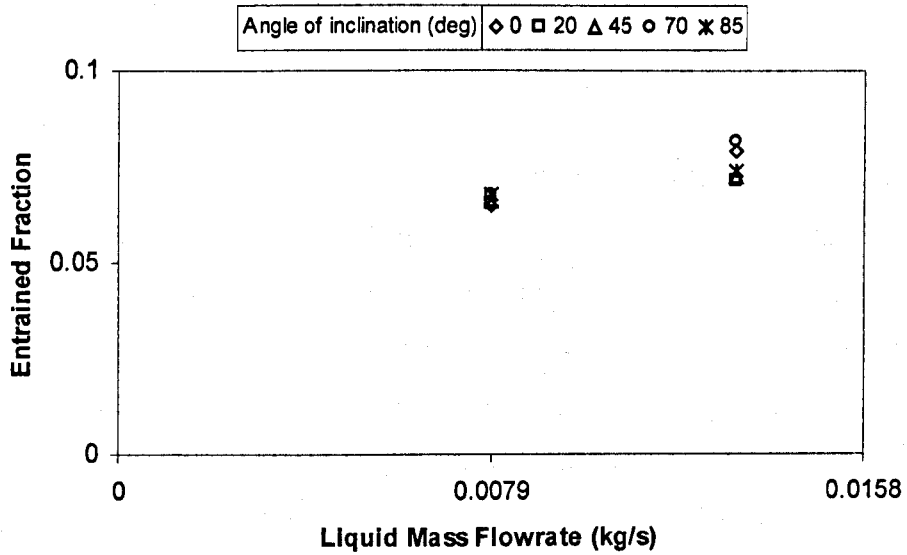


Figure 4.1.17: Entrained fraction variation with liquid mass flowrate in the main section. Gas mass flowrate=0.03 kg/s

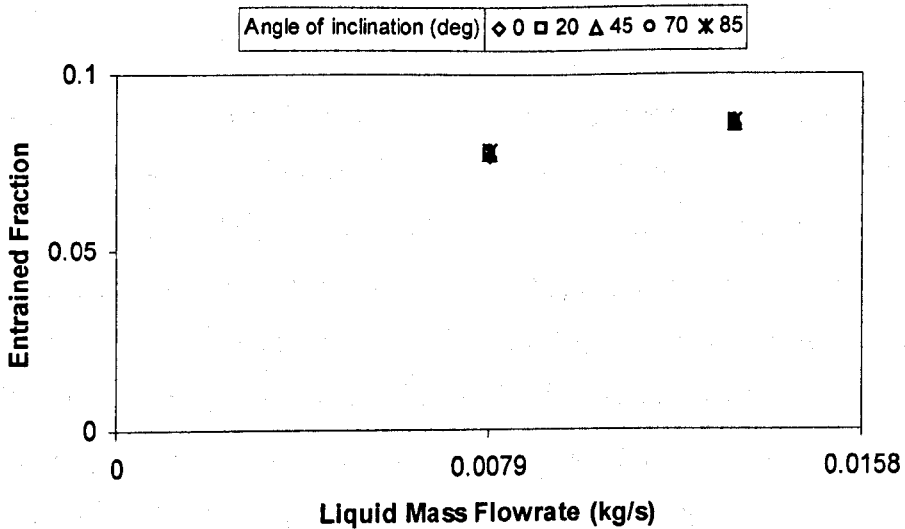
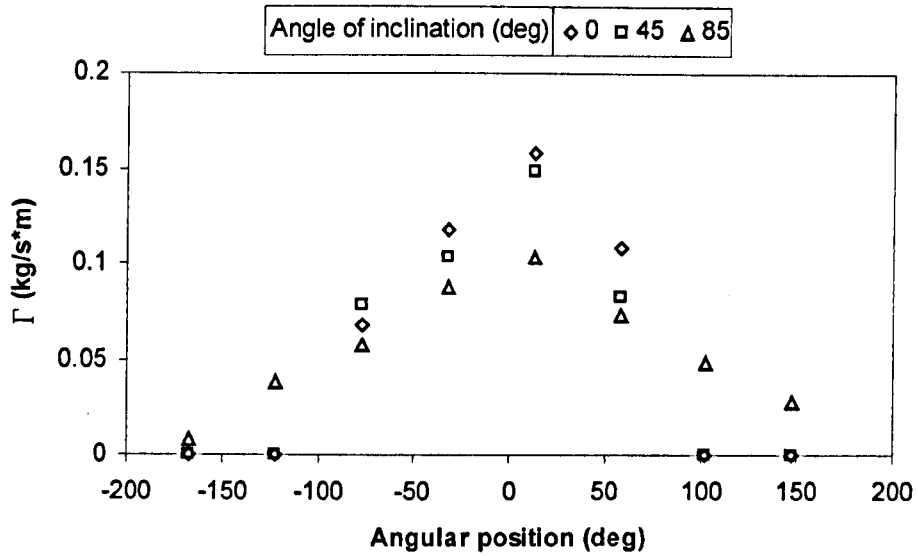


Figure 4.1.18: Entrained fraction variation with liquid mass flowrate in the main section. Gas mass flowrate=0.04 kg/s

## 4.2 Results in the throat of the Venturi

Figures 4.2.1 and 4.2.2 show how the peripheral liquid mass flow rate  $\Gamma_x$  varies with the inclination in the throat of the Venturi. The abscissa refers to the linear position of the centre of the window while the ordinate refers to the liquid film flowrate measured by the window divided by the width of the window. The peripheral film flowrate  $\Gamma_x$  is not the true local value but it is an average over perimeter  $b$ . To check the symmetry about the vertical plane, both sides of the channel are studied and one side is distinguished from the other by positive and negative angle  $\theta$ , table 4.1. Figures 4.2.1 and 4.2.2 show that the profiles are symmetric about zero. The peripheral film flowrate has the same trend of the film thickness studied and described in Chapter 5. For the three inclinations analysed, the peripheral liquid film flowrate is higher around the bottom side of the throat, it is decreasing on the sides and it is lower around the top. These results show coherency with the results found for the main pipe. However, the variations of the peripheral flow rate in the throat are less marked than those found in the main pipe. This is due to the different diameters of the two sections. In fact, the liquid is more easily moved at the top when the area of the channel is smaller. In a smaller channel the gravitation forces that keep the liquid at the bottom are lower and, therefore, the peripheral film flowrate  $\Gamma_x$  is more uniform around the section. Once known the eight peripheral liquid flowrates around the circumference, the liquid film mass flowrate  $M_{LF}$  is calculated by the equation 4.2. The variation of  $M_{LF}$  with the inclination  $\alpha$  can also be indicated by superimposing the graphics which show the variation of  $\Gamma_x$  around the throat cross-section for different inclinations and analysing them using light.



**Figure 4.2.1:** Liquid flow rate variation with the angle of inclination from horizontal. Gas mass flowrate=0.04 kg/s, liquid mass flowrate=0.0079 kg/s

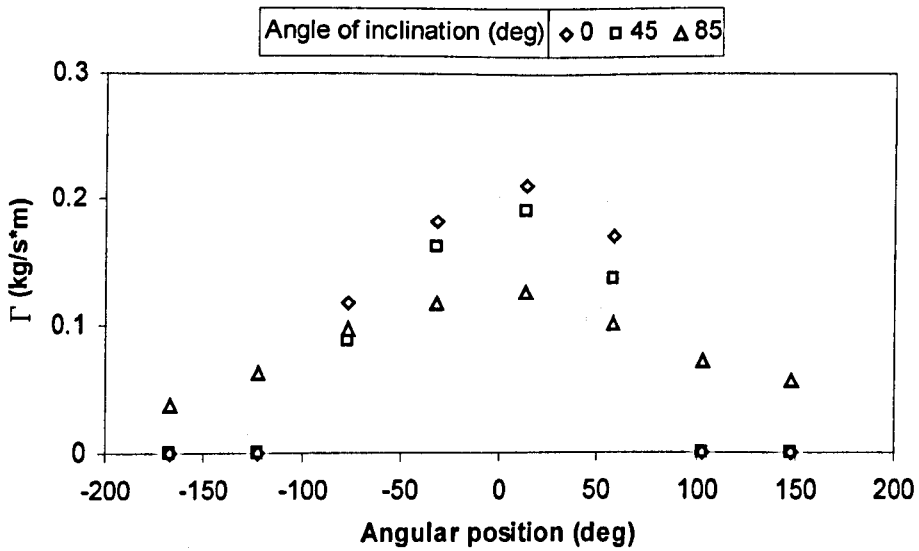


**Figure 4.2.2:** Liquid flow rate variation with the angle of inclination from horizontal. Gas mass flowrate=0.04 kg/s, liquid mass flowrate=0.0131 kg/s

Figures 4.2.3 and 4.2.4 show that, for a total liquid flowrate,  $M_l$ , the peripheral film flow rate  $\Gamma_x$  slightly increases with  $M_g$  around the bottom. Around the rest of the section there are not evident changes. The increments at the bottom of the throat are slightly more significant than those found in the main pipe. This is due to the different cross section area of the two pipes. It can be said that the variations of  $\Gamma_x$  with  $M_g$  are more significant in a smaller channel. However, these variations would be more remarkable with higher ranges of total liquid flowrate.

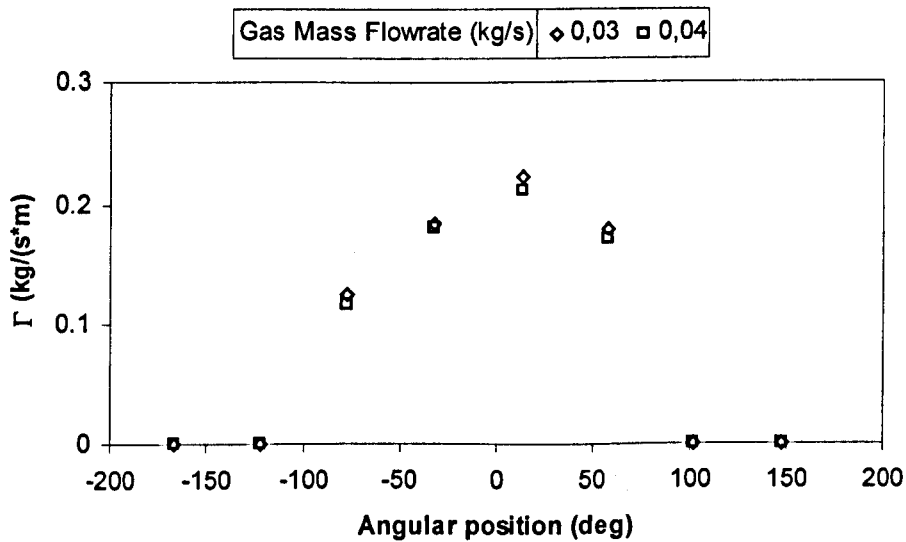


**Figure 4.2.3:** Liquid flow rate variation with gas mass flowrate in the throat section. Liquid mass flowrate=0.0131 kg/s, angle of inclination from horizontal=0°

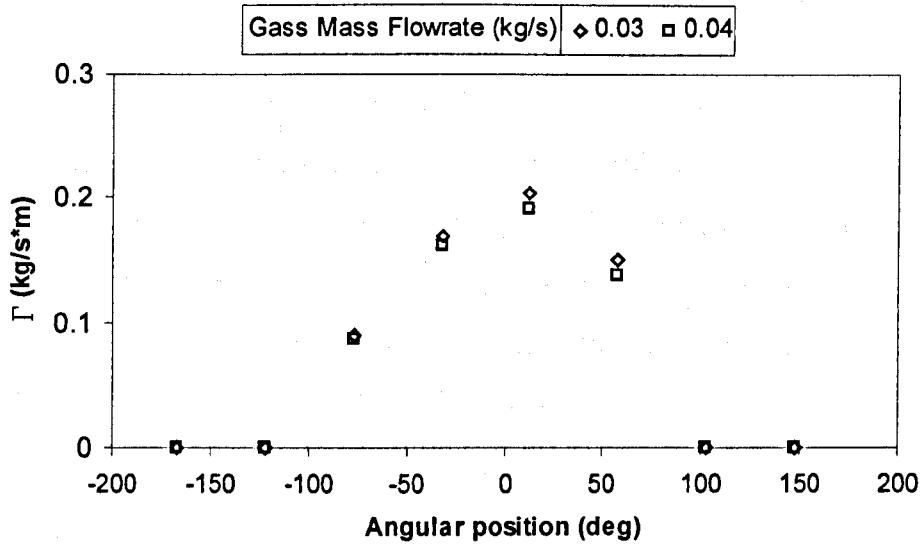


Figure 4.2.4: Liquid flow rate variation with gas mass flowrate in the throat section. Liquid mass flowrate=0.0131 kg/s, angle of inclination from horizontal=45°

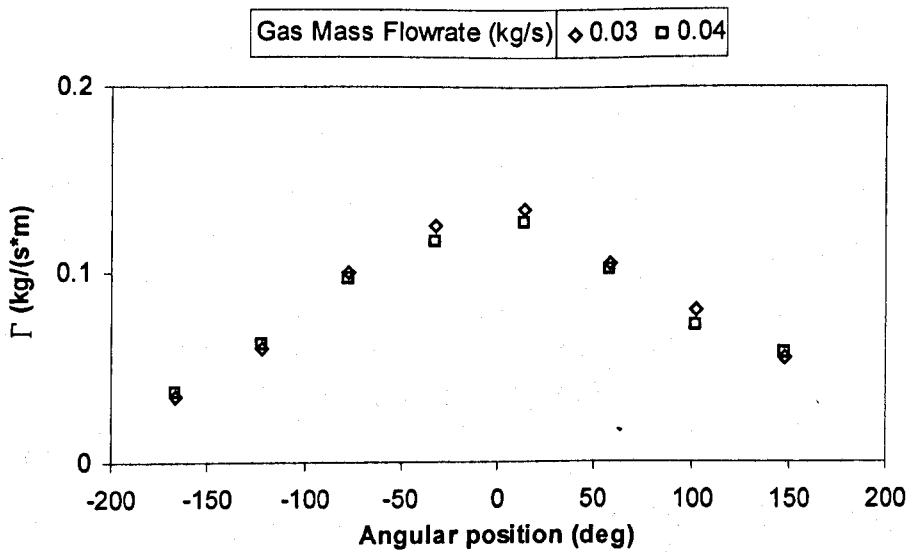
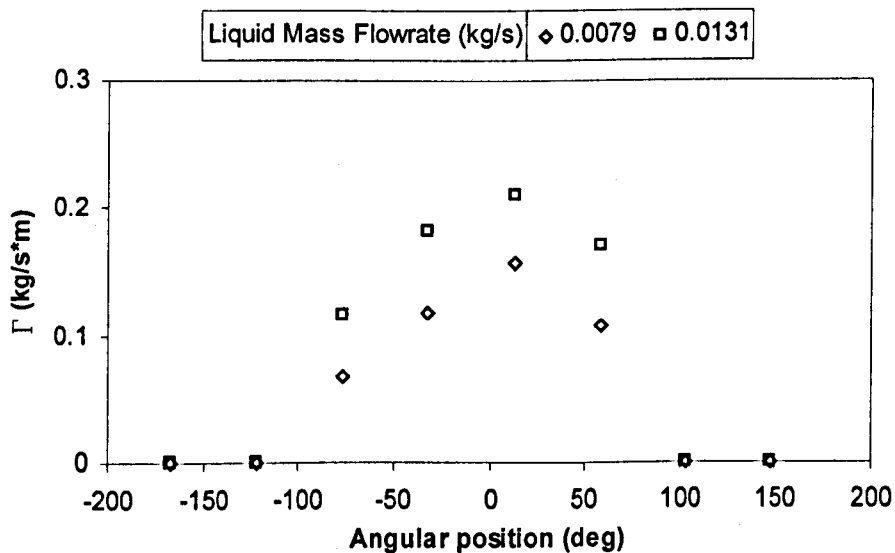


Figure 4.2.5: Liquid flow rate variation with gas mass flowrate in the throat section. Liquid mass flowrate=0.0131 kg/s, angle of inclination from horizontal=85°

Figures 4.2.6 to 4.2.8 show how the peripheral liquid mass flowrate  $\Gamma_x$  increases with the liquid flowrate  $M_l$ , especially at the bottom of the pipe. An increment of  $M_l$  results in a higher liquid entrainment and also in a bigger film annular area  $A_{LF}$  as shown in Chapter 5. Figures 4.2.6 and 4.2.7 illustrate that the variation of  $\Gamma_x$  with  $M_l$  is remarkable only at the bottom side of the pipe. Figure 4.2.8 illustrates that in  $85^\circ$  inclined flow the increment of  $\Gamma_x$  with  $M_l$  is equal around the entire section. Moreover, at this inclination the peripheral film flowrate becomes more uniform. These results agree with those found for the main pipe.



**Figure 4.2.6:** Liquid flow rate variation with liquid mass flowrate in the throat section. Gas mass flowrate=0.04 kg/s, angle of inclination from horizontal= $0^\circ$

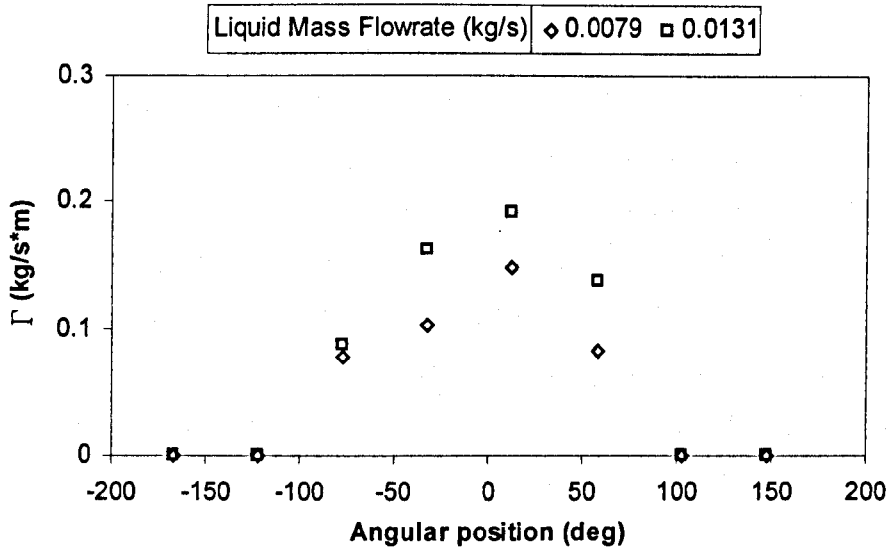


Figure 4.2.7: Liquid flow rate variation with liquid mass flowrate in the throat section. Gas mass flowrate=0.04 kg/s, angle of inclination from horizontal=45°

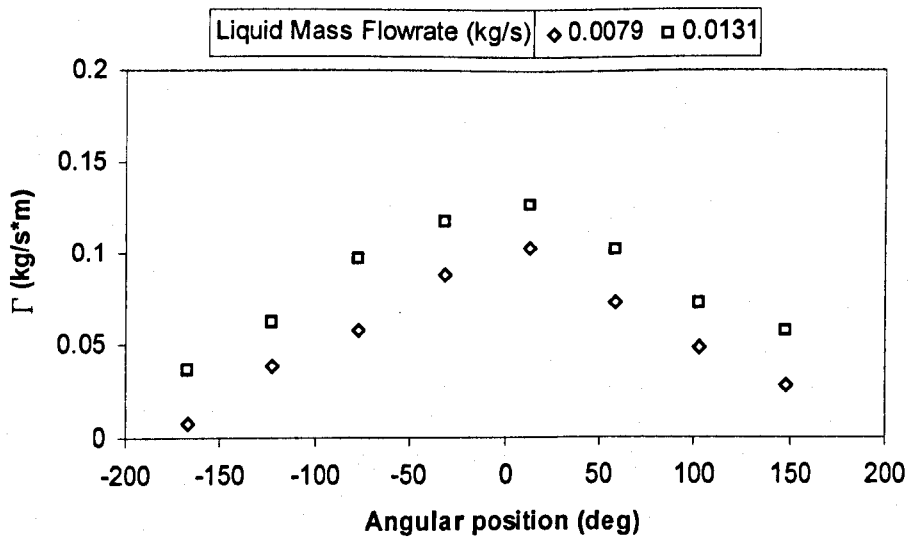
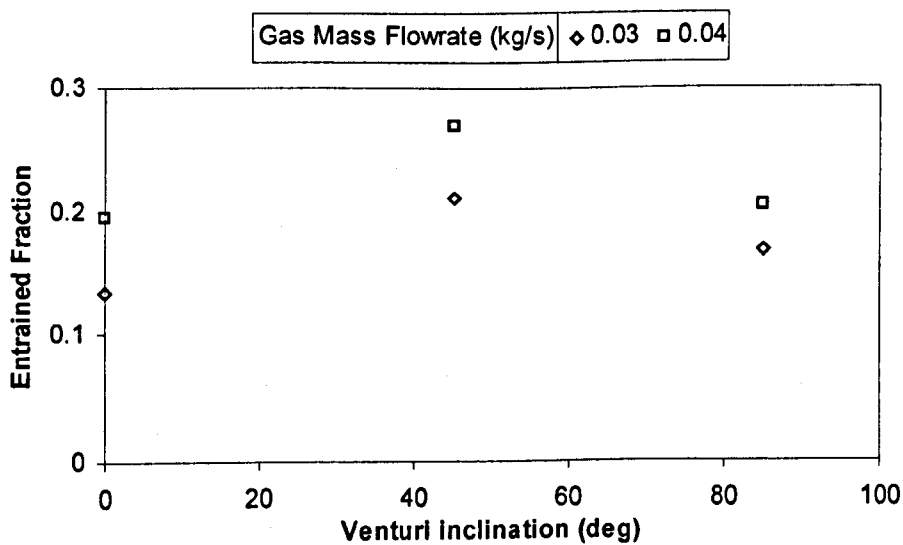
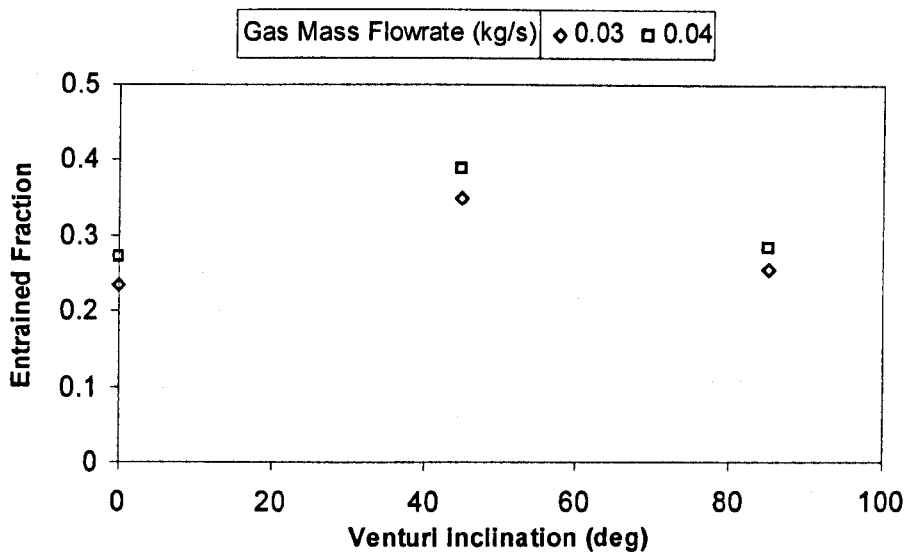


Figure 4.2.8: Liquid flow rate variation with liquid mass flowrate in the throat section. Gas mass flowrate=0.04 kg/s, angle of inclination from horizontal=85°

Figures 4.2.9 and 4.2.10 show the variation of the entrained fraction  $E$  with the pipe orientation. It is evident that the effect of the inclination is more remarkable in the throat than in the pipe upstream the Venturi. The highest entrained fraction would be expected in  $85^\circ$  inclined flow. In fact, this is the condition with highest shear between gas and liquid. This study shows that the horizontal flow is the condition with the lowest liquid entrained. Moreover, figures 4.2.9 and 4.2.10 show that the entrained fraction in the throat has the highest value in  $45^\circ$  inclined pipe. This result is a consequence of the chaotic and unstable two-phase flow in the throat. The annular flow is not fully developed in this section and the presence of the convergence upstream contributes to disturb significantly the flow.



**Figure 4.2.9:** Entrained fraction variation with inclination from horizontal in the throat section. Liquid mass flowrate=0.0079 kg/s



**Figure 4.2.10:** Entrained fraction variation with inclination from horizontal in the throat section. Liquid mass flowrate=0.0131 kg/s

Figures 4.2.11 and 4.2.12 show that, in the throat, the entrained fraction  $E$  increases with the gas flowrate,  $M_g$ . This is an obvious effect as the increment of  $M_g$  results in a stronger interaction between gas and liquid with consequent more liquid entrainment. It is also shown that, for the three inclinations analysed, the variation of  $E$  with  $M_g$  has the same trend. In other words, the variation of  $E$  with the gas mass flowrate does not change considerably with the angle of inclination. This shows coherency with the results of the main pipe. Figures 4.2.11 and 4.2.12 also show that, the points do not lie on the same curve. The reason is that, in the throat, the entrained fraction  $E$  varies with inclination, figure 4.2.8 and 4.2.9.

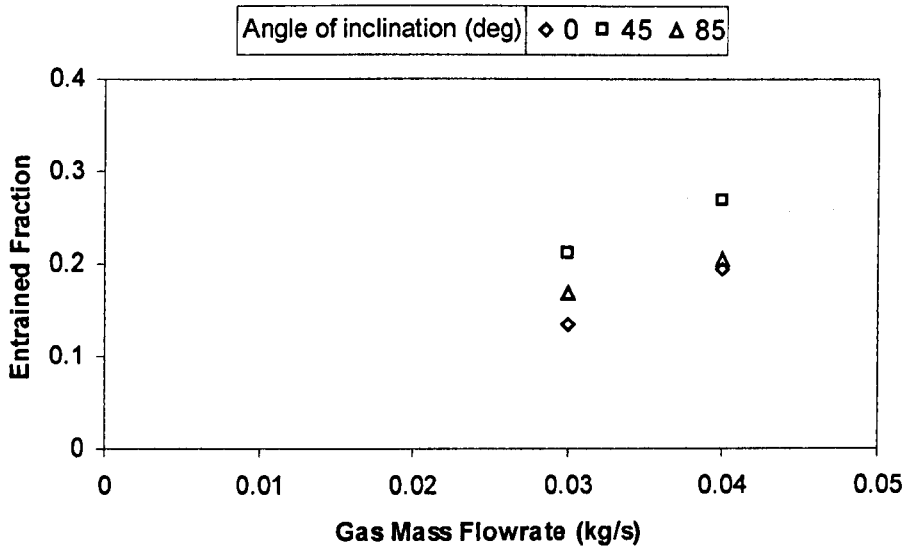


Figure 4.2.11: Entrained fraction variation with gas mass flowrate in the throat section. Liquid mass flowrate=0.0079 kg/s

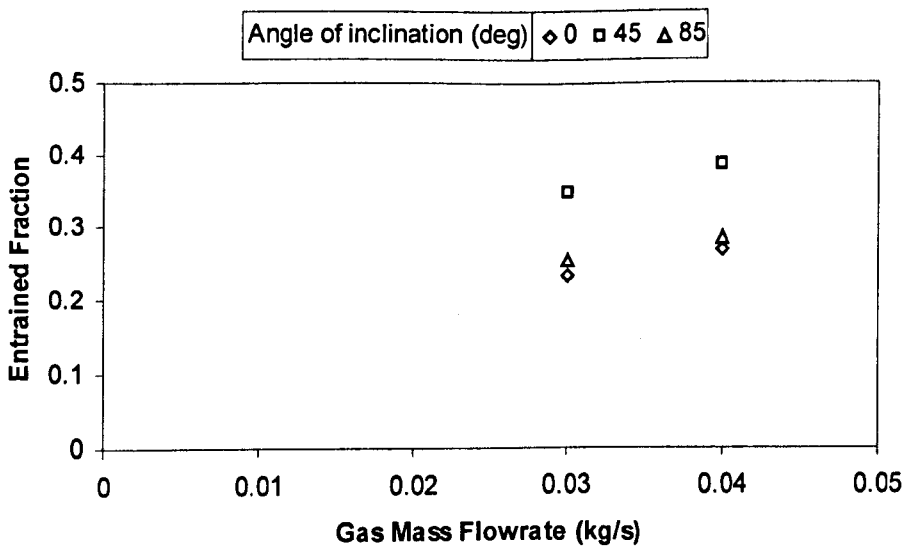
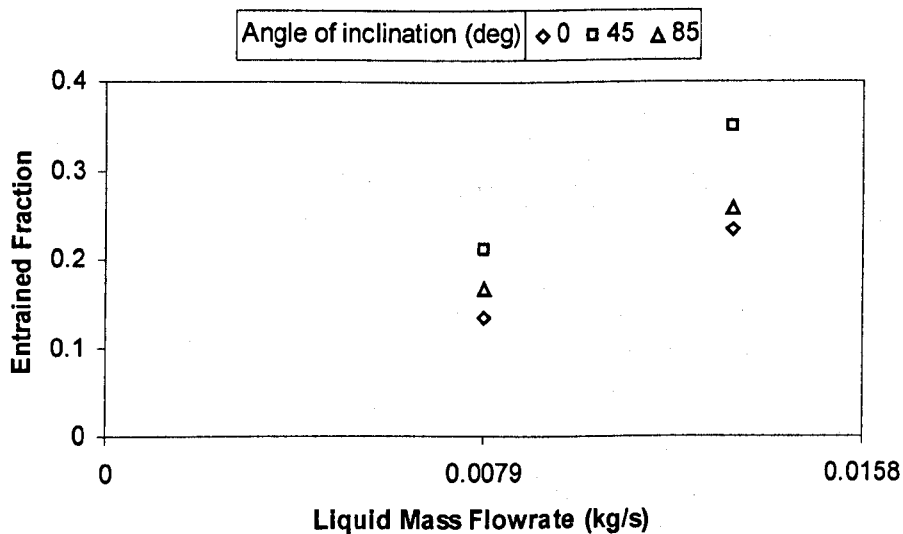


Figure 4.2.12: Entrained fraction variation with gas mass flowrate in the throat section. Liquid mass flowrate=0.0131 kg/s

Figures 4.2.13 and 4.2.14 show that the entrained fraction,  $E$  increases with liquid mass flowrate,  $M_l$ . This means that when the value of  $M_l$  is increased the liquid entrained into the main gas core increases consequently. A higher value of  $M_l$  results in more liquid moved along the channel and this has the effect to produce a higher film area  $A_{LF}$  and a higher liquid entrainment. Figures 4.2.13 and 4.2.14 also show that the increment of the entrained fraction with the variation of  $M_l$  does not change considerably with inclination. Figures 4.2.15 and 4.2.16 show the effect of the gas and liquid mass flux on the entrained fraction both in the pipe and in the Venturi throat. It is evident how the effect of the flow conditions on the liquid entrainment is larger in the throat.



**Figure 4.2.13:** Entrained fraction variation with liquid mass flowrate in the throat section. Gas mass flowrate=0.03 kg/s

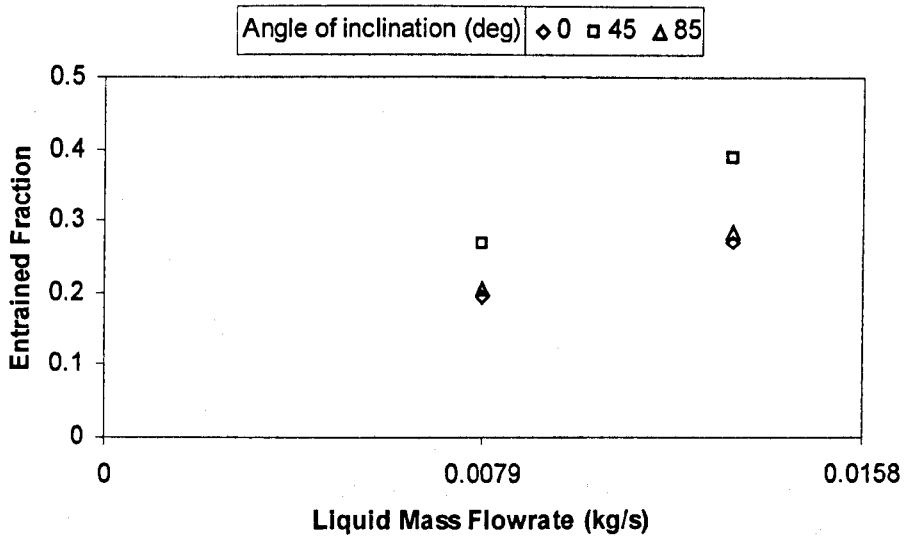


Figure 4.2.14: Entrained fraction variation with liquid mass flowrate in the throat section. Gas mass flowrate=0.04 kg/s

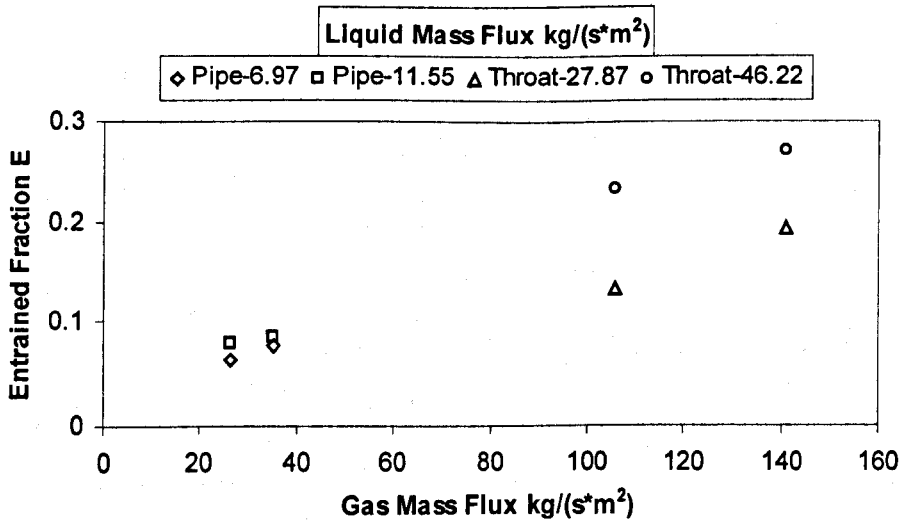
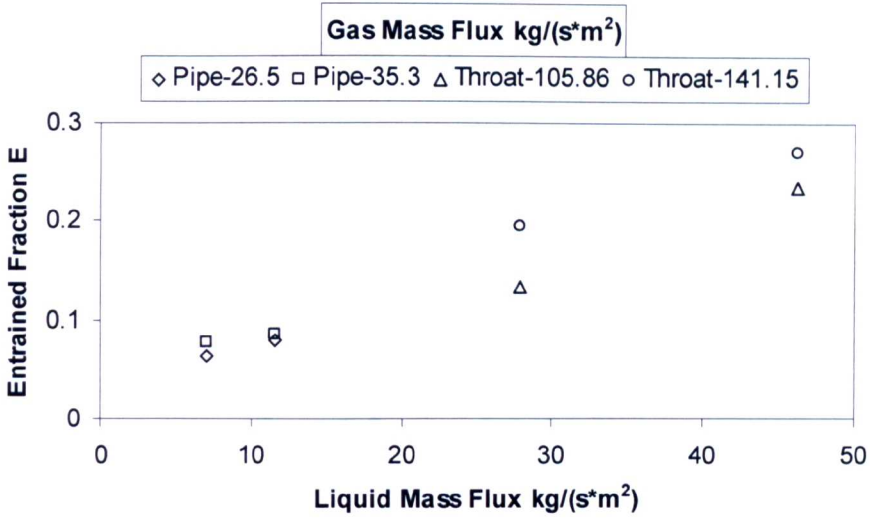
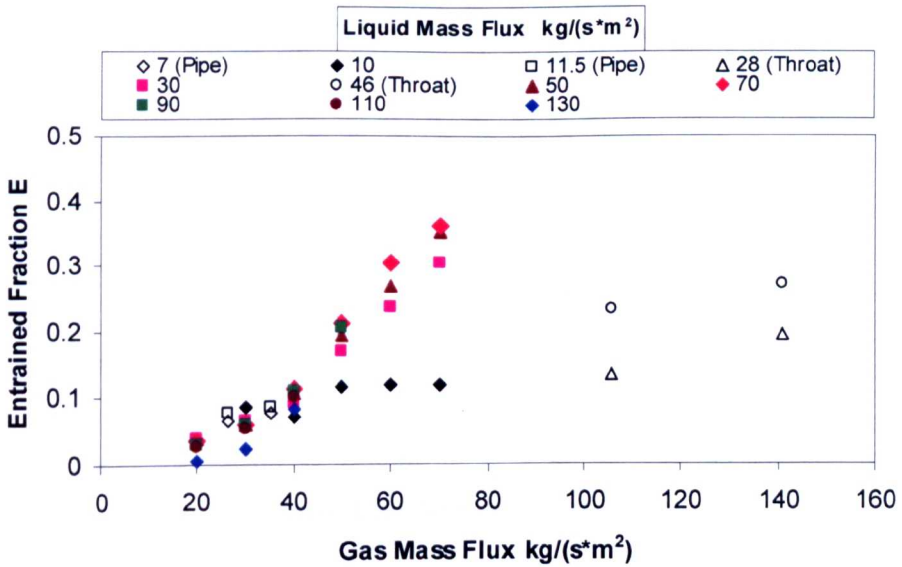


Figure 4.2.15: Entrained fraction variation with the gas mass flux. Angle of inclination=0°.



**Figure 4.2.16:** Entrained fraction variation with the liquid mass flux. Angle of inclination=0°.



**Figure 4.2.17:** Entrained fraction variation with the gas mass flux. Angle of inclination=0°. Open symbols are the present data. Coloured symbols are data of Ribeiro *et al.* (1995) [i.d.=32mm]

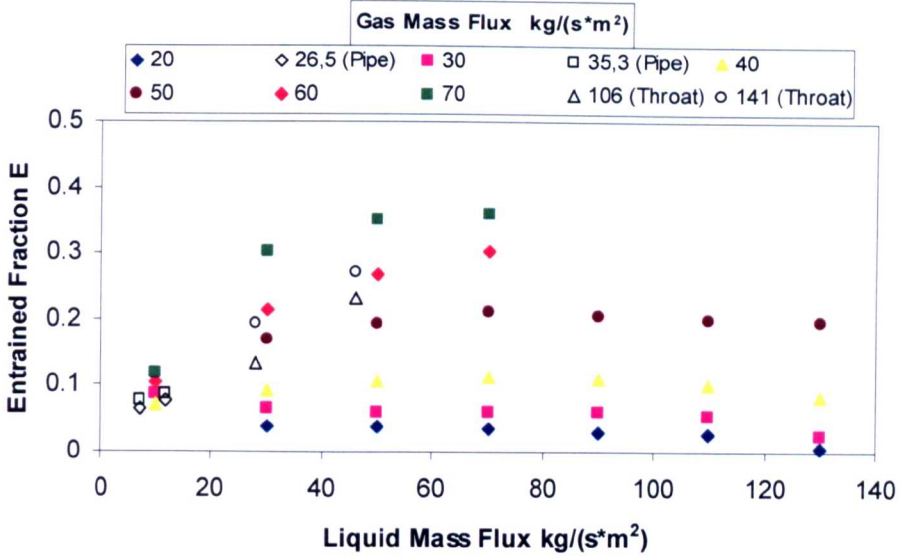


**Figure 4.2.18:** Entrained fraction variation with the liquid mass flux. Angle of inclination= $0^\circ$ . Open symbols are the present data. Coloured symbols are data of Ribeiro *et al.* (1995) [i.d.=32mm]

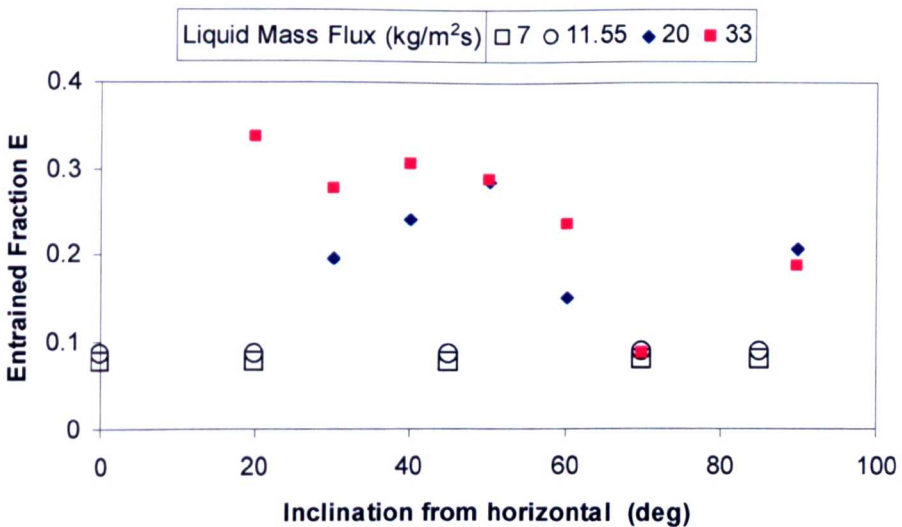


**Figure 4.2.19:** Entrained fraction variation with inclination. Gas velocity=21.5 m/s. Open symbols are the present data. Coloured symbols are data of Azzopardi *et al.* (1997)

## CHAPTER 5

### Liquid Film Thickness Results

As noted in Chapter 2, in contrast to the numerous investigations of film thickness in horizontal or near horizontal flow where circumferential variations have been reported, only one paper provides such data for steeply inclined pipes, Paz & Shoham (1994). This chapter goes some way to rectifying this lack of data and reports information of film thickness in a 38 mm i.d pipe at inclinations of  $0^\circ$ ,  $30^\circ$ ,  $45^\circ$ ,  $60^\circ$  and  $85^\circ$  from horizontal. The circumferential variation that occurs when the same flows pass through the throat of a Venturi is also reported. In this latter case the measurements were made at inclinations of  $-2^\circ$ ,  $0^\circ$ ,  $2^\circ$ ,  $30^\circ$ ,  $45^\circ$ ,  $60^\circ$  and  $85^\circ$  from the horizontal. For the pipe upstream of the Venturi, both the parallel wire and the flush-mounted pin electrode arrangements were employed. For the throat of the Venturi, only the second technique was used.

The gas mass flowrates employed and the corresponding superficial velocities in the pipe and in the Venturi throat are given in table 5.1. The same liquid flowrates were used at all gas flowrates. These, together with the corresponding superficial velocities are given in table 5.2

**Table 5.1: Gas mass flowrates and gas velocities**

Gas mass flowrate (kg/s)	Gas velocity in the pipe (m/s)	Gas velocity in the throat (m/s)
0.03	15	61.8
0.04	21.5	86.3

**Table 5.2: Liquid mass flowrates and liquid velocities**

Liquid mass flowrate (kg/s):	Liquid velocity in the pipe (m/s)	Liquid velocity in the throat (m/s)
0.0079	0.007	0.028
0.0131	0.011	0.046
0.0317	0.028	0.111
0.0527	0.046	0.185
0.0899	0.079	0.317

## 5.1 Results in the pipe upstream of the Venturi

For each experimental run, the liquid film thickness in the main section was measured at thirteen locations by using ten pairs of flush-mounted probes and three pairs of wire probes. Chapter 3 shows the details of the two test sections and the exact positions of the probes.

A typical time series of film thickness is shown in figure 5.1.1. As can be seen, due to the utilization of a high speed data acquisition system, the data clearly depict the complex wavy structure of the annular flow interface. In the present study, several characteristics of the film thickness are studied. One of these, the time average, is given by a horizontal line, figure 5.1.1. The raw data of film thickness are enclosed in the DVD.

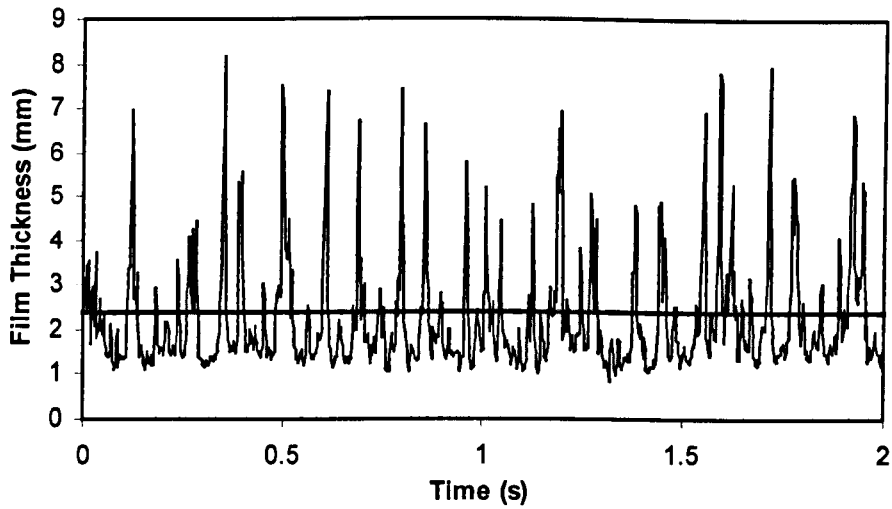


**Figure 5.1.1:** Film thickness signal in the main section. Gas mass flowrate=0.04 kg/s, liquid mass flowrate=0.0131 kg/s, angle of inclination from horizontal=45°, wires B

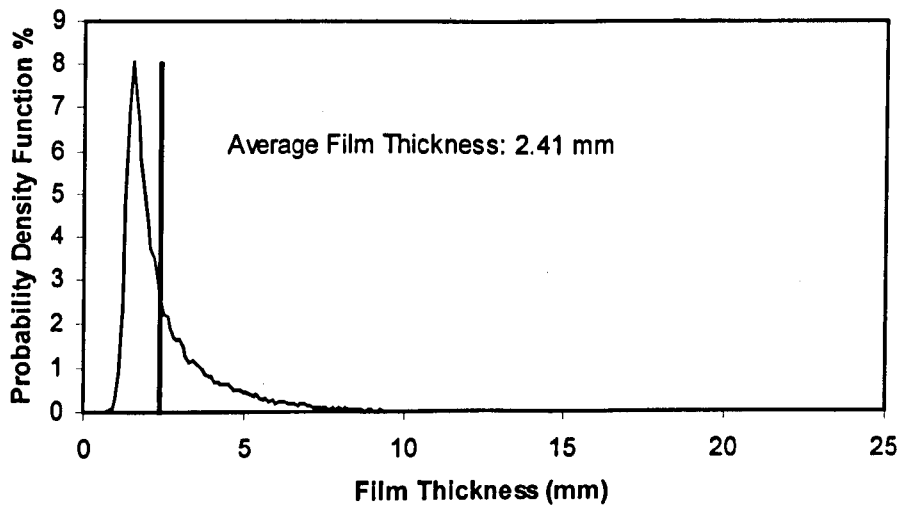


**Figure 5.1.2:** PDF of film thickness in the main section. Gas mass flowrate=0.04 kg/s, liquid mass flowrate=0.0131 kg/s, angle of inclination from horizontal=45°, wires B

Figure 5.1.2 shows the probability density function (PDF) of the film thickness trace in figure 5.1.1. The PDF shows the probability of occurrence of a liquid film of height  $h$ . The most probable value represents the base film thickness of the trace. In figure 5.1.2 the average film thickness (2.41mm) is bigger than the base film thickness (1.45mm). Figure 5.1.2 also shows that the average film thickness is closer to the base film thickness than to the thicker values at the wave peaks. From this it can be deduced that wave amplitude is several times the mean and base film thickness as reported by Hewitt & Nicholls (1964) for vertical flow and by Pearce (1979) for horizontal flow.

The data presented in figure 5.1.1 clearly suggested that, at the bottom, the wave structure is dominated by large disturbance waves. The present study shows that, at relatively small gas flowrates, where gravity is important, these waves are very pronounced, especially along the lower half of the pipe. Moreover, their amplitude and frequency depends on liquid mass flowrate and pipe inclination. In the present study, the wave height  $h_w$  is measured from the base film thickness. In Nencini & Andreussi (1983) and in Paras & Karabelas (1991) the wave height is measured from the pipe surface and the amplitude of the waves is defined as one-half the height difference  $\Delta h$  between a minimum in the film trace and the subsequent maximum.

In figures 5.1.3 to 5.1.5 the average film thickness is plotted in polar coordinates in a cross-section of the pipe. These figures present the film distribution around the circumference and show the changes with the pipe inclination. The cross-section of the pipe is also done in polar coordinates. A linear interpolation is applied between the measured points<sup>1</sup>.

---

<sup>1</sup> By using polar coordinates the linear interpolation of the liquid film thickness leads to arcs.

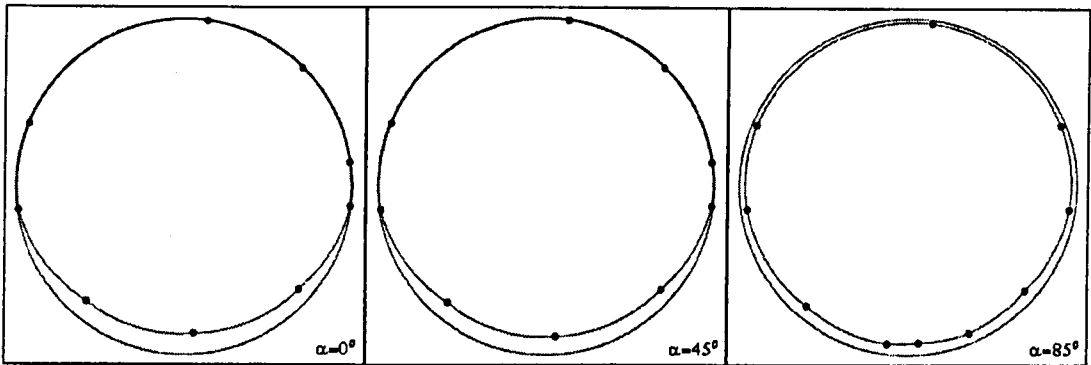


**Figure 5.1.3:** Average liquid film thickness distribution in the main section. Gas mass flowrate=0.04 kg/s, liquid mass flowrate=0.0079 kg/s

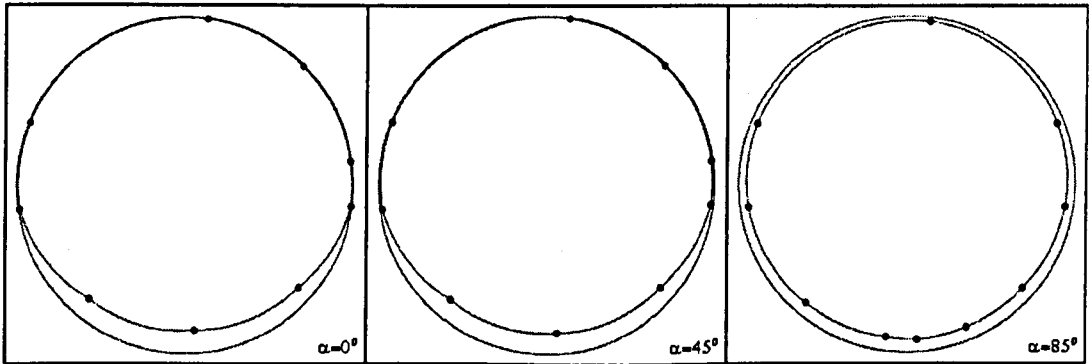


**Figure 5.1.4:** Average liquid film thickness distribution in the main section. Gas mass flowrate=0.04 kg/s, liquid gas mass flowrate=0.0131 kg/s

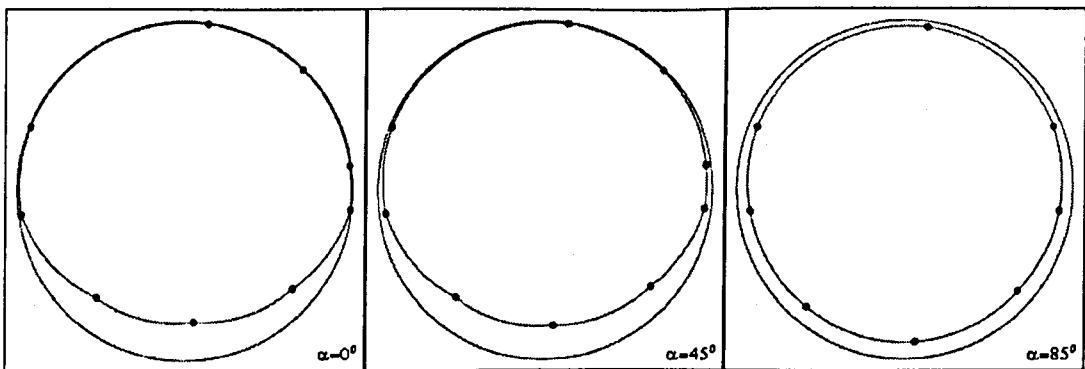


**Figure 5.1.5:** Average liquid film thickness distribution in the main section. Gas mass flowrate=0.04 kg/s, liquid mass flowrate=0.0317 kg/s

Figures 5.1.3 to 5.1.5 illustrate the effect of the inclination angle on the liquid film thickness around the pipe periphery. The variation of the liquid film thickness with the two highest liquid mass flowrates (table 5.2) is not shown because the liquid film was higher than 2 mm and this caused the saturation of the probes. The film distribution is not symmetrical for the three inclinations shown. Clearly, as the inclination angle deviates from horizontal, the film thickness distribution becomes less pronounced at the bottom. Due to gravity the film thickness decreases at the bottom and increases at the top. Figures 5.1.3 to 5.1.5 show that the profile of the film thickness does not change significantly when the inclination is increased from  $0^\circ$  to  $45^\circ$ . At both inclinations, the liquid film is mainly located at the bottom. In  $85^\circ$  inclined flow, the liquid film is less thick at the bottom and thicker at the top but it is still not uniform. Although this presentation is useful for giving an idea of how, in a mean sense, the liquid film varies into the pipe cross section, it is not easy to quantify the information. For this reason, Fukano & Ousaka (1989) presented their data on film circumferential distribution in logarithmic scale.

Because of the lack of quantitative information of figures 5.1.3 to 5.1.5, subsequent results will be illustrated in Cartesian coordinates, e.g., figure 5.1.6. Here, the abscissa is the angular position of the middle point between the probes and the zero is assumed at the bottom of the pipe. The profile has the shape of a "bell" and it is symmetric at zero.

Figures 5.1.7 to 5.1.11 show, in Cartesian coordinates, the variation of the time average film thickness that occurs when the inclination angle varies from horizontal to  $85^\circ$ . It is evident that the film thickness is not uniform. Due to gravity the liquid film tends to flow around the upper part of the pipe. This results in a thicker film at the bottom and a thinner film at the top. Also the  $85^\circ$  inclined flow shows this trend.

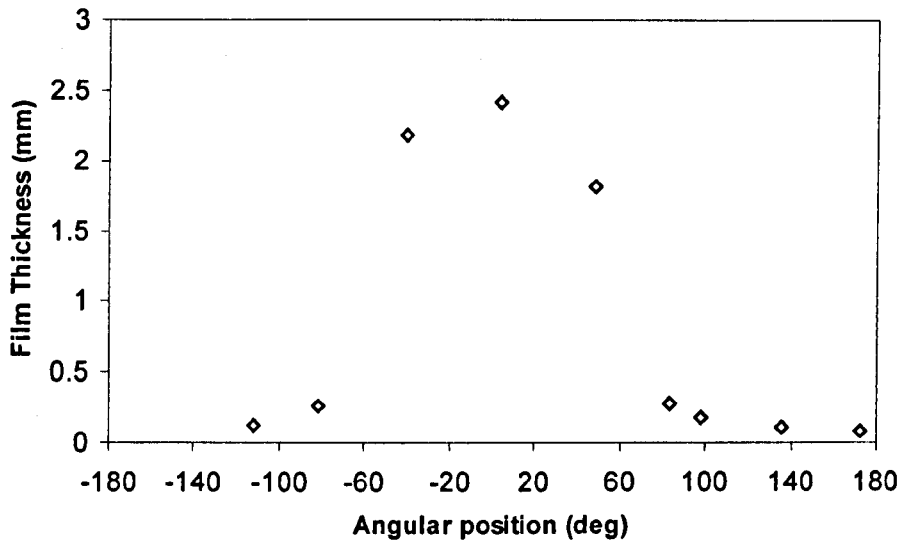


Figure 5.1.6: Liquid film thickness distribution. Gas mass flowrate=0.04 kg/s, liquid mass flowrate=0.0131 kg/s, angle of inclination from horizontal=45°

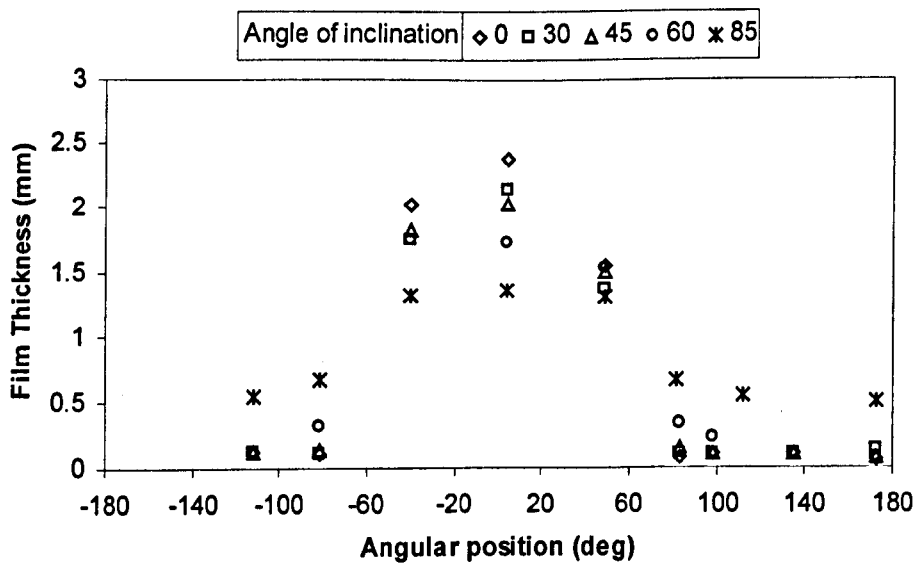
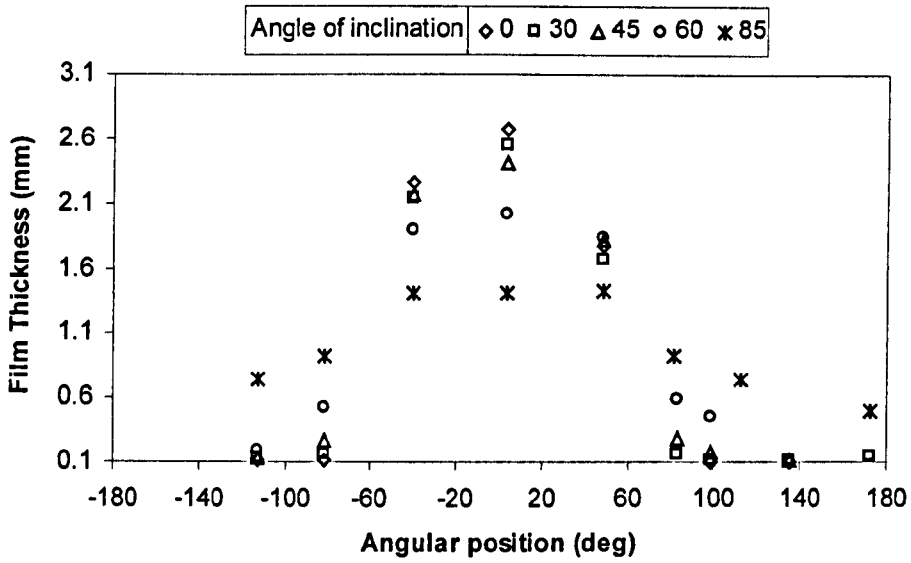
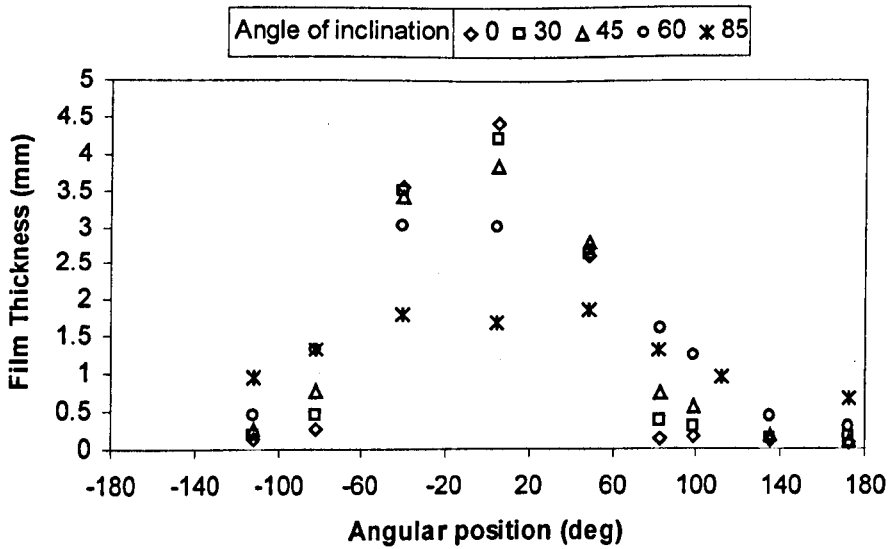


Figure 5.1.7: Liquid film thickness variation with angle of inclination from horizontal. Gas mass flowrate=0.04 kg/s, liquid mass flowrate=0.0079 kg/s



**Figure 5.1.8:** Liquid film thickness variation with angle of inclination from horizontal. Gas mass flowrate=0.04 kg/s, liquid mass flowrate=0.0131 kg/s



**Figure 5.1.9:** Liquid film thickness variation with angle of inclination from horizontal. Gas mass flowrate=0.04 kg/s, liquid mass flowrate=0.0317 kg/s

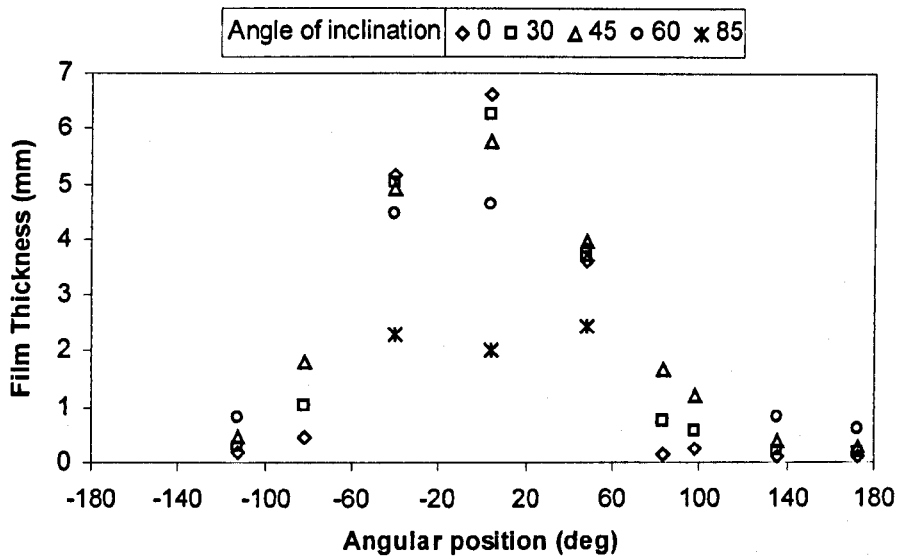


Figure 5.1.10: Liquid film thickness variation with angle of inclination from horizontal. Gas mass flowrate=0.04 kg/s, liquid mass flowrate=0.0527 kg/s

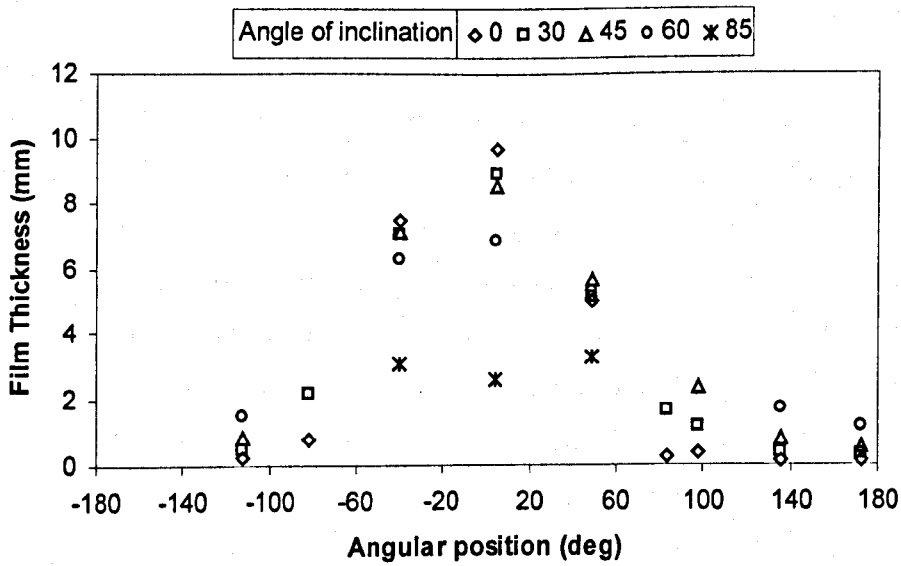


Figure 5.1.11: Liquid film thickness variation with angle of inclination from horizontal. Gas mass flowrate=0.04 kg/s, liquid mass flowrate=0.0899 kg/s

The void fraction can be obtained from the film thickness data:

$$\varepsilon_g = 1 - \frac{A_{LF}}{A_i} = 1 - \frac{4}{\pi \cdot D_i^2} \int_0^{2\pi} s \cdot d\theta \quad (5.1)$$

where  $A_{LF}$  is given by:

$$A_{LF} = \int_0^{2\pi} s \cdot d\theta \quad (5.2)$$

These calculations show that there is not remarkable variation of  $A_{LF}$  with the pipe inclination,  $\alpha$ . In horizontal flow, a higher annular area  $A_{LF}$  would be expected since the liquid is more easily moved than in other inclinations. On the other hand, a higher area  $A_{LF}$  means a higher liquid entrained. This two opposing effects result in an insignificant variation of  $A_{LF}$  with inclination. This very small variation of  $A_{LF}$  with  $\alpha$  can be clearly seen by superimposing figure 5.1.3 to 5.1.5 and analysing them using light. The fact that the liquid film area and, therefore, the void fraction do not vary with inclination is related to the very small change of entrained fraction with the pipe orientation. However, in order to give quantitative information, it is fundamental the analysis of the liquid film velocity with varying inclination<sup>2</sup>. This analysis was not carried on in the present study but it can be conducted with a second test section located downstream. Once known the effect of the pipe orientation on the film velocity,  $U_{LF}$ , an unambiguous relation between  $A_{LF}$  and the entrained fraction can be given at varying inclination. However, with regards to the entrained fraction it can be asserted that the insignificant effect of the inclination on  $E$  is due to the small variation with inclination of the friction at the gas-liquid interface and of wave frequency, see Chapter 4.

---

<sup>2</sup> Liquid film mass flowrate, liquid film area and liquid film velocity are all related together:  
 $M_{LF} = \rho_l A_{LF} U_{LF}$

Figures 5.1.12 to 5.1.16 show the variation of the average film thickness with liquid mass flowrate,  $M_l$ . As  $M_l$  increases, the film thickness distribution changes around the pipe and the annular film becomes higher. The film thickness increases particularly along the bottom of the pipe because the gravity forces tend to keep the liquid along this side.

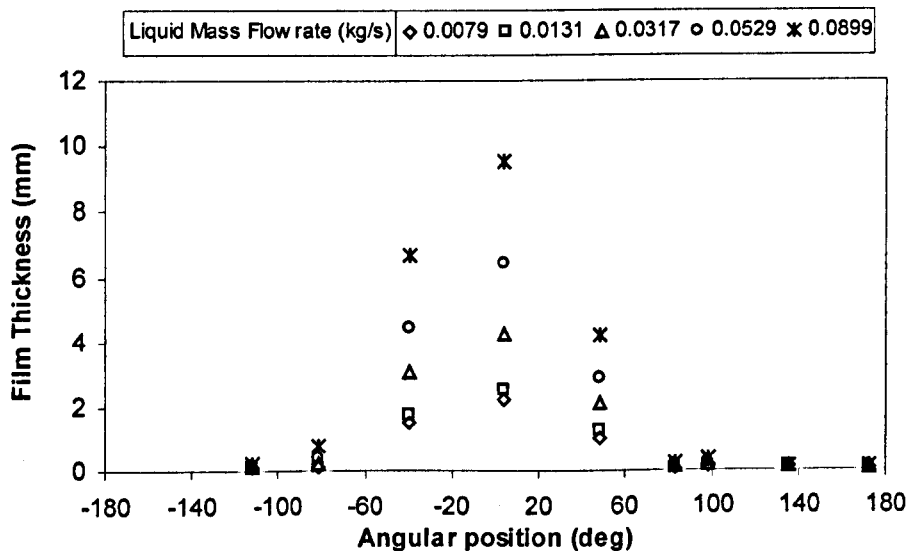


**Figure 5.1.12:** Liquid film thickness variation with liquid mass flowrate. Gas mass flowrate=0.04 kg/s, angle of inclination from horizontal=0°

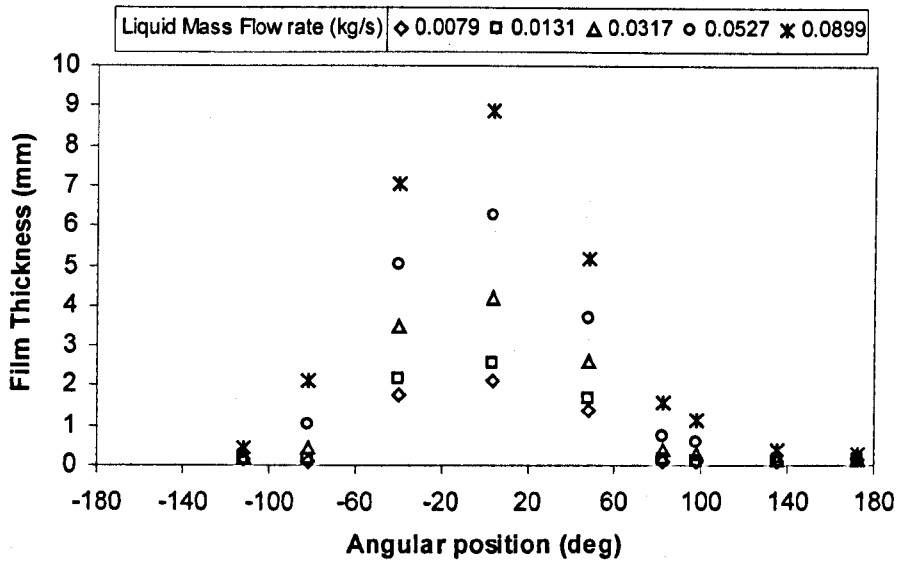


Figure 5.1.13: Liquid film thickness variation with liquid mass flowrate. Gas mass flowrate=0.04 kg/s, angle of inclination from horizontal=30°

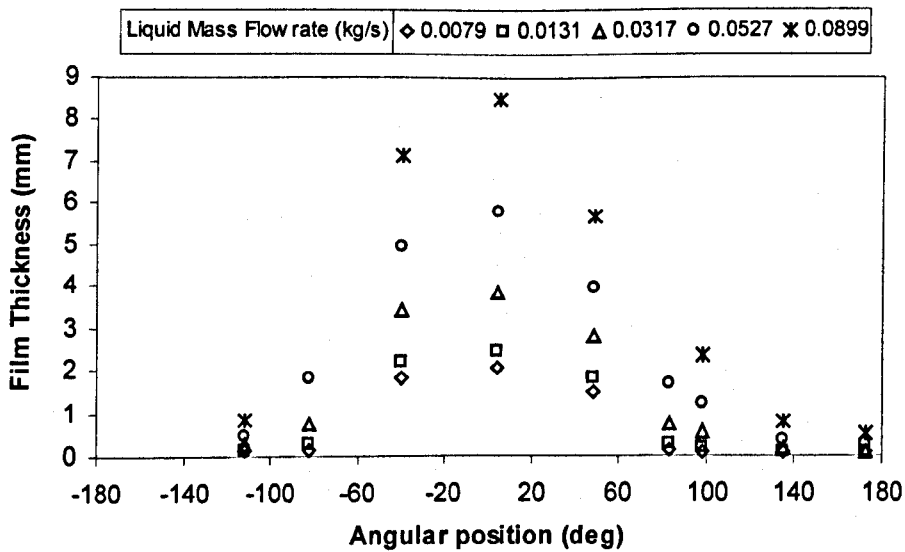


Figure 5.1.14: Liquid film thickness variation with liquid mass flowrate. Gas mass flowrate=0.04 kg/s, angle of inclination from horizontal=45°

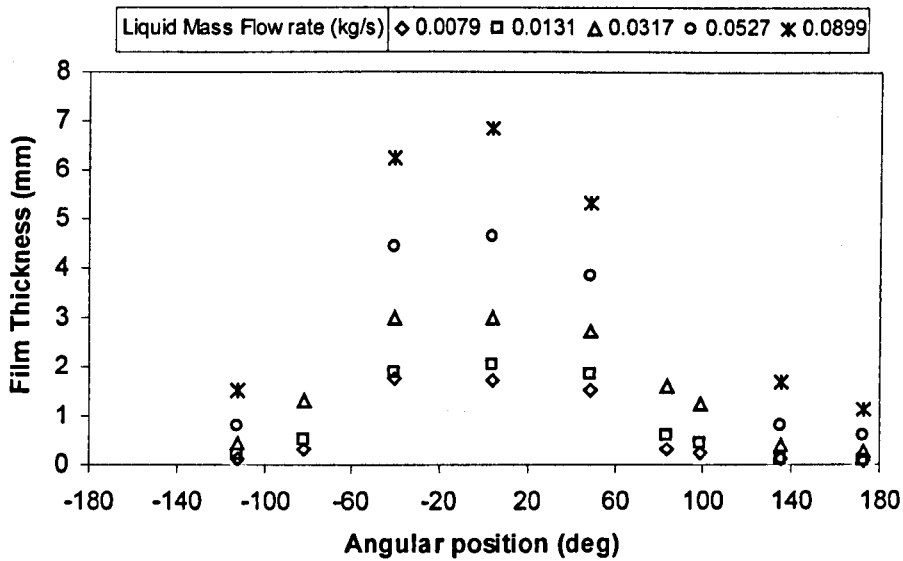


Figure 5.15: Liquid film thickness variation with liquid mass flowrate. Gas mass flowrate=0.04 kg/s, angle of inclination from horizontal=60°

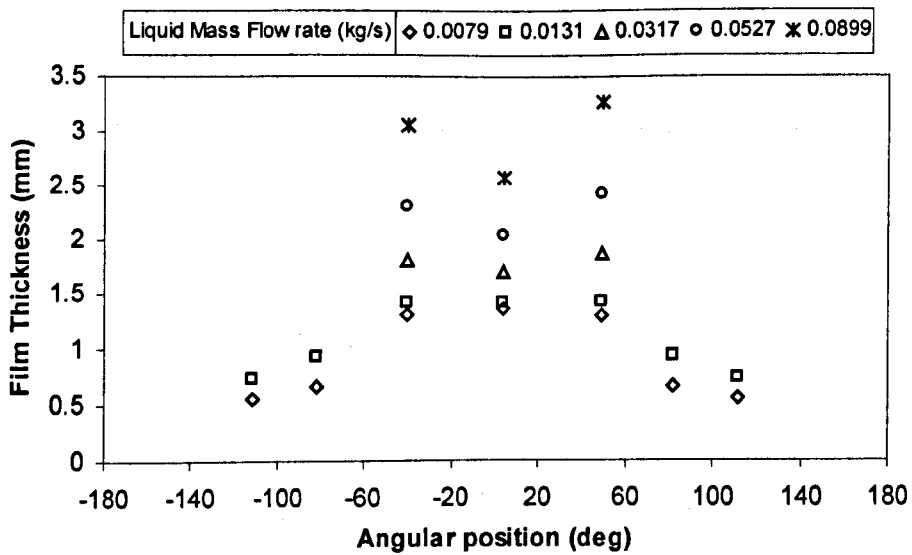
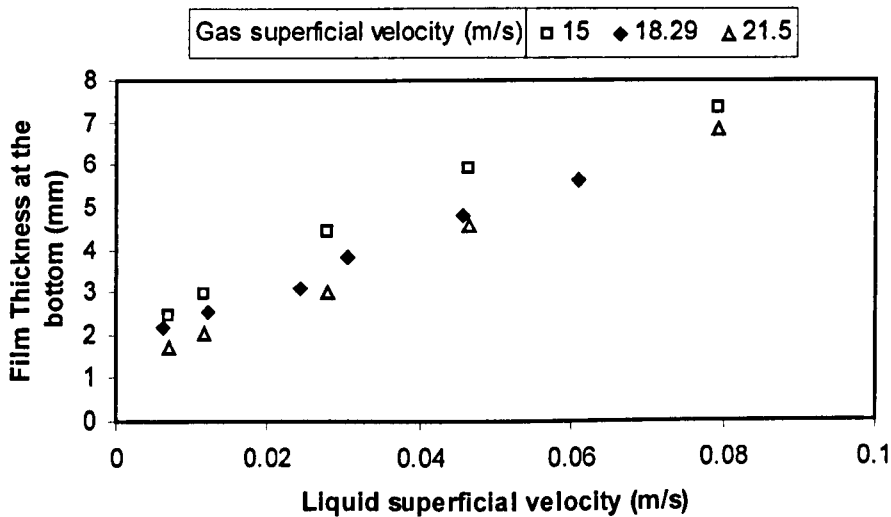


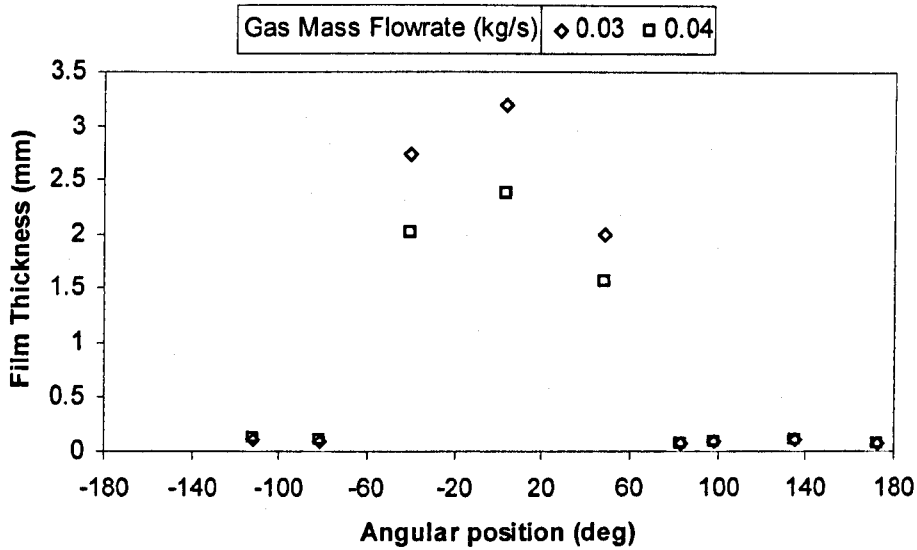
Figure 5.16: Liquid film thickness variation with liquid mass flowrate. Gas mass flowrate=0.04 kg/s, angle of inclination from horizontal=85°

Figure 5.1.17 shows a comparison between the present data and the data of Paz & Shoham (1994). The data show the variations of the liquid film thickness at the bottom with the liquid superficial velocity. The pipe inclination considered is  $60^\circ$ . The comparison shows a good agreement of the three sets of results.



**Figure 5.1.17:** Variation of film thickness at the bottom with liquid superficial velocity. Angle of inclination from horizontal= $60^\circ$ . Open symbols are the present data. Filled symbols are data of Paz & Shoham (1994)

Figures 5.1.18 to 5.1.22 show that the height of the liquid film decreases when the gas mass flowrate is increased. This is due to the action of the gas on the liquid film which increases the atomization at the gas-liquid interface. The gas strips liquid off the waves and the droplets, so formed, are dragged into the main gas core, see figure 2.3.1. This results in a less thick film around the section and in a higher liquid entrained. The annular area  $A_{LF}$  occupied by the liquid film is obtained by integrating the liquid film thickness around the section perimeter, see equation 5.2. These calculations show that  $A_{LF}$  decreases with the gas mass flowrate,  $M_g$ .



**Figure 5.18:** Liquid film thickness variation with gas mass flowrate. Liquid mass flowrate=0.0079 kg/s, angle of inclination from horizontal=0°

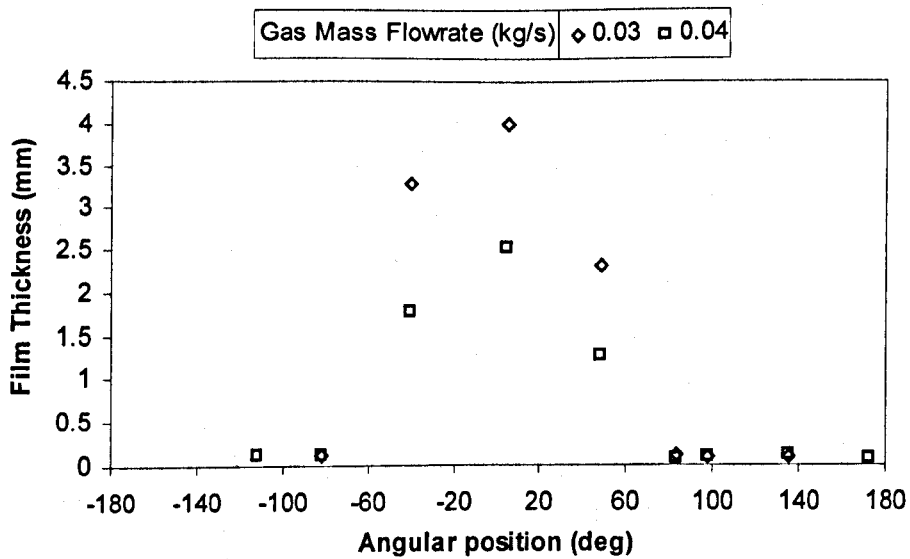


**Figure 5.19:** Liquid film thickness variation with gas mass flowrate. Liquid mass flowrate=0.0131 kg/s, angle of inclination from horizontal=0°

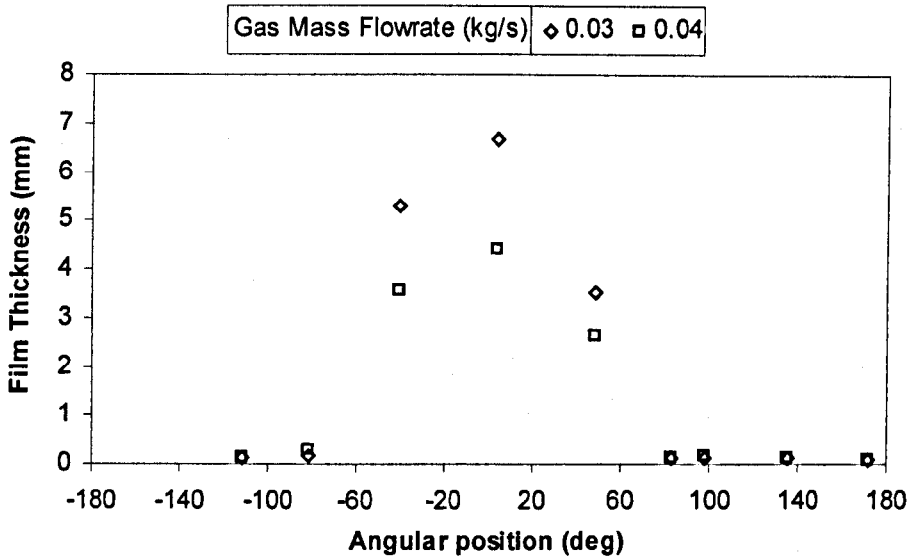


Figure 5.1.20: Liquid film thickness variation with gas mass flowrate. Liquid mass flowrate=0.0317 kg/s, angle of inclination from horizontal=0°

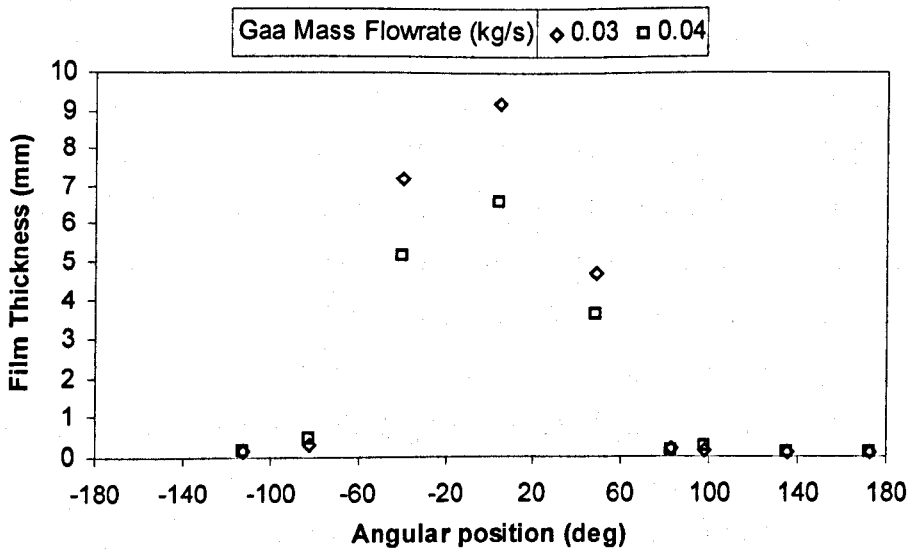
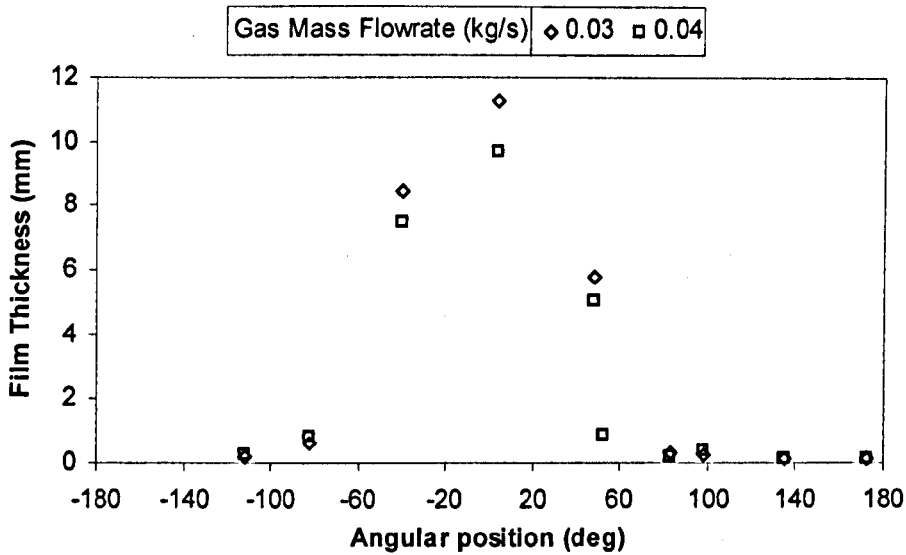


Figure 5.1.21: Liquid film thickness variation with gas mass flowrate. Liquid mass flowrate=0.0527 kg/s, angle of inclination from horizontal=0°



**Figure 5.1.22:** Liquid film thickness variation with gas mass flowrate. Liquid mass flowrate=0.0899 kg/s, angle of inclination from horizontal=0°

With the range of gas mass flowrates considered in this study, the film thickness distribution is very asymmetric; it changes little in the upper half of the tube; and reduces drastically between the bottom and the side of the tube. The study of liquid film thickness at higher gas velocity ( $U_{sg} > 20$  m/s) would be of particular interest. However, the limitations of the main air supply did not allow higher ranges of gas flowrates. Paras & Karabelas (1991) showed the reduction of liquid film thickness with increasing gas velocity ( $31 \text{ m/s} \leq U_{sg} \leq 66 \text{ m/s}$ ) in a 50.8 mm i.d. horizontal pipe. They also found that the amplitude of waves is greater at lower gas mass flowrate. Their data pointed out the large influence of gravity on liquid distribution at relatively low gas velocity. For low gas velocity ( $U_{sg} < 40$  m/s) and liquid velocity between 0.019 and 0.2 m/s, the liquid film was highly asymmetric due to gravity. As the mass flowrate was increased, the liquid film height, as well as the rest of the film properties, tended to be distributed more uniformly around the circumference, implying that the role of gravity was almost negligible under those conditions. For instance, at  $U_{sg} > 50$  m/s the film thickness at the top of the pipe was almost 80% of

the value at the bottom. In the present study, for the low range of gas rates considered, the influence of gravity is very high. A small deviation from vertical ( $85^\circ$  from horizontal) has the effect to give a non-uniform circumferential distribution of the liquid film thickness.

Many researchers have pointed out that local film thickness at a specific circumferential location is, for practical purposes, equal to the average film thickness. For Paras & Karabelas (1991) this location is approximately  $60^\circ$  from the pipe bottom. The same result was obtained by Andritsos (1986) in 25 mm i.d pipe. Sekoguchi *et al.* (1982) also reported a similar characteristic value ( $\theta=60$ ) obtained in a 26 mm i.d. pipe. In this study, although no measurements were taken at  $60^\circ$ , the film thickness at  $48.24^\circ$  from the bottom shows a satisfactory approximation. The characteristic value for large diameter (i.d > 60 mm) pipe appears to be smaller.

In order to give a more detailed examination of the liquid film characteristics as well as of the disturbance waves two selected cases of data are presented. The first is shown in figures 5.1.23 to 5.1.27. Here, different time series of film thickness are shown. However, figure 5.1.27 shows the liquid film trace only at the locations measured by wires B and C. In this figure, the characteristics of the film at the other locations are not presented because the liquid film was higher than 2 mm and this caused the saturation of the probes. Gas and liquid mass flowrates are respectively  $M_g = 0.04$  kg/s and  $M_l = 0.0131$  kg/s. Five film thickness traces measured at locations between  $0^\circ$  and  $180^\circ$  are presented. The first two are measured by wires B and C, the other three by probes 3(2), 4(2) and 5(2). Figures 3.3.1 and 3.3.9 of Chapter 3 show the angular positions of the probes.

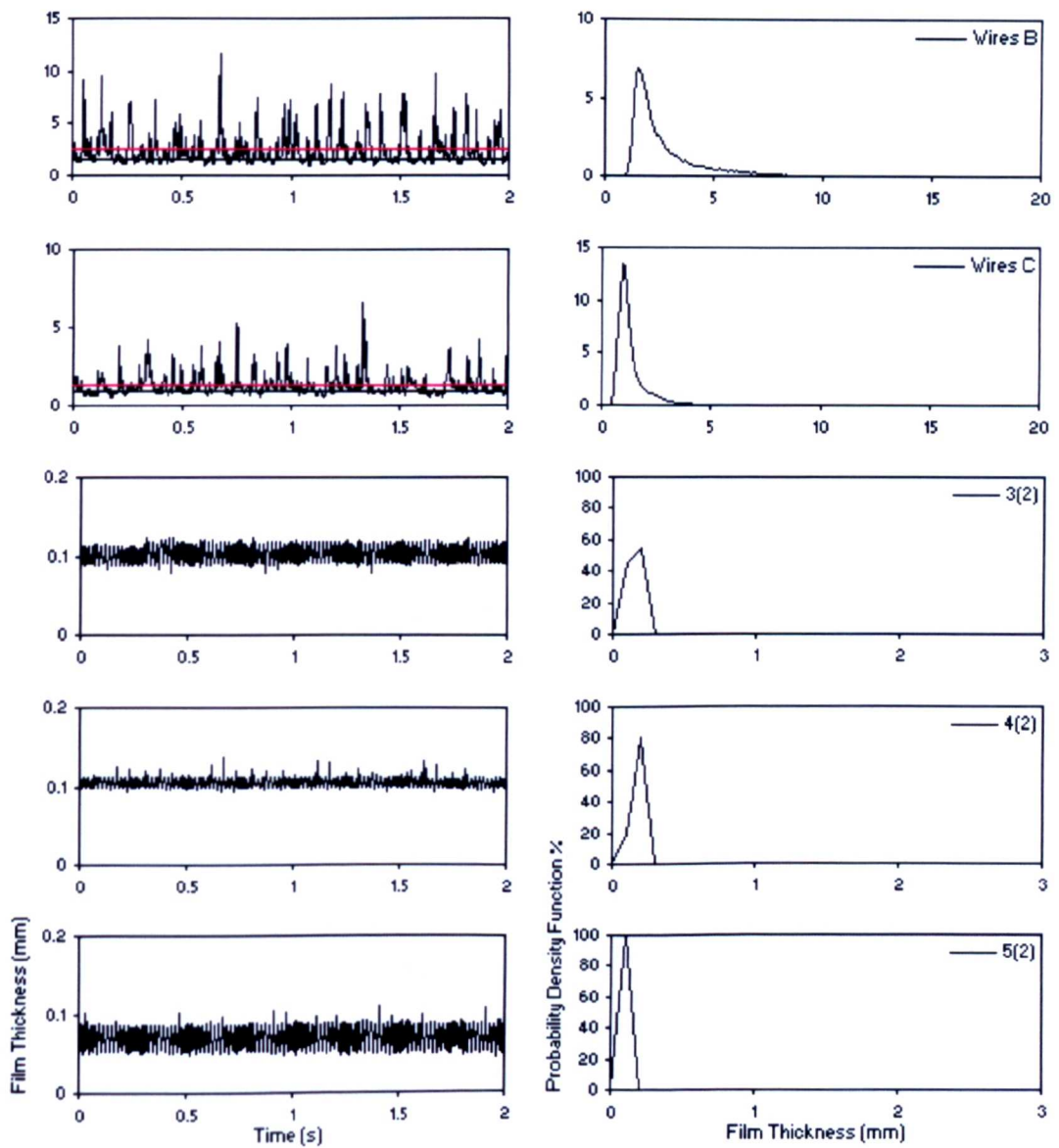


**Figure 5.1.23:** On the right variation of film thickness with time and on the left probability density function of film thickness. Gas mass flowrate=0.04 kg/s, liquid mass flowrate=0.0131 kg/s and angle of inclination from horizontal=0°

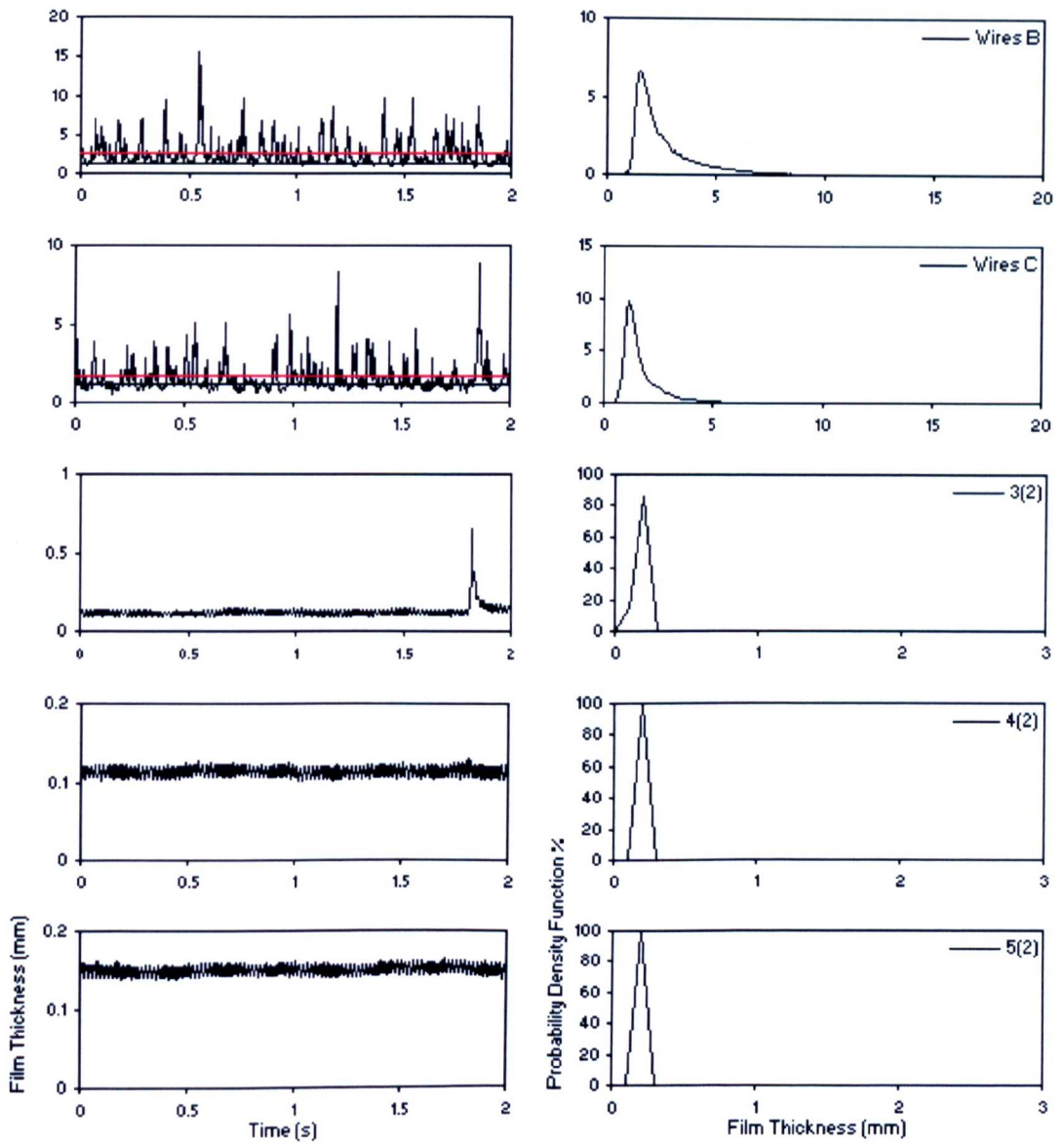


**Figure 5.1.24:** On the right variation of film thickness with time and on the left probability density function of film thickness. Gas mass flowrate=0.04 kg/s, liquid mass flowrate=0.0131 kg/s and angle of inclination from horizontal=30°

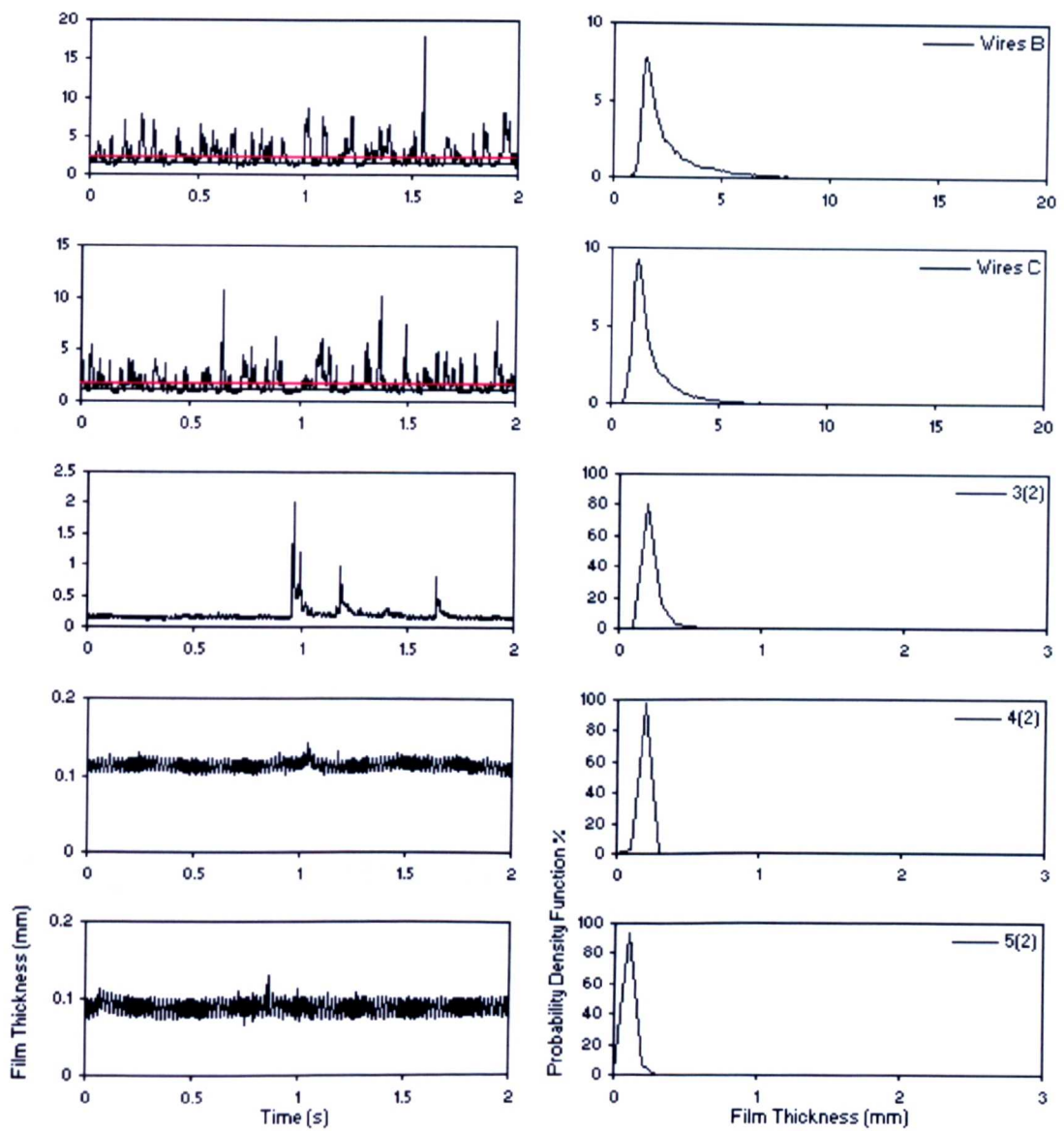


**Figure 5.1.25:** On the right variation of film thickness with time and on the left probability density function of film thickness. Gas mass flowrate=0.04 kg/s, liquid mass flowrate=0.0131 kg/s and angle of inclination from horizontal=45°

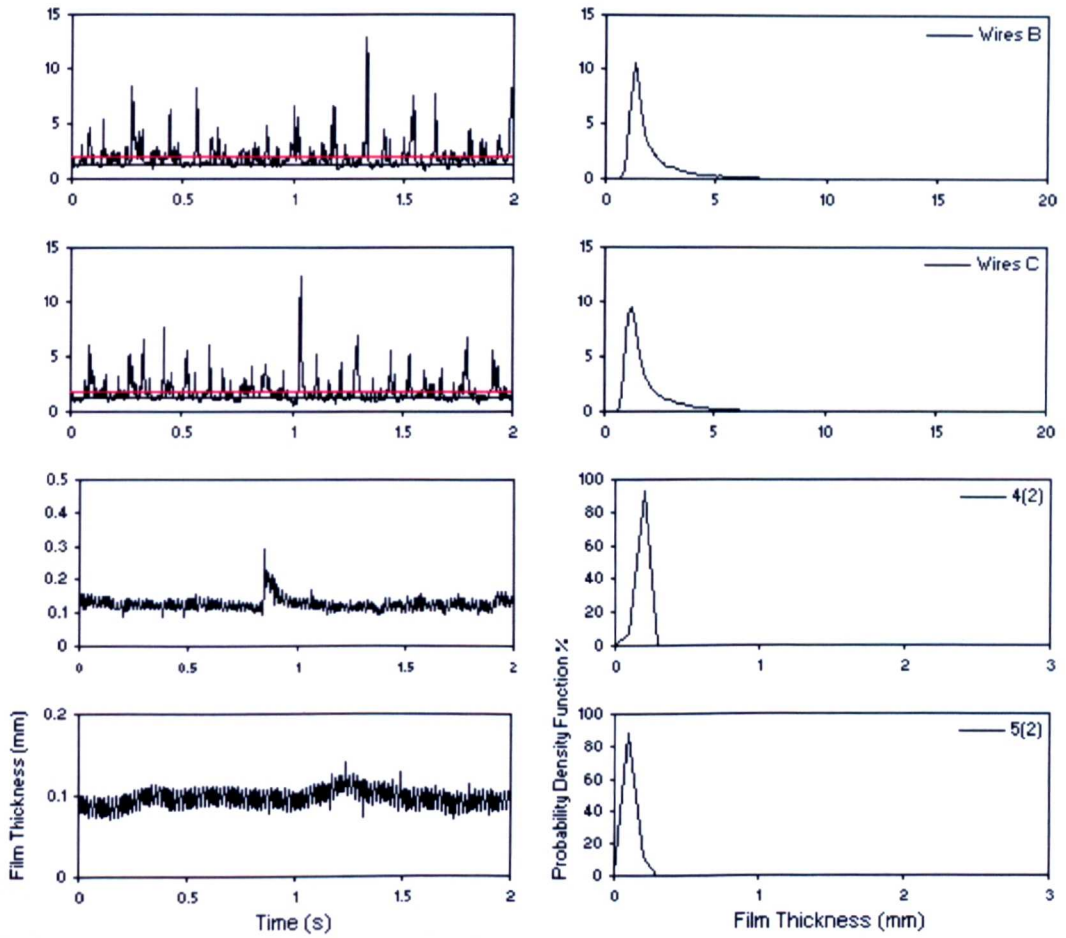


**Figure 5.1.26:** On the right variation of film thickness with time and on the left probability density function of film thickness. Gas mass flowrate=0.04 kg/s, liquid mass flowrate=0.0131 kg/s and angle of inclination from horizontal=60°

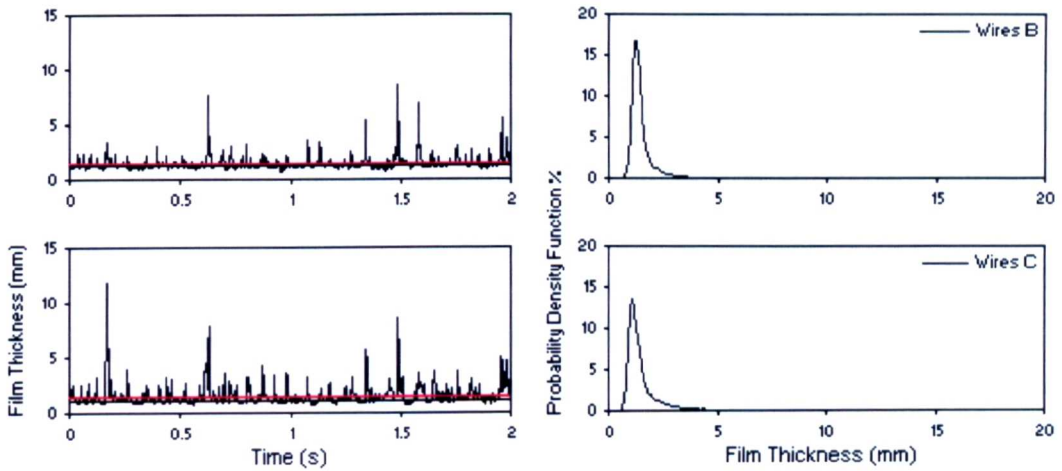


**Figure 5.1.27:** On the right variation of film thickness with time and on the left probability density function of film thickness. Gas mass flowrate=0.04 kg/s, liquid mass flowrate=0.0131 kg/s and angle of inclination from horizontal=85°

Figure 5.1.23 shows that in horizontal flow the film at the bottom (wires B and C) is very agitated and is characterized by rather regular disturbance waves with high peaks, see table 5.1.1. In contrast, at the other locations around the pipe, the film measured by probes 3(2), 4(2) and 5(2) is very thin, waves are not present and the wall is wetted by liquid droplets. The transition from disturbed liquid film (along the lower half of the pipe) to flat one (along the upper part) is shown clearly with the probability density functions (PDF) of the film thickness traces. Moving from the bottom to the top of the pipe, the peak of the PDF becomes more dominant and the base film thickness have a higher probability of occurrence. The PDF has its peak at a film thickness of 1.51 mm at the bottom and at a film thickness of 0.06 mm at the top. Those two values are the base film thicknesses. Once the base film thickness is known, the wave height is calculated by the difference between local film thickness and base film thickness. The average wave height is maximum at the bottom where the waves are 10 times higher than the base film thickness. Base film thickness and

average wave height are shown respectively with a black and a red line<sup>3</sup>. The characteristics of the film thickness are shown in table 5.1.1. Figure 5.1.5 shows that the characteristics of the film in 30° inclined flow are slightly different from those of horizontal flow. In 30° inclined flow the film is still characterized by disturbance wave pattern at the lower part of the pipe (wires B and C). Table 5.1.1 shows that the base and average thickness of the film measured by wires B are lower at this inclination compared to horizontal flow while those of the film measured by wires C are higher. Also the characteristics of the waves (highest peak and average) follow the same trend. This is in accord with the effect of the pipe orientation on the liquid film. At the location measured by probes 3(2) the film is wetted periodically by small waves (or surges) of much lower frequency (of the order of 1Hz), with film draining down between these surges, Jayanti (1990). At the top, the liquid film measured by probes 5(2) is very thin and flat. Figure 5.1.6 shows the characteristics of the film thickness for a pipe inclination of 45°. The liquid film at the lower part of the pipe (wires B and C) is still characterized by disturbance wave pattern. At the side of the pipe the film measured by probes 3(2) is wetted periodically by big waves with film draining down between these waves. At the top, the film is thin and flat. Figure 5.1.7 shows that, for a pipe inclination of 60°, the film is wetted by regular disturbance waves along the lower half of the pipe. At the location measured by probes 3(2), the average liquid film thickness is increased and the film is regularly disturbed by big waves. However, the characteristics of the film measured at this location are not shown in figure 5.1.7 because of the saturation of the probes. At the location measured by probes 4(2), the film is wetted periodically by surges with film draining down between these small waves. At the top the liquid film measured by probes 5(2) is thin with a small presence of surges. At the inclination of 85°, a wavy liquid film is present around the entire section of the pipe. Figure 5.1.8 shows the liquid film trace only at the locations measured by wires B and C. The characteristics of the film at

---

<sup>3</sup> The average wave height was not calculated for the other locations measured by probes 3(2), 4(2) and 5(2).

the other locations are not presented in table 5.1.1 because the liquid film was higher than 2 mm and this caused the saturation of the probes.

**Table 5.1.1:** Characteristics of the liquid film at different inclinations, gas mass flowrate=0.04 kg/s, liquid mass flowrate=0.0131 kg/s

	$\alpha$	Wires B	Wires C	3(2)	4(2)	5(2)
<b>Base Film Thickness (mm)</b>	0	1.51	0.91	0.1	0.1	0.06
	30	1.42	1.11	0.11	0.11	0.15
	45	1.4	1.16	0.16	0.11	0.09
	60	1.25	1.25	0.27	0.11	0.09
	85	1.18	1.09	Saturated	Saturated	Saturated
<b>Occurrence based on the first decimal %</b>	0	6.8	13.3	54.8	80.8	99.7
	30	6.6	9.7	85.7	99.8	100
	45	7.8	9.2	80	96.7	93.1
	60	10.5	9.5	34.2	92.4	87.6
	85	16.7	13.5	Saturated	Saturated	Saturated
<b>Average Film Thickness (mm)</b>	0	2.75	1.45	0.1	0.1	0.07
	30	2.54	1.66	0.11	0.11	0.15
	45	2.41	1.81	0.18	0.11	0.09
	60	2	1.84	0.45	0.11	0.09
	85	1.41	1.42	Saturated	Saturated	Saturated
<b>Highest Peaks (mm)</b>	0	16	7.5	0	0	0
	30	15.5	9	0.65	0	0
	45	18	11	2	0.15	0.13
	60	13	12.5	(7)	0.3	0.14
	85	8.5	11.8	Saturated	Saturated	Saturated
<b>Average Wave Height (mm)</b>	0	1.24	0.54	0	0	0
	30	1.13	0.55	0	0	0
	45	1.01	0.66	0.02	0	0
	60	0.78	0.59	0.18	0	0
	85	0.23	0.33	Saturated	Saturated	Saturated

The same results shown in figure 5.1.23 to 5.1.27 are presented in a different way in figures 5.1.28 to 5.1.32. Here, it is shown the effect of the inclination on the liquid film thickness at the same pipe circumferential location. It can be seen that the film along the bottom (wires B and C) is characterized by the presence of disturbance waves. At the location measured by wires B, the average film thickness, the base film thickness and the wave height average decrease with increasing inclination. At the location measured by wires C, the average film thickness, the base film thickness and the average wave height increase moving from horizontal to  $60^\circ$  and after decrease moving towards higher inclinations. The characteristics of the liquid film at the other locations of the section are shown in table 5.1.1. The probability density functions of the film thickness show that the peak becomes more dominant where the liquid film is less disturbed by the presence of waves. Therefore, at the top side of the pipe, the film thickness corresponding to the peak is a very accurate indication of the base film thickness and its value is close to the average film thickness.

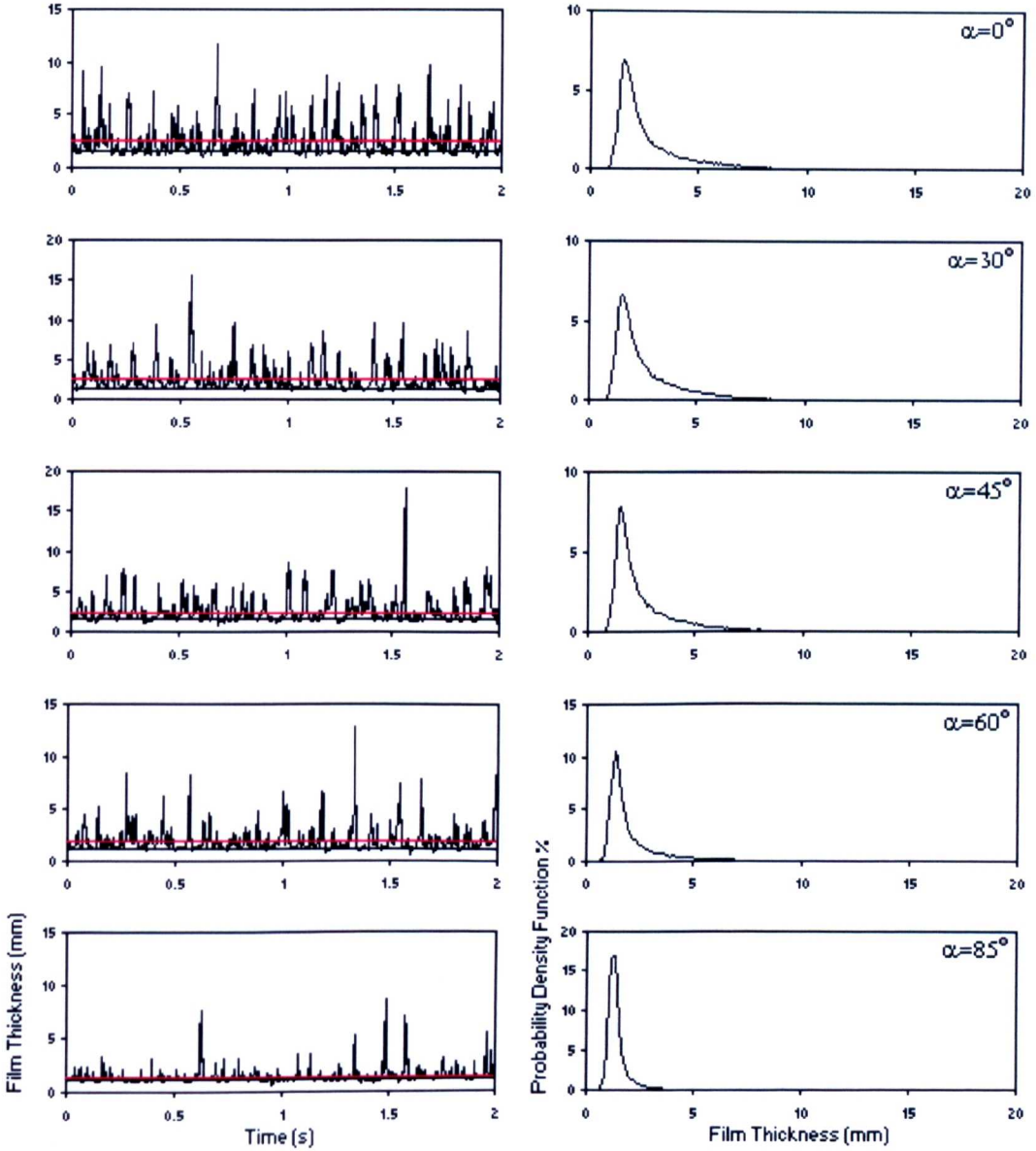


**Figure 5.1.28:** On the right, variation with time of film thickness measured by wires B. On the left, probability density function of film thickness. Gas mass flowrate=0.04 kg/s, liquid mass flowrate=0.0131 kg/s

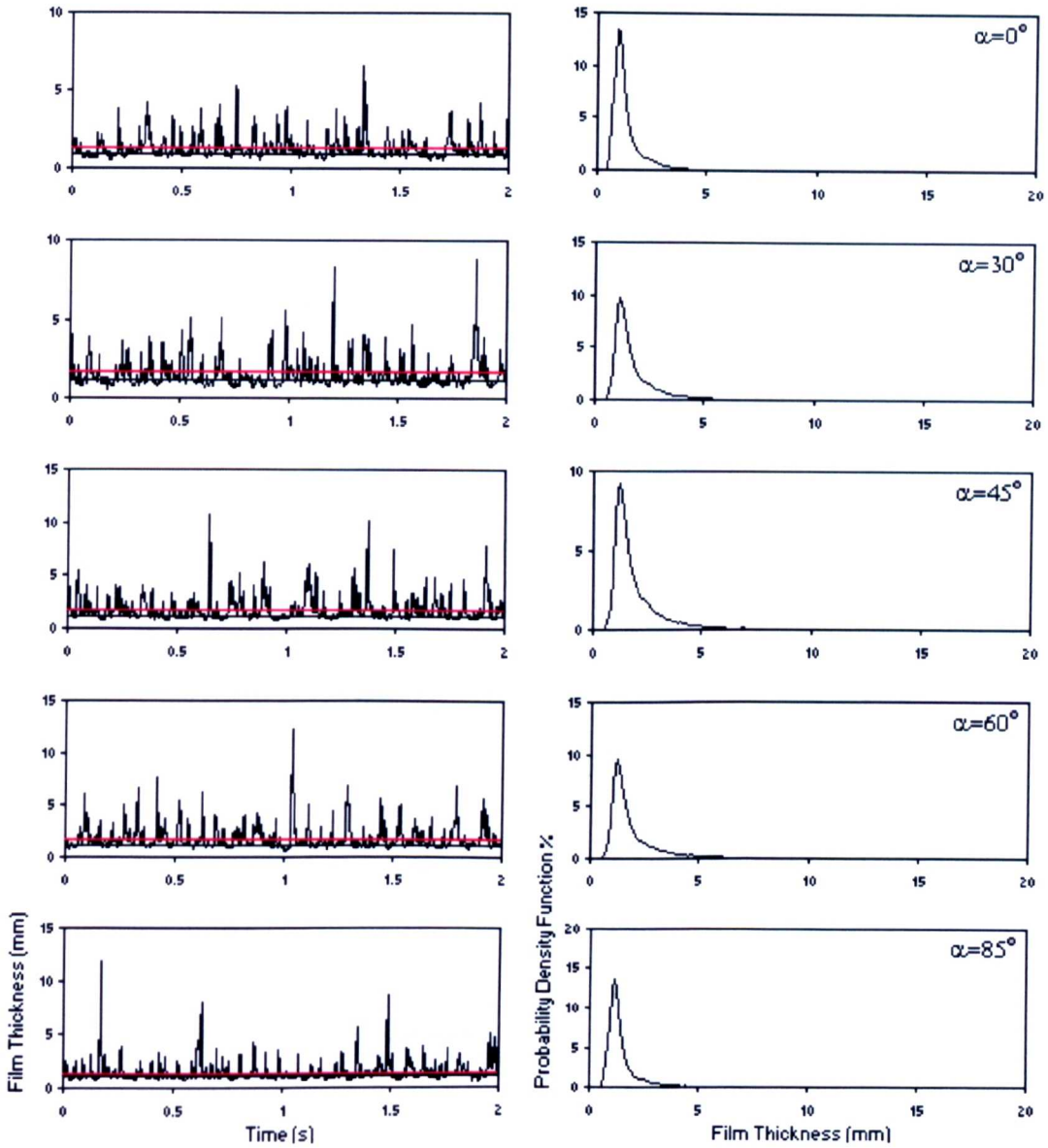


**Figure 5.1.29:** On the right, variation with time of film thickness measured by wires C. On the left, probability density function of film thickness. Gas mass flowrate=0.04 kg/s, liquid mass flowrate=0.0131 kg/s

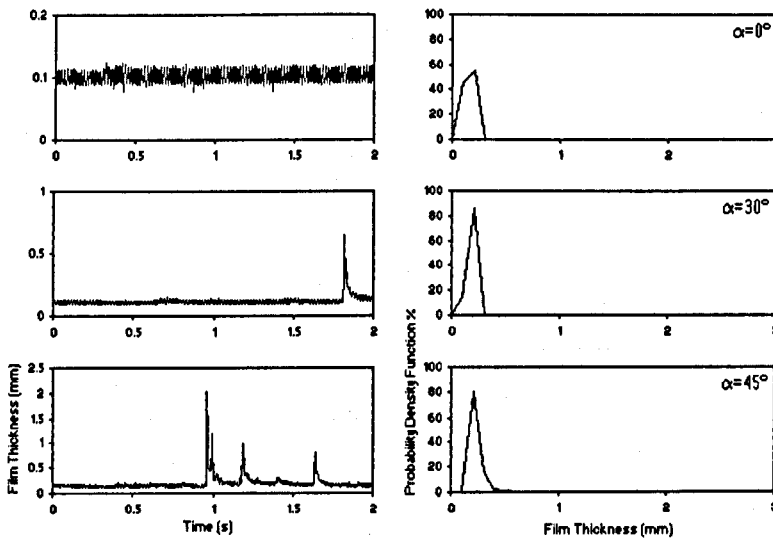


**Figure 5.1.30:** On the right, variation with time of film thickness measured by probes 3(2). On the left, probability density function of film thickness. Gas mass flowrate=0.04 Kg/s, liquid mass flowrate=0.0131 kg/s

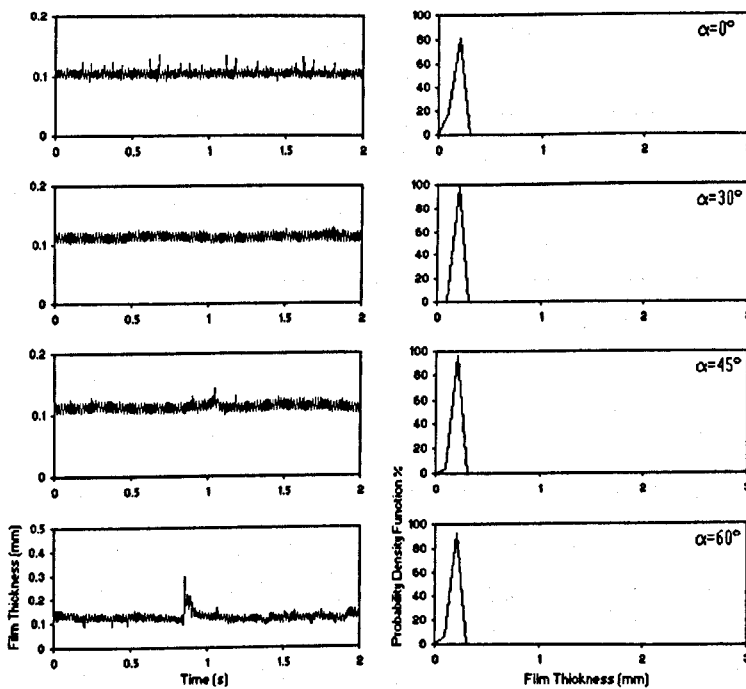


**Figure 5.1.31:** On the right, variation with time of film thickness measured by probes 4(2). On the left, probability density function of film thickness. Gas mass flowrate=0.04 Kg/s, liquid mass flowrate=0.0131 kg/s

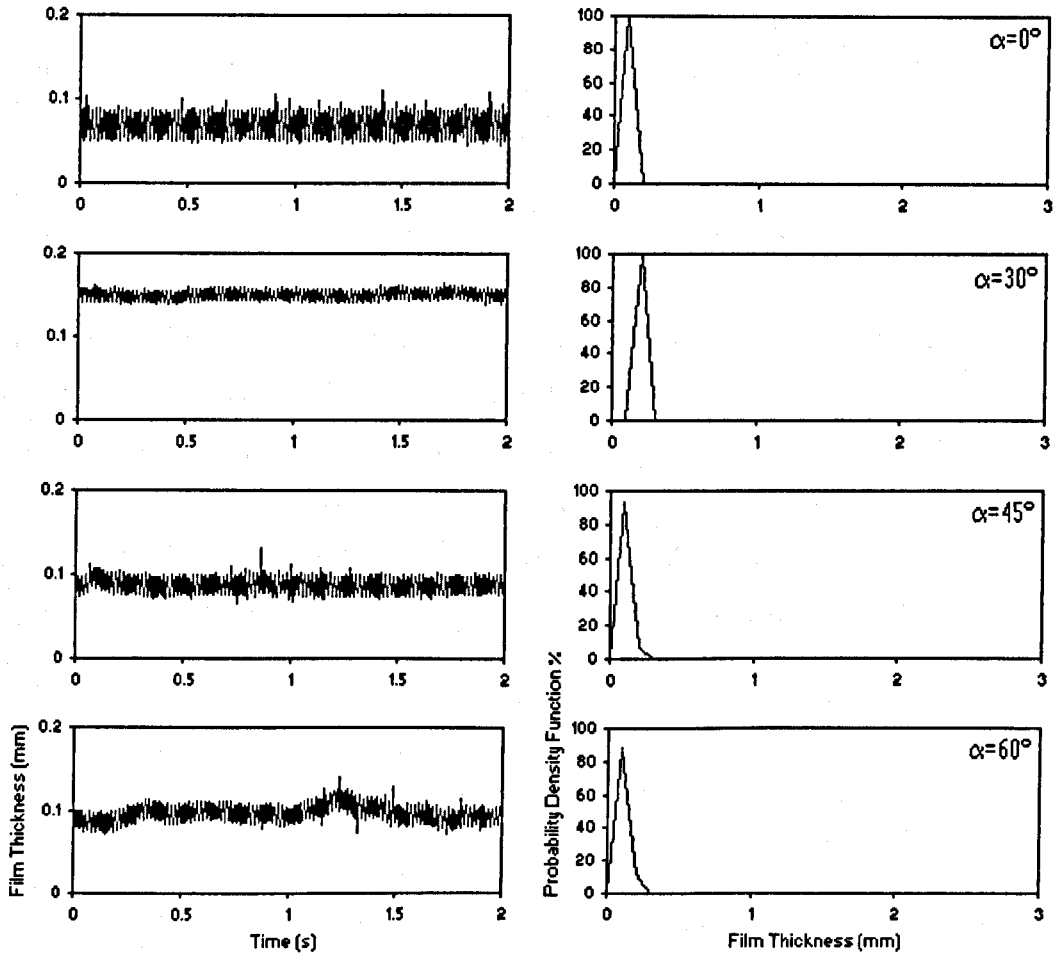
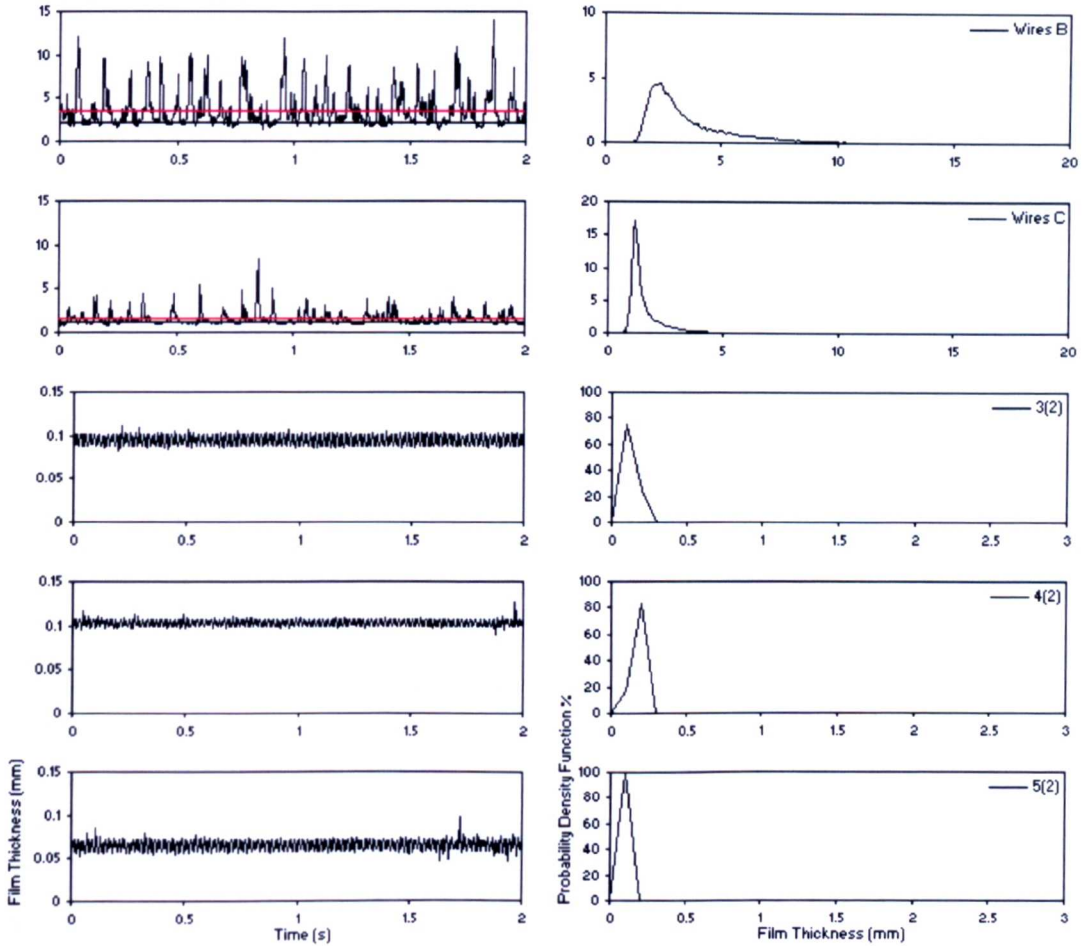


Figure 5.1.32: On the right, variation with time of film thickness measured by probes 5(2). On the left, probability density function of film thickness. Gas mass flowrate=0.04 Kg/s, liquid mass flowrate of 0.0131 kg/s

In figures 5.1.28 to 5.1.32, it is evident that the variation of inclination has the effect to change the film distribution around the circumference. By increasing the inclination, the liquid moves towards the side. Chapter 4 shows that the effect of inclination is relevant also on wave frequency.

If the data at the same liquid flowrate but at lower gas flowrate ( $M_g=0.03$  kg/s) are examined, figures 5.1.33 to 5.1.37, it is seen that at horizontal inclination, the disturbance of waves is increased. Paras & Karabelas (1994) showed that, at gas velocity of the order of 10 m/s and relatively small liquid flowrates, wavy stratified flow prevails in a 50.8 mm i.d. horizontal pipe and it is characterised by large amplitude roll waves otherwise known as Kelvin-Helmholtz waves (Andritsos & Hanratty, 1987). For this two-phase flow pattern, they defined the “atomization” region which represents a transition from stratified to annular flow.



**Figure 5.1.33:** On the right variation of film thickness with time and on the left probability density function of film thickness. Gas mass flowrate=0.03 kg/s, liquid mass flowrate=0.0131 kg/s and angle of inclination from horizontal=0°

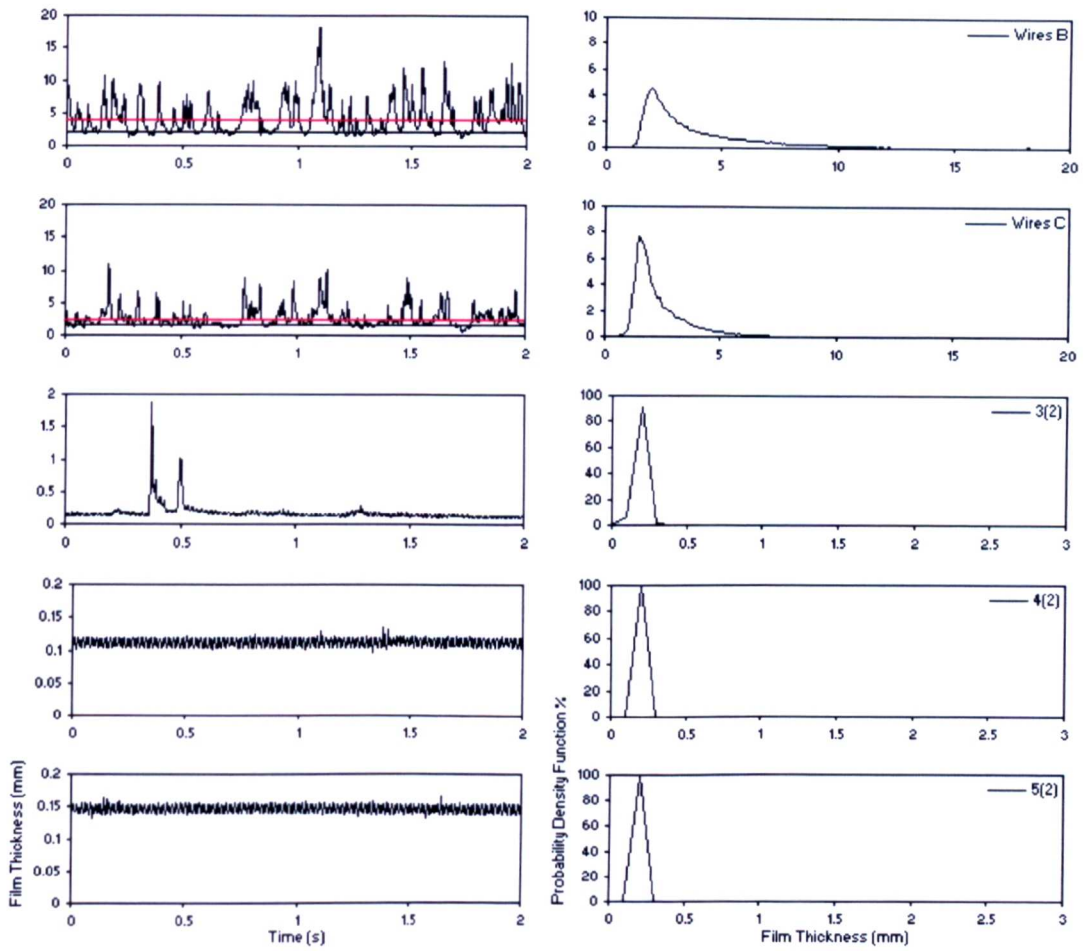


**Figure 5.134:** On the right variation of film thickness with time and on the left probability density function of film thickness. Gas mass flowrate=0.03 kg/s, liquid mass flowrate=0.0131 kg/s and angle of inclination from horizontal=30°

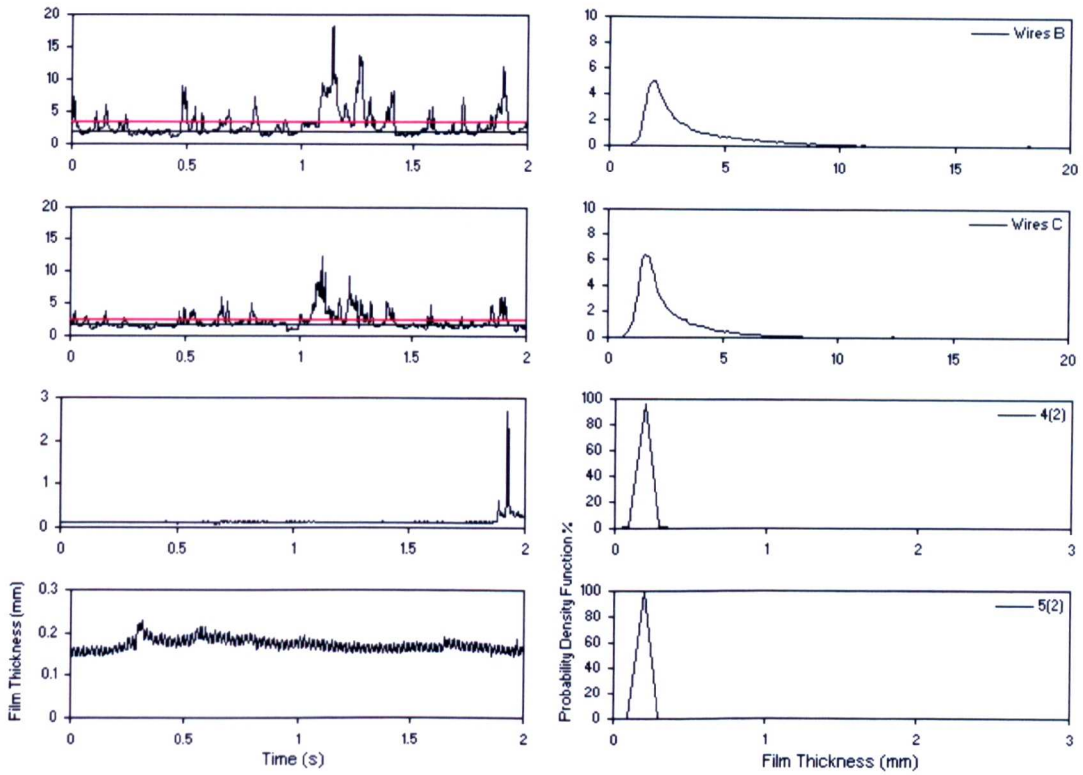


**Figure 5.1.35:** On the right variation of film thickness with time and on the left probability density function of film thickness. Gas mass flowrate=0.03 kg/s, liquid mass flowrate=0.0131 kg/s and angle of inclination from horizontal=45°

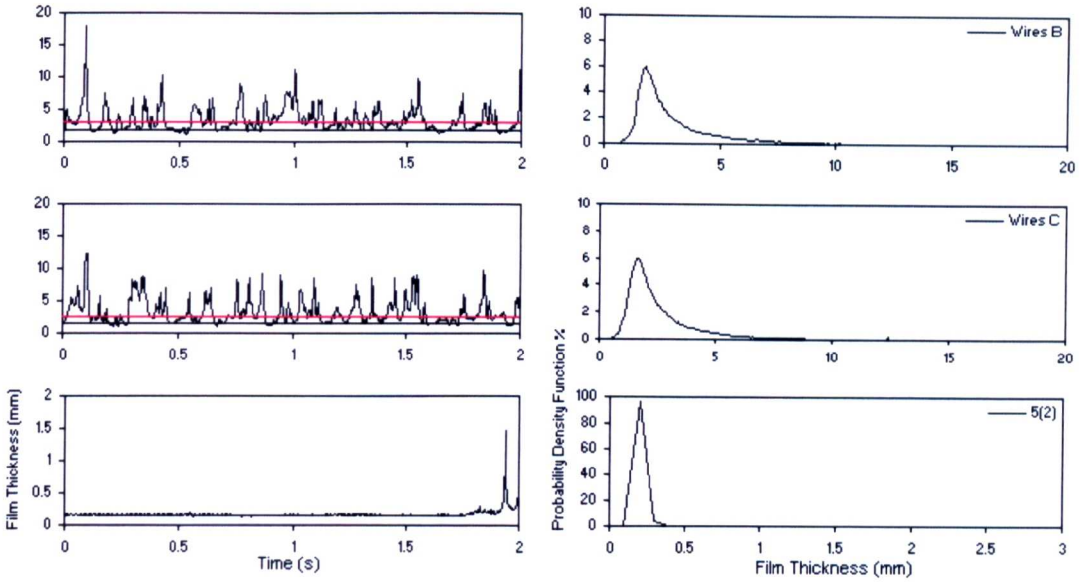


**Figure 5.1.36:** On the right variation of film thickness with time and on the left probability density function of film thickness. Gas mass flowrate=0.03 kg/s, liquid mass flowrate=0.0131 kg/s and angle of inclination from horizontal=60°

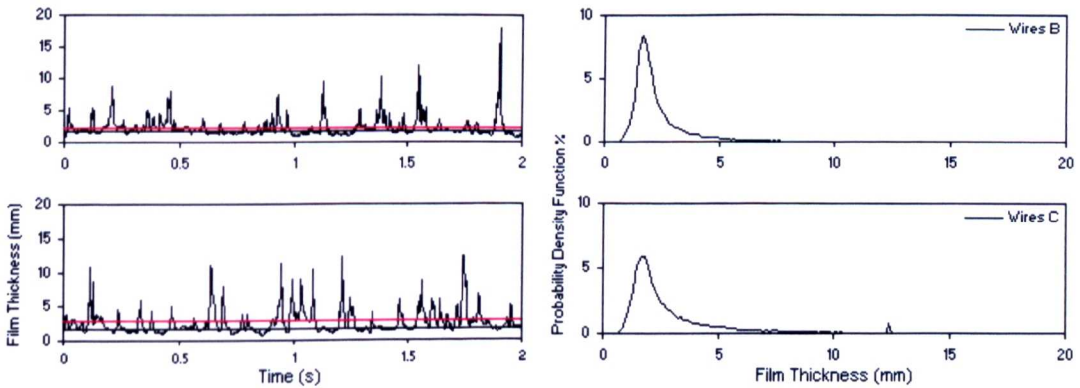


**Figure 5.1.37:** On the right variation of film thickness with time and on the left probability density function of film thickness. Gas mass flowrate=0.03 kg/s, liquid mass flowrate=0.0131 kg/s and angle of inclination from horizontal=85°

With lower mass flowrate the base and the average film thickness are higher around the entire section of the pipe. Also, the peaks and the average heights of the waves are higher. With decreasing  $M_g$  the interaction between air and water becomes less strong and, therefore, the liquid-gas interface is less disturbed with consequent less entrainment as shown in Chapter 4. This results in a higher liquid film thickness around the entire section. Figures 5.1.33 to 5.1.34 show that the film at the bottom side is characterised by very high peaks (10 times the base film thickness). Differently from the first case at  $M_g = 0.04 \text{ kg/s}$ , the presence of disturbance waves is detected also in  $45^\circ$  inclined flow (figure 5.1.35) at the location measured by probes 4(2) and at the top in  $60^\circ$  inclined flow (figure 5.1.36). This means that, at these locations of the pipe, a gas velocity of 15 m/s has the effect to develop high waves which disappear as soon as the velocity is increased up to 21.5 m/s. At the inclination of  $85^\circ$ , the liquid film is wavy around the entire section. However, the amplitude of the waves at the bottom side is lower at this inclination. Figure 5.1.37 shows only the film thickness measured by wires B and C because the film thickness was higher than 2mm at the other locations and this caused the saturation of the probes. The characteristics of the circumferential liquid film thickness are shown in table 5.1.2.

**Table 5.1.2:** Characteristics of liquid film at different inclinations, gas mass flowrate=0.03 kg/s, liquid mass flowrate=0.0131 kg/s

	$\alpha$	Wires B	Wires C	3(2)	4(2)	5(2)
<b>Base Film Thickness (mm)</b>	0	2.11	1.13	0.09	0.1	0.07
	30	2.08	1.46	0.12	0.11	0.15
	45	1.95	1.73	Saturated	0.12	0.16
	60	1.77	1.53	Saturated	Saturated	0.16
	85	1.64	1.74	Saturated	Saturated	Saturated
<b>Occurrence based on the first decimal %</b>	0	4.5	17.2	74.8	83	100
	30	4.5	7.7	91.2	99.8	99.9
	45	5	6.4	Saturated	96.6	99.9
	60	6	5.9	Saturated	Saturated	95.7
	85	8.3	5.9	Saturated	Saturated	Saturated
<b>Average Film Thickness (mm)</b>	0	3.98	2	0.09	0.1	0.07
	30	3.81	2.35	0.12	0.11	0.15
	45	3.48	2.58	Saturated	0.13	0.16
	60	2.96	2.59	Saturated	Saturated	0.16
	85	2.27	2.80	Saturated	Saturated	Saturated
<b>Highest Peaks (mm)</b>	0	18	12.5	0	0	0
	30	18	12.5	2	0	0
	45	18	12.5	Saturated	2.75	0.23
	60	18	12.5	Saturated	Saturated	1.5
	85	18	12.5	Saturated	Saturated	Saturated
<b>Average Wave Height (mm)</b>	0	1.87	0.87	0	0	0
	30	1.74	0.89	0	0	0
	45	1.53	0.85	Saturated	0	0
	60	1.24	1.07	Saturated	Saturated	0
	85	0.64	1.06	Saturated	Saturated	Saturated

Figures 5.1.38 to 5.1.42 show the same results of figure 5.1.33 to 5.1.37 but they illustrate the variation of the film thickness at the same circumferential location. It can be seen that the film at the bottom is characterized by the presence of disturbance

waves. At the location measured by wires B, the average film thickness, the base film thickness and the average wave height decrease with increasing inclination. At the location measured by wires C, the average film thickness, the base film thickness and the average wave height increase with increasing inclination. The characteristics of the liquid film at the other locations are shown in table 5.1.2. The probability density functions of the film thickness show that the peak becomes more dominant at the top, where the film is less disturbed by waves.

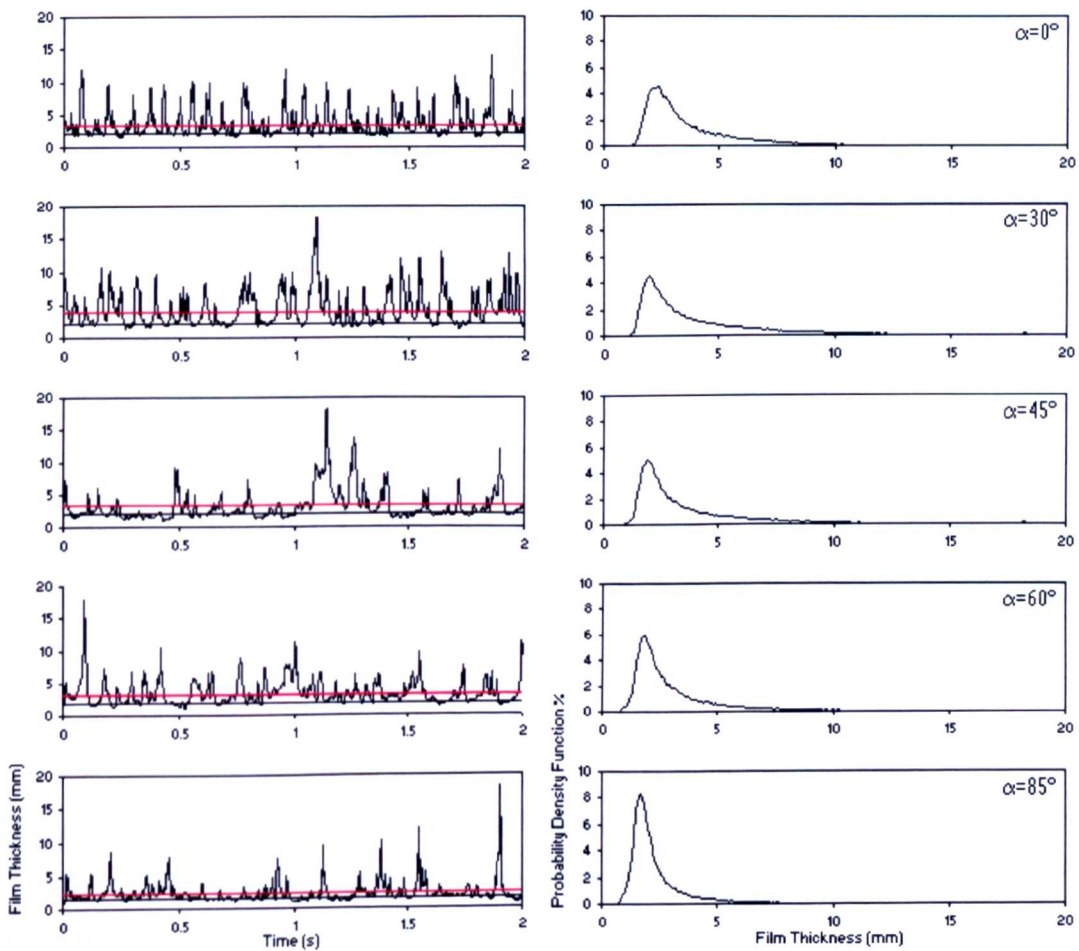


**Figure 5.1.38:** On the right, variation with time of film thickness measured by wires B. On the left, probability density function of film thickness. Gas mass flowrate=0.03 kg/s, liquid mass flowrate=0.0131 kg/s

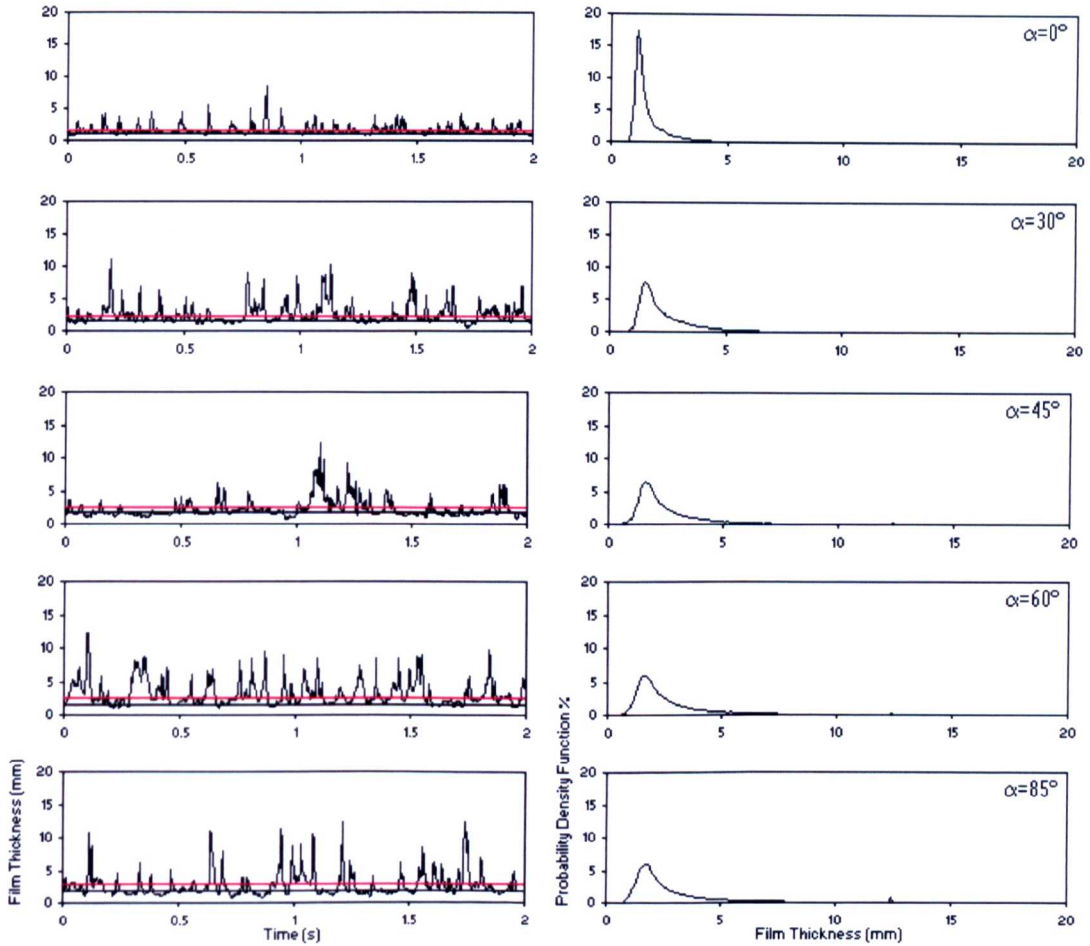


**Figure 5.1.39:** On the right, variation with time of film thickness measured by wires C. On the left, probability density function of film thickness. Gas mass flowrate=0.03 kg/s, liquid mass flowrate=0.0131 kg/s

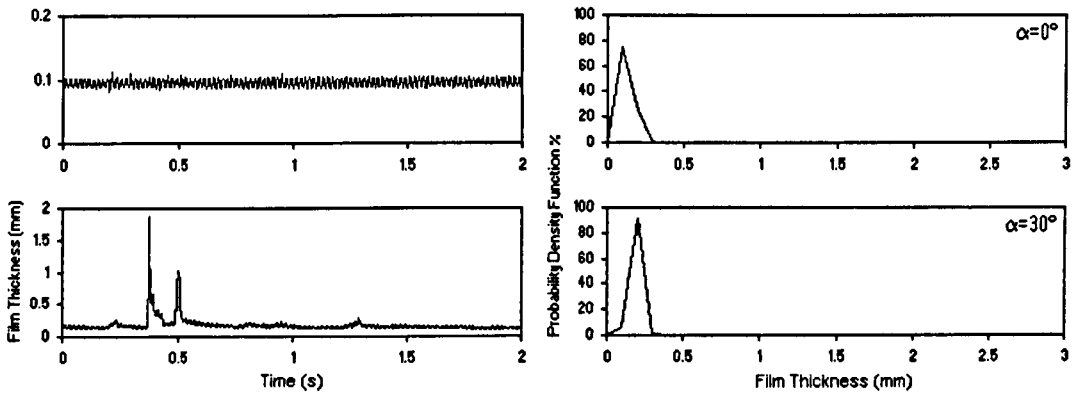


**Figure 5.1.40:** On the right, variation with time of film thickness measured by probes 3(2). On the left, probability density function of film thickness. Gas mass flowrate=0.03 kg/s, liquid mass flowrate=0.0131 kg/s

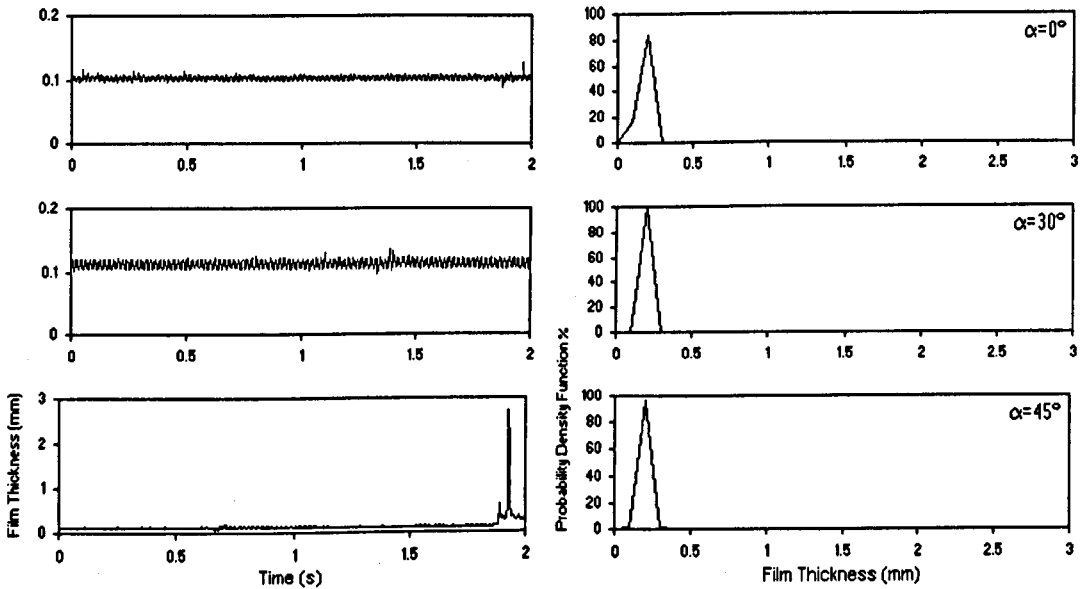


**Figure 5.1.41:** On the right, variation with time of film thickness measured by probes 4(2). On the left, probability density function of film thickness. Gas mass flowrate=0.03 kg/s, liquid mass flowrate=0.0131 kg/s

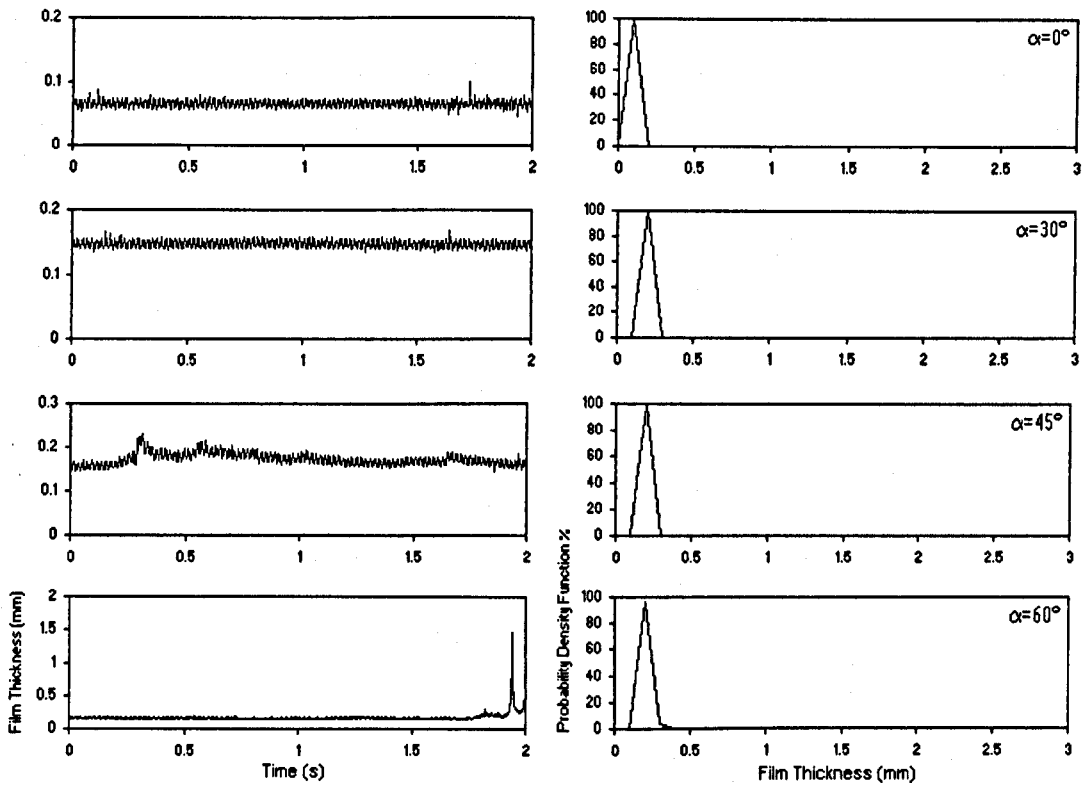


**Figure 5.1.42:** On the right, variation with time of film thickness measured by probes 5(2). On the left, probability density function of film thickness. Gas mass flowrate=0.03 kg/s, liquid mass flowrate=0.0131 kg/s

Figure 5.1.43 shows power spectra of film thickness at the three locations measured by wires A, B and C. Gas and liquid flowrates considered are  $M_g = 0.04$  kg/s and  $M_l = 0.0131$  kg/s. The study of the power spectrum density at the upper part was not carried on. The reason is the absence of waves along this side in the majority of the cases studied. The amplitude of the spectrum attains its maximum at the bottom (wires B) and decreases moving towards the side of the pipe. This trend is in accord with the circumferential distribution of the liquid film thickness. Figure 5.1.43 also shows that there is not appreciable change of dominant frequency in these spectra. To reduce the sidelobes in the power spectrum, the correlation function was multiplied with a cosine windowing function, see Appendix D. Although the presence of leakages is not completely eliminated, it can be clearly seen that the

highest signal power in the frequency domain, for the specified flow conditions and inclination of figure 5.1.43, occurs at 7.3 Hz. This frequency represents the wave frequency at the bottom side.

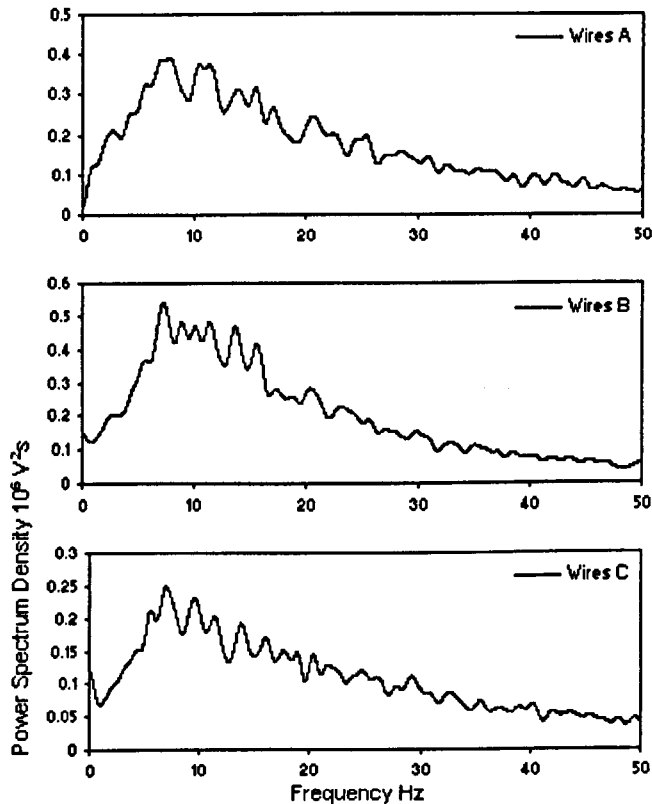


**Figure 5.1.43:** Power spectrum density at the bottom. Gas mass flowrate=0.04 kg/s, liquid mass flowrate=0.0131 kg/s, angle of inclination from horizontal=45°

Also the variation of the wave frequency with the flow inlet conditions and pipe inclination was studied. Figure 5.1.44 shows power spectra of film thickness measured at the bottom at increasing liquid mass flowrate,  $M_l$ .

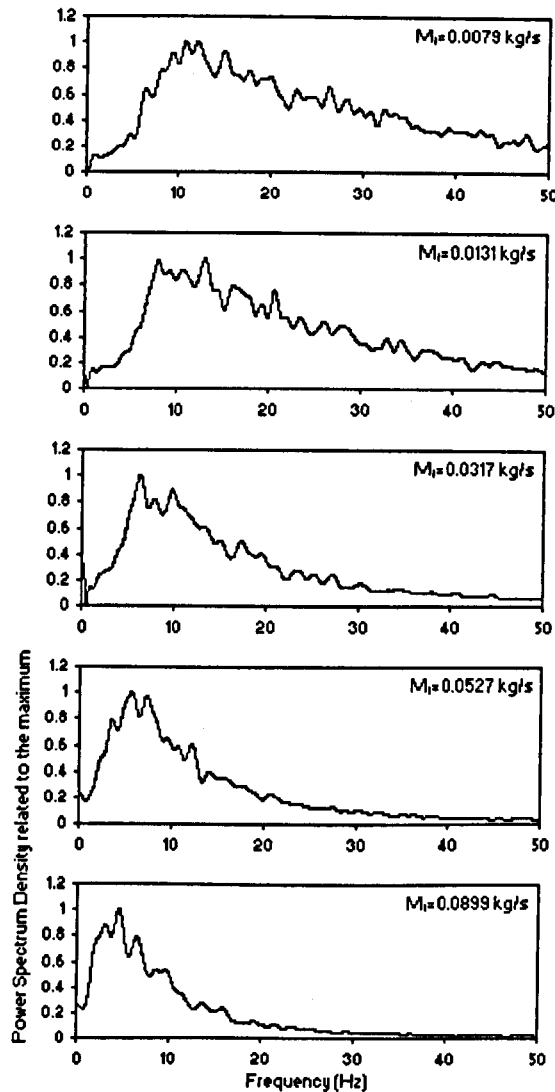


**Figure 5.1.44:** Effect of liquid mass flowrate on power spectrum density at the bottom (wires B). Gas mass flowrate=0.04 kg/s, liquid mass flowrate=0.0131 kg/s, angle of inclination from horizontal=0°

Figure 5.1.44 shows that a large portion of wave energy at the bottom is carried by waves of frequency  $\leq 12$  Hz. There is not a big influence of liquid velocity on the form of the spectra. However, with increasing liquid mass flowrate the dominant frequency appears to decrease and there is a less distribution of energy among waves of higher frequency. The same result was obtained by Paras & Karabelas (1991).

They also showed that, for a fixed liquid rate, an increasing gas velocity ( $U_{sg} = 31$  to  $66$  m/s) tends to distribute the energy to waves of higher frequency. Moreover, in their results, it is noticed that the spectra tend to flatten out with increasing  $U_{sg}$ , due to the more uniform distribution of energy among waves of a broad frequency range.

Jayanti (1990) investigated the liquid film thickness in a 32 mm i.d. horizontal pipe with a liquid velocity ranged from 0.080 to 0.159 m/s and a gas velocity ranged from 20.5 to 35.8 m/s. He found that, at high liquid velocity ( $U_{ls} = 0.119$  m/s) and low gas velocity ( $U_{gs} = 22$  m/s), all the waves are not circumferentially coherent and at the top only low frequency waves are present. Increasing the gas rate, the disturbance wave frequency appears in the power spectrum at  $135^\circ$ , showing that waves have spread up to this height of the tube. At still higher air flowrates, all power spectra show the presence of disturbance waves, indicating that these have spread to the top of the tube. On the other hand, at the bottom of the pipe, an increasing gas rate tends to give power spectra with a broad range of dominant frequency. Therefore, it is evident that the results of Jayanti (1990) with regards to the effect of gas velocity on wave frequency are in accord with the present results. Jayanti (1990) also investigated the effect of the liquid flowrate. It was shown that an increasing liquid velocity does not influence the form of the spectra at the bottom. However, the frequency appears to decrease with increasing liquid flowrate. This is in accord with Paras & Karabelas (1991) and the present work.

The effect of inclination on the wave frequency at the bottom side is illustrated in figure 5.1.45. The amplitude of power spectra decreases with increasing inclination. Moreover, the spectra tend to flatten out with increasing inclination, due to a more uniform film distribution which results in a reduced amount of wave energy at the bottom. Figure 5.1.46 shows the effect of the liquid flowrate on the wave frequency at the bottom while 5.1.47 shows the effect of the pipe inclination. Figure 5.1.48 shows the Strouhal number/Lockhart-Martinelli parameter correlation (described in section 2.6.3) applied to the wave frequency.

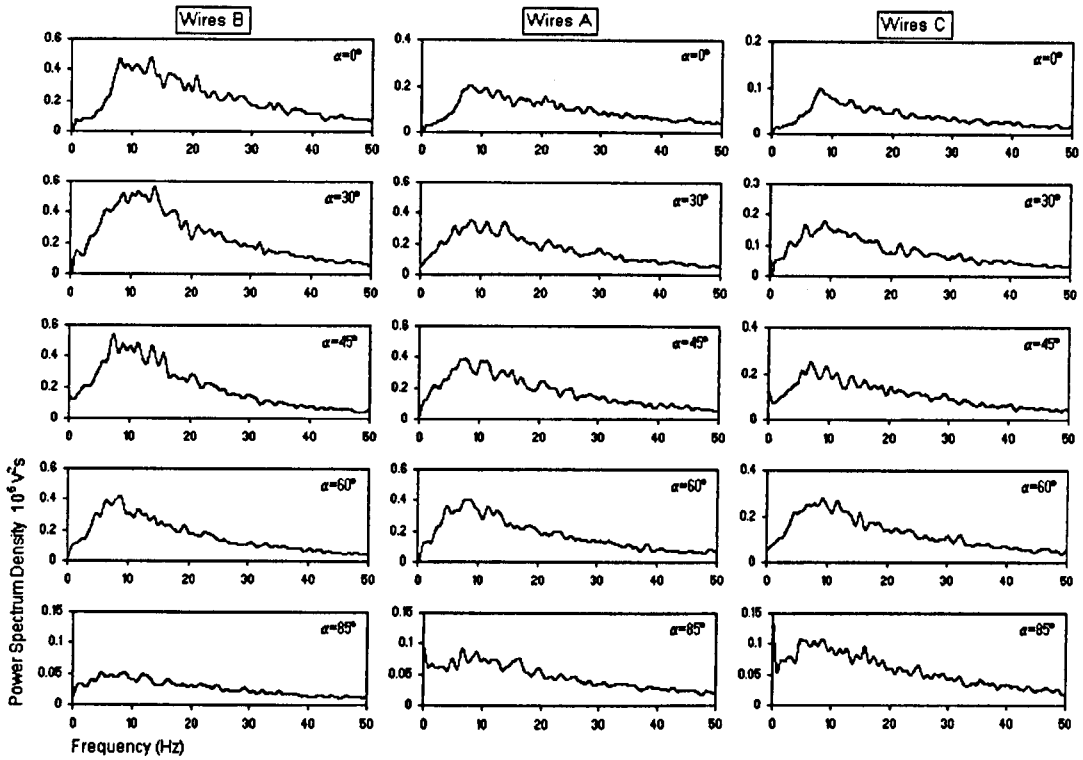


Figure 5.145: Effect of inclination on power spectrum density along the lower part of the pipe. Gas mass flowrate=0.04 kg/s, liquid mass flowrate=0.0131 kg/s

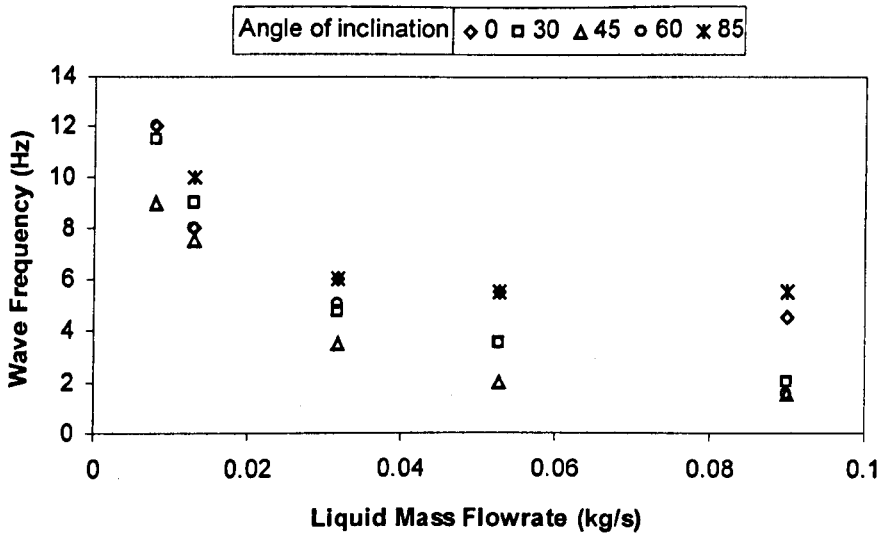


Figure 5.146: Frequency variation with liquid mass flowrate. Gas mass flowrate=0.04 kg/s

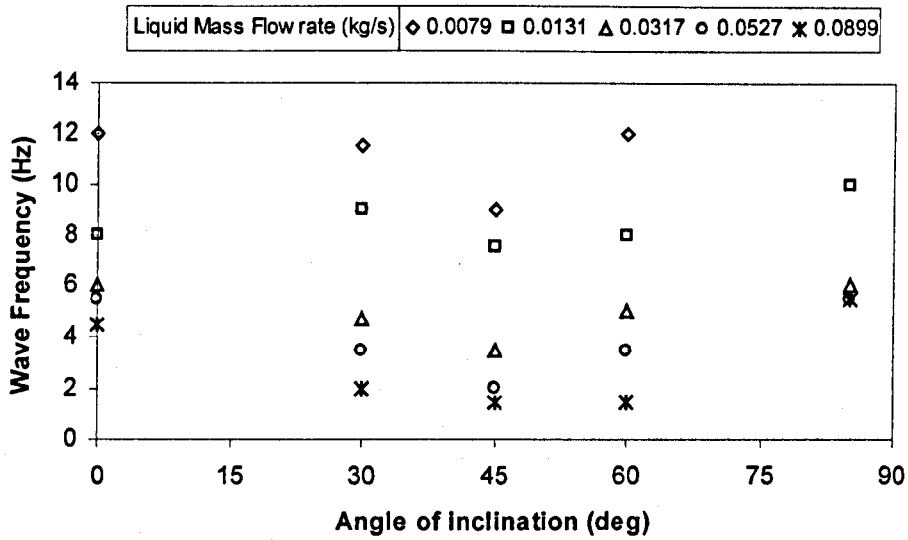


Figure 5.1.47: Frequency variation with angle of inclination from horizontal. Gas mass flowrate=0.04 kg/s

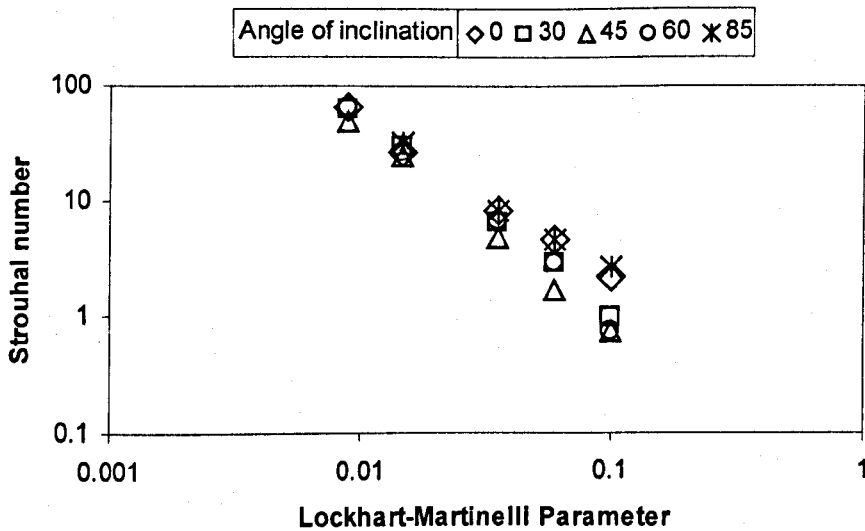


Figure 5.1.48: Liquid based Strouhal number plotted against Lockhart-Martinelli parameter

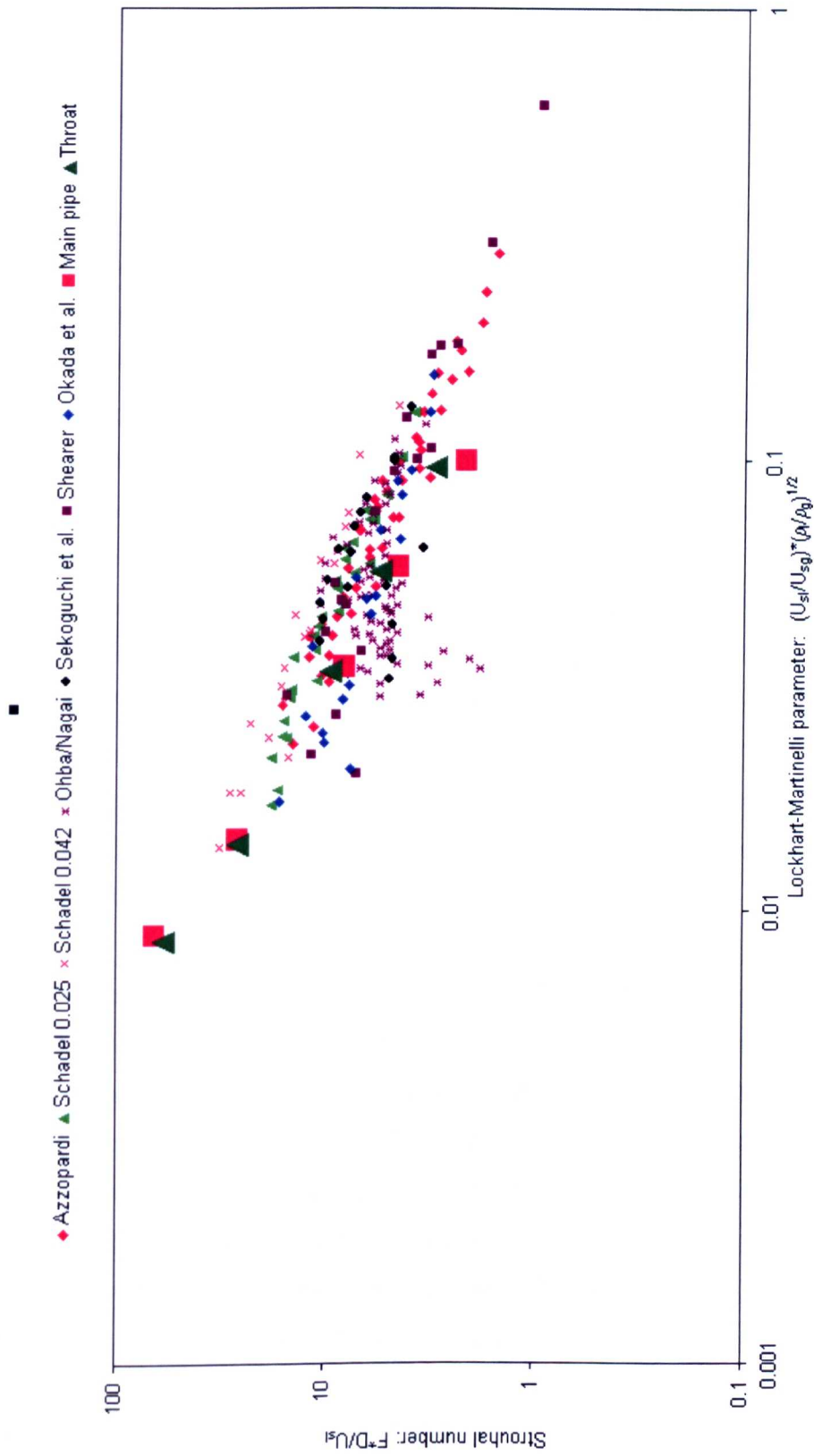


Figure 5.1.49: Liquid based Strouhal number plotted against Lockhart-Martinelli parameter

Figure 5.1.46 shows that the frequency decreases with  $M_l$  for the five inclinations studied. This means that the more it is the liquid flowing in the pipe, the lower it is the frequency of waves. In horizontal flow the frequency reaches a plateau with  $M_l$ , figure 5.1.46. At the inclinations of  $30^\circ$ ,  $45^\circ$  and  $60^\circ$ , the frequency decreases monotonically with  $M_l$ . Waves become slower with increasing inclination due to the effect of gravity on the liquid. In  $85^\circ$  inclined flow the frequency reaches a plateau with  $M_l$  because the more uniform distribution of liquid around the channel facilitates the formation of new waves and counteracts the action of gravity. Therefore, wave frequency is higher in horizontal and  $85^\circ$  inclined flow as shown in figure 5.1.47. As discussed in Chapter 2, Strouhal number/Lockhart-Martinelli parameter correlation leads to linear profiles of data. The present experimental data shown in figure 5.1.48 are in accord with this correlation. Moreover, as many other air/water data presented in literature, they lie on one line, figure 5.1.49. However, it is evident a slight deviation from straight line of the three profiles obtained at the pipe inclinations of  $30^\circ$ ,  $45^\circ$  and  $60^\circ$ . This is a consequence of the effect of liquid mass flowrate on wave frequency shown in figure 5.1.46. In fact, at the inclinations of  $30^\circ$ ,  $45^\circ$  and  $60^\circ$ , wave frequency decreases with increasing liquid mass flowrate also at higher liquid rates while at the other two inclinations (horizontal and  $85^\circ$  inclined) wave frequency reaches a plateau.

The standard deviation RMS of the film thickness changes with the circumferential position. It is higher at the bottom where the liquid height fluctuations are higher and it is lower at the top where the film is less disturbed. It is also influenced by the conductance technique used. In fact, the characteristics of measurement of flush-mounted pins and parallel wires are different, e.g. input and output ranges, sensitivity, repeatability, saturation, non-linearity<sup>4</sup>. The standard deviation of the film thickness measured by pins tends to be higher due to the non-linear characteristic of the output. Therefore, particular attention was given to the range of applications of these probes.

---

<sup>4</sup> Accuracy and resolution mainly depend on the data acquisition card. The same DAQ card was used for both techniques.

The effect of the liquid flowrate is also relevant. Figure 5.1.50 shows that RMS increases with liquid mass flowrate, especially at the bottom. Therefore, the standard deviation displays the same trends of the film thickness

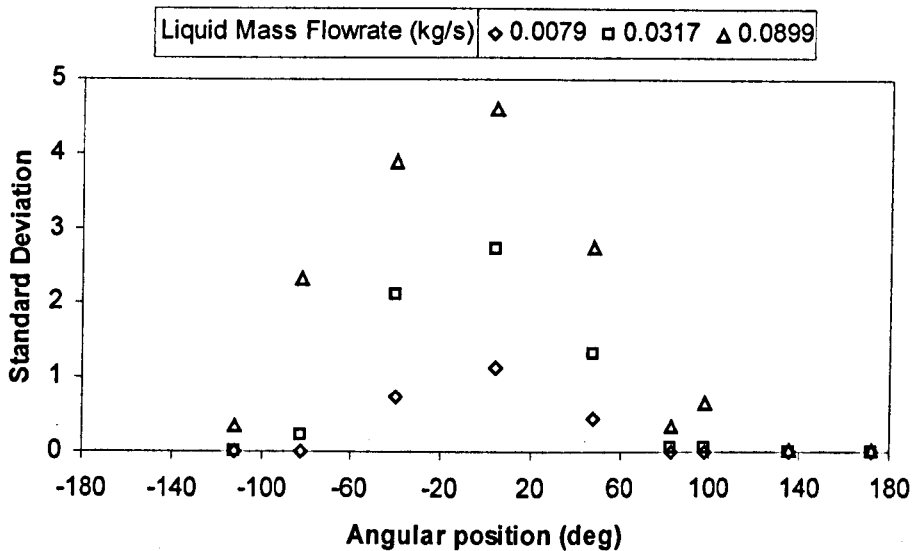


**Figure 5.1.50:** Variation of RMS with liquid mass flowrate. Gas mass flowrate=0.04 kg/s, angle of inclination from horizontal=0°

This implies that the large waves are mainly responsible for the magnitude of the RMS of the fluctuating liquid layer. Moreover, RMS along the circumference tends to become uniform with increasing inclination, figure 5.1.51. This is in accord with the variation of the film thickness and with the propagation of the disturbance waves along the two sides of the pipe. The fluctuations of liquid height, and therefore the standard deviation, increase as soon as the film is disturbed by the presence of the disturbance waves. Along the upper part of the pipe, the fluctuations are insignificant in accord with the liquid film thickness traces. The effect of gas velocity on RMS results to be insignificant at low gas velocity ( $U_{sg} < 20$  m/s). Paras & Karabelas (1991) showed that the effect of gas velocity is relevant only for  $U_{sg} > 30$  m/s.

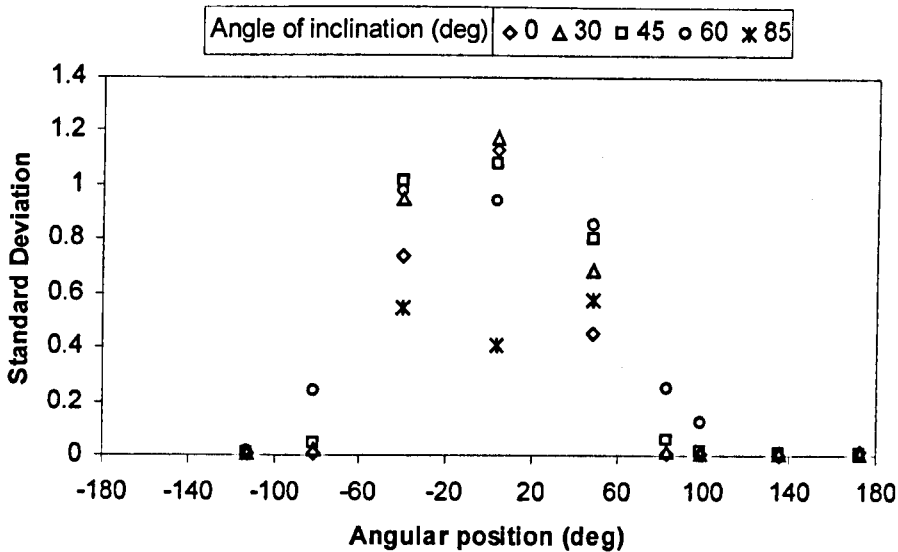


**Figure 5.1.51:** Variation of standard deviation RMS with angle of inclination from horizontal. Gas mass flowrate=0.04 kg/s, liquid mass flowrate=0.0079 kg/s

Typical circumferential profiles of RMS (standard deviation) of the film thickness fluctuations are presented by Paras & Karabelas (1991). In their results, there is a strong affect of liquid flowrate on the RMS values, especially at the lower half of the pipe. Otherwise, the RMS profiles exhibit the same trends as the film thickness  $s$ , with regards to gas velocity and gravity effects. Paras & Karabelas (1991) also defined the intensity  $RMS/s$  where  $s$  and RMS are the local values of the time-averaged film thickness and its standard deviation. They found that the highest values of intensity are observed at low gas and high liquid flowrates. At high gas flowrates ( $U_{sg} > 50$  m/s) the intensity of liquid height fluctuations is almost symmetric around the pipe circumference, whereas at low gas rates it is very asymmetric with the highest values at the lower half of the pipe. Moreover, for low gas velocity ( $U_{sg} = 30$  m/s) and relatively high liquid velocities ( $U_{sl} > 0.06$  m/s),  $RMS/s$  attains its maximum value at  $\theta \approx 45^\circ$  rather than at  $\theta \approx 0^\circ$ , where the maximum for all other cases is observed. In this study  $RMS/s$  attains its maximum value at  $\theta \approx 0^\circ$ . This value is independent from liquid and gas mass flowrates and from inclination.

In figure 5.1.52 to 5.1.53, the inverse of the film thickness  $1/s$  is plotted against  $\cos\theta$  for two sets of flow conditions. It can be seen that there is a good agreement between the model of Butterworth (1969) presented in Chapter 2 and the experimental data. The above model predicts that the plot of  $1/s$  against  $\cos\theta$  is a straight line (equation 2.60 in Chapter 2). The experimental results approximately obey this relationship. The values of 'a' are approximately  $6.9 \text{ (mm)}^{-1}$  for the flow condition in figure 5.1.52 and  $7.2 \text{ (mm)}^{-1}$  for those in figure 5.1.53. A comparison of this model with the experimental data gives the values of the circumferential transport coefficients, which are  $k= 30.37 \text{ mm}$  for the first set of flow condition and  $k=31.59$  for the second one.

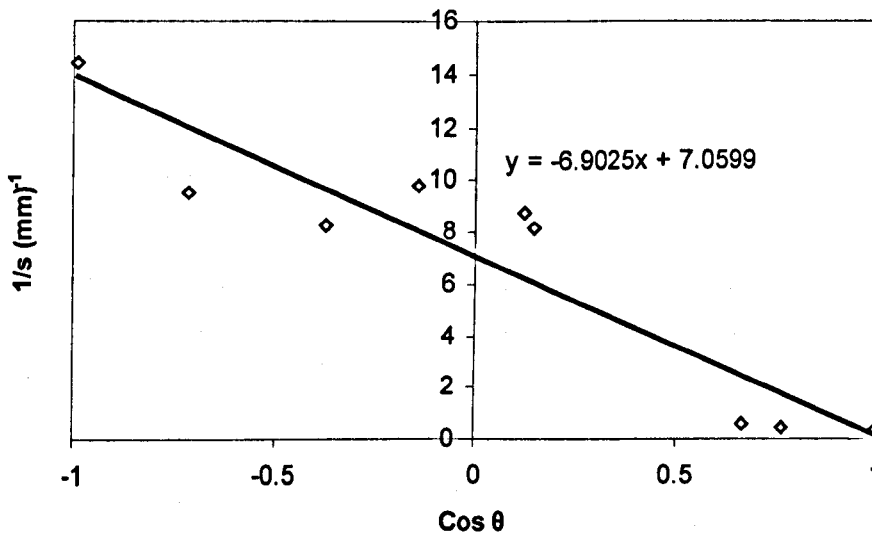


**Figure 5.1.52:** Profile of  $1/s$  plotted against  $\cos\theta$ . Gas mass flowrate= $0.04 \text{ kg/s}$ , liquid mass flowrate= $0.0131 \text{ kg/s}$ , angle of inclination from horizontal= $0^\circ$

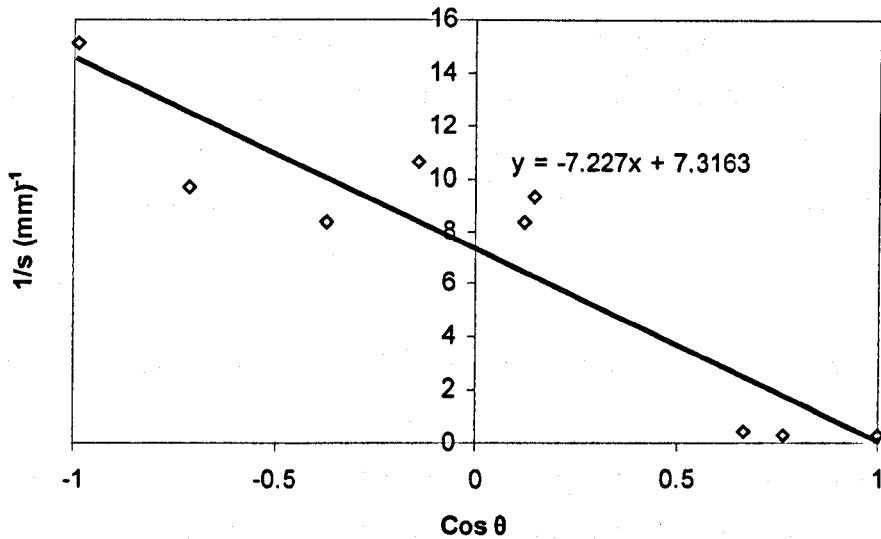


**Figure 5.1.53:** Profile of  $1/s$  plotted against  $\cos\theta$ . Gas mass flowrate=0.03 kg/s, liquid mass flowrate=0.0131 kg/s, angle of inclination from horizontal=0°

## 5.2 Results in the throat of the Venturi

In contrast to numerous investigations of liquid film thickness in straight pipe where circumferential variation have been reported, only this work provides such data in horizontal and inclined throat of a Venturi.

The study of the properties of the liquid film in the throat of the Venturi was conducted in the same way as in the main pipe. However, the data analysis in the throat has resulted more difficult for different reasons. Firstly, the annular flow in this section cannot be considered fully developed. This means that the characteristics of the liquid film are not constant with time. This has implicated a very low repeatability of results. For this reason, a large number of experimental runs was necessary. Moreover, diverse published physical based models could not be applied to this case.

In section 5.1, it is pointed out the strong effect of gravity on the liquid film distribution in horizontal and inclined pipe. The maintenance of liquid film at the top is facilitated in a cross-section with small area. In fact, the smaller it is the pipe diameter, the smaller it is the action of gravity on liquid. Therefore, it is expected a more uniform circumferential distribution of film thickness in the throat than in the pipe.

In the throat section, the liquid film thickness was measured at six different locations by using flush-mounted probes. Figure 3.3.2 of Chapter 3 shows the angular positions of the probes. In figures 5.2.1 to 5.2.3 the average film thickness is plotted in polar coordinates in a cross-section of the throat. These figures illustrate the effect of inclination on the average liquid film thickness around the throat. In the three inclinations analysed, the film distribution is not symmetrical. Clearly, as the angle of inclination deviates from the horizontal, the film thickness becomes less pronounced at the bottom. Due to gravity the film thickness decreases at the bottom and increases at the top. Moreover, figures 5.2.1 to 5.2.3 show that, for the range of liquid velocities considered, the average liquid film thickness does not vary significantly when the inclination is changed from horizontal to  $45^\circ$ . Evident changes of average liquid film thickness are present only at orientations  $\alpha > 45^\circ$ .

Figure 5.2.4 shows a typical circumferential distribution of the average film thickness in Cartesian coordinates. The abscissa is the angular position of the middle point between the pairs of probes and the zero is assumed at the bottom. Figures 5.2.5 to 5.2.9 show the variation of average film thickness that occurs as the inclination varies from horizontal to  $85^\circ$ . It is also shown the increment of liquid height with increasing liquid mass flowrate. As well as in the pipe, in the throat the film annular area  $A_{LF}$  is calculated by integrating the liquid film thickness around the entire section, see equation 5.2. These calculations show that there is not a remarkable variation of  $A_{LF}$  with the inclination,  $\alpha$ . Chapter 4 shows that the angle of inclination has a small effect also in the entrained fraction.

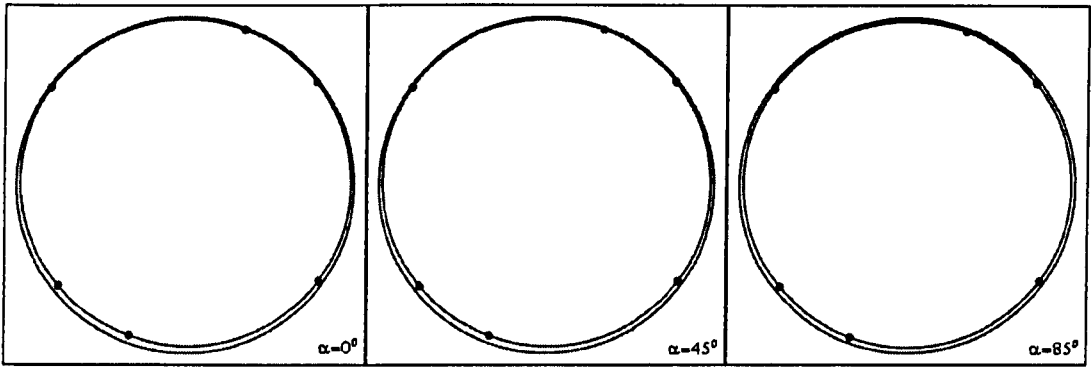


**Figure 5.2.1:** Effect of inclination on liquid film thickness distribution in the throat section. Gas mass flowrate=0.04 kg/s, liquid mass flowrate=0.0079 kg/s

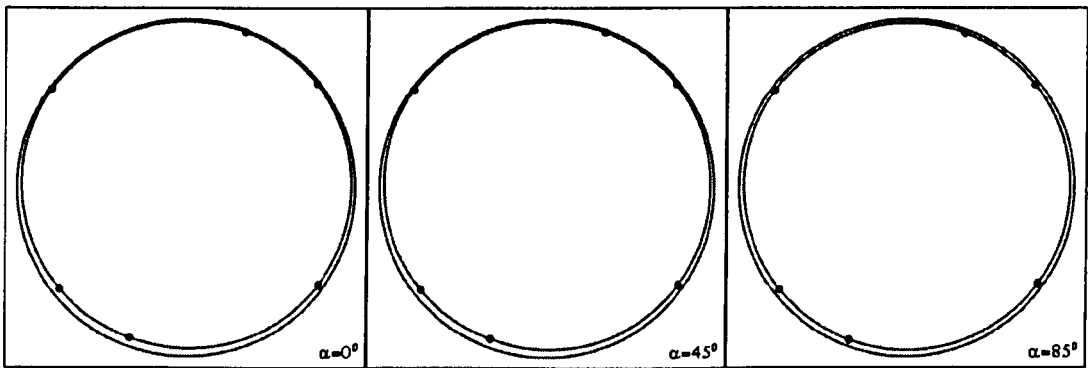


**Figure 5.2.2:** Effect of inclination on liquid film thickness distribution in the throat section. Gas mass flowrate=0.04 kg/s, liquid mass flowrate=0.0131 kg/s

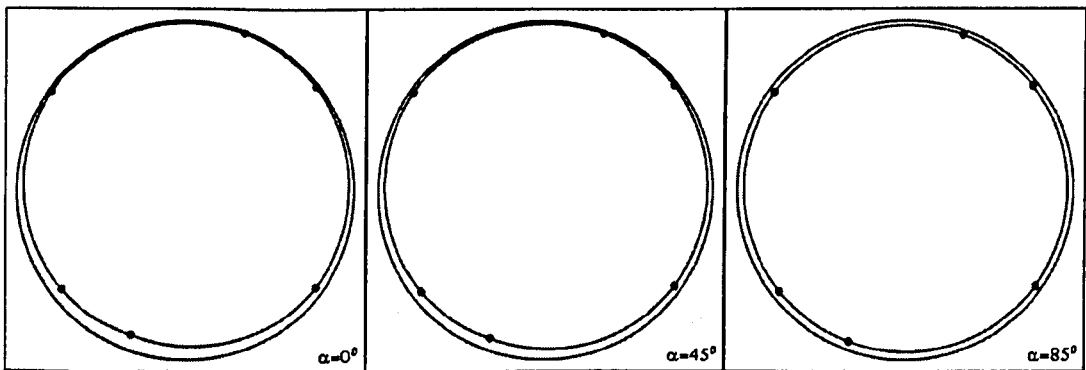


**Figure 5.2.3:** Effect of inclination on liquid film thickness distribution in the throat section. Gas mass flowrate=0.04 kg/s, liquid mass flowrate=0.0317 kg/s

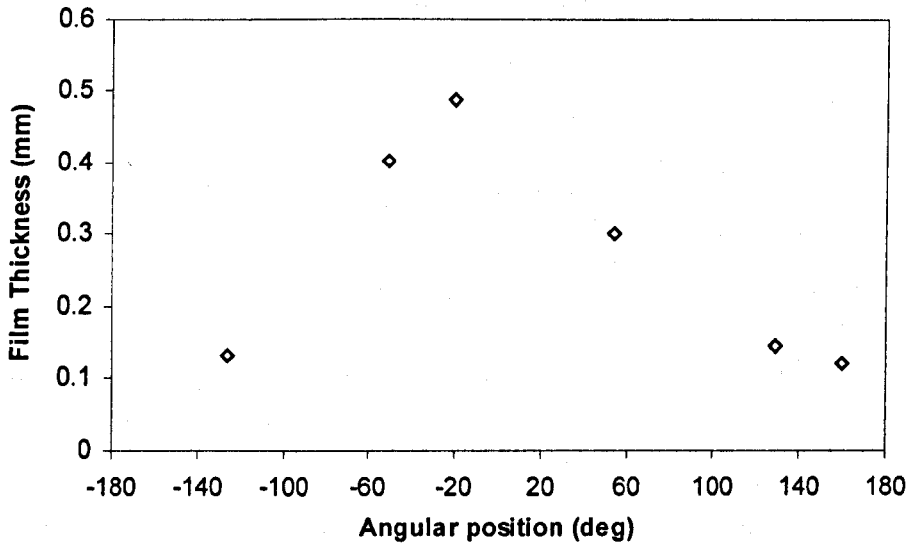


Figure 5.2.4: Liquid film thickness distribution. Gas mass flowrate=0.04 kg/s, liquid mass flowrate=0.0131 kg/s, angle of inclination from horizontal=45°

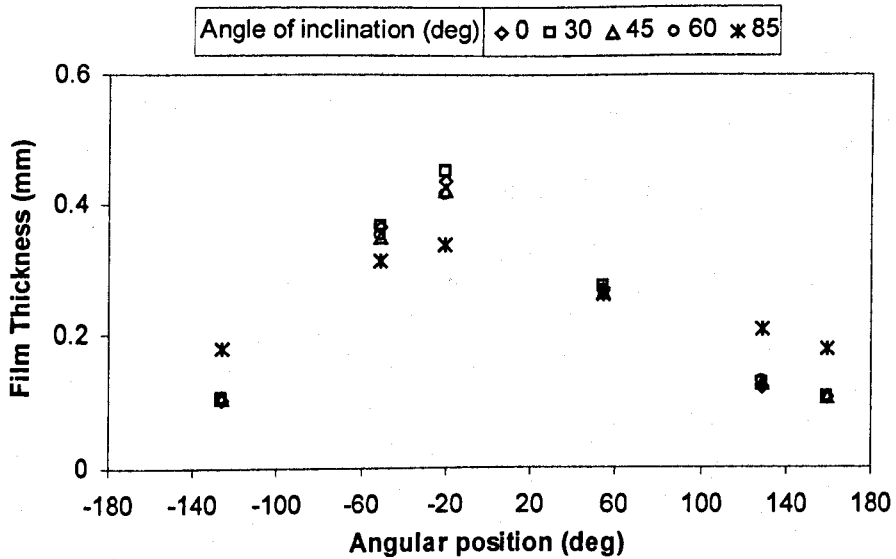


Figure 5.2.5: Liquid film thickness variation with angle of inclination from horizontal. Gas mass flowrate=0.04 kg/s, liquid mass flowrate=0.0079 kg/s

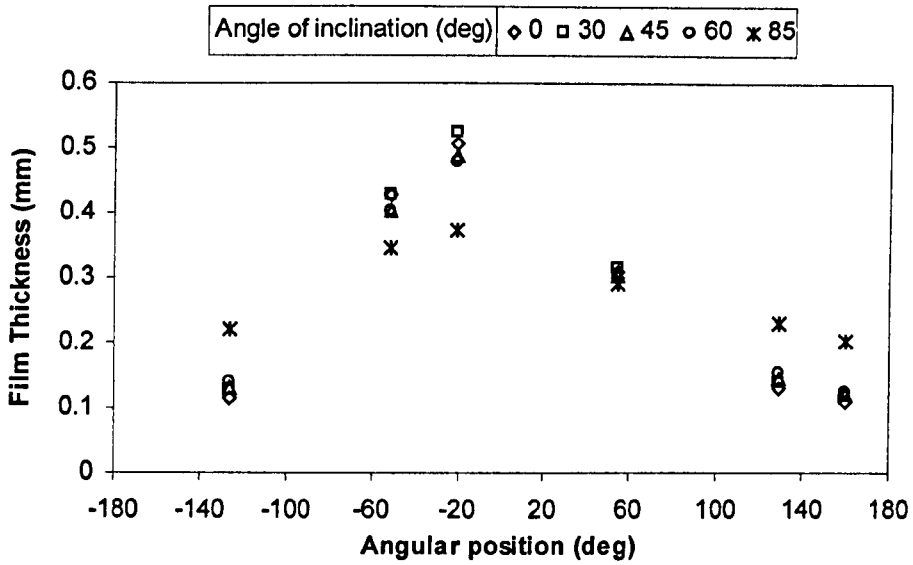


Figure 5.2.6: Liquid film thickness variation with angle of inclination from horizontal. Gas mass flowrate=0.04 kg/s, liquid mass flowrate=0.0131 kg/s

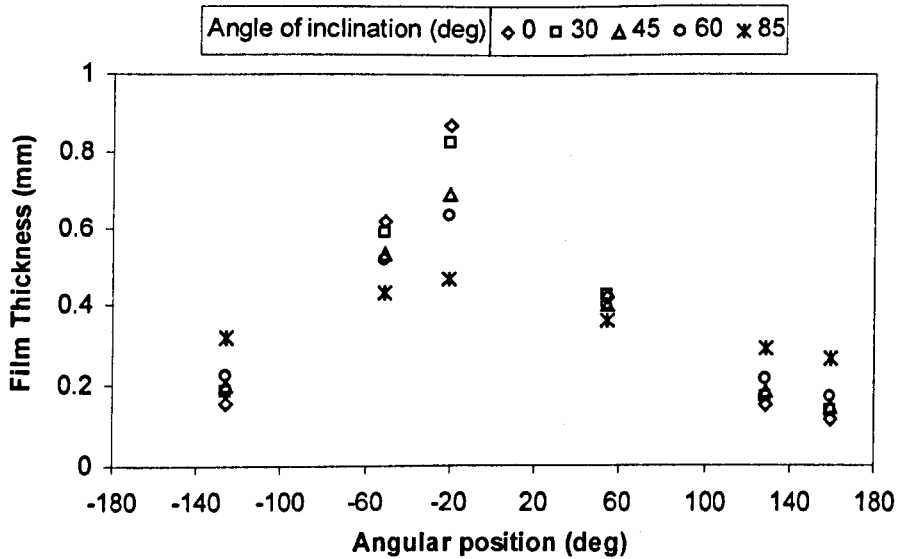


Figure 5.2.7: Liquid film thickness variation with angle of inclination from horizontal. Gas mass flowrate=0.04 kg/s, liquid mass flowrate=0.0317 kg/s

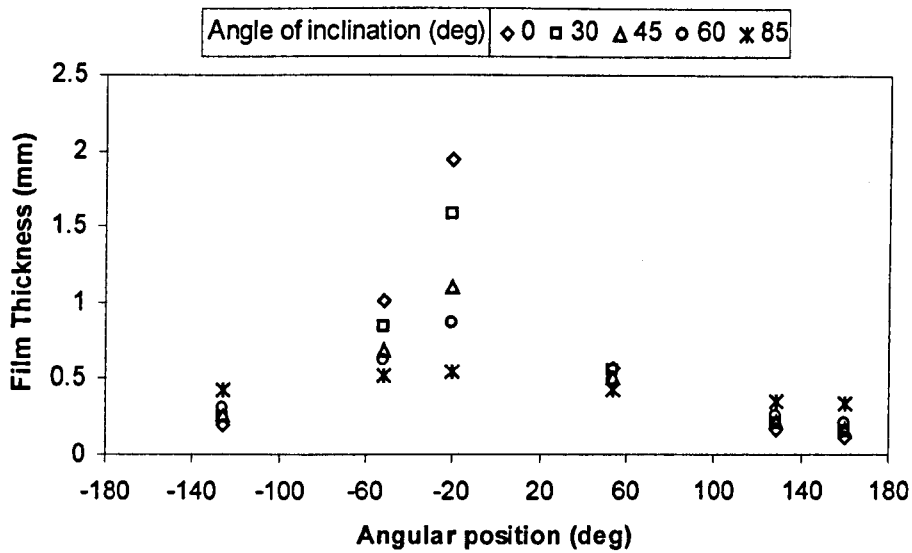


Figure 5.2.8: Liquid film thickness variation with angle of inclination from horizontal. Gas mass flowrate=0.04 kg/s, liquid mass flowrate=0.0527 kg/s

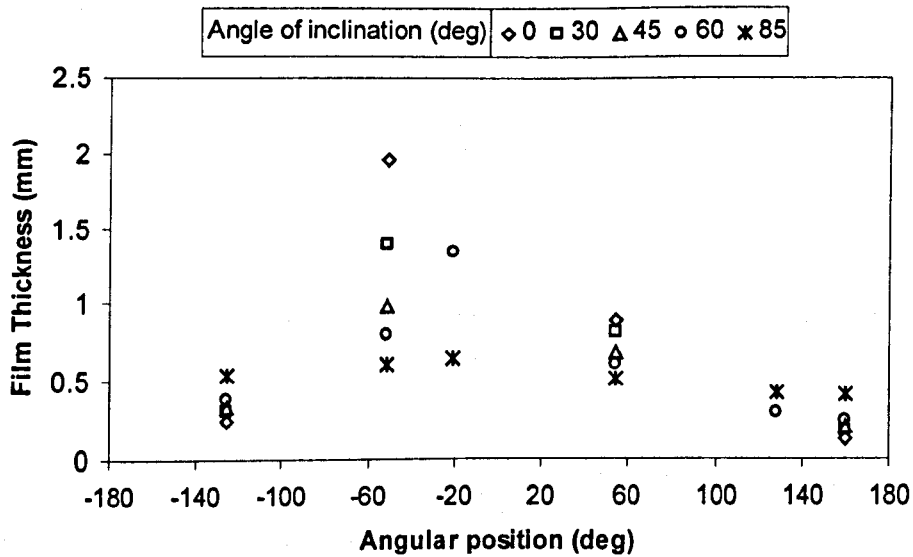
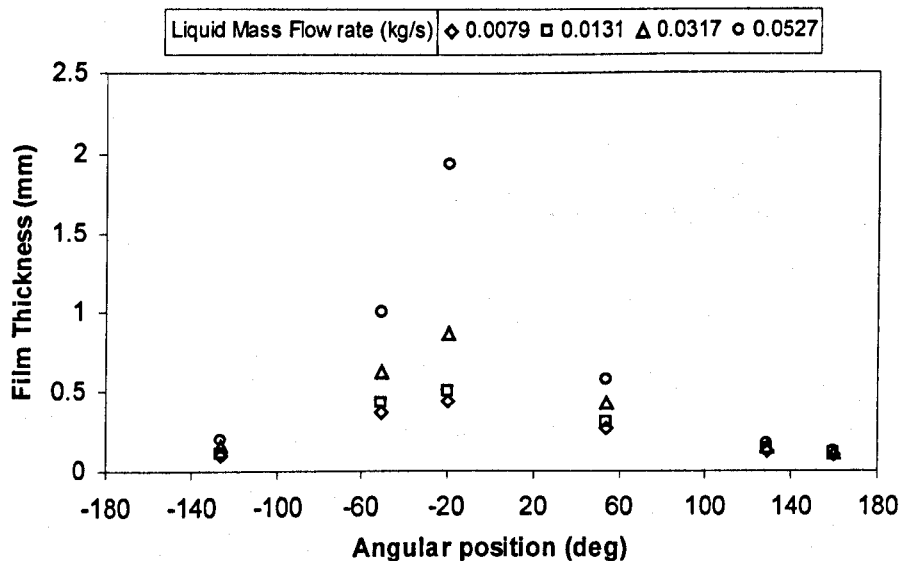


Figure 5.2.9: Liquid film thickness variation with angle of inclination from horizontal. Gas mass flowrate=0.04 kg/s, liquid mass flowrate=0.0899 kg/s

Figures 5.2.10 to 5.2.14 show the variation of average film thickness with liquid mass flowrate,  $M_l$ . As  $M_l$  is increased, the film becomes higher, especially at the bottom of the pipe. Moreover, the film thickness distribution is more uniform at  $85^\circ$  inclined flow. Chapter 4 shows that an increasing liquid flowrate results also in a higher liquid entrained fraction. Therefore, it can be concluded that both average liquid film thickness and liquid entrainment increase with increasing liquid velocity. These results are in accord with those found for the main pipe.



**Figure 5.2.10:** Liquid film thickness variation with liquid mass flowrate. Gas mass flowrate=0.04 kg/s, angle of inclination from horizontal= $0^\circ$

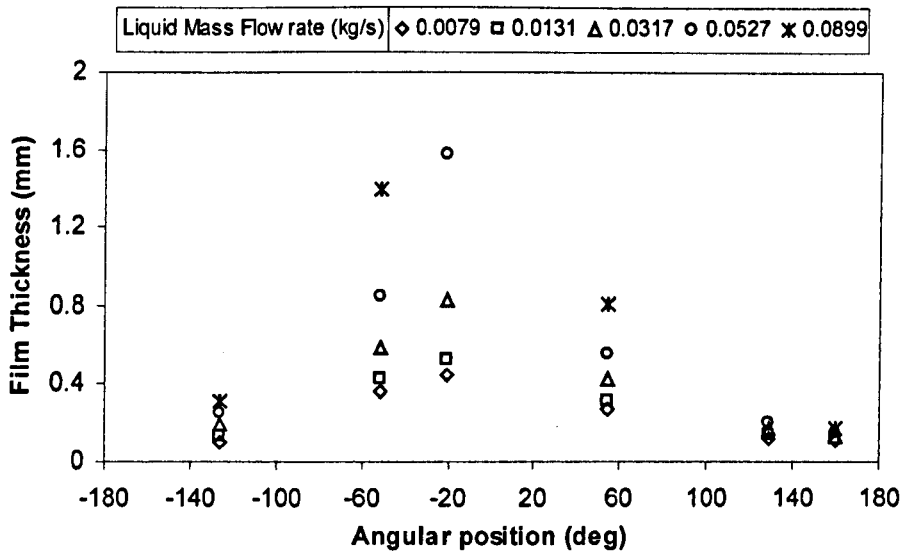


Figure 5.2.11: Liquid film thickness variation with liquid mass flowrate. Gas mass flowrate=0.04 kg/s, angle of inclination from horizontal=30°

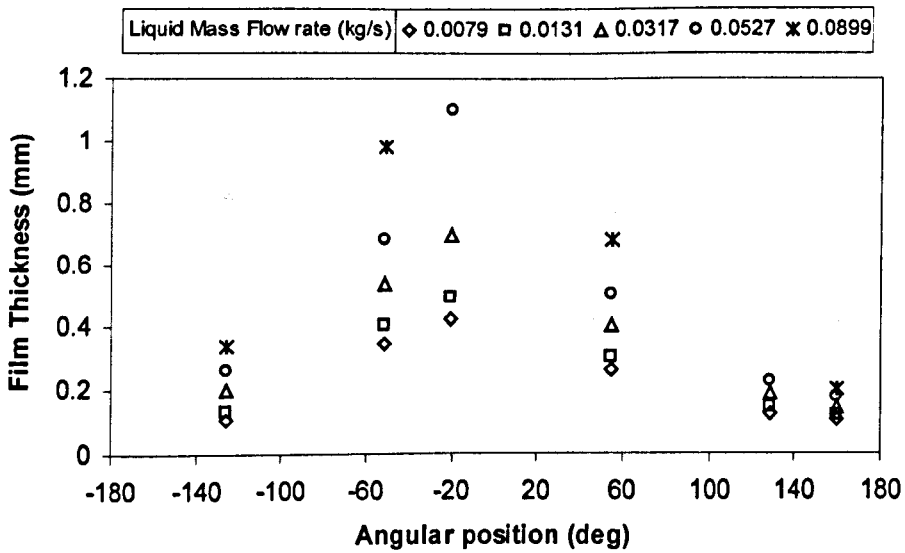


Figure 5.2.12: Liquid film thickness variation with liquid mass flowrate. Gas mass flowrate=0.04 kg/s, angle of inclination from horizontal=45°

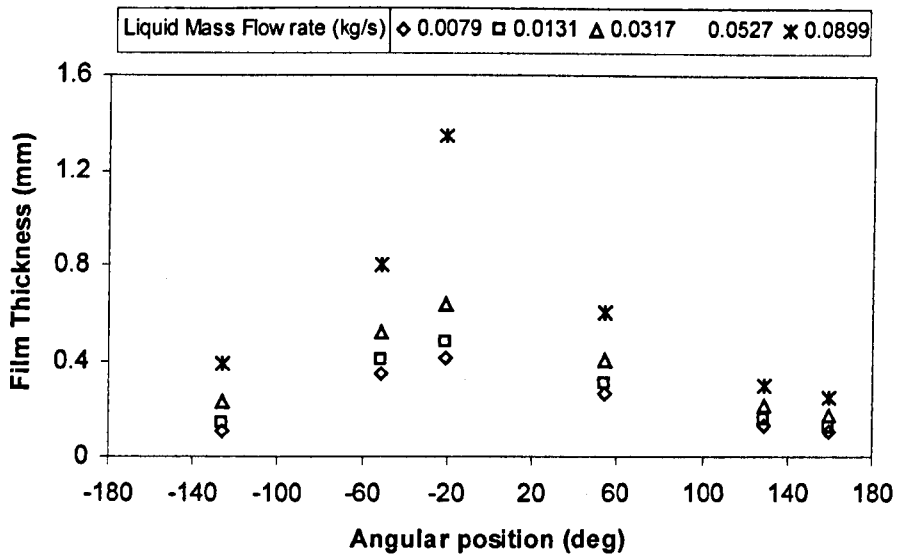


Figure 5.2.13: Liquid film thickness variation with liquid mass flowrate. Gas mass flowrate=0.04 kg/s, angle of inclination from horizontal=60°

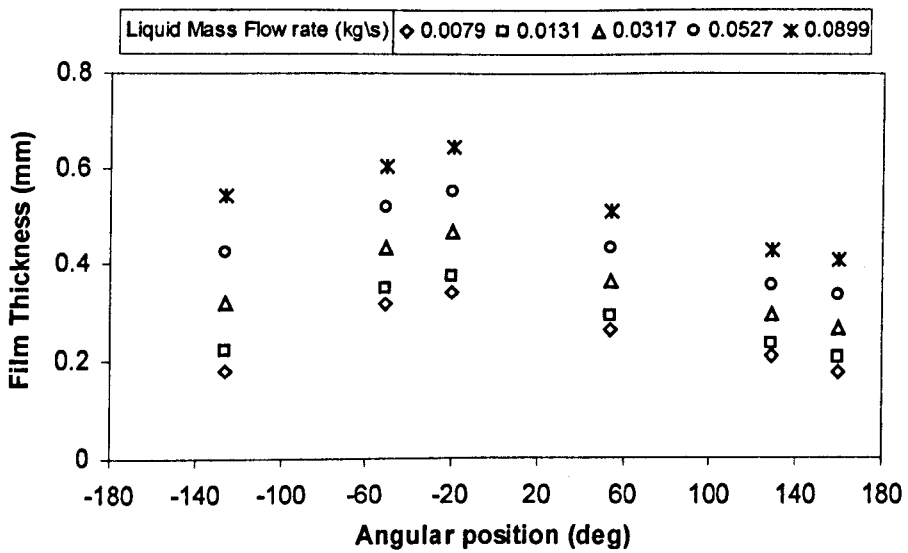
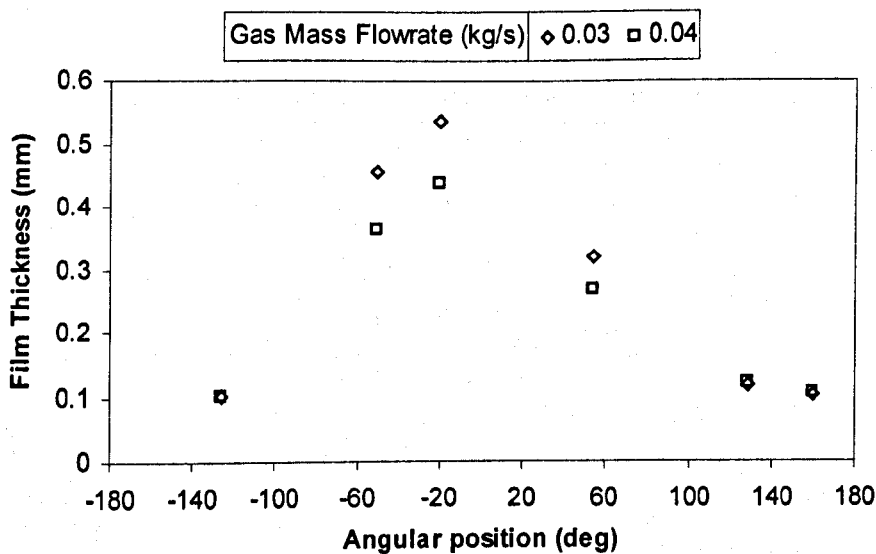
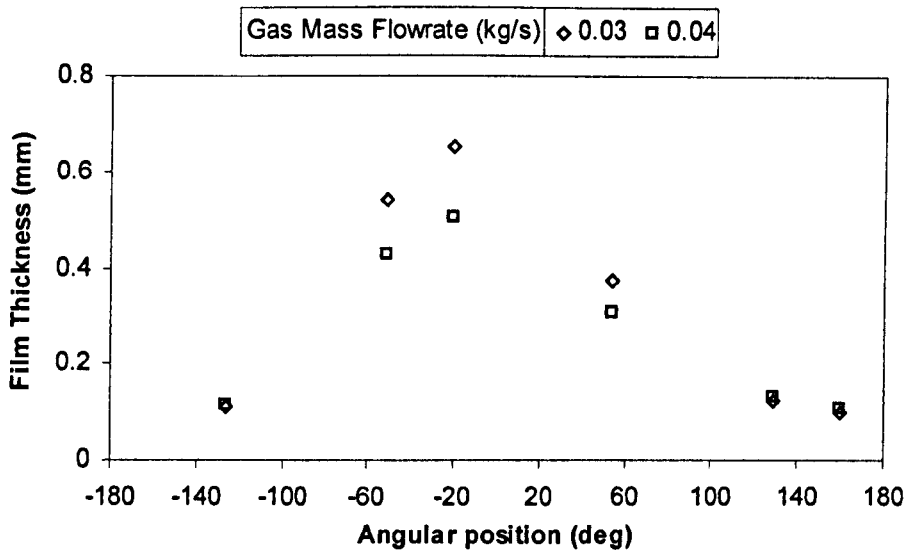


Figure 5.2.14: Liquid film thickness variation with liquid mass flowrate. Gas mass flowrate=0.04 kg/s, angle of inclination from horizontal=85°

Figures 5.2.15 to 5.2.18 show the variation of average film thickness with gas mass flowrate,  $M_g$ . As the gas mass flowrate is increased the height of the liquid film decreases. This is due to the stronger action of the gas on the liquid film (especially on the disturbance waves) which tends to increase the atomization at the liquid-gas interface and, therefore, reduce the liquid film height. In Chapter 4, it is analysed the variation of the liquid entrained fraction with gas mass flowrate. It is shown that the liquid entrained fraction increases with gas mass flowrate. Therefore, the results on film thickness are in accord with those on liquid entrainment. As a rule of thumb, it can be said that an increasing gas velocity has the effect to increase the liquid entrainment and to reduce the average film thickness. This agrees with the results found for the main pipe upstream of the Venturi.



**Figure 5.2.15:** Liquid film thickness variation with gas mass flowrate. Liquid mass flowrate=0.0079 kg/s, angle of inclination from horizontal=0°



**Figure 5.2.16:** Liquid film thickness variation with gas mass flowrate. Liquid mass flowrate=0.0131 kg/s, angle of inclination from horizontal=0°

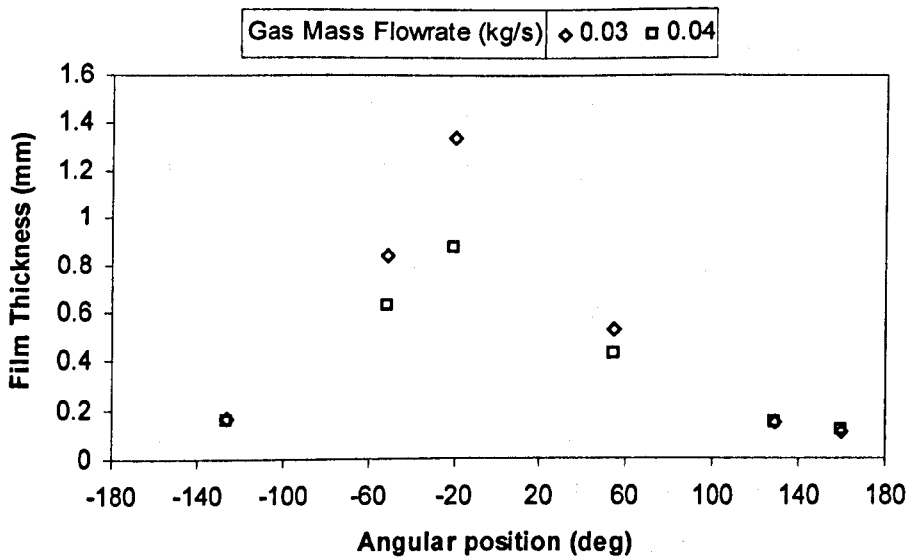


**Figure 5.2.17:** Liquid film thickness variation with gas mass flowrate. Liquid mass flowrate=0.0317 kg/s, angle of inclination from horizontal=0°

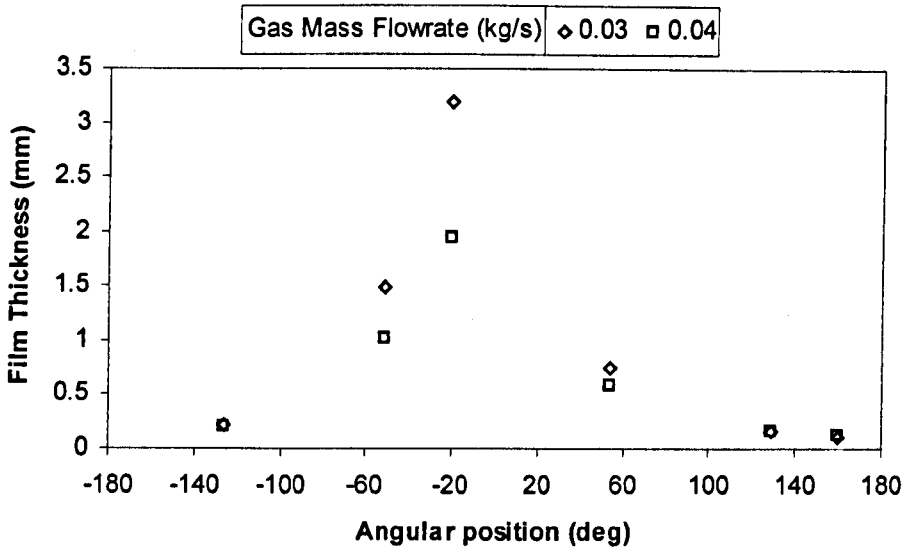


**Figure 5.2.18:** Liquid film thickness variation with gas mass flowrate. Liquid mass flowrate=0.0527 kg/s, angle of inclination from horizontal=0°

As well as for the pipe upstream the Venturi, two selected cases of data are selected and presented in order to give a more detailed examination of the liquid film in the throat. The first case is shown in figures 5.2.19 to 5.2.23. Here, time series of film thickness measured between 0° to 180° by probes 1(2), 4(1), 3(2) and 3(1) and the probability density function (PDF) of the film traces are illustrated. The gas and liquid mass flowrates considered are respectively  $M_g = 0.04 \text{ kg/s}$  and  $M_l = 0.0131 \text{ kg/s}$ . The characteristics of the film are given in table 5.2.1.

In horizontal flow, figure 5.2.19, the film measured by probes 1(2) is very agitated and is characterised by rather regular disturbance waves with high peaks, see table 5.2.1. The liquid film measured by probes 4(1) is less agitated. Moreover, at this location the height and the frequency of the big waves are lower and the peak of the probability density function is more dominant. At the location measured by 3(2), the film is wetted periodically by small waves (or surges) of much lower frequency (of the order of 1 Hz), with film draining down between these surges. At the top of the

pipe, the film is very thin and waves are not present. In  $30^\circ$  inclined flow, the characteristics of the film are similar to those of the film in horizontal flow: big disturbance waves at the bottom, small surges along the side and flat film at the top of the pipe. In  $45^\circ$  and  $60^\circ$  inclined flow, the waves along the side have higher peaks and at the top, there is a presence of waves with small amplitude (surges). At the inclination of  $85^\circ$ , the film average film thickness is more uniform. Big waves are present around the entire section of the throat. However, these waves are higher at the bottom and lower at the top.

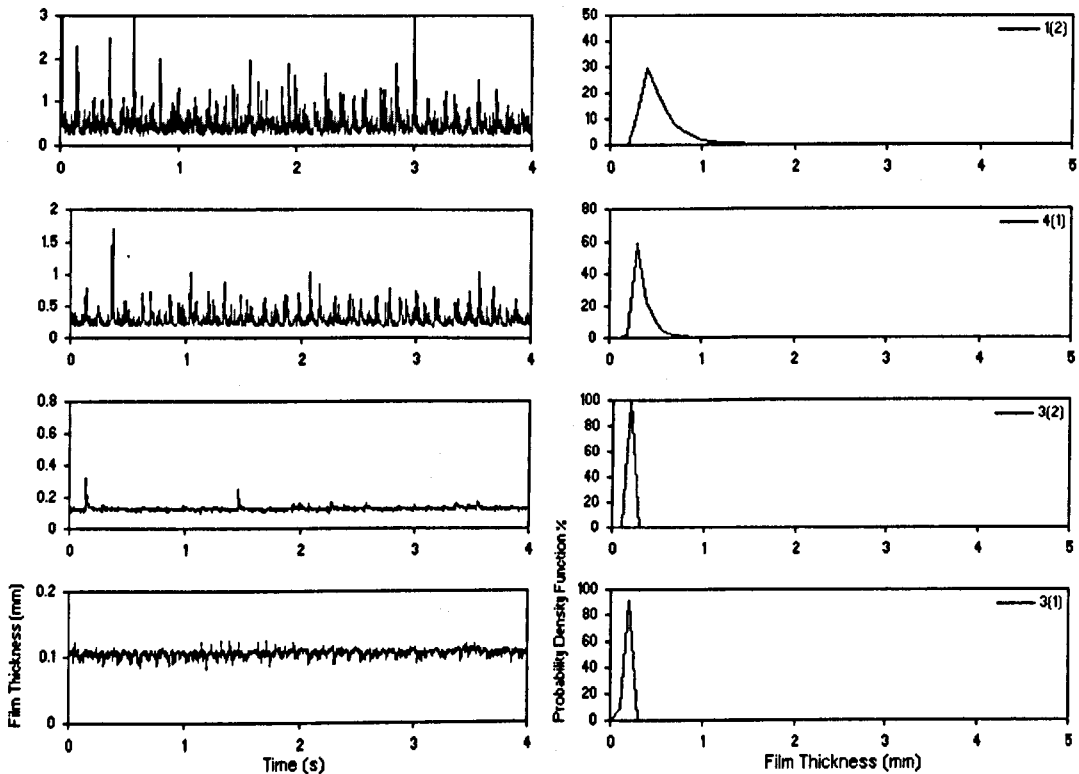


**Figure 5.2.19:** On the right, variation with time of film thickness. On the left, probability density function of film thickness. Gas mass flowrate=0.04 kg/s, liquid mass flowrate=0.0131 kg/s, angle of inclination from horizontal= $0^\circ$

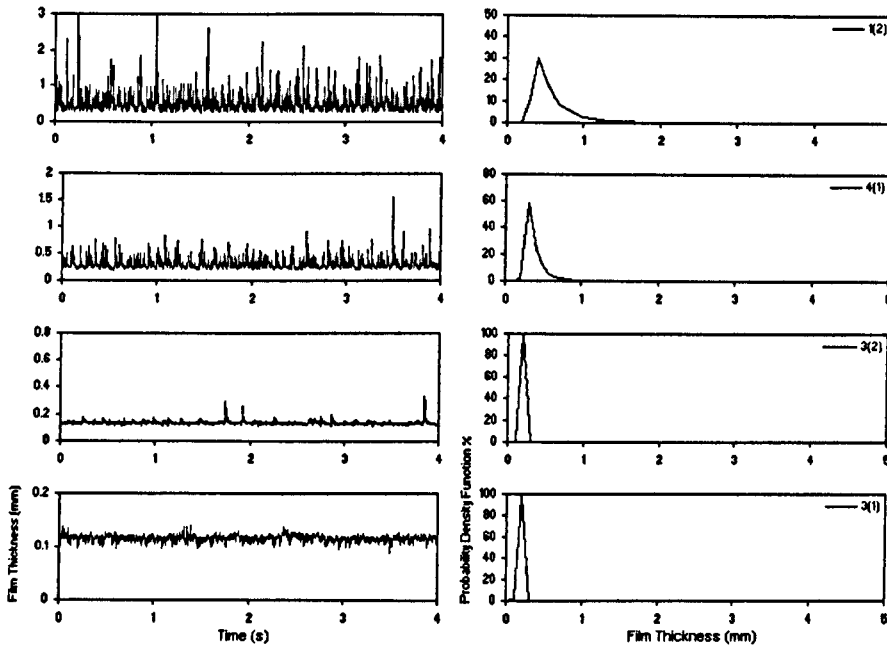


Figure 5.2.20: On the right, variation with time of film thickness. On the left, probability density function of film thickness. Gas mass flowrate=0.04 kg/s, liquid mass flowrate=0.0131 kg/s, angle of inclination from horizontal=30°

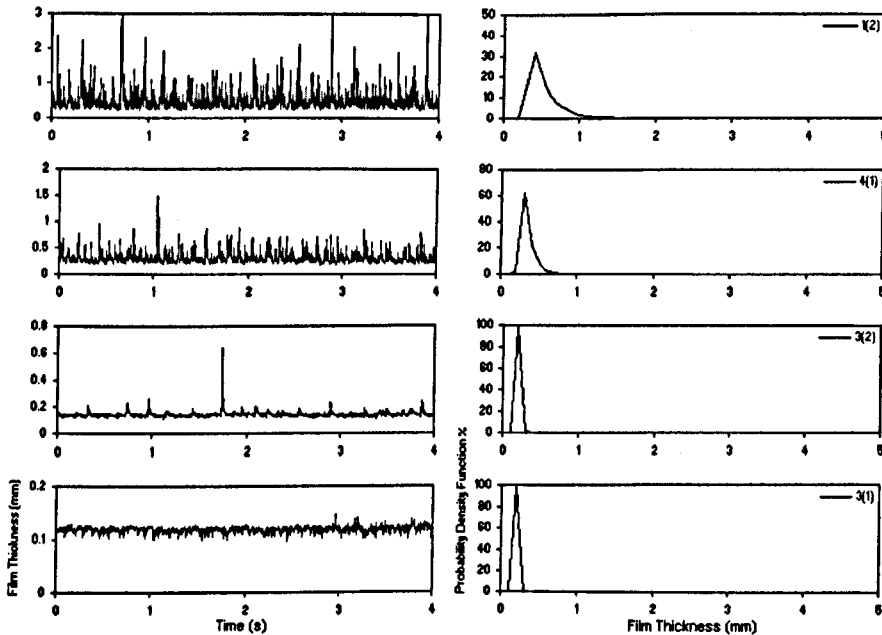


Figure 5.2.21: On the right, variation with time of film thickness. On the left, probability density function of film thickness. Gas mass flowrate=0.04 kg/s, liquid mass flowrate=0.0131 kg/s, angle of inclination from horizontal=45°

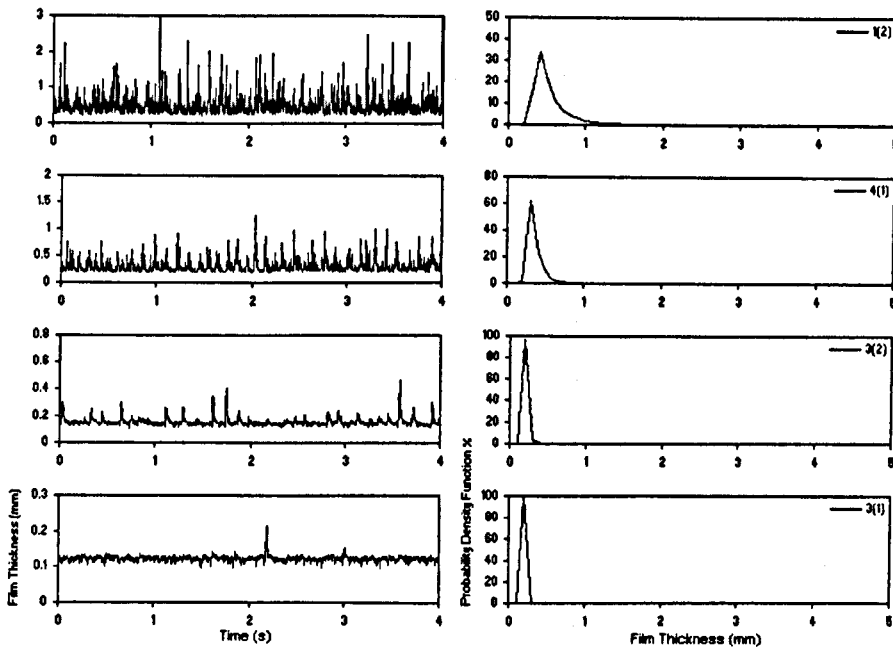


Figure 5.22: On the right, variation with time of film thickness. On the left, probability density function of film thickness. Gas mass flowrate=0.04 kg/s, liquid mass flowrate=0.0131 kg/s, angle of inclination from horizontal=60°

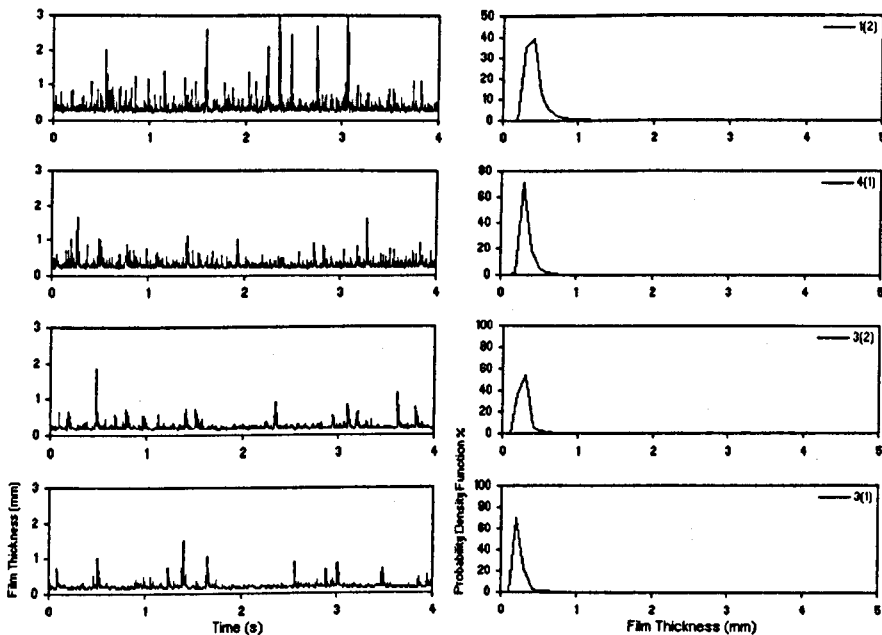


Figure 5.23: On the right, variation with time of film thickness. On the left, probability density function of film thickness. Gas mass flowrate=0.04 kg/s, liquid mass flowrate=0.0131 kg/s, angle of inclination from horizontal=85°

**Table 5.2.1:** Characteristics of the liquid film at different inclinations, gas mass flowrate=0.04 kg/s, liquid mass flowrate=0.0131 kg/s

	A	1(2)	4(1)	3(2)	3(1)
<b>Base Film Thickness (mm)</b>	0	0.32	0.24	0.13	0.11
	30	0.32	0.24	0.14	0.12
	45	0.3	0.23	0.14	0.12
	60	0.31	0.24	0.15	0.12
	85	0.29	0.24	0.2	0.18
<b>Occurrence based on the first decimal %</b>	0	29.6	58.8	99.9	91.7
	30	30	57.5	99.5	99.2
	45	31.75	62.5	98.7	99.8
	60	33.7	62	95.9	99.8
	85	35.6	70.5	53.8	70.3
<b>Average Film Thickness (mm)</b>	0	0.50	0.31	0.13	0.11
	30	0.52	0.31	0.14	0.12
	45	0.49	0.30	0.14	0.12
	60	0.48	0.30	0.15	0.12
	85	0.37	0.29	0.23	0.20
<b>Highest Peaks (mm)</b>	0	3	1.7	0.32	0
	30	3	1.5	0.35	0
	45	3	1.5	0.65	0
	60	3	1.3	0.48	0.22
	85	3	1.7	1.8	1.5
<b>Average Wave Height (mm)</b>	0	0.18	0.7	0	0
	30	0.20	0.7	0	0
	45	0.19	0.7	0	0
	60	0.19	0.6	0	0
	85	0.8	0.5	0.03	0.02

Figures 5.2.24 to 5.2.27 show the effect of the inclination on the liquid film thickness at the same circumferential location. The gas and liquid mass flowrates are still  $M_g = 0.04$  kg/s and  $M_l = 0.0131$  kg/s. It can be seen that, for the five different inclinations, the film at the lower half of the throat is characterized by disturbance waves 10 times higher than the base film thickness. The same ratio was found in the pipe. At the location measured by probes 1(2) the base film thickness does not vary with inclination while the average film thickness and the average wave height<sup>5</sup> are lower at the inclination of 85°. The base film thickness and the average wave height are shown respectively with a yellow and a red line. At the location measured by probes 4(1) the characteristics of the film does not change considerably with inclination. The characteristics of the liquid film at the other locations of the section are shown in table 5.2.1. The probability density functions of the film thickness traces show that the peak becomes more dominant when the liquid film is less disturbed by the presence of waves. Therefore, at the top side of the pipe, the base film thickness is closer to the average film thickness.

---

<sup>5</sup> The same calculation was not carried on for the other locations around the pipe as the height of the waves was not remarkable.

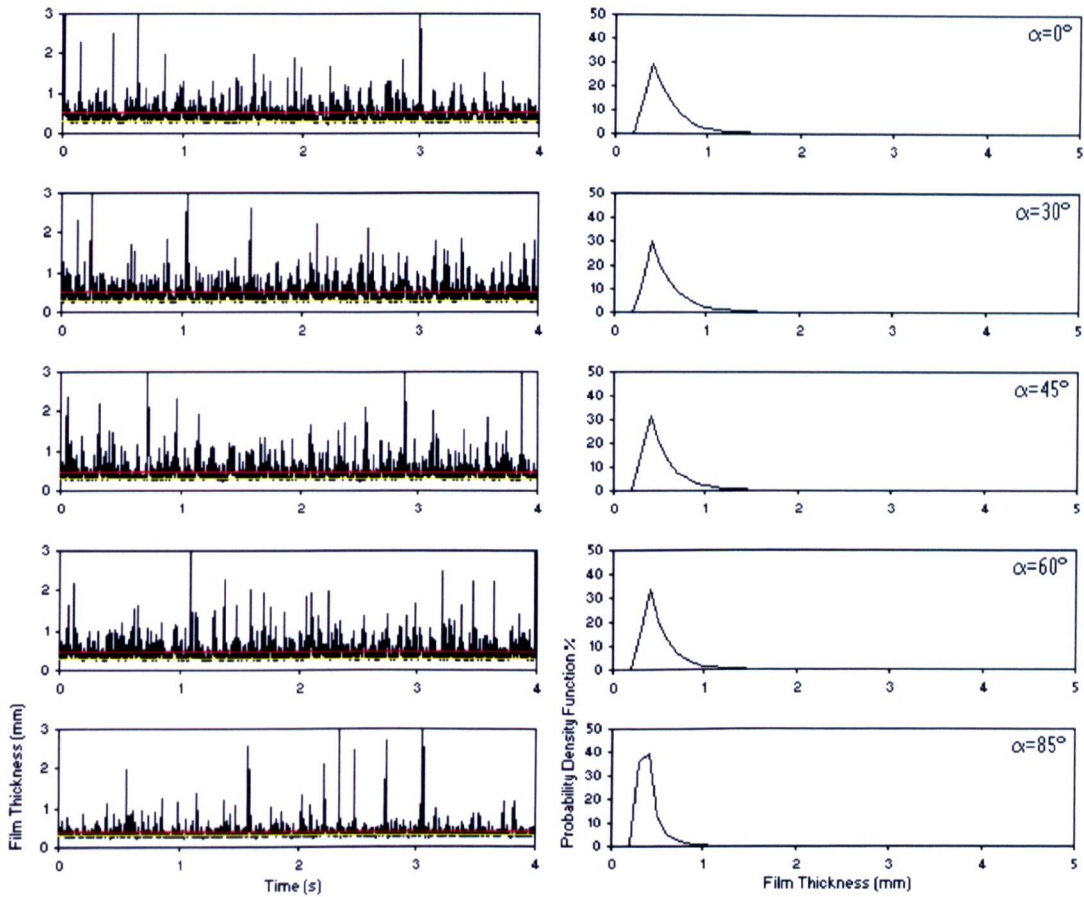


**Figure 5.2.24:** On the right, variation with time of film thickness measured by wires 1(2). On the left, probability density function of film thickness. Air flowrate of 0.04 kg/s, water flowrate of 0.0131 kg/s

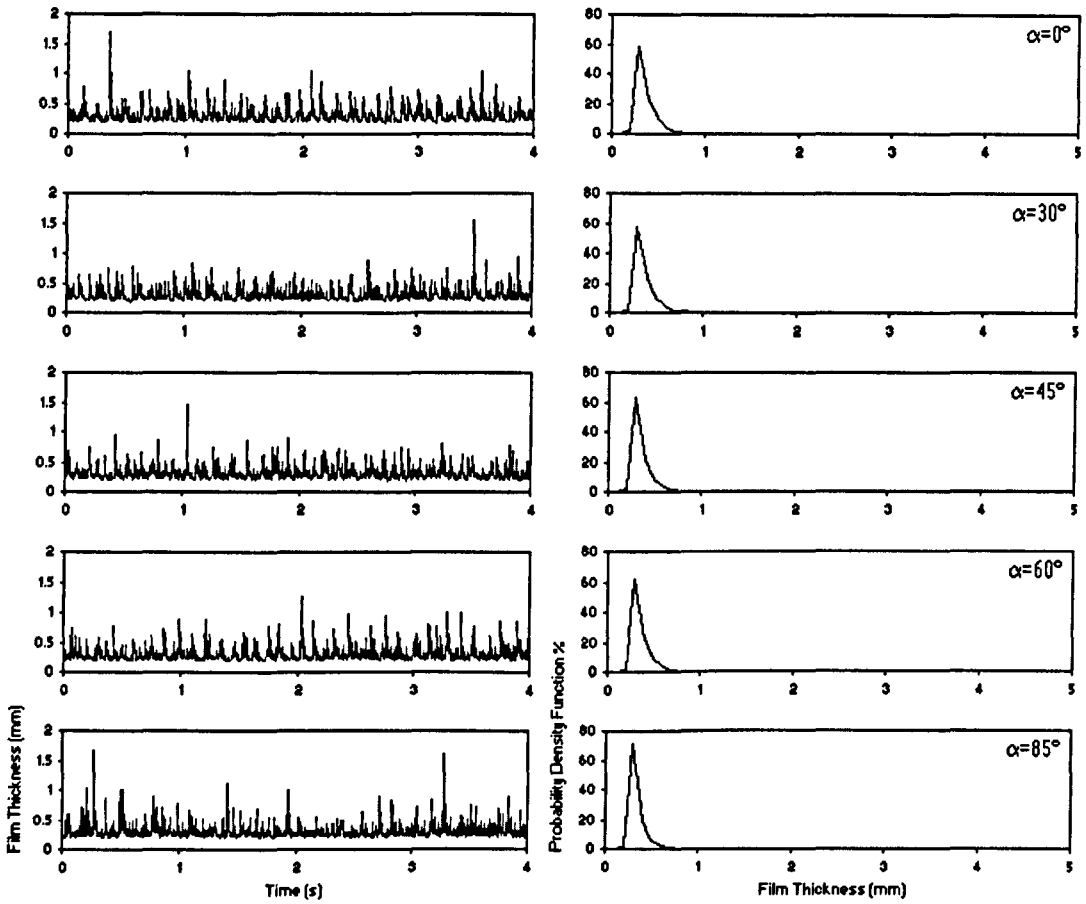


**Figure 5.2.25:** On the right, variation with time of film thickness measured by wires 4(1). On the left, probability density function of film thickness. Air flowrate of 0.04 kg/s, water flowrate of 0.0131 kg/s

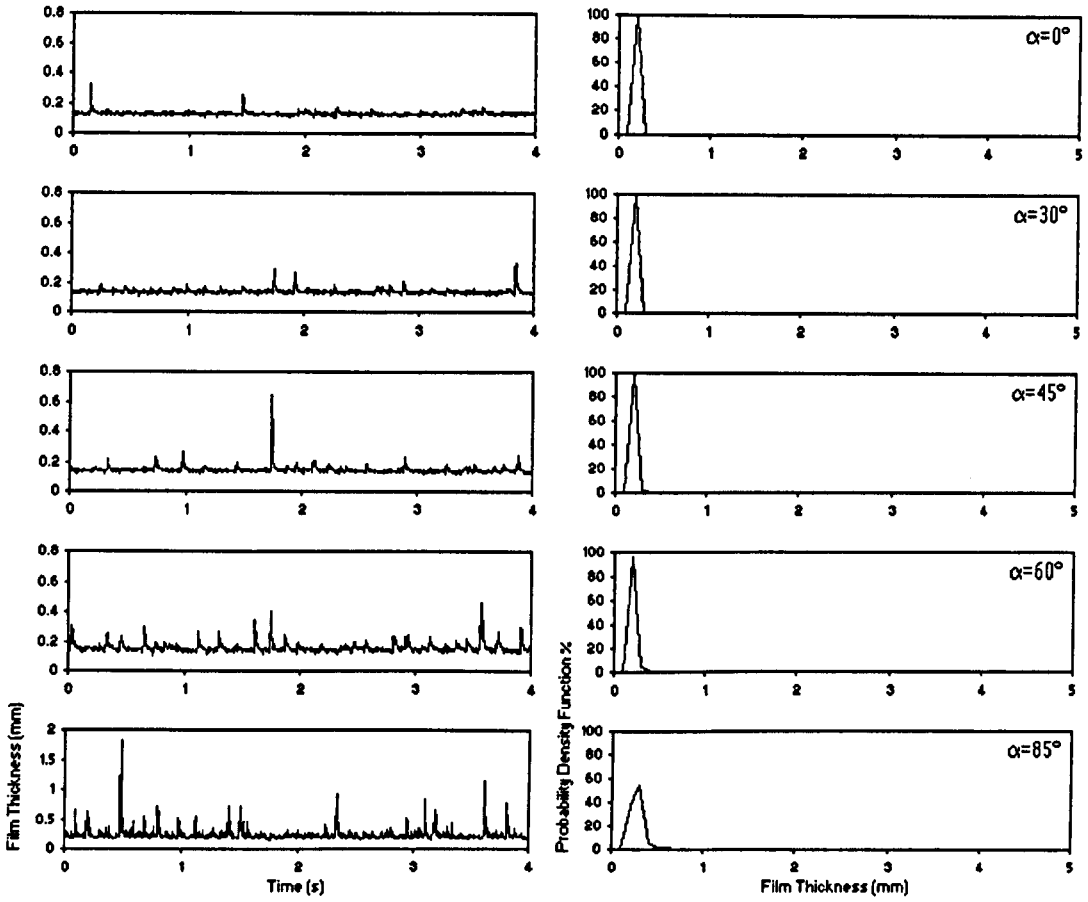
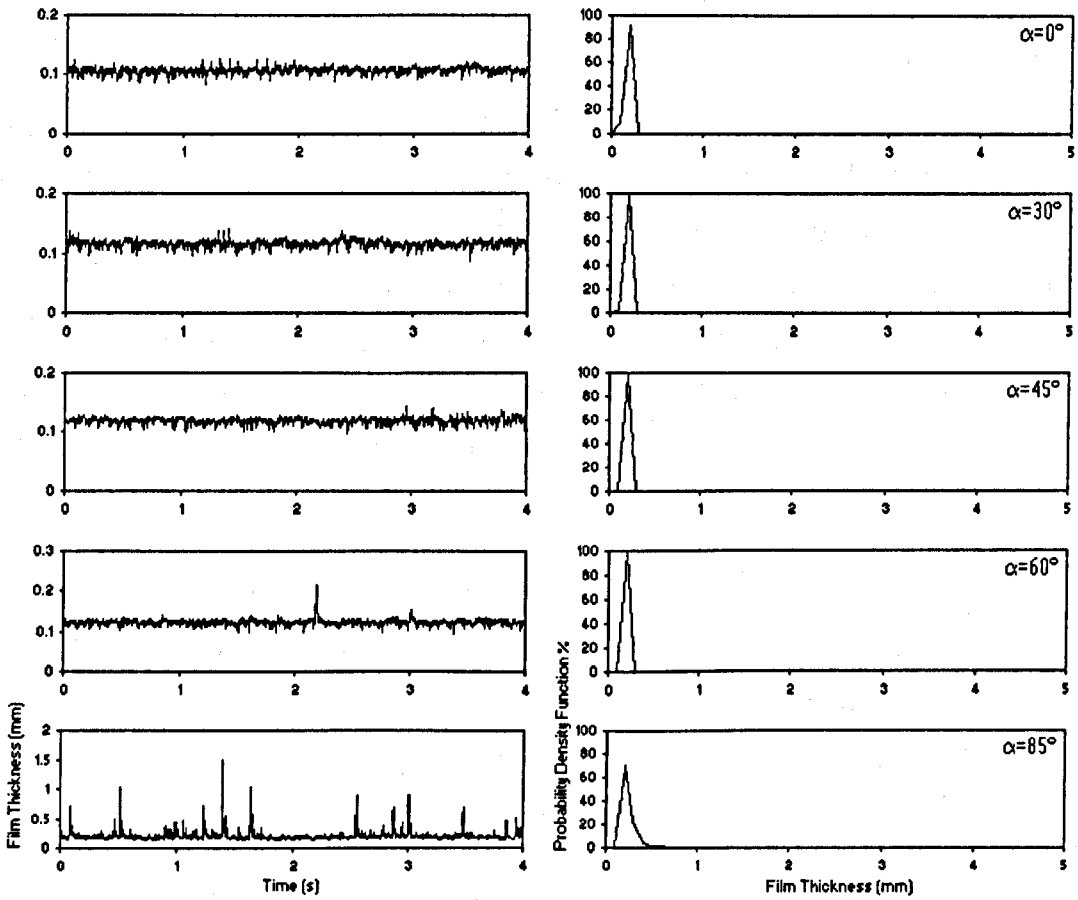
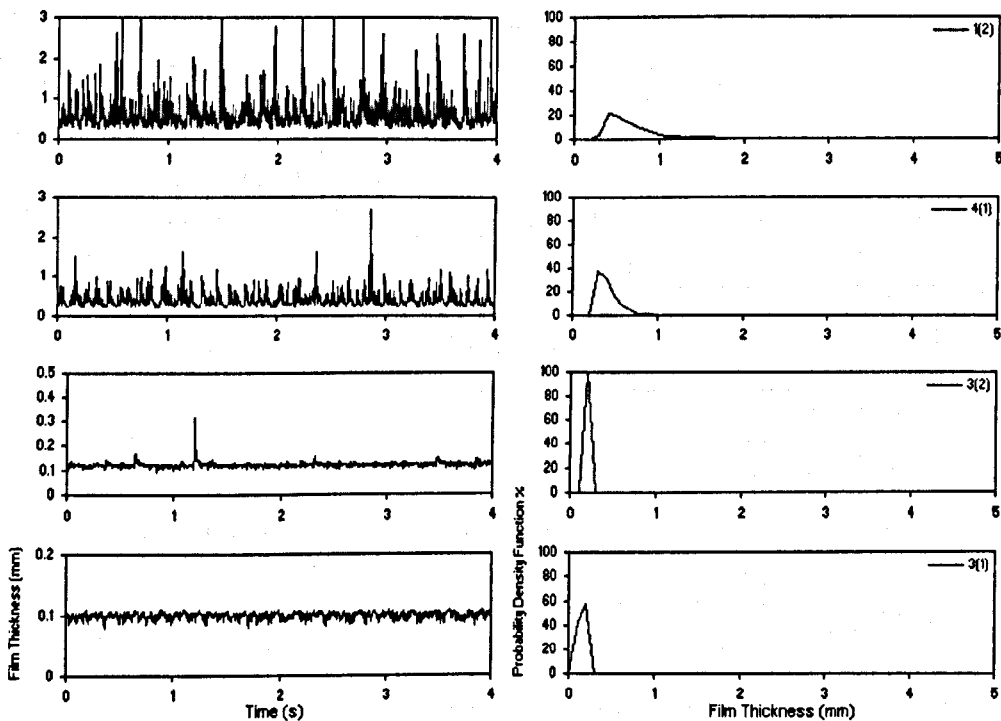


Figure 5.2.26: On the right, variation with time of film thickness measured by wires 3(1). On the left, probability density function of film thickness. Air flowrate of 0.04 kg/s, water flowrate of 0.0131 kg/s



**Figure 5.2.27:** On the right, variation with time of film thickness measured by wires 3(2). On the left, probability density function of film thickness. Air flowrate of 0.04 kg/s, water flowrate of 0.0131 kg/s

As well as in the main pipe, with lower mass flowrate ( $M_g=0.03$  kg/s) and the same liquid mass flowrate ( $M_l = 0.0131$  kg/s) the interaction between air and water becomes less strong and, therefore, the liquid-gas interface is less disturbed with consequent less entrainment, see Chapter 4. This results in higher base and average film thickness around the entire section of the pipe. Also the wave average height is higher, especially at the bottom. Figures 5.2.28 to 5.2.32 show that at the bottom side the film is characterised by very high peaks (10 times the base film thickness) with frequency slightly higher than in first case ( $M_g = 0.04$  kg/s). It is also shown that big waves are present along the side in  $60^\circ$  inclined flow (figure 5.2.31) and at the top side in  $85^\circ$  inclined flow (figure 5.2.32). This means that the liquid tends to spread more around the periphery with lower gas mass flowrate. A complete view of the liquid film thickness characteristics is shown in table 5.2.2.



**Figure 5.2.28:** On the right, variation with time of film thickness. On the left, probability density function of film thickness. Gas mass flowrate=0.03 kg/s, liquid mass flowrate=0.0131 kg/s, angle of inclination from horizontal= $0^\circ$

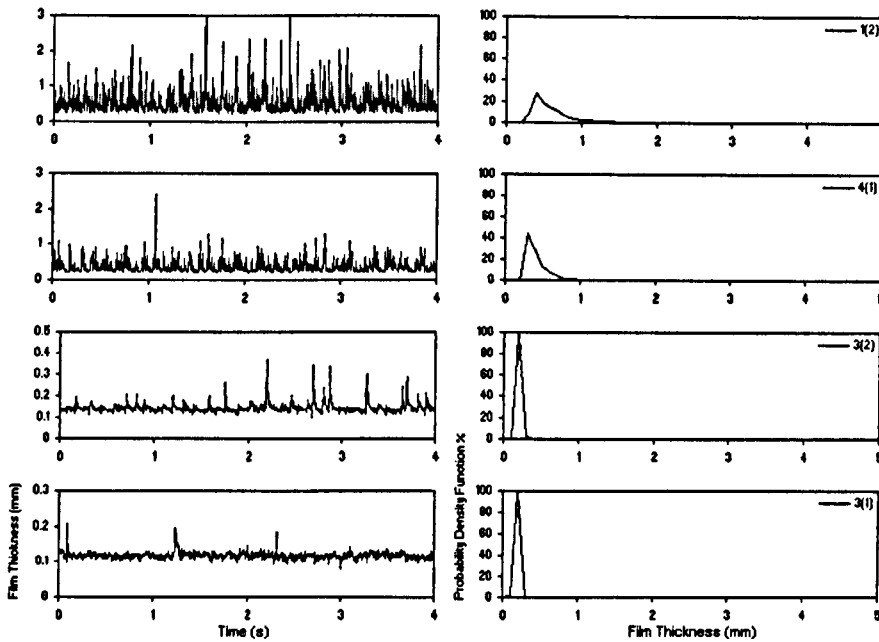


Figure 5.2.29: On the right, variation with time of film thickness. On the left, probability density function of film thickness. Gas mass flowrate=0.03 kg/s, liquid mass flowrate=0.0131 kg/s, angle of inclination from horizontal=30°

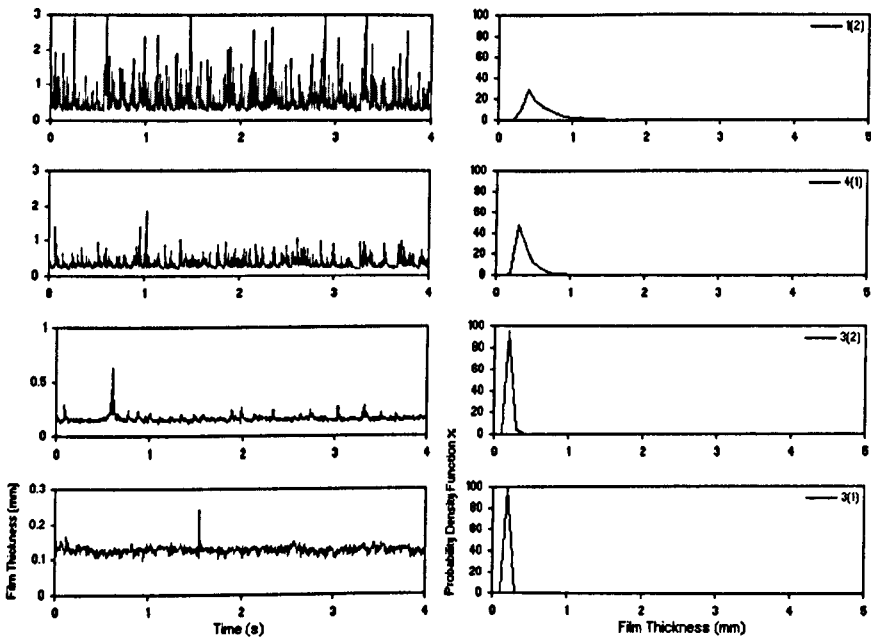


Figure 5.2.30: On the right, variation with time of film thickness. On the left, probability density function of film thickness. Gas mass flowrate=0.03 kg/s, liquid mass flowrate=0.0131 kg/s, angle of inclination from horizontal=45°

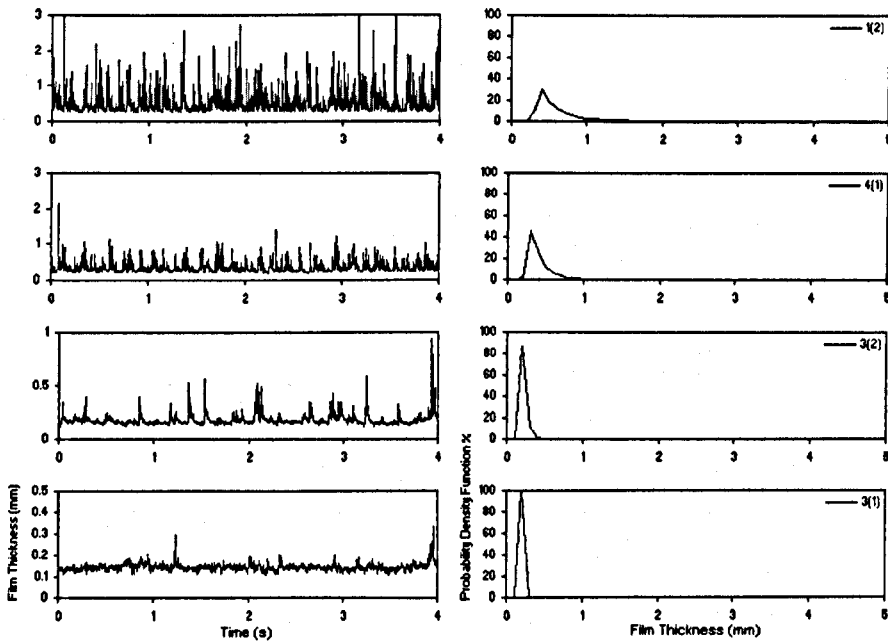


Figure 5.2.31: On the right, variation with time of film thickness. On the left, probability density function of film thickness. Gas mass flowrate=0.03 kg/s, liquid mass flowrate=0.0131 kg/s, angle of inclination from horizontal=60°

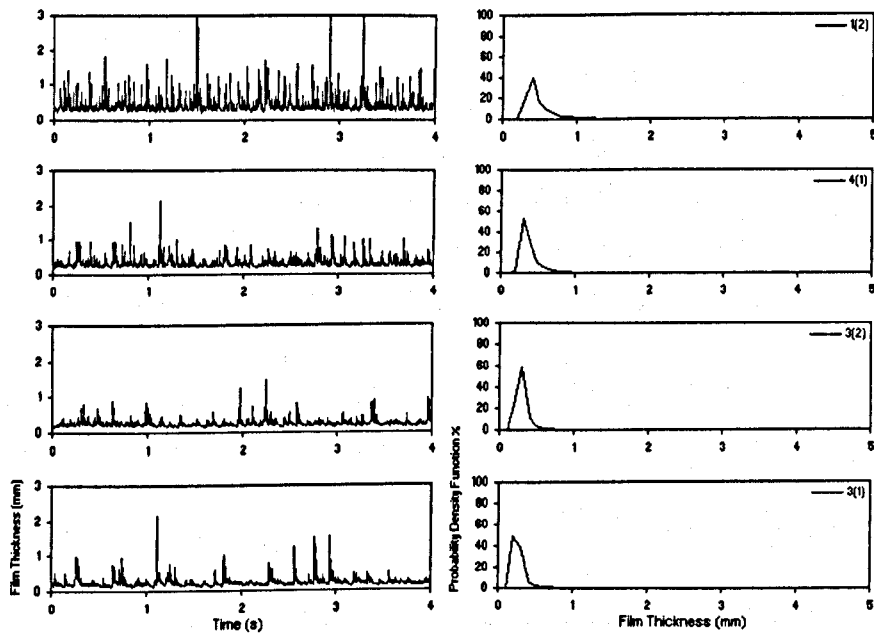
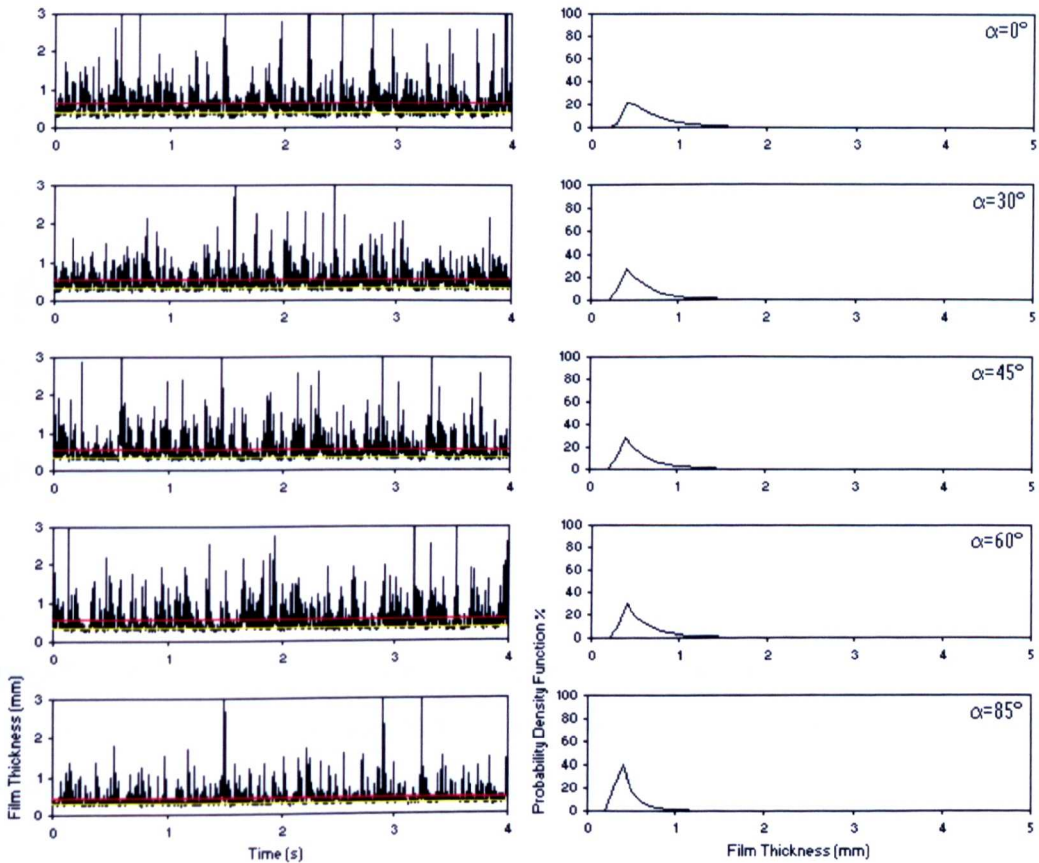


Figure 5.2.32: On the right, variation with time of film thickness. On the left, probability density function of film thickness. Gas mass flowrate=0.03 kg/s, liquid mass flowrate=0.0131 kg/s, angle of inclination from horizontal=85°

**Table 5.2.2:** Characteristics of liquid film at different inclinations, gas mass flowrate=0.03 kg/s, liquid mass flowrate=0.0131 kg/s

	$\alpha$	1(2)	4(1)	3(2)	3(1)
<b>Base Film Thickness (mm)</b>	0	0.39	0.27	0.12	0.1
	30	0.34	0.25	0.14	0.12
	45	0.33	0.25	0.15	0.13
	60	0.33	0.25	0.16	0.13
	85	0.31	0.25	0.22	0.21
<b>Occurrence based on the first decimal %</b>	0	21	31.4	99.8	99
	30	27.4	44.3	97.7	99
	45	29.2	47.6	95.5	99.8
	60	30.1	45.4	86.5	99.5
	85	39.9	52.3	59	48.6
<b>Average Film Thickness (mm)</b>	0	0.65	0.37	0.12	0.1
	30	0.56	0.35	0.14	0.12
	45	0.57	0.35	0.15	0.13
	60	0.57	0.36	0.17	0.13
	85	0.45	0.34	0.26	0.23
<b>Highest Peaks (mm)</b>	0	3	2.8	0.31	0
	30	3	2.4	0.38	0.2
	45	3	2	0.62	0.25
	60	3	2.2	0.9	0.32
	85	3	2.2	2.2	2.2
<b>Average Wave Height (mm)</b>	0	0.26	0.17	0	0
	30	0.22	0.15	0	0
	45	0.24	0.15	0	0
	60	0.24	0.11	0.01	0
	85	0.14	0.09	0.01	0.02

Figures 5.2.33 to 5.2.36 show the variation of the film thickness with increasing inclination at the same circumferential location. The gas and liquid flowrates are  $M_g = 0.03 \text{ kg/s}$  and  $M_l = 0.0131 \text{ kg/s}$ . At the four inclinations analysed the film measured by probes 1(2) and 4(1) is characterised by the presence of disturbance waves. At the location measured by probes 1(2) the base film thickness and the average wave height decrease with increasing inclination. In particular, they are lower at the inclination of  $85^\circ$ , table 5.2.2. At the location measured by probes 4(1) the characteristics of the film do not change considerably with inclination. The characteristics of the liquid film at the other locations of the section are shown in table 5.2.2.



**Figure 5.2.33:** On the right, variation with time of film thickness measured by probes 1(2). On the left, probability density function of film thickness. Gas mass flowrate= $0.03 \text{ kg/s}$ , liquid mass flowrate= $0.0131 \text{ kg/s}$

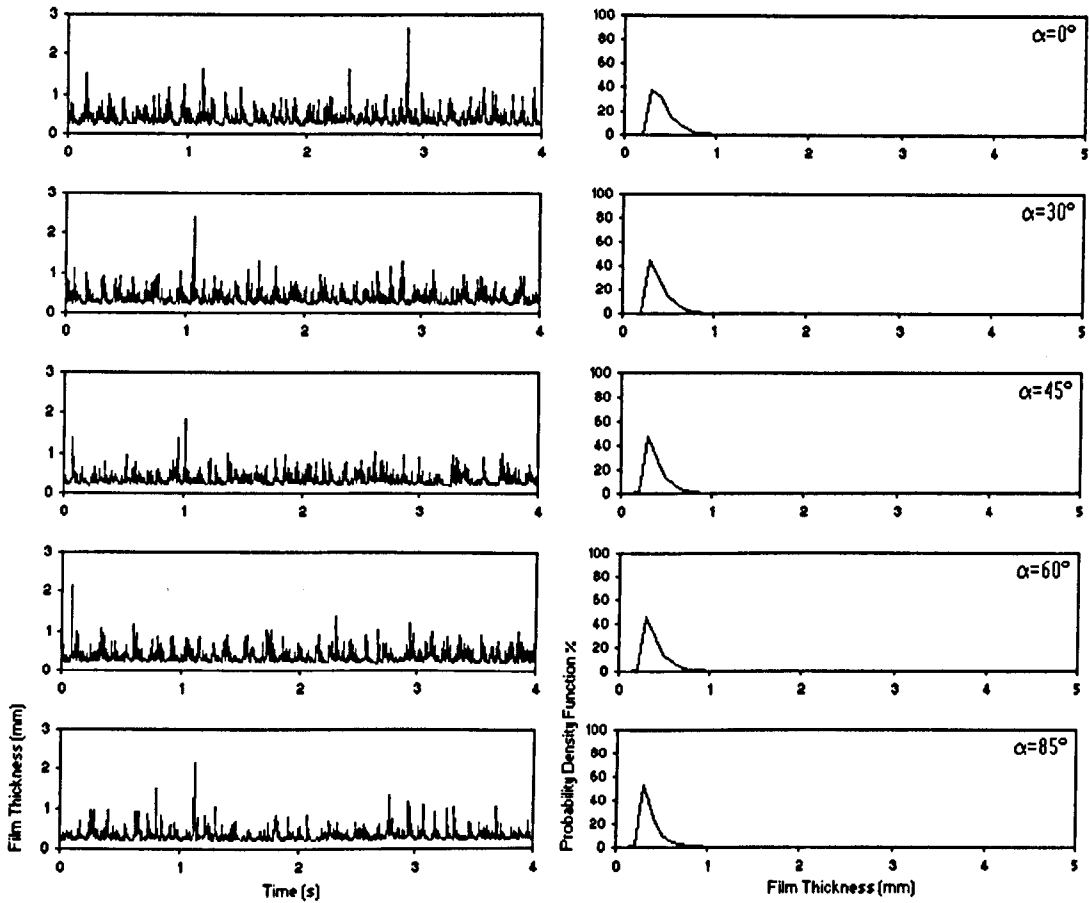


**Figure 5.2.34:** On the right, variation with time of film thickness measured by probes 4(1). On the left, probability density function of film thickness. Gas mass flowrate=0.03 kg/s, liquid mass flowrate=0.0131 kg/s.

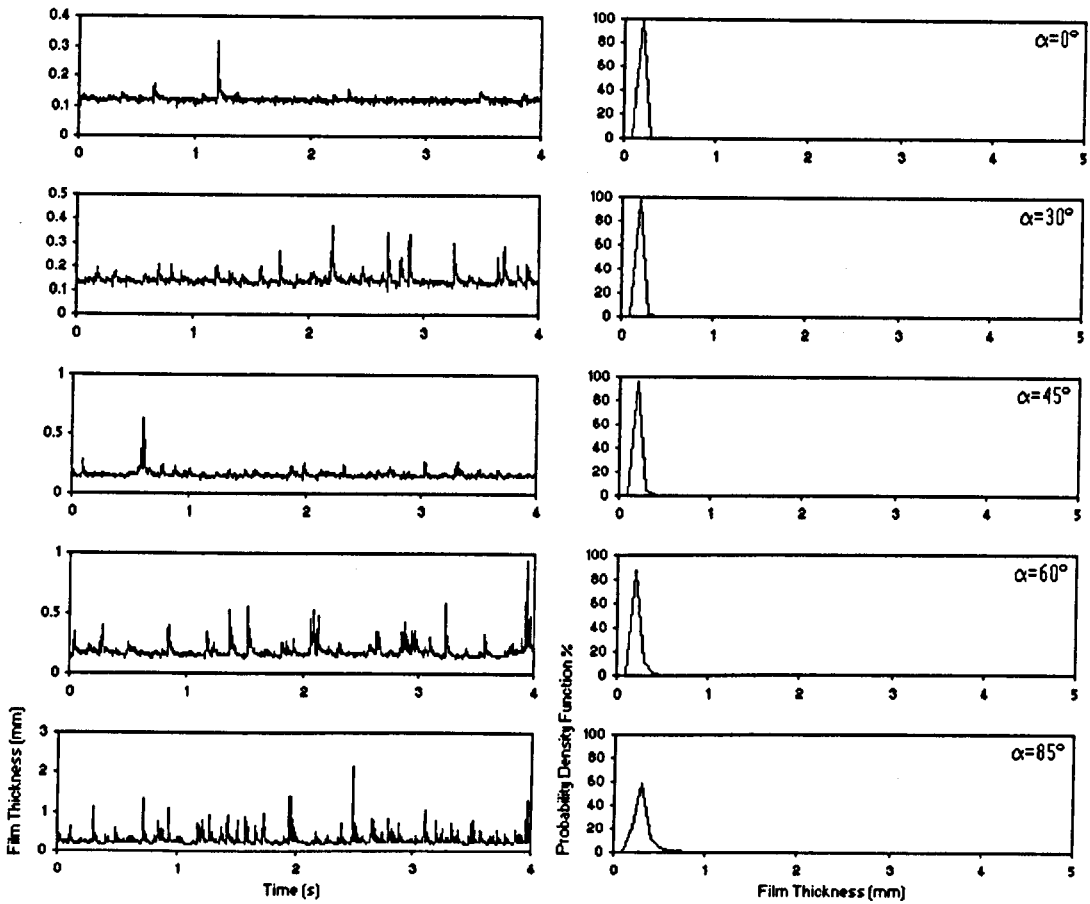


**Figure 5.2.35:** On the right, variation with time of film thickness measured by probes 3(2). On the left, probability density function of film thickness. Gas mass flowrate=0.03 kg/s, liquid mass flowrate=0.0131 kg/s

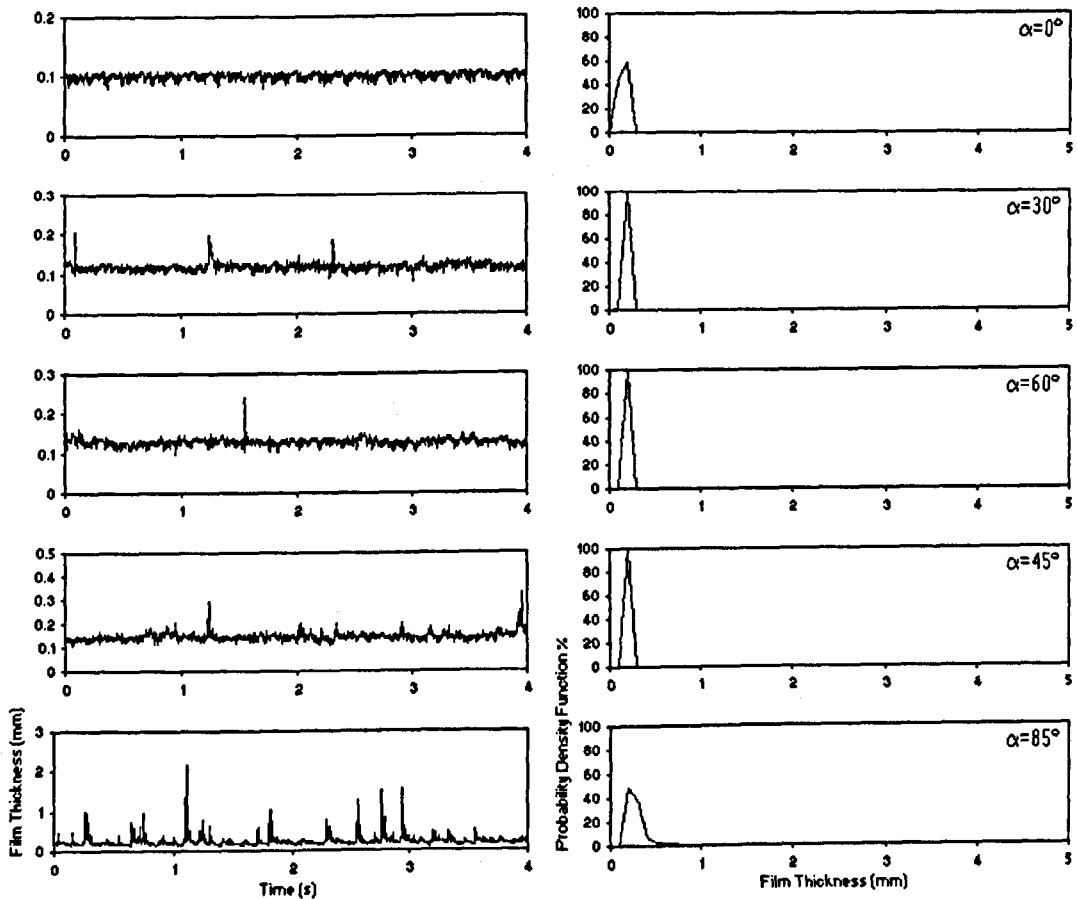


**Figure 5.2.36:** On the right, variation with time of film thickness measured by probes 3(1). On the left, probability density function of film thickness. Gas mass flowrate=0.03 kg/s, liquid mass flowrate=0.0131 kg/s

Figure 5.2.37 shows power spectra density of the film thickness at the lower half of the throat. The amplitude of the spectrum decreases moving from the bottom towards the side of the pipe. The reduction of film thickness in the circumferential direction is in accord with the above trend. Moreover, figure 5.2.37 shows that there is not appreciable change of the dominant frequency in these spectra. The study of the variation of the power spectrum density was not carried on at the upper half of the section. The reason was the absence of waves at the inclinations of  $0^\circ$ ,  $30^\circ$  and  $45^\circ$ . To reduce the sidelobes of the power spectrum, the correlation function was multiplied by a cosine windowing function. Although the presence of leakages is not

completely eliminated, it can be clearly seen that the highest signal power, for the flow conditions and inclination of figure 5.2.37, occurs for 8.8 Hz in the throat. This represents the frequency of the disturbance waves. It can also be seen a relevant peak at zero as the frequency 0 has a certain spectral width.

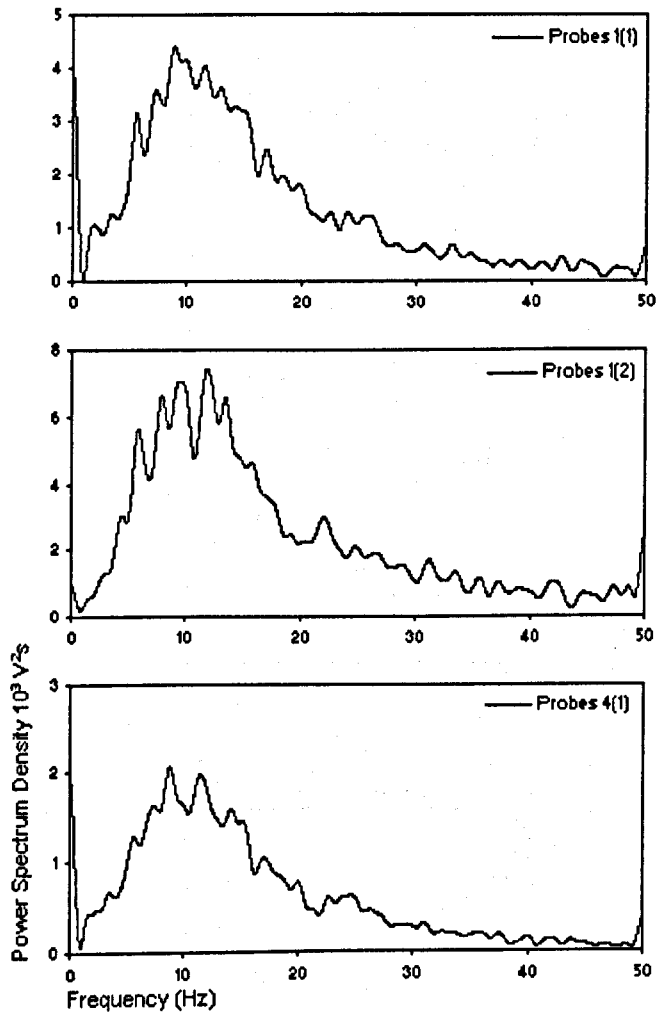


**Figure 5.2.37:** Power spectrum density at the lower part of the throat section. Gas mass flowrate=0.04 kg/s, liquid mass flowrate=0.0131 kg/s, angle of inclination from horizontal=45°

The variation of the wave frequency with flow inlet conditions and pipe inclination was also studied. Figure 5.2.38 shows power spectra of film thickness traces at the bottom at increasing liquid mass flowrate,  $M_l$ . Differently from the main pipe, in the throat it is evident a less distribution of energy among waves of higher frequency also at low liquid flowrates. In other words, in a smaller pipe such as the throat the presence of disturbance waves is highly dominant also at very low liquid velocities.

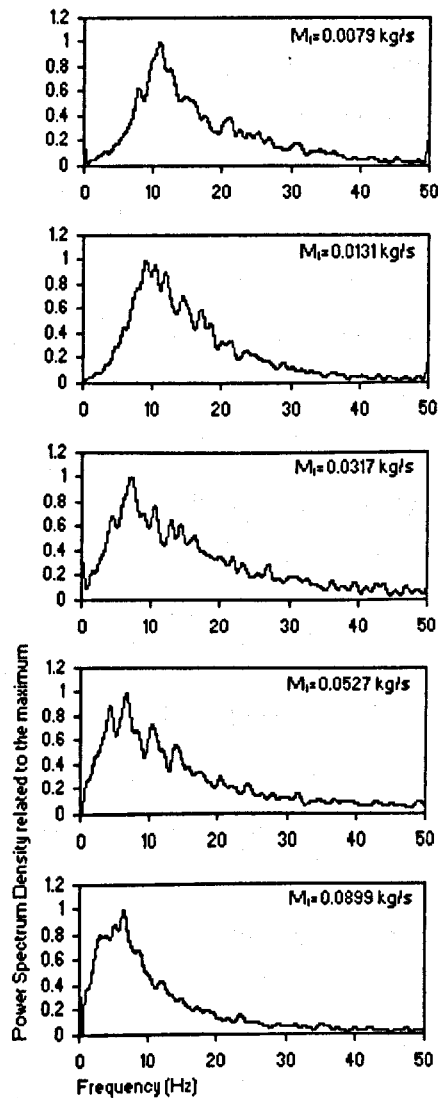


**Figure 5.2.38:** Effect of liquid mass flowrate on power spectrum density of film thickness measured by probes 1(1). Gas mass flowrate=0.04 kg/s, liquid mass flowrate=0.0131 kg/s, angle of inclination from horizontal=0°

Figure 5.2.38 shows that a large portion of wave energy at the lower half of the throat is carried by waves of frequency  $\leq 12$  Hz. There is not a significant influence of liquid velocity on the form of the spectra. However, the dominant frequency appears to decrease with increasing liquid flowrate. Moreover, in accord with the film thickness trend, the amplitude of the spectrum increases with increasing liquid velocity. This means that, at higher liquid velocity, there is a higher distribution of energy among waves. These results are in accord with those on wave frequency in the main section. Thus, in the pipe upstream of the Venturi and in the Venturi throat the wave frequency varies coherently with the liquid velocity.

The effect of the inclination on the wave frequency along the lower part of the throat is illustrated in figure 5.2.39. The amplitude of power spectra decrease with increasing inclination. Moreover, the spectrum tends to flatten out at inclination approaching the vertical position, due to the more uniform circumferential distribution of liquid film thickness which results in a reduced amount of wave energy at the bottom. These results are in accord with those on wave frequency in the main pipe. In  $85^\circ$  inclined flow, it is evident the presence of a second peak at lower frequency (2 Hz). This means that, at this inclination, there is a high distribution of energy to waves of lower frequency and not only to the disturbance waves. These waves are called substrate waves and have lower amplitude.

Figures 5.2.40 and 5.2.41 show respectively the variation of frequency with the liquid mass flowrate and the angle of inclination. Figure 5.2.42 shows the correlation Strouhal number/Lockhart-Martinelli parameter correlation applied to the wave frequency.

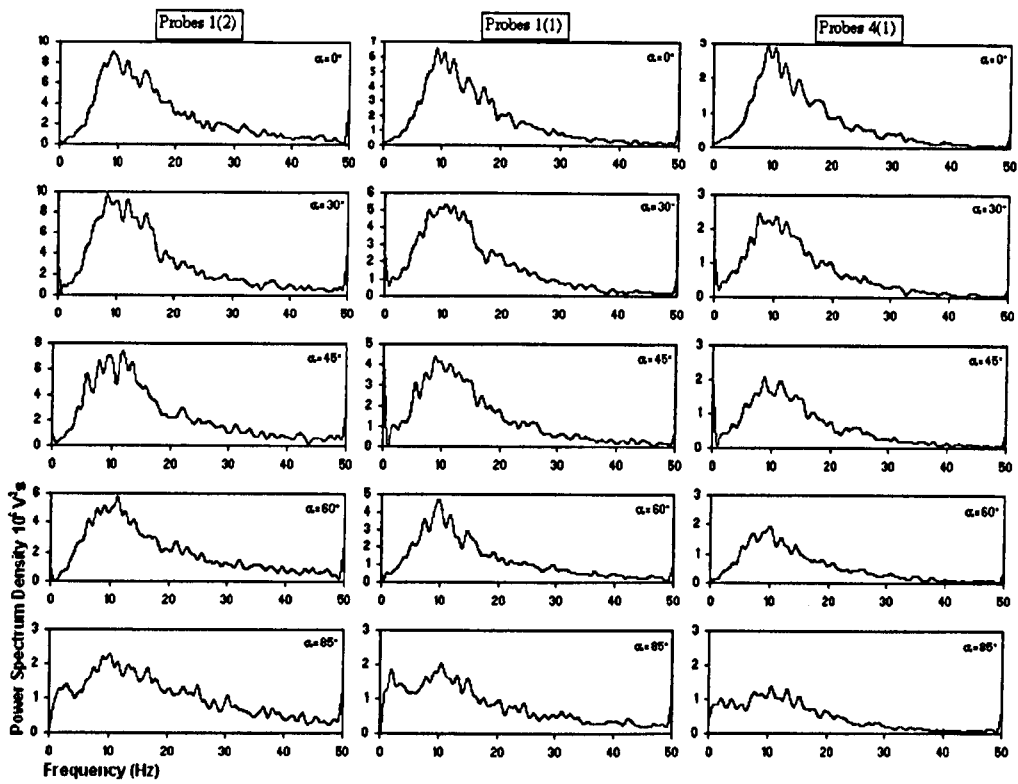


Figure 5.2.39: Effect of inclination on power spectrum density along the lower part of the throat. Gas mass flowrate=0.04 kg/s, liquid mass flowrate=0.0131 kg/s

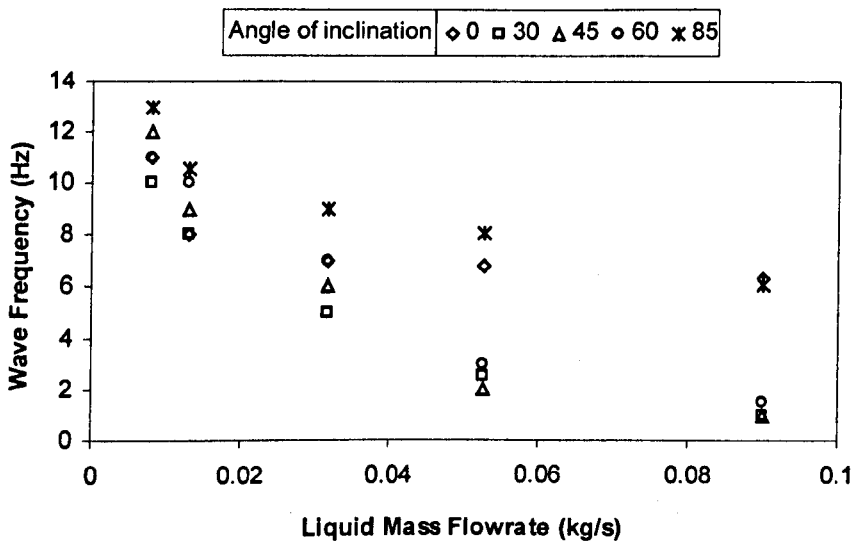


Figure 5.2.40: Frequency variation with liquid mass flowrate. Gas mass flowrate=0.04 kg/s

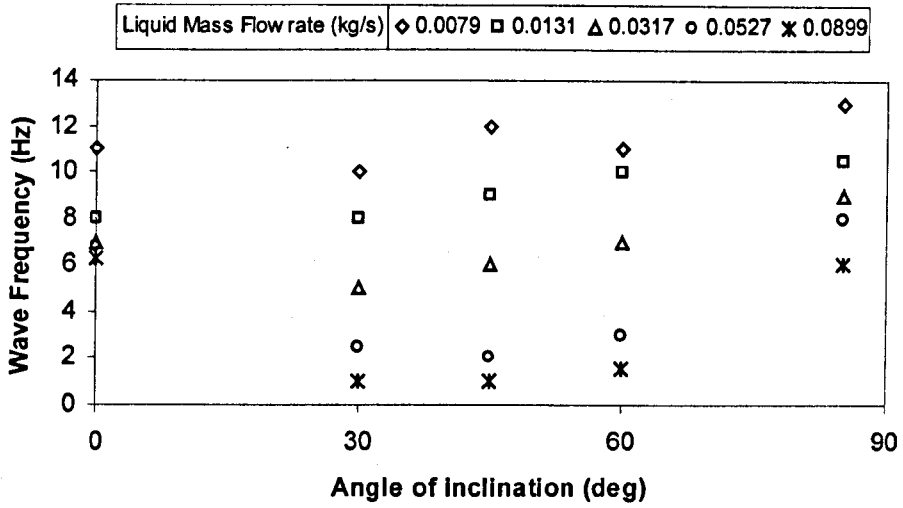


Figure 5.2.41: Frequency variation with angle of inclination from horizontal. Gas mass flowrate=0.04 kg/s

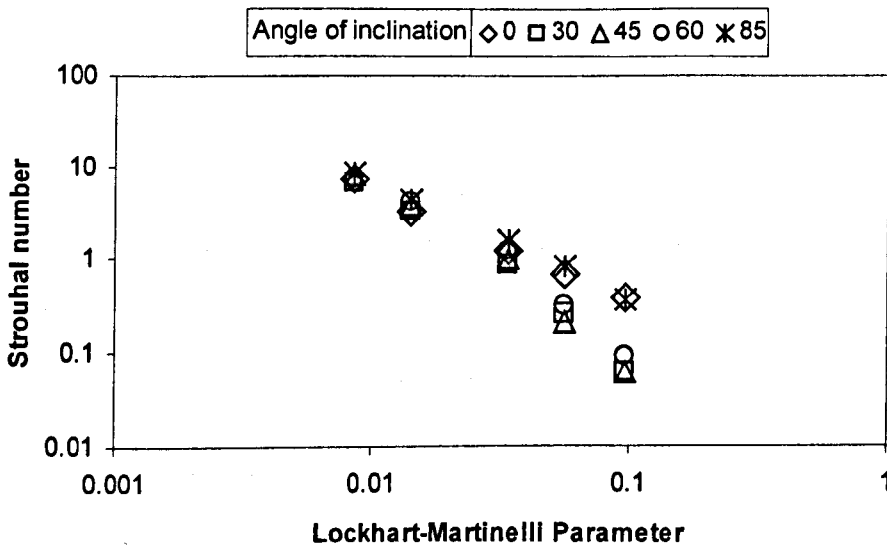


Figure 5.2.42: Liquid based Strouhal number plotted against Lockhart-Martinelli parameter in the throat section

Figure 5.2.40 shows that the frequency decreases with liquid mass flowrate for the five inclinations studied. In horizontal and 85° inclined flow, the frequency reaches a plateau. For the inclinations of 30°, 45° and 60°, the frequency decreases monotonically with liquid mass flowrate. For the same reasons discussed with regard to the main pipe, wave frequency is higher in horizontal and 85° inclined flow at higher liquid rates, figure 5.2.41. Figure 5.2.42 shows that the experimental data obtained in the throat are in accord with Strouhal number/Lockhart-Martinelli parameter correlation: as well as the data of the main pipe, they lie on one line. However, it is evident a slight deviation from straight line of the three profiles obtained at the pipe inclinations of 30°, 45° and 60°. This is a consequence of the effect of the liquid mass flowrate on wave frequency shown in figure 5.2.40.

The standard deviation RMS of the film thickness in the throat changes with the circumferential position as well as in the main pipe. However, changes are more regular in the throat. The reason is that the film thickness was measured only by flush-mounted probe technique and, therefore, the characteristics of measurement were similar, e.g. input and output ranges, sensitivity, saturation and non-linearity.

As well as in the main pipe, RMS is higher at the bottom where the liquid height fluctuations are higher and it is lower at the top where the film is less disturbed, figure 5.2.43. The effect of the liquid flowrate is also relevant. RMS increases with liquid mass flowrate, especially at the bottom. Therefore, the standard deviation shows the same trends of the film thickness. This implies that the large disturbance waves are mainly responsible for the magnitude of RMS of the fluctuating liquid layer. Moreover, the standard deviation tends to become more uniform with increasing inclination, figure 5.2.44. However, the effect of the inclination is smaller than in the main pipe.

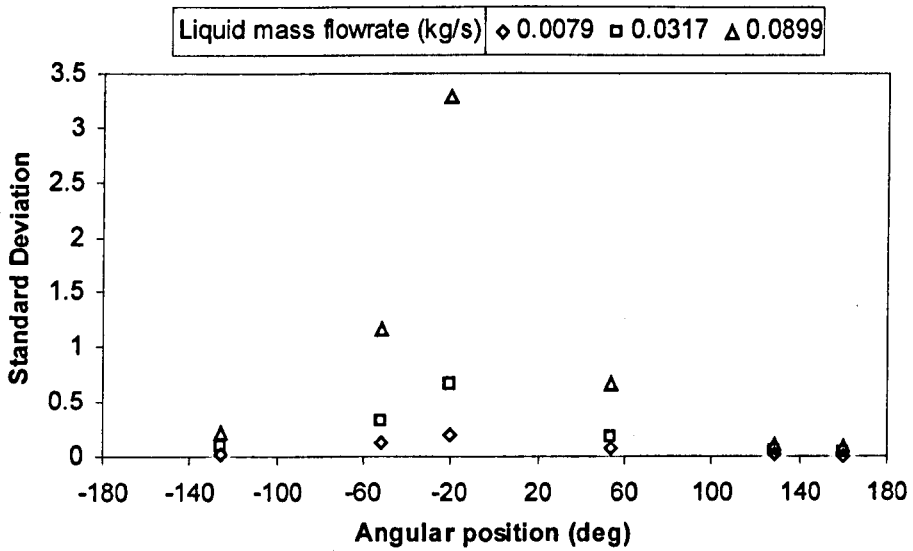


Figure 5.2.43: Variation of RMS with liquid mass flowrate. Gas mass flowrate=0.04 kg/s, angle of inclination from horizontal=60°

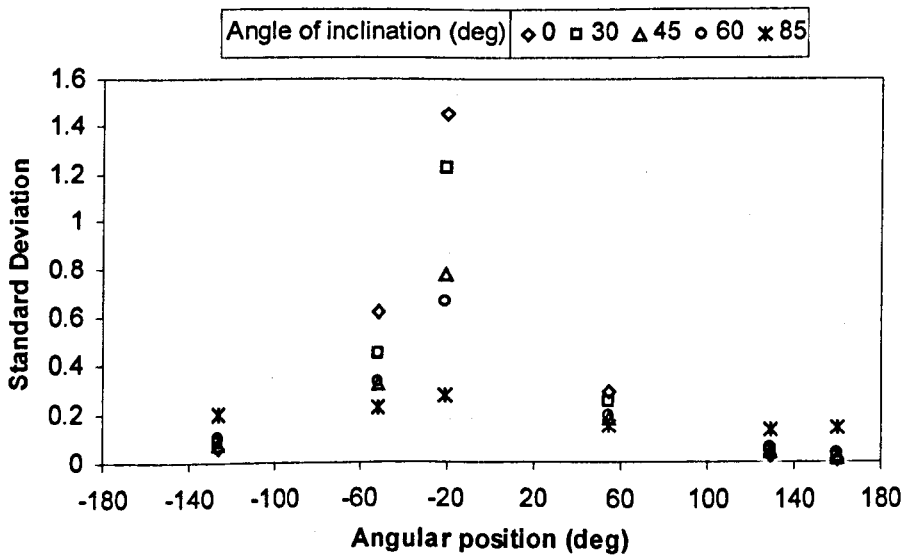
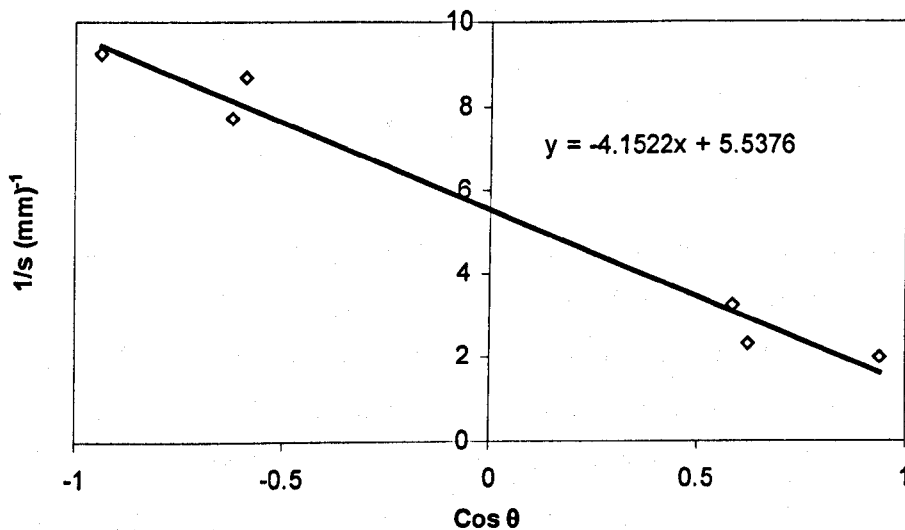
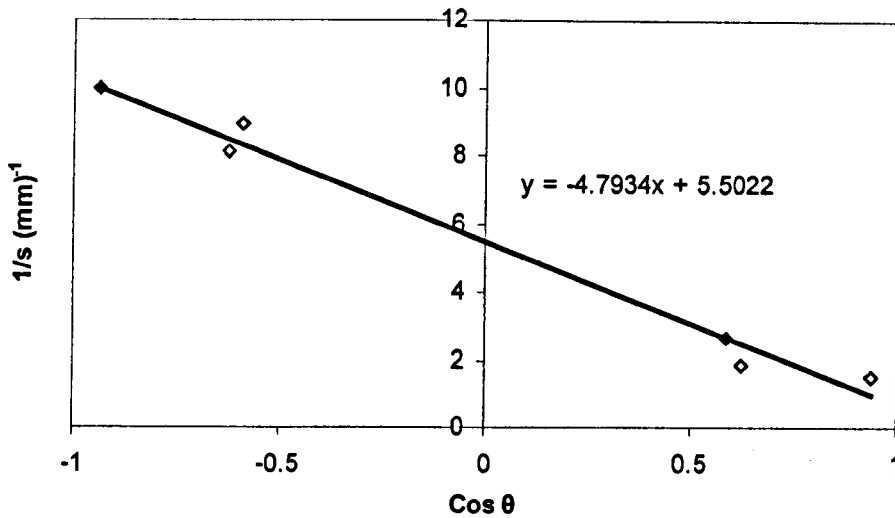


Figure 5.2.44: Variation of standard deviation RMS with angle of inclination from horizontal. Gas mass flowrate=0.04 kg/s, liquid mass flowrate=0.0079 kg/s

In figures 5.2.45 and 5.2.46 the inverse of the film thickness  $1/s$  is plotted against  $\cos\theta$  for two sets of flow conditions. It can be seen that there is a good agreement between the model of Butterworth (1969) and the experimental data. The above model predicts that the plot of  $1/s$  against  $\cos\theta$  is a straight line (equation 2.60 in Chapter 2). The experimental results approximately obey this relationship. In the throat section the slopes of these lines, which give the values of the coefficient  $a$ , are approximately  $4 \text{ (mm)}^{-1}$  for the first set of flow condition and  $4.64 \text{ (mm)}^{-1}$  for the second one. A comparison of this model with the experimental data gives the values of the circumferential transport coefficients, which are  $k=9 \text{ mm}$  for the first set of flow condition and  $k=10.47$  for the second one.



**Figure 5.2.45:** Profile of  $1/s$  plotted against  $\cos\theta$  in the throat section. Gas mass flowrate=0.04 kg/s, liquid mass flowrate=0.0131 kg/s, angle of inclination from horizontal= $0^\circ$



**Figure 5.2.46:** Profile of  $1/s$  plotted against  $\cos\theta$  in the throat section. Gas mass flowrate=0.03 kg/s, liquid mass flowrate=0.0131 kg/s, angle of inclination from horizontal=0

### 5.2.1 Results in slightly inclined Venturi.

Small inclinations could have a noticeable effect on the inlet-throat differential pressure as well as on the total pressure loss. This effect has not been studied in the previous researches. Therefore, experimental data on film thickness and pressure drop in slightly inclined Venturi have been gathered. Inclinations smaller than half of the angle of the diffuser ( $2.3^\circ$ ) have been chosen, e.g.,  $2^\circ$  upwards and  $2^\circ$  downwards. The results on film thickness are reported in this section.

The figures 5.2.47 and 5.2.48 show the liquid film thickness variation with  $M_l$  in the throat respectively for  $2^\circ$  upwards and  $2^\circ$  downwards. Figures 5.2.49 shows the liquid film thickness variation with the inclination,  $\alpha$ . Figures 5.2.50 and 5.2.51 show the liquid film thickness variation with the liquid mass flowrate,  $M_g$ .

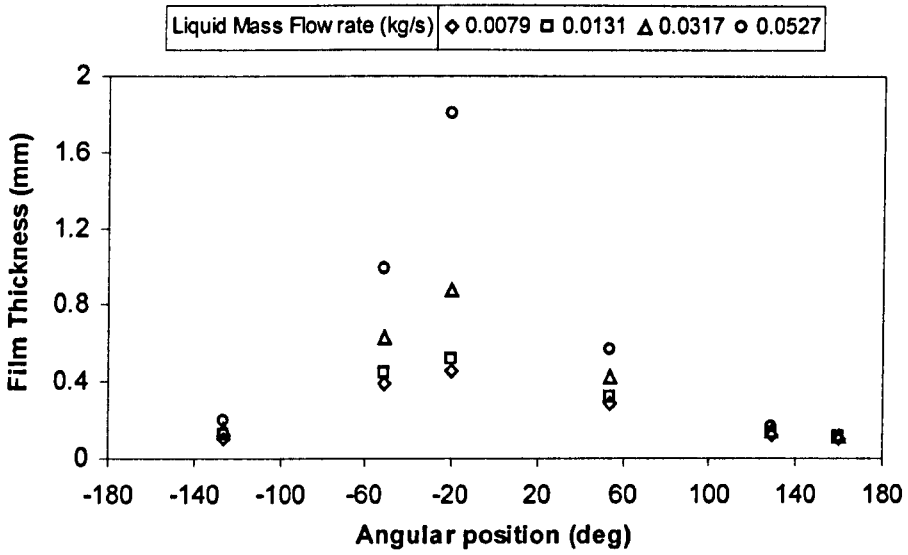


**Figure 5.2.47:** Effect of liquid mass flowrate on the liquid film thickness distribution in the throat. Gas mass flowrate=0.04 kg/s, angle of inclination from horizontal=2° downwards

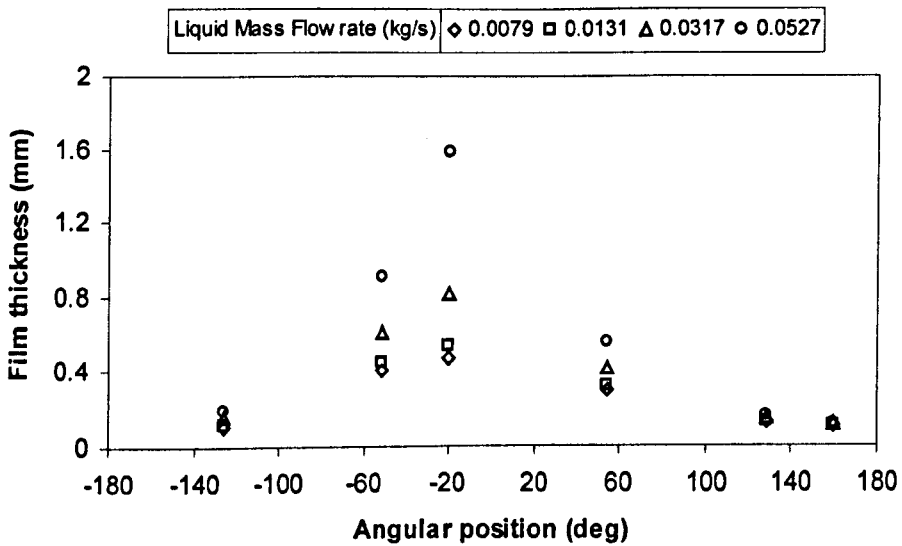


**Figure 5.2.48:** Effect of liquid mass flowrate on the liquid film thickness distribution in the throat. Gas mass flowrate=0.04 kg/s, angle of inclination from horizontal=2° upwards

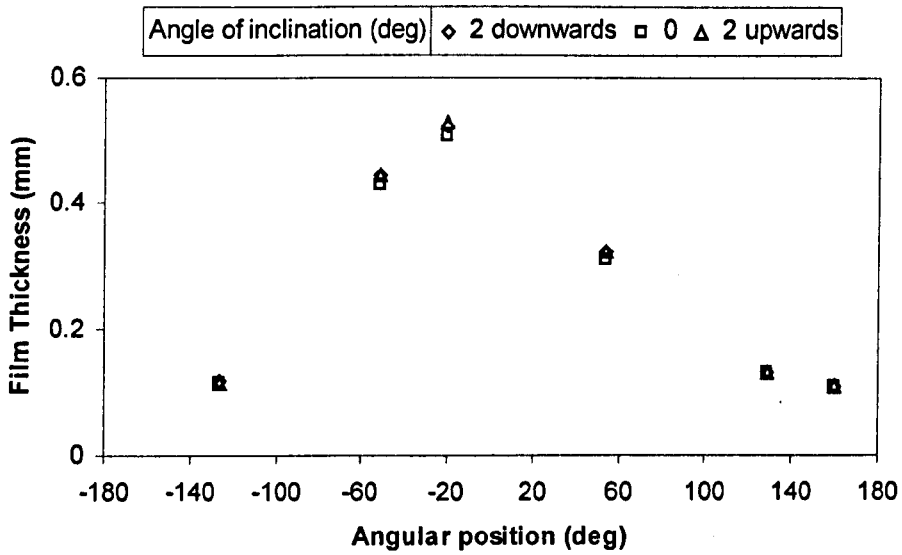


Figure 5.2.49: Liquid film thickness variation with angle of inclination from horizontal. Gas mass flowrate=0.04 kg/s, liquid mass flowrate=0.0131 kg/s

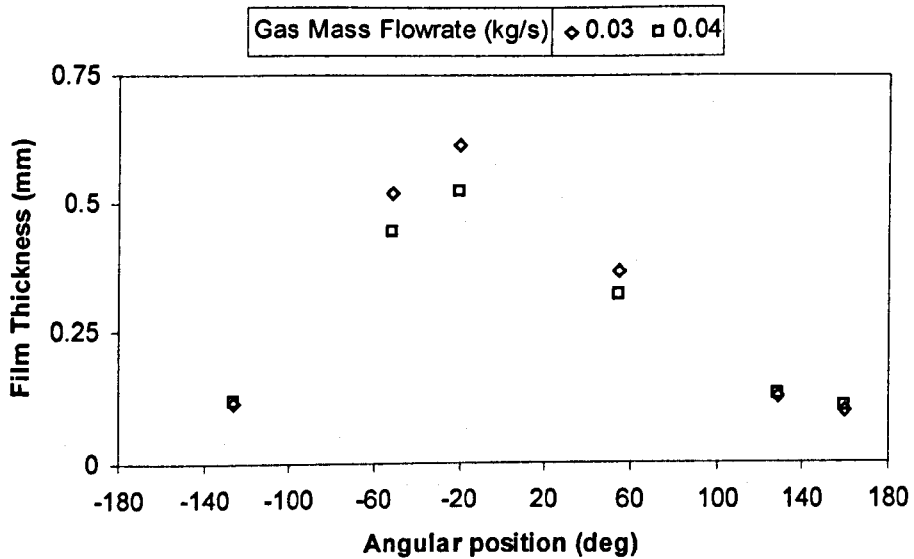
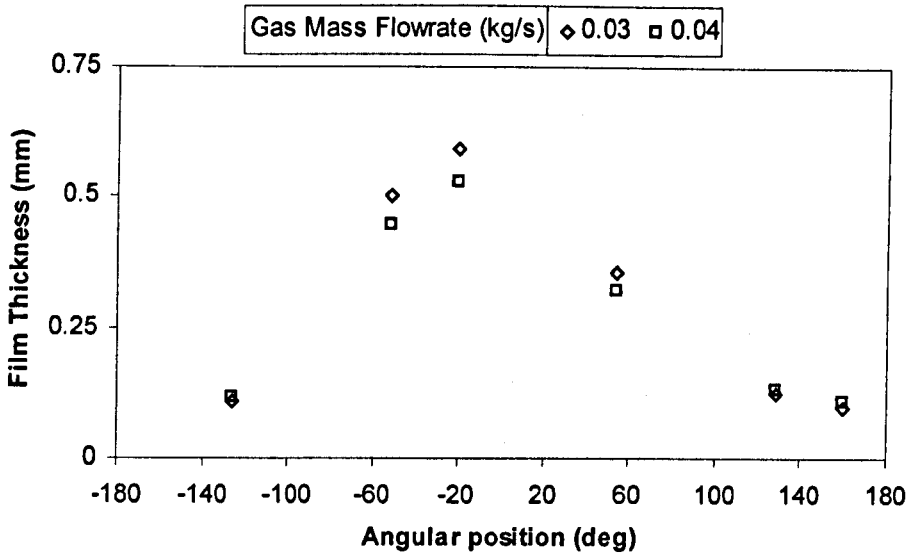


Figure 5.2.50: Liquid film thickness variation with gas mass flowrate. Liquid mass flowrate=0.0131 kg/s, angle of inclination from horizontal=2 downwards



**Figure 5.2.51:** Liquid film thickness variation with gas mass flowrate. Liquid mass flowrate=0.0131 kg/s, angle of inclination from horizontal=2 upwards

Figures 5.2.47 and 5.2.48 show that the film thickness distribution changes with liquid mass flowrate,  $M_l$ . By increasing  $M_l$  the annular film becomes higher especially at the bottom of the pipe. This agrees with the conclusions achieved for the other inclinations, figures 5.2.10 to 5.2.14.

Figure 5.2.49 does not show clearly the variation of the film distribution with the pipe inclination,  $\alpha$ . This is due to the small range of inclinations considered.

Figures 5.2.50 and 5.2.51 show that the uniformity of the liquid film circumferential distribution is slightly higher as the gas mass flowrate is increased. This agrees with the conclusions achieved for the other inclinations, figures 5.2.15 to 5.2.18.

### 5.3 Modelling of liquid film thickness

In this section, a comparison between the liquid film thickness results and the model developed by Fukano & Ousaka (1989) is discussed. This model was not applied to the throat because in this short section the flow is not considered as fully developed.

The model of Fukano & Ousaka (1989), developed to predict the circumferential film thickness distribution in horizontal and near horizontal annular two-phase flows, is based on the theory of disturbance wave flow which consists of disturbance waves and a base film. The liquid is transferred in the circumferential direction by the pumping action of disturbance waves, which counteracts the drainage due to gravity. Moreover, the model assumes that the effect of the secondary flow in the gas flow on the interfacial shear stress and the surface tension force have minor effect on the formation of the liquid film near the top of the tube cross section.

Fukano & Ousaka (1989) assumed that the disturbance waves are propagated in the axial direction by the pressure difference between the rear and the front of the disturbance waves. The height of the disturbance waves is greater near the bottom of the pipe and smaller near the top. The crest of the disturbance waves juts into the gas flow with a higher velocity at the bottom of the tube than at the top. On the other hand, the gas flow breaks up in the region of the disturbance waves. Therefore, the static pressure rise caused by the stagnation of the gas flow behind the disturbance wave is larger at the bottom and decreases towards the top. Hence, a negative pressure gradient is generated along the disturbance wave from the bottom to the top. Due to this pressure gradient the liquid included in the disturbance waves is pumped up towards the top. At the same time, part of the pumped up liquid is discharged continuously behind the disturbance waves and forms the base film. As a result, the disturbance wave gradually reduces in scale towards the top of the pipe. Liquid in the base film drains into the bottom and is reabsorbed into the next disturbance wave.

The model of Fukano and Ousaka (1989) is based on the numerical solution of a set of ordinary differential equations derived by integrating the mass and moment conservation equations from the wall to the interface. Constitutive equations, some of which are based on experimental data in horizontal annular flow while others are extensions of results in vertical annular flow, are used for the estimation of basic quantities such as rates of entrainment and deposition, internal shear stress. The equations are reduced to the form

$$c_1T_1 + c_2T_2 + c_3T_3 + c_4T_4 = c_5T_5 \quad (5.3)$$

where  $T_{1-4}$  are terms modelling the contribution of each mechanism: surface tension, interfacial shear stress due to secondary flow in the gas, wave spreading and entrainment and deposition. The sum of these is balanced by the drainage term,  $T_5$ . In this model, the term of interfacial stress due to secondary flow in the gas is neglected and all but one constant are fixed.

The model requires the value of the film thickness at the bottom. However, the values of the constants are changed from one set of conditions to another to provide good agreement. Another limitation is that the model does not consider either frequency of the interfacial waves or the mean film thickness. A curious result of this is that, for a given set of flow conditions, the model predicts that the drainage is always nearly exactly balanced by the pumping action, whereas for the same conditions, the model of Laurinat *et al.* (1985) shows that it is the secondary flow mechanism which is dominant, Fukano & Ousaka (1989).

Figures 5.3.1 and 5.3.2 show comparisons between liquid circumferential distributions predicted by the model of Fukano & Ousaka (1989) and those obtained from the experimental data.

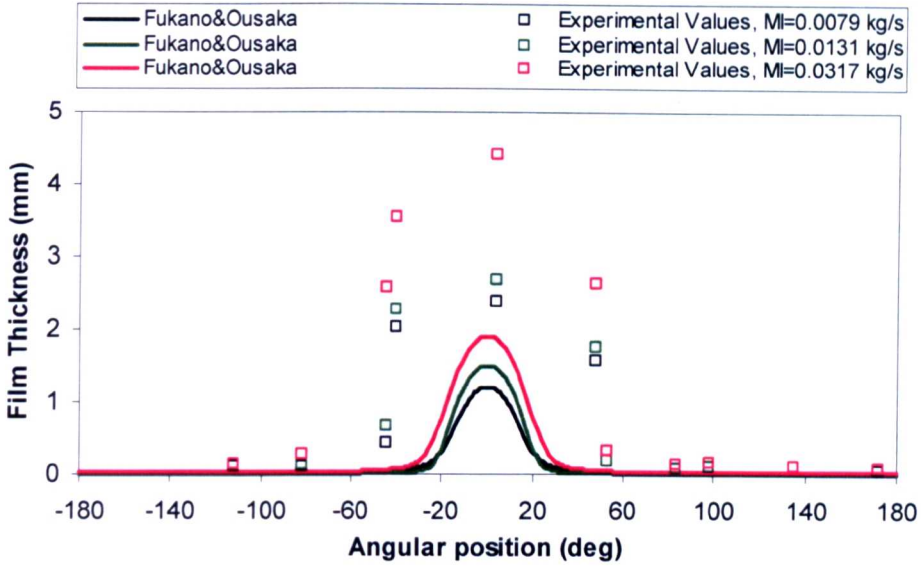


**Figure 5.3.1:** Comparison between experimental data and the model of Fukano and Ousaka (1989). Gas mass flowrate = 0.04 kg/s, angle of inclination from horizontal = 0°

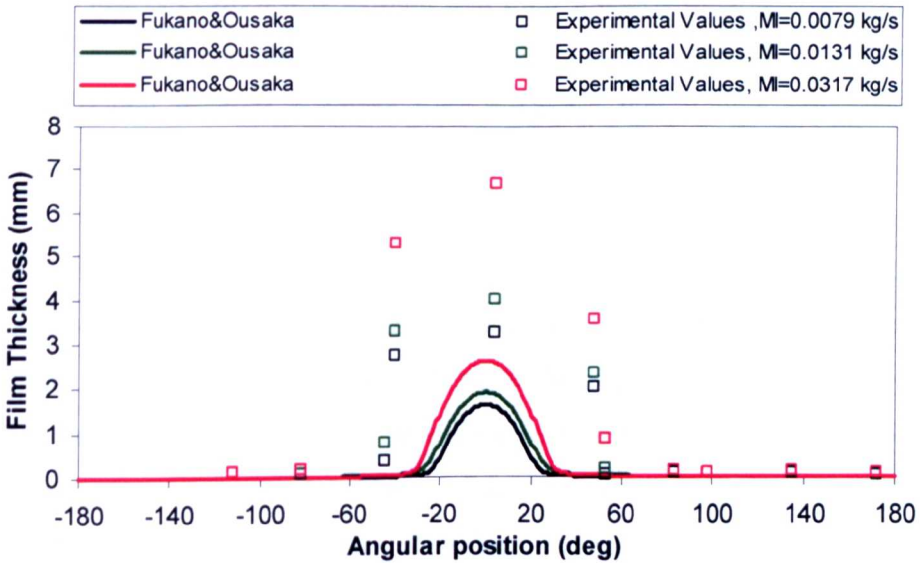


**Figure 5.3.2:** Comparison between experimental data and the model of Fukano and Ousaka (1989). Gas mass flowrate = 0.03 kg/s, angle of inclination from horizontal = 0°

Figures 5.3.1 and 5.3.2 show that the model under predicts the liquid film thickness around the main pipe, especially at the lower half of the pipe. In particular, the model predicts a film thickness at the bottom two times smaller than the experimental one. Also, the liquid film thickness variation from the bottom to the sides of the pipe is different. In fact, the predicted profiles present a dominant film height at the very bottom followed by a dramatic decrease from the bottom to the circumferential location of  $30^\circ$ . From  $30^\circ$  to the top the film is very thin with height of the order of 0.01 mm. Thus, the film thickness predicted by this model seems to define a stratified or semi-annular rather than annular flow. In this case, the very thin film at the upper part could indicate a wall wetted by ripples coming from the entrained liquid and not a permanent and moving liquid film. This is not surprising if it is considered that, in the flow pattern map of Taitel & Dukler (1976), the liquid and gas velocities considered result in a region of annular flow close to the region of stratified wavy flow.

In Fukano & Ousaka (1989), it is evident that their model works satisfactorily with gas velocities  $U_{sg} \geq 30$  m/s. However, figures 5.3.1 and 5.3.2 show that, at lower gas velocity, the model predicts a lower film thickness than found experimentally. Moreover, this under-prediction increases with decreasing gas velocity.

From the computational work it is deduced that the model does not predict satisfactorily because is unable to obtain a balance between the liquid mass flowrate given as input and the liquid mass flowrate obtained from the liquid circumferential distribution predicted on the basis of the experimental film thickness at the bottom. In other words, the mass flowrate obtained from the value of the experimental film thickness at the bottom results bigger. Therefore, the input film thickness has to be reduced until the mass balance is achieved and this reduction results in a considerable under-prediction of the model. Thus, it can be concluded that the model tends to work better with thinner liquid film at the bottom. This is due to the theoretical limitation of this model which does not consider either frequency of the interfacial

waves or mean film thickness. On the other hand, the present experimental data are based on time average film thickness, which is sensibly high due to the significant presence of large disturbance waves.

Moreover, the model is based on experimental data in horizontal annular flow and on extensions of results obtained in vertical annular flow. Therefore, inlet flow conditions and geometric characteristics different from those considered by Fukano & Ousaka (1989) are other possible reasons of the unsatisfactory predictions of the model.

## CHAPTER 6

### Pressure Drop Results

#### 6.1 Pressure drop in the Venturi

As with flow in straight pipes, the frictional pressure drop for gas-liquid flow in Venturi is larger than that for gas only flow due to the presence of disturbance waves and liquid entrained. This can be easily understood: as the average density of the fluid is higher than that of the gas alone, the  $\Delta p$  should be higher as well. However, the amount by which it is higher cannot be explained by the increase in average density alone. Experimental data have been used to find correlations, which describe this so-called "overreading" of orifices and Venturis for practical applications, see Chapter 1.

In this Chapter, results of measurements of the pressure profile along a Venturi, through which a gas-liquid mixture is flowing, are reported. In the experiments described, the effects of liquid flowrate and orientation of the Venturi were studied. The Venturi was positioned with its axis horizontal, at  $2^\circ$  upwards inclination, at  $2^\circ$  downwards inclination and at  $85^\circ$  upwards from the horizontal. The data were taken at a constant gas flowrate of 0.04 kg/s and at a gas pressure before the convergence

between 0.3 and 0.5 barg. This corresponds to a gas superficial velocity of 21.5 m/s in the pipe upstream of the Venturi and to a gas superficial velocity of 86.2 m/s in the Venturi throat. The liquid flowrates of 0.0079, 0.0187, 0.0317 and 0.0527 kg/s were examined. However, only 0.0079 and 0.0317 kg/s as well as gas only were considered in 85° inclined flow. Gas and liquid velocities were reproduced to an uncertainty respectively of 8.62 and 4.1 %. The error analysis conducted with the method of Taylor (1997) is shown in Appendix C. Tables of results on pressure drop are presented in the DVD enclosed with the thesis.

Ten tappings were positioned along the Venturi: 1 in the upstream pipe located 40 mm before the start of the convergence, 1 in the convergence, 2 in the throat, 5 in the diffuser and 1 in the downstream pipe. The tapping located in the upstream pipe is the reference one. The exact locations of the tappings are shown in figure 6.1.1

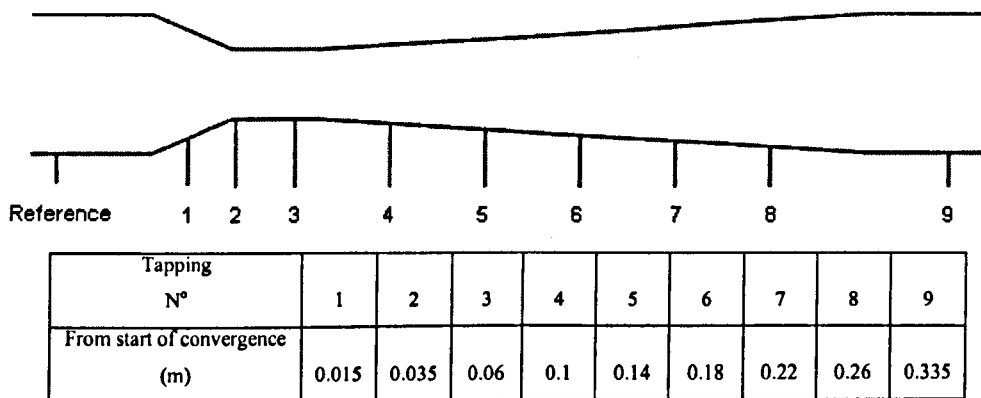


**Figure 6.1.1:** Positions of pressure tappings

Figures 6.1.2 to 6.1.5 show the effect of liquid mass flowrate on pressure drop in the Venturi. Figures 6.1.6 to 6.1.9 illustrate the effect of the pipe orientation. From the earliest researches (Johnstone *et al.*, 1954 or Lapple & Kamack, 1955) it has been recognised that the variations of pressure increase with liquid to gas ratio. The gas velocity has the effect of accelerating the liquid droplets, entrained in the gas, and it is

also responsible for the drag between the film and the gas. The transfer of momentum is generated by friction between the two phases and this friction is cause of energy dissipation. The deceleration of liquid is partially done in a similar way as the acceleration<sup>1</sup>, but it is largely generated by friction between the liquid and the wall. A higher liquid to gas ratio means more liquid to be accelerated and decelerated and this results in higher pressure variations and energy dissipations.

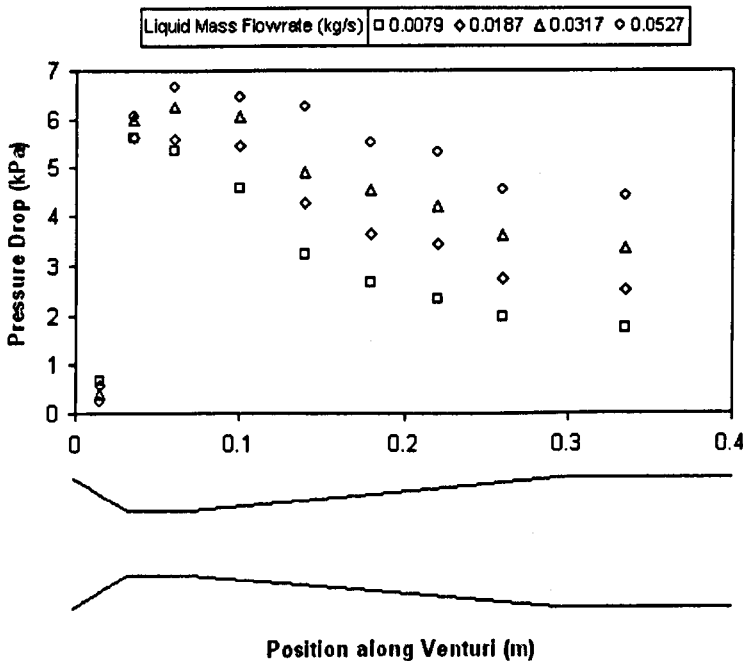


**Figure 6.1.2:** Effect Pressure drop along Venturi. Gas mass flowrate=0.04 kg/s, angle of inclination from horizontal=0°

<sup>1</sup> Mostly for the droplets.

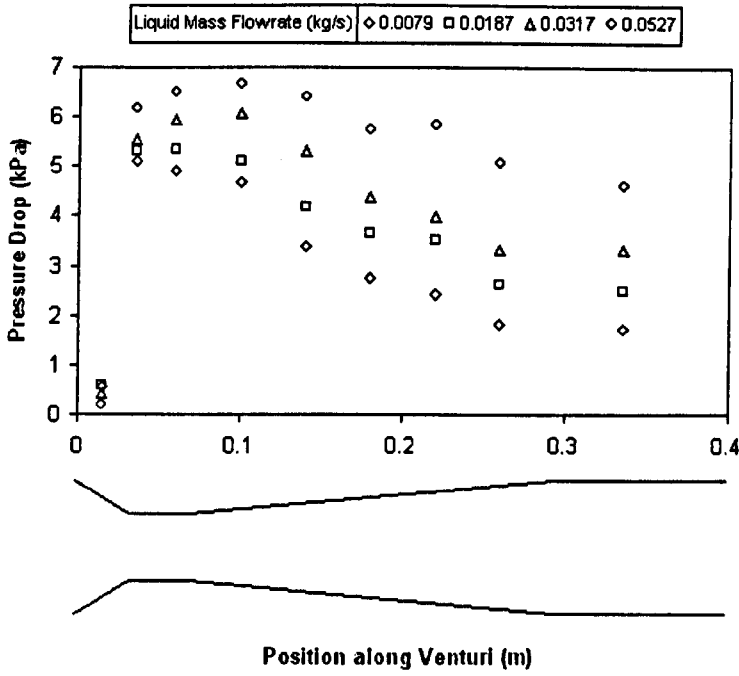


Figure 6.1.3: Pressure drop along Venturi. Gas mass flowrate=0.04 kg/s, angle of inclination from horizontal=2° upwards

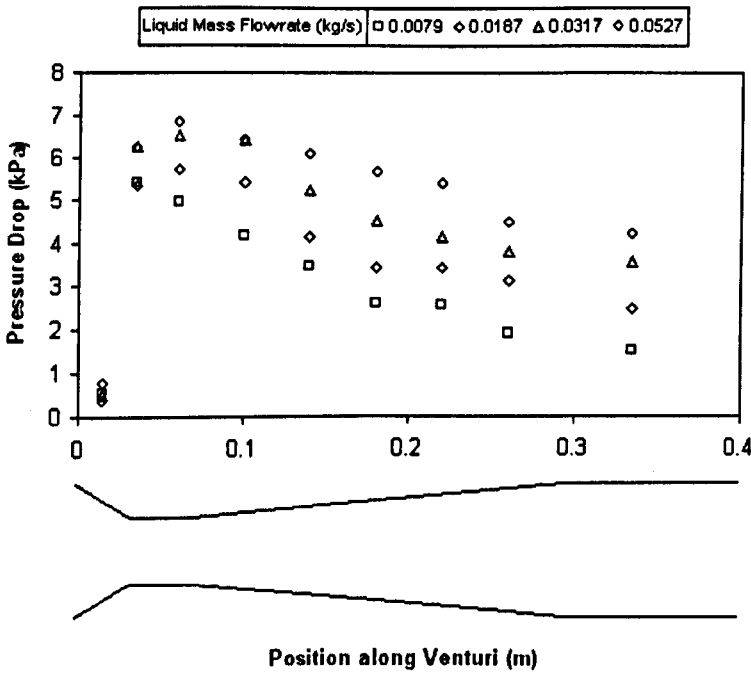


Figure 6.1.4: Pressure drop along Venturi. Gas mass flowrate=0.04 kg/s, angle of inclination from horizontal=2° downwards

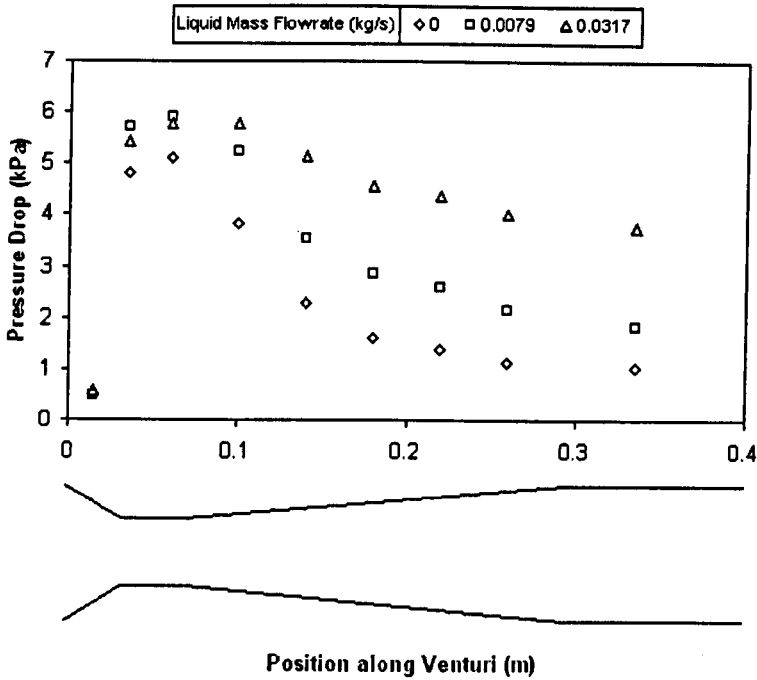


Figure 6.1.5: Pressure drop along Venturi. Gas mass flowrate=0.04 kg/s, angle of inclination from horizontal=85°

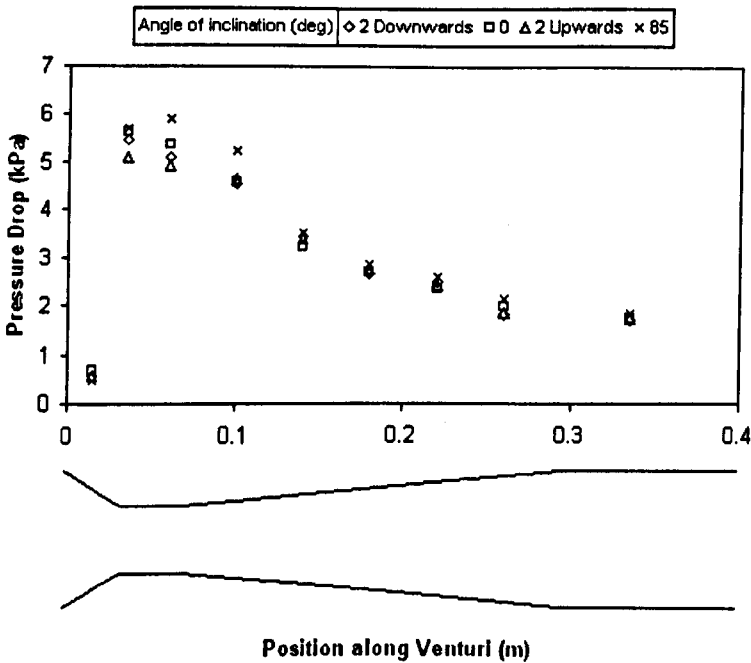


Figure 6.1.6: Effect of angle of inclination on pressure drop. Gas mass flowrate=0.04 kg/s, liquid mass flowrate=0.0079 kg/s

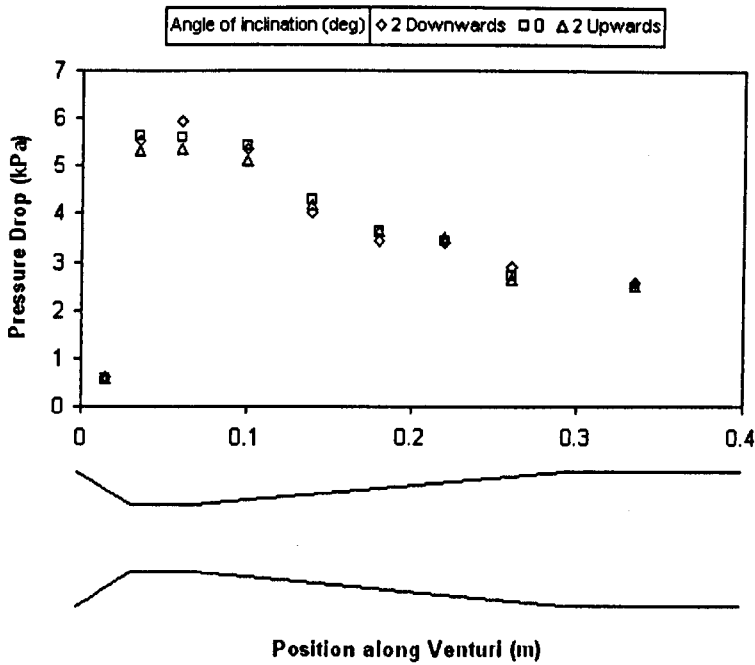


Figure 6.1.7: Effect of angle of inclination on pressure drop. Gas mass flowrate=0.04 kg/s, liquid mass flowrate=0.0187 kg/s

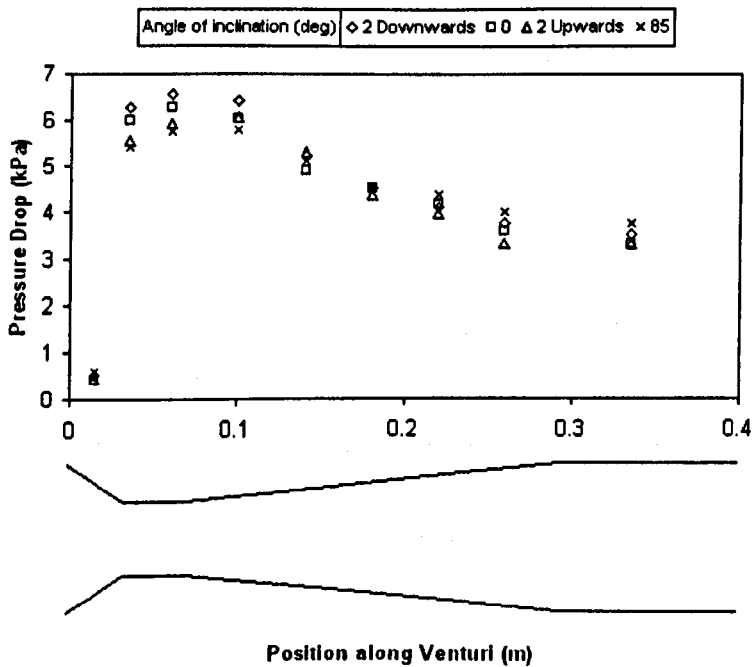
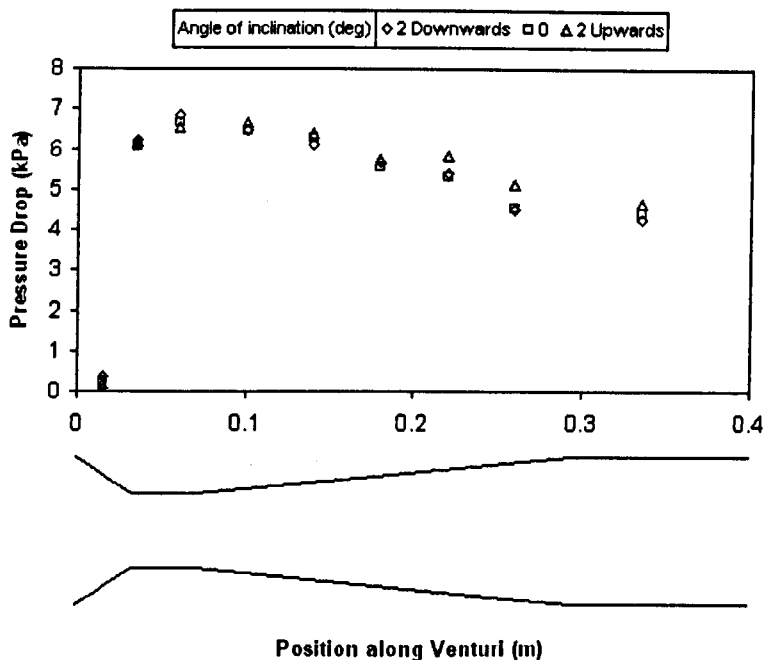


Figure 6.1.8: Effect of angle of inclination on pressure drop. Gas mass flowrate=0.04 kg/s, liquid mass flowrate=0.0317 kg/s



**Figure 6.1.9:** Effect of angle of inclination on pressure drop. Gas mass flowrate=0.04 kg/s, liquid mass flowrate=0.0527 kg/s

Parameters of significant interest are the total pressure drop and the pressure recovery of the Venturi. These have been extracted from the above data and are shown in figures 6.1.10 and 6.1.11. The total pressure drop is obtained as the difference between the reference pressure and the Venturi outlet pressure (pressure tapping n° 9). The pressure recovery is defined as the difference between the highest pressure drop which is the pressure drop at the throat and the Venturi outlet pressure (pressure tapping n° 9). These variables define a Venturi in terms of energy dissipation.

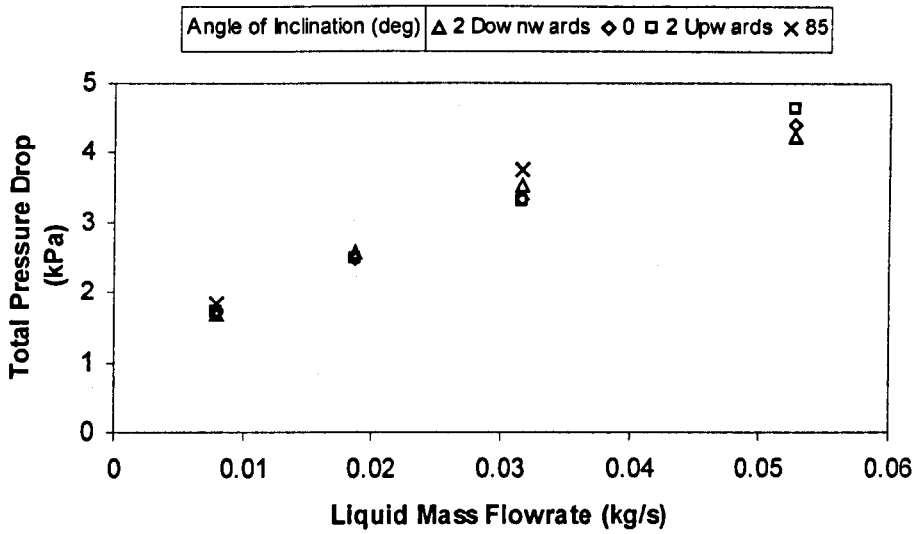


Figure 6.1.10: Effect of liquid mass flowrate on total pressure drop in Venturi. Gas mass flowrate=0.04 kg/s

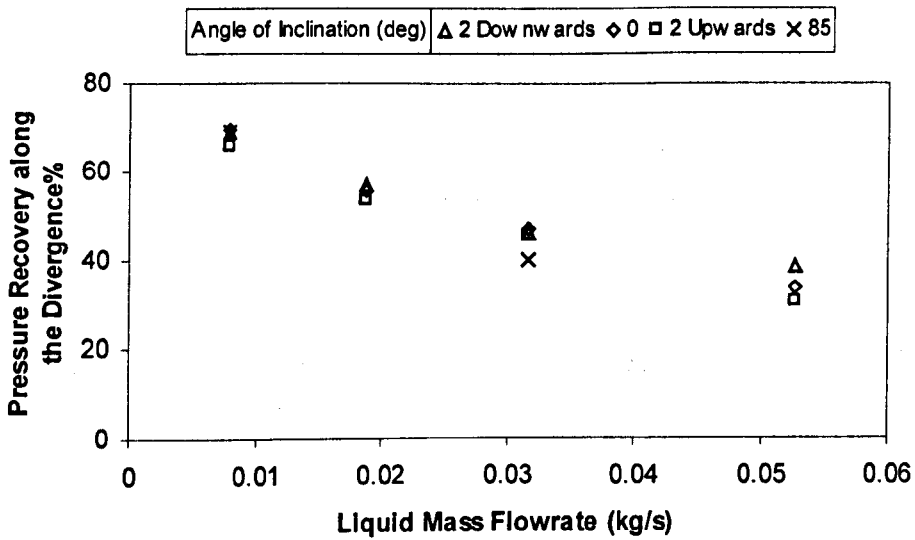


Figure 6.1.11: Effect of liquid mass flowrate on pressure recovery in the diffuser. Gas mass flowrate=0.04 kg/s

As shown in figures 6.1.2 to 6.1.5, the pressure variation in the Venturi is characterised by a sharp increase along the convergence, a small change along the throat and a slow decrease along the divergence. In the convergence, the gas is accelerated due the sudden restriction and this acceleration produces a big pressure change. Except for 85° inclined flow, at liquid flowrates lower than  $M_l = 0.0187$  kg/s the pressure along the throat decreases initially and increases afterwards. The reasons of this pressure behaviour are the low range of liquid flowrates and the influence of the diffuser on the throat. In fact, a low liquid flowrate results in a small amount of liquid to be accelerated. In addition, the short length of the throat and the presence of the diffuser downwards influence significantly the variation of pressure. As shown in figure 6.1.6, the pressure increases as soon as the flow reaches the diffuser. The presence of the divergence influences also the pressure of the gas travelling along the throat. The throat behaves as a “pre-diffuser” and, therefore, the pressure tends to increase slightly. The pressure behaviour described above is not shown in 85° inclined flow and at the other inclinations at liquid mass flowrate higher than  $M_l=0.0187$  kg/s. Figures 6.1.2 and 6.1.4 show that in these cases the pressure decreases monotonically along the entire throat section and the peak of the pressure drop profile shifts downstream. In vertical upward flow this is due to the positive contribution of the gravitational forces while at the other inclinations it is due to the higher liquid to gas ratio.

In the diffuser, the pressure recovery is expected due to the deceleration of gas and liquid droplets. Figures 6.1.2 to 6.1.5 show that the recovery is not complete and a consequently part of the energy is lost. It also shows that the recovery decreases with increasing liquid mass flowrate, figure 6.1.11. By increasing the liquid mass flowrate, the pressure recovery varies from the 70% to the 33% of the pressure drop at the throat. The gas acceleration in the convergent section is not a cause of permanent pressure loss. Also the pressure loss in the throat is negligible. The largest part of the permanent pressure loss is created in the divergent section of the Venturi due to the growth of boundary layer. This can result in the generation of

turbulence. The turbulence levels in the divergent section of the Venturi can be so high that flow reversal occurs. This causes dissipation of energy. The largest part of the permanent pressure loss is caused by the loss of kinetic energy of the liquid. The kinetic energy that the liquid had gained in the convergent section and the throat of the Venturi is not converted into pressure, but dissipated due to the friction with the gas, but mostly with the wall.

Azzopardi *et al.* (1989) shows that the effect of the orientation on the pressure profile is smaller at lower liquid mass flowrate and it is bigger when the liquid flowrate is increased, figure 6.1.12. They also show that the geometric characteristics of the Venturi influence the pressure variation. The smaller it is the diameter of the throat, the bigger it is the effect of the liquid mass flowrate. Figure 6.1.13 shows the effect of the liquid mass flowrate on the pressure drop at the throats of two different Venturis. The internal diameters of the two Venturi throats were 0.010 and 0.019 m. The pipe upstream of the Venturis had internal diameter of 0.032 m. It can be observed that the effect of the liquid mass flowrate is insignificant in the Venturi with smaller throat diameter. The Venturi considered in the present study has a throat internal diameter only two times smaller than the internal diameter of the main pipe and this ratio does not have a big effect on the variation of pressure drop with liquid mass flowrate.

Figures 6.1.6 to 6.1.9 show that the pressure profile does not vary considerably when the inclination is moved from horizontal to 85° inclined. To understand the reason of this, it is important to illustrate the influence of disturbance waves and liquid entrained on pressure drop. Frequency and amplitude of waves influence the pressure behaviour. The higher these characteristics are, the higher it is the interaction between gas and liquid. In general, the frequency would be expected decreasing with increasing inclination. In fact, the liquid is less easily moved in inclined upwards pipe than in horizontal. However, the study in Chapter 5 shows that at low liquid mass flowrate ( $M_l < 0.0317$  kg/s) the frequency is the same in horizontal and 85°

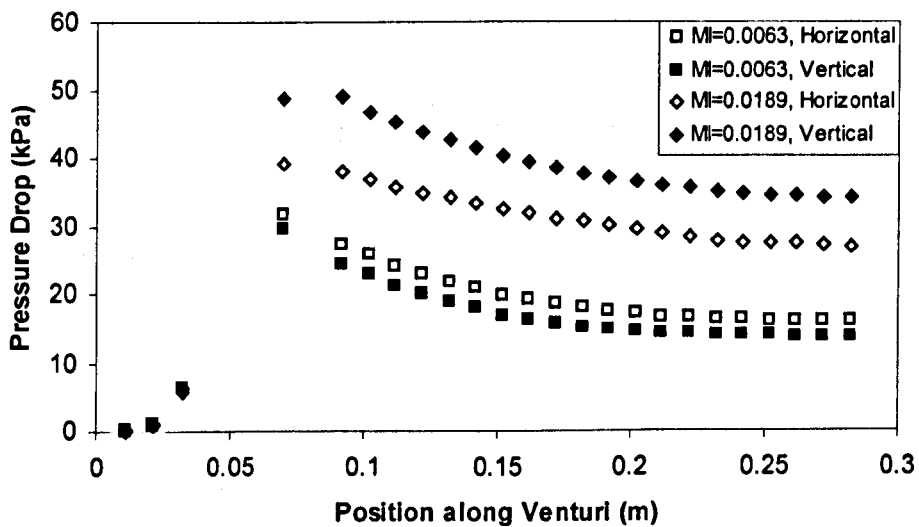
inclined flow, figure 5.1.26. The reason is that, in  $85^\circ$  inclined flow, the more uniform distribution of liquid around the channel facilitates the formation of new waves and counteracts the opposing action of gravity.

The liquid entrainment is another aspect that influences the pressure drop. A higher presence of liquid droplets in the gas core means, firstly, more friction between liquid and gas and secondly, more liquid to be accelerated. Chapter 4 shows that the liquid entrained has an insignificant variation with inclination. This is due to the phenomenon of wave spreading around the periphery. When the inclination is increased, the amplitude of waves decreases at the lower side of the pipe and, at the periphery, it is observed the formation of waves. Thus, the interaction between these new waves and the gas at the upper half of the pipe balances the lower interaction at the bottom. Therefore, although the shear between liquid and gas is higher in  $85^\circ$  inclined pipe, the total friction between waves and gas can be considered comparable. The fact that both wave frequency and liquid entrainment are not varying considerably with inclination is the reason of the pressure variations shown in figures 6.1.6 to 6.1.9. Pressure changes along Venturi are not remarkably influenced by pipe orientation at the gas mass flowrate of 0.04 kg/s and at the liquid mass flowrates included between 0.0079 and 0.0317 kg/s.

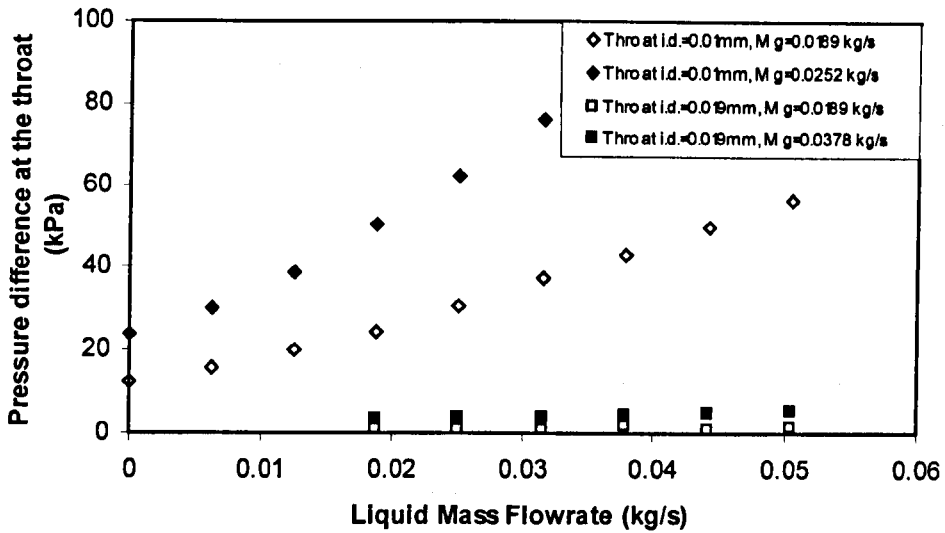
Figure 6.1.10 shows the variation of the total pressure drop with the liquid mass flowrate,  $M_l$ . The total pressure drop represents the total pressure loss across the Venturi. It can be seen that the pressure loss grows almost linearly. Figure 6.1.10 also shows the variation of the total pressure drop with inclination. The variation is zero at low liquid mass flowrates and small at higher values. As discussed previously, the reasons are the low range of liquid flowrates considered and the geometric characteristics of the Venturi.

Figure 6.1.11 shows the variation of the pressure recovery in the diffuser with the liquid mass flowrate. The pressure recovery decreases almost linearly. It is also

shown the variation of the pressure recovery with inclination. It is zero at low liquid mass flowrates and small at higher values.



**Figure 6.1.12:** Effect of liquid mass flowrate on pressure drop variations with inclination. Gas mass flowrate=0.0189 kg/s. Data taken from Azzopardi *et al.* (1989), Venturi A



**Figure 6.1.13:** Effect of Venturi geometrical characteristics on pressure difference at the throat for different flow conditions. Data taken from Azzopardi *et al.* (1989), Venturi A and D

## 6.2 Modelling of pressure drop in Venturi

In this section, it is presented and discussed a comparison between the experimental pressure drop and the model developed by Azzopardi & Co-workers (Azzopardi & Govan, 1984 and Azzopardi & Govan, 1985), including growth of the boundary layer in the diffuser (Azzopardi *et al.*, 1991).

Figures 6.2.1 and 6.2.2 show the agreement between the model of Azzopardi & Co-workers and the experimental data shown in Section 6.1. The model was not developed for the prediction of pressure drop at other inclinations. It can be observed that the model generally predicts higher pressure drops than found experimentally, especially at higher liquid mass flowrate. The model predicts well the pressure variation in the convergence. The pressure variation predicted across the throat is generally higher than the experimental values. Moreover, it predicts a pressure

decrease across this section also at low liquid mass flowrates. On the other hand, the experimental data show that the pressure increases at the same range of liquid velocities. The model does not perform satisfactorily also in the diffuser, predicting a higher pressure recovery. As the liquid velocity raises, the prediction of the model, in the throat and the diffuser, becomes less close to the experimental values. Thus, it appears that the model is capable of predicting the pressure variations for low liquid mass flowrate but it needs improvement for higher values, figure 6.2.3. Both experimental and predicted pressure profiles show that a higher liquid velocity has a higher effect on the pressure variations. As a rule of thumb, it can be said that a higher liquid mass flowrate results in higher pressure changes. Chapter 4 shows that a higher liquid mass flowrate has the effect to increase the entrained fraction. Therefore, the pressure variations increase with higher entrained fraction. This leads to the conclusion that the model of Azzopardi and Co-workers over-predicts the entrained fraction when the liquid mass flowrate is increased. This limitation is also discussed in Fernandez (2000).

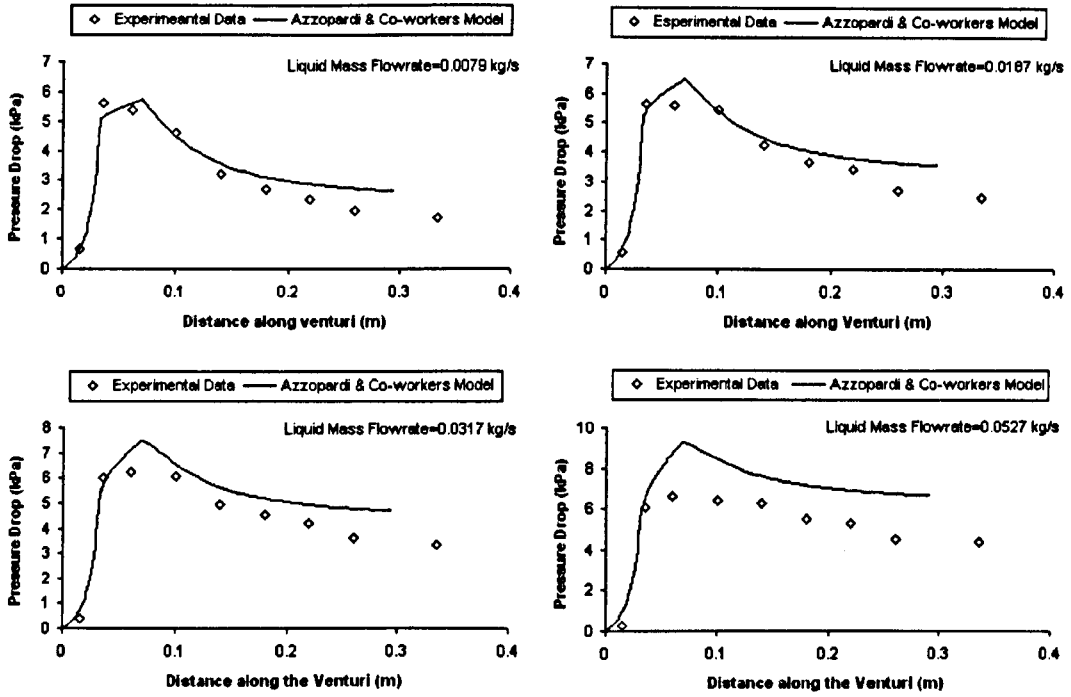


Figure 6.2.1: Comparison between experimental data and model of Azzopardi & Co-workers. Gas mass flowrate=0.04 kg/s, angle of inclination from horizontal=0°

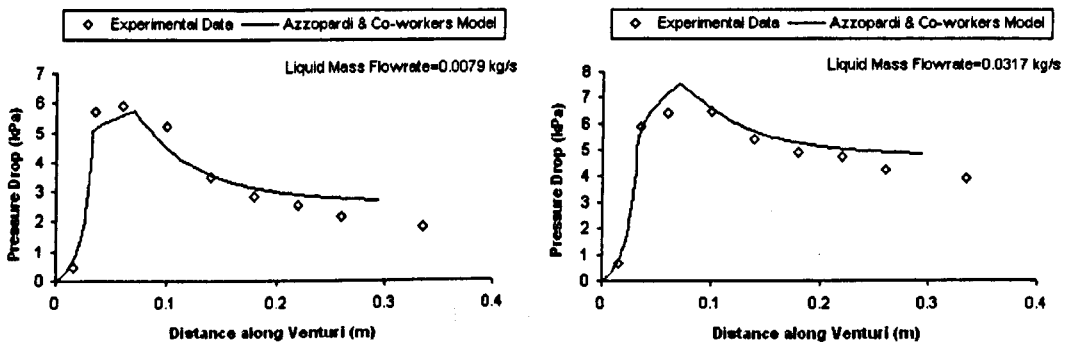


Figure 6.2.2: Comparison between experimental data and model of Azzopardi & Co-workers. Gas mass flowrate=0.04 kg/s, angle of inclination from horizontal=85°

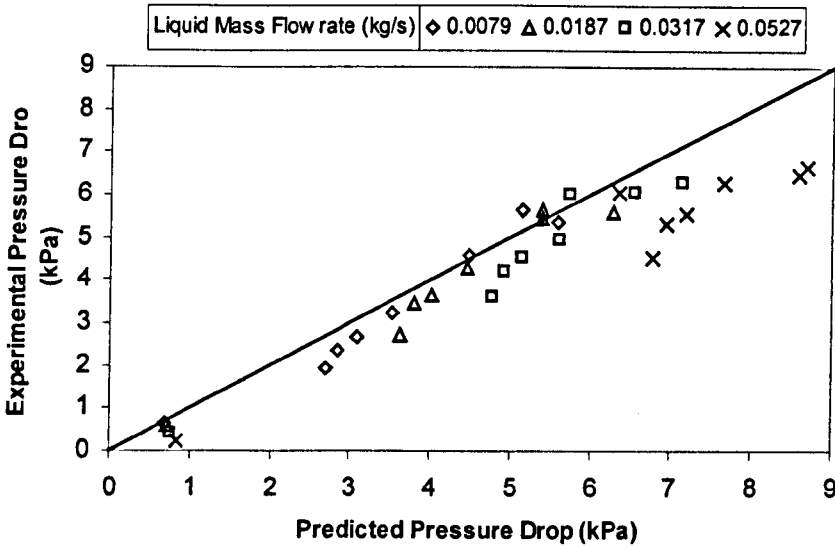


Figure 6.2.3: Comparison between experimental and predicted pressure drop. Gas mass flowrate=0.04 kg/s, angle of inclination from horizontal=0°

Figures 6.2.4 and 6.2.5 show the effect of liquid mass flowrate on predicted and experimental total pressure drop. It can be seen that both profiles grow linearly and that the model predicts a higher total pressure drop. Moreover, as the liquid velocity raises, the prediction of the model becomes less close to the experimental values.

Figures 6.2.6 and 6.2.7 show the effect of liquid mass flowrate on predicted and experimental pressure recovery. It can be seen that both profiles grow linearly and that the model predicts a lower pressure recovery. Moreover, as the liquid velocity is increased, the prediction of the model becomes closer to the experimental values.

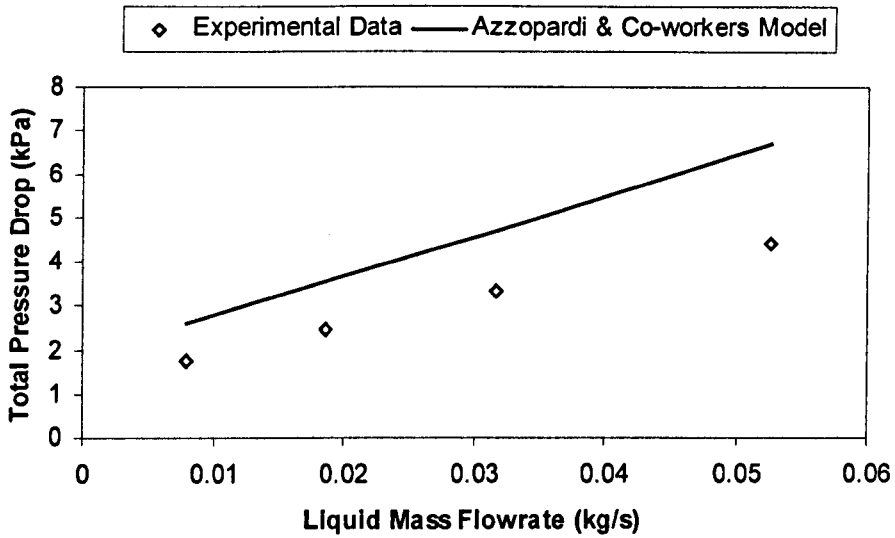


Figure 6.2.4: Comparison between experimental and predicted variation of total pressure drop with liquid mass flowrate. Gas mass flowrate=0.04 kg/s, angle of inclination from horizontal=0°

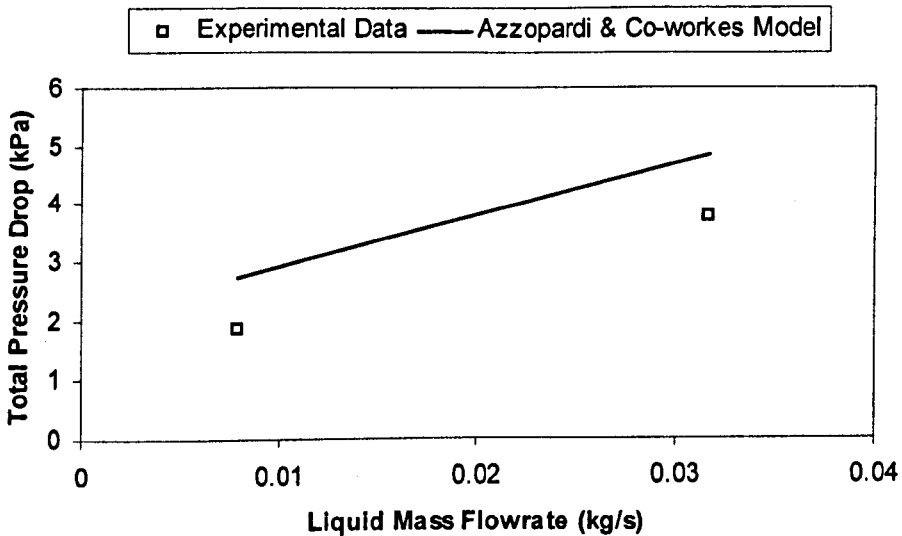
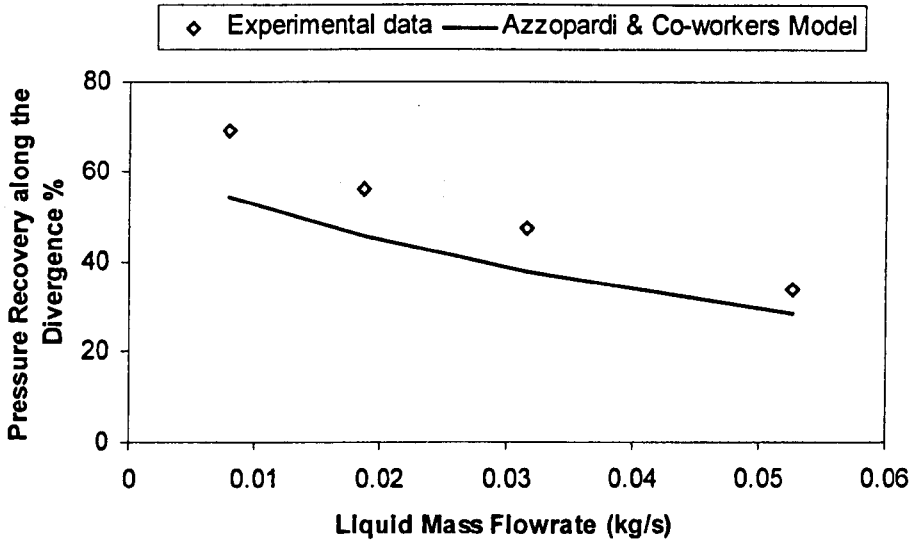
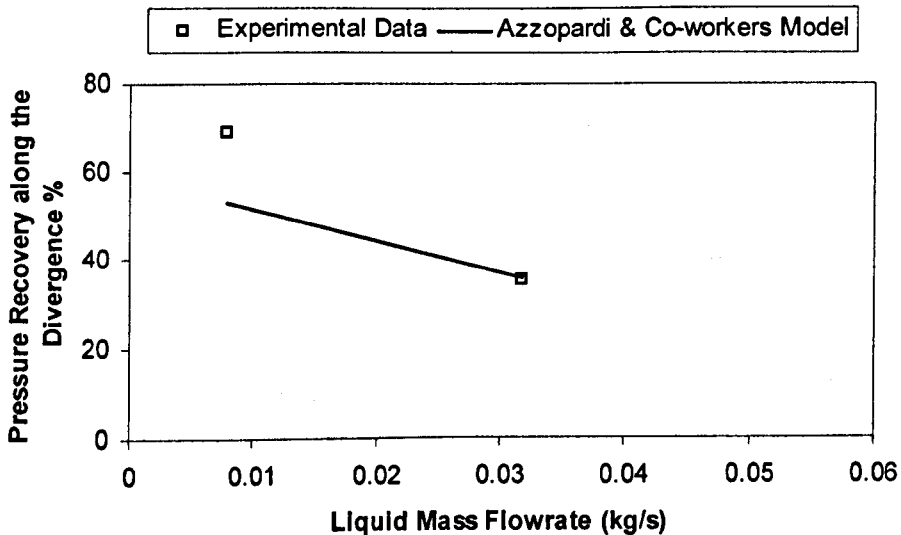


Figure 6.2.5: Comparison between experimental and predicted variation of total pressure drop with liquid mass flowrate. Gas mass flowrate=0.04 kg/s, angle of inclination from horizontal=85°



**Figure 6.2.6:** Comparison between experimental and predicted variation of pressure recovery with liquid mass flowrate. Gas mass flowrate=0.04 kg/s, angle of inclination from horizontal=0°



**Figure 6.2.7:** Comparison between experimental and predicted variation of pressure recovery with liquid mass flowrate. Gas mass flowrate=0.04 kg/s, angle of inclination from horizontal=85°

# CHAPTER 7

## Final conclusions

and

## Future Work

In this section the importance and the consequences of the work presented will be summarised. Further work related to the subject of the present study is also proposed.

### 7.1 Introduction

A comprehensive study of hydrodynamics in annular two-phase flow in Venturis has been presented in the previous Chapters. Experimental data on three different dependent variables (liquid film flowrate, film thickness and pressure drop) has given a good insight into the phenomena that occur in Venturis. This analysis was carried out by varying liquid and gas mass flowrates and inclination. Such a comprehensive study had not been carried out previous to the present work. The great amount of data collected gives an idea of the number of experimental tests carried out.

Literature on pressure drop, film thickness and entrained fraction in Venturis is available either for horizontal or vertical flows, but it is scarce for inclined flows. Special attention was paid to the effect of the inclination on the liquid film characteristics and the liquid entrainment. Therefore, it was necessary to conduct a comprehensive study considering different flow conditions and an extensive range of

inclinations. A wide range of experimental data was presented for this purpose. Additionally, data from other authors were introduced, discussed and compared to the present data. Results from other works concerning frequency of disturbance waves and entrained fraction were confirmed.

## **7.2 Conclusions for liquid film mass flowrate and entrainment determination**

- In the pipe upstream of the Venturi and in the throat of the Venturi, the liquid flowrate profile is symmetric about the vertical plane for zero. In a horizontal pipe, the liquid flows prevalently along the bottom. The variation of inclination from horizontal has the effect to distribute the liquid more uniformly around the cross-section.
- In the main pipe and in the Venturi throat, the entrained fraction is not influenced by pipe orientation and shows a horizontal linear profile at low gas and liquid mass flowrates. This is due to the fact that friction at the gas-liquid interface and wave frequency do not vary considerably with inclination at low ranges of gas and liquid velocities.
- In the main pipe and in the Venturi throat, the entrained fraction increases with increasing gas mass flowrate. As the gas velocity is increased, the amount of liquid droplets stripped off from the high waves increases. Consequently, the amplitude of the waves and, therefore, the average liquid film thickness decreases.

### 7.3 Conclusions for film thickness measurements

- In the pipe upstream of the Venturi and in the throat of the Venturi, the distribution of the liquid film is symmetric about the vertical plane for zero. In horizontal pipe, the liquid film thickness is higher at the bottom, it is decreasing along the two sides and it is lower at the top. The liquid distribution becomes more uniform with increasing inclination. At inclinations  $\alpha > 60^\circ$ , it is observed the formation of disturbance waves also at the side and at the top of the sections. Moreover, due to gravity, a little deviation from vertical, e.g.,  $5^\circ$  results in an asymmetric film thickness profile.
- In the main pipe and in the throat, an increase in gas velocity has the effect to flatten out the liquid film thickness. This is due to the higher interaction at the liquid-gas interface. The effects of the higher interaction are lower amplitudes of the disturbance waves and higher entrained fraction.
- The ratio between average wave height and base film thickness is the same in the main pipe and in the throat. This means that the fluctuating waves and the base film thickness have the same proportion in the two sections. However, the amplitude of the disturbance waves is different.
- For the same flow conditions and inclination, the frequency of the disturbance waves is the same at the lower half of the main pipe and the throat. Furthermore, the variation of the frequency with the liquid mass flowrate has the same trend. In other words, the frequency of the disturbance waves decreases equally in the two sections with increasing liquid velocity.
- The present data agrees with the model of Butterworth (1969). The above model predicts that the plot of  $1/s$  against  $\cos\theta$  is a straight line. The experimental results in the main pipe and in the Venturi throat approximately obey this relationship.

- The effect of the inclination on the liquid film mass flowrate  $M_{LF}$  is not significant. This is a consequence of the fact that the entrained fraction  $E$  does not change with the tube orientation.

#### **7.4 Conclusions for pressure profile and pressure drop studies**

- The experimental data give further evidence that pressure drop in the Venturi increases with increasing liquid to gas ratio.
- At low liquid flowrates the pressure along the throat decreases initially and increases afterwards due to the influence of the diffuser on this section.
- The effect of the inclination is not remarkable on the pressure drop. This is a consequence of the very small influence of the pipe orientation on the wave frequency and liquid entrainment.
- The total pressure loss across the Venturi grows almost linearly with the liquid mass flowrate. Furthermore, the pressure recovery decreases almost linearly with the liquid mass flowrate.
- The model of Azzopardi & Co-workers generally predicts higher pressure changes than found experimentally, especially at higher liquid mass flowrate. The model predicts satisfactorily the pressure variations in the convergence. As the liquid velocity is increased, the predictions of the model, in the throat and the diffuser, digress from the experimental values. The reason is that the model of Azzopardi & Co-workers over-predicts the entrained fraction when the liquid mass flowrate is increased.

## 7.5 Recommendations for future experimental work

- The Venturi should be made in transparent material (plexiglas) to allow visual observations of the annular flow. These could help in order to gather information on the liquid film, e.g., liquid distribution, film thickness and wave height. A straight pipe, also in plexiglas, should be located before the Venturi.
- Further experiments on pressure drop in the Venturi should be carried out. A wider variety of angles from horizontal to vertical should be explored experimentally. A further investigation would confirm the results found on the effect of the inclination on pressure drop.
- The effect of liquid mass flowrate on pressure drop should be investigated. A wide range of  $M_g$  would allow the analysis of the effect of gas velocity on total pressure loss and pressure recovery along the diffuser. Azzopardi *et al.* (1989) shows that an increasing gas flowrate results in an increasing pressure drop along the Venturi.
- The study of pressure drop in the Venturi with different liquids and gases would be of particular interest. This study would be particularly useful in the oil & gas industry applications of the Venturi as flow meter. In these applications liquids and gases have different properties from those involved in the present work.
- Measurements of liquid film thickness along the top of the main section by using the wire probe technique are required. This would allow a study of the characteristics of the film at higher liquid mass flowrates. Also, the same technique should be applied at the bottom of the throat section. This would allow a comparison with the results obtained at the two highest liquid mass flowrates by using the flush-mounted probe technique.
- Measurements of liquid film thickness at higher gas mass flowrates,  $M_g$ , are required. This would allow the study of the variation of the wave frequency

with  $M_g$ . Paras *et al.* (1994) shows that the dominant frequency of the waves displays a tendency to increase with gas mass flowrate. In their experimental data it is evident an almost linear dependence of the characteristic frequency on gas velocity, whereas the influence of liquid velocity appears to be of less significance. They also asserted that a class of frequency around 1 Hz persists, even at relatively high gas velocities. These waves may be associated with the Kelvin-Helmholtz instability.

- Future works could consider the use of another probe test section located upstream. This would allow the measurement of the liquid film velocity and of the wave celerity. Paras *et al.* (1994) shows that wave celerity increases markedly with the gas as well as with the liquid velocity. Also, it is evident a nearly linear dependence of wave celerity on gas velocity. This is observed also in the data of Andritsos (1992).
- Further study on liquid film mass flowrate considering a partial take-off unit with higher fins could be considered. A wider range of liquid mass flowrates would allow the analysis of the variation of the liquid entrainment with higher liquid film velocities. Butterworth and Pulling (1973) used inclined fins.
- The availability of data on film thickness and film flowrate would enable an interesting comparison of results. This study was not carried on because the measurements of the partial film flowrates were taken at circumferential locations different from those considered for the film thickness. Future work could consider more carefully this aspect.

## 7.6 Recommendations for future developments of models

- Further analysis of the process of atomisation at the corner between the convergence and the throat should be considered. This study would provide a closer insight into the phenomena that take place and, in particular, how exactly the liquid is entrained.
- The model of Azzopardi & co-workers needs improvements, especially at higher liquid mass flowrate,  $M_l$ . The model of Azzopardi & Co-workers reasonably predicts pressure drop in the Venturi for very different operating conditions. However, some recommendations can be made in order to improve this model. The part of the model concerning the growth of the boundary layer in the diffuser requires very complicated algorithms. In addition, some problems are encountered concerning the numerical solution of the equations of the boundary layer. Therefore, this aspect of the model would require further improvements. A semi-empirical approach to the growth of the boundary layer would significantly simplify the model and it would allow easier implementation of the model by the engineer.
- The model of Fukano & Ousaka (1989) tends to predict lower liquid film thickness than found experimentally, especially at lower gas flowrates. Inlet flow conditions and geometric characteristics different from those considered by Fukano & Ousaka (1989) result in unsatisfactory predictions of the model. This is due to the theoretical limitations of this model, which is not based on rigorous physical assumptions. The mechanism of the wave pumping action due to pressure forces does not consider either frequency of the interfacial waves or the mean film thickness. Furthermore, the model is based on experimental data in horizontal annular flows and on extensions of results obtained in vertical annular flows.

## Appendix A

### Venturi Scrubbers

Venturi scrubbers are usually classified as "wet scrubbers". Wet scrubbers transfer the pollutant from the gas to the liquid. Wet collection is advantageous when good efficiencies are required chiefly on coarser dust, for low loading where only moderate efficiencies are required, or in situations where there is a significant risk of explosion.

The advantages and disadvantages of wet scrubbers have been summarised by Muir (1992). His lists are reproduced in table 1.1. It must be noted that Venturi scrubbers are the most efficient cleaners among wet scrubbers. Venturi scrubbers in particular have one main disadvantage: high efficiencies can only be achieved at the cost of high pressure drop. The cost of pumping to overcome that pressure drop can be as high as 20% of the total energy running cost of a coal power station. Another important cost is that one relating to the consumption and treatment of the scrubbing liquid, water. In contrast to these disadvantages, the capital cost involved is very low (Vatavuk & Neveril, 1981).

A Venturi scrubber consists of a constriction in the duct carrying the dust-laden gas that raises its velocity to between 60-90 m/s, or higher (See Fig. 1.1). The geometry is that of a Venturi in order to obtain the lowest pressure drop. Scrubbing liquid can be introduced in a number of different ways. A "Pearce-Anthony" Venturi scrubber is characterised by the introduction of liquid through nozzles pointing downstream. If liquid is introduced as a film, the conventional name is "wetted approach" Venturi scrubber, or wetted approach operation. The high gas velocity atomises the liquid,

and the high relative velocity between the accelerating liquid droplets and the dust particles in the gas leads to a very efficient collection of even the fine particles.

**Table A.1: Advantages and disadvantages of wet scrubbers (Muir, 1992)**

<b>ADVANTAGES:</b>
<ul style="list-style-type: none"> <li>-Compactness and hence low capital cost</li> <li>-Elimination of fire and explosion hazards</li> <li>-Possible neutralisation of corrosive material by the selection of an appropriate scrubbing liquid</li> <li>-Simultaneous removal of gaseous and particulate contaminants</li> <li>-Simplicity of operation</li> <li>-Lack of secondary dust problems in disposal</li> <li>-Material is recovered in a form which can be pumped</li> <li>-Efficiency is largely dependent of scale</li> <li>-Continuously rated at a constant pressure drop</li> <li>-Possibility of cooling and dedusting in same plant</li> <li>-Can be used to collect sticky dusts</li> <li>-Insensitive to changes in gas temperature near the dew point</li> <li>-Potential for low grade recovery systems</li> </ul>
<b>DISADVANTAGES:</b>
<ul style="list-style-type: none"> <li>-Requirement of a slurry treatment plant</li> <li>-Extra cost of water usage</li> <li>-Loss of thermal buoyancy in the stack plume</li> <li>-Increased visibility of the stack due to water vapour condensation</li> <li>-Efficiencies do not approach 100%, and therefore: <ul style="list-style-type: none"> <li>(i) Cleaned air cannot be re-circulated into working areas</li> <li>(ii) Not necessarily suitable for high inlet burdens</li> <li>(iii) The fine fraction, if not collected, can make the plume visible</li> <li>(iv) High pressure drop, and hence high power consumption is necessary for operation at high efficiency or on sub-micron particles</li> </ul> </li> <li>-Frequent inspection and regular maintenance usually required</li> <li>-Possibility of scrubbing liquid freezing, foaming, frothing, or gelling</li> <li>-Possibility of retarded settling of the collected material</li> <li>-Possibility of adverse chemical reactions with the scrubbing liquid, which might lead to corrosion or deposition problems</li> </ul>

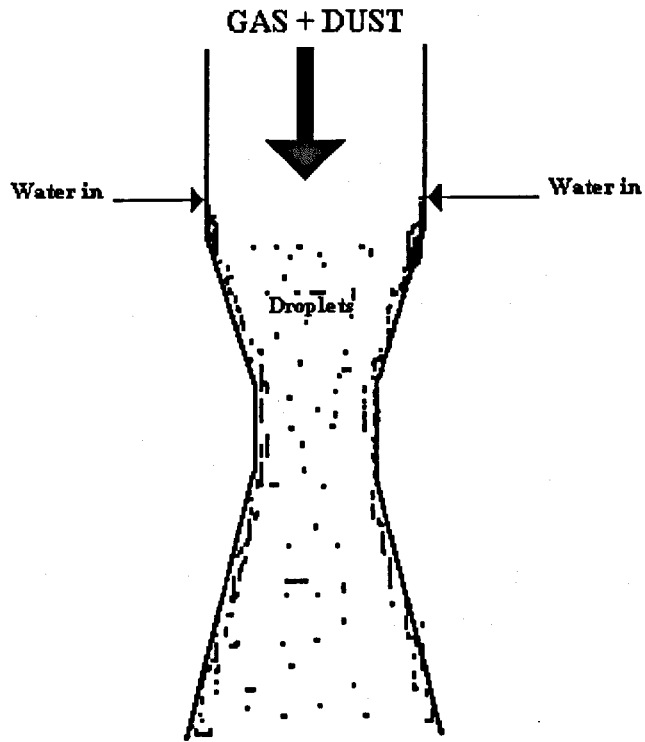
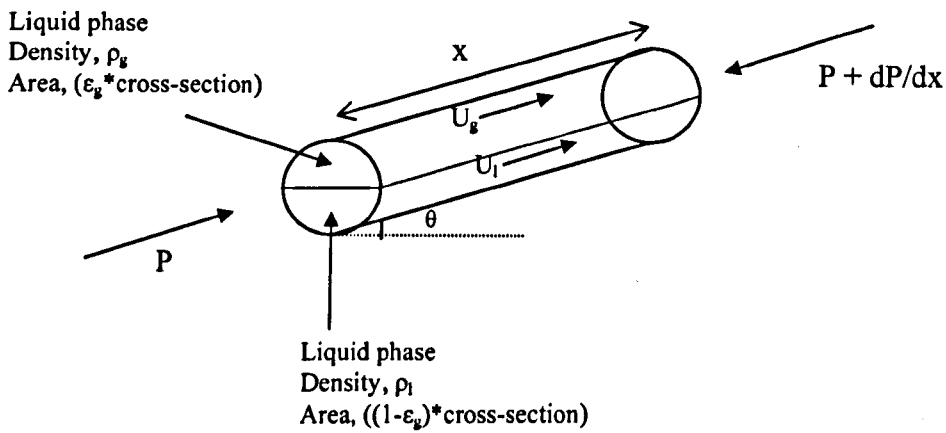


Figure A.1: Wetted approach Venturi scrubber

## Appendix B.1

### Theoretical details on separated flow

#### Momentum balance on an element of duct with separated flow



**Figure B.1:** Simple momentum balance on an element of duct with separated flow

Assumptions made:

- The static pressure is constant over any cross section;

- In each region, the fluids density is  $\rho_g$  over the fraction  $\varepsilon_g$  of the cross section and  $\rho_l$ , over the reminder  $(1-\varepsilon_g)$ ;
- In each region, the velocity is constant and equal to the mean averaged velocity of the respective phase;
- The wall shear stress,  $\tau_0$ , is constant around the periphery of the channel.

For a small element of a channel, a force balance can be obtained by equalizing the net applied force in the direction of the flow to the rate of the momentum increase in the direction of the flow.

$$\begin{aligned} \text{Net force} &= \int_A P dA - \int (P + \frac{dP}{dx} \delta x) dA - \int_A \rho g \sin \theta \delta x dA - \int_P \tau \delta x dp \\ \text{Net force} &= -\frac{dP}{dx} \delta x A - [\varepsilon_g \rho_g + (1 - \varepsilon_g) \rho_l] g \sin \theta \delta x A - \tau \delta x p \end{aligned} \quad (\text{B.1})$$

$$\text{Rate of momentum transport across any cross section, } \gamma = \int_A U \rho dA$$

The rate of increase of momentum across the element is:

$$\begin{aligned} \left[ \gamma_l + \frac{d\gamma}{dx} \delta x \right] - \gamma_l &= \left[ \frac{d}{dx} \int_A U^2 \rho dA \right] \delta x \\ \frac{d\gamma}{dx} \delta x &= \frac{d}{dx} \left[ (\bar{U}_g^2 \rho_g \varepsilon_g + \bar{U}_l^2 \rho_l (1 - \varepsilon_g)) A \right] \delta x = \frac{d}{dx} \left[ m^2 \left( \frac{x_g}{\varepsilon_g \rho_g} + \frac{(1 - x_g)^2}{(1 - \varepsilon_g) \rho_l} \right) A \right] \delta x \end{aligned} \quad (\text{B.2})$$

$$\text{where } \bar{U}_g = \frac{m x_g}{\rho_g \varepsilon_g} \text{ and } \bar{U}_l = \frac{m(1 - x_g)}{\rho_l (1 - \varepsilon_g)}$$

By equalizing B.1 and B.2:

$$-\frac{dP}{dx} = \bar{\tau} \frac{p}{A} + [\varepsilon_g \rho_g + (1 - \varepsilon_g) \rho_l] g \sin \beta + \frac{d}{dx} \left[ m \left( \frac{x_g^2}{\varepsilon_g \rho_g} + \frac{(1 - x_g)^2}{(1 - \varepsilon_g) \rho_l} \right) \right] \quad (\text{B.3})$$

## Appendix B.2

### Methods for Calculation of Frictional Pressure Gradient

#### B.2.1 Lockhart and Martinelli (1949)

Lockhart and Martinelli (1949) suggested a correlation with the function  $X^2$ :

$$X^2 = \frac{\Delta P_l}{\Delta P_g} \quad (\text{B.1})$$

$$\phi_l^2 = \frac{\Delta P_{TP}}{\Delta P_l} \quad (\text{B.2})$$

$$\phi_g^2 = \frac{\Delta P_{TP}}{\Delta P_g} \quad (\text{B.3})$$

$\Delta P_l$  and  $\Delta P_g$  are pressure drops when the liquid or gas phases are flowing alone. Lockhart and Martinelli suggested four conditions seen on figure 2.1.3 of Chapter 2: vv, vt, tv, tt where v = viscous and t = turbulent and liquid is quoted first. For example, vt means liquid is viscous while the gas is turbulent. According to Holt (1996), a simpler form of  $X^2$  is as follow:

$$X^2 = \frac{\Delta P_l}{\Delta P_g} = \left( 2 \frac{f m_{TP}^2 (1-x_g)^2}{D \rho_l} \right) \left( \frac{1 D \rho_g}{2 f m_{TP}^2 x_g^2} \right) = \frac{\rho_g (1-x_g)^2}{\rho_l x_g^2} \quad (\text{B.4})$$

### B.2.2 Chisholm (1973)

Chisholm (1973) suggested a more generalized form of a Lockhart and Martinelli equation:

$$\phi_l = 1 + \frac{C}{X} + \frac{1}{X^2} \quad \text{or} \quad \phi_g = 1 + CX + X^2 \quad (\text{B.5})$$

### B.2.3 Friedel (1979)

Friedel (1979) (see Holt (1996)) proposed an algebraic correlation for the two-phase multiplier used for determination of frictional pressure gradient for vertical upwards whereby  $\phi_l^2 = A_1 + A_2$ :

$$A_1 = (1 - x_g)^2 + x_g^2 \frac{\rho_l f_l}{\rho_g f_g} \quad (\text{B.6})$$

$$A_2 = \frac{3.24 x_g^{0.8} (1 - x_g)^{0.224} \left( \frac{\rho_l}{\rho_g} \right)^{0.91} \left( 1 - \frac{\mu_g}{\mu_l} \right)^{0.7} \left( \frac{\mu_g}{\mu_l} \right)^{0.19}}{Fr^{0.045} We^{0.035}} \quad (\text{B.7})$$

where  $Fr = \frac{m_{TP}^2}{\rho_{TP,H}^2 Dg}$  and  $We = \frac{m_{TP}^2 D}{\rho_{TP,H} \sigma}$

## Appendix C

### Error Analysis

In this Appendix is presented an error analysis based on the method of Taylor (1997) applied to a set of inlet flow condition considered for the experimental runs. This error analysis is related to the essential parts of the rig e.g. air and water rotameters, pressure gauges, tanks and etc, and therefore is applicable for any sort of experiments. For this case, the gas superficial velocity,  $U_{sg}$ , is 17.5 m/s ( $M_g=0.04$  kg/s), the liquid superficial velocity,  $U_{sl}$ , is 0.0115 m/s ( $M_l=0.0131$  kg/s), the air inlet pressure,  $P_{inlet}$ , is 1.6 bara and the pressure difference between the two sections of the orifice plate,  $\Delta P_{cell}$ , is 1.05 PSI.

*Error analysis on the superficial air velocity:*

The air superficial velocity is given by:

$$U_{sg} = C * \frac{(\Delta P_{cell} * P_{inlet})^{1/2}}{P_{inlet}} \quad (C.1)$$

where:

$\Delta P_{cell}$  is the reading of the pressure difference across the orifice plate.

$P_{inlet}$  is air inlet pressure reading

$$C \text{ is a constant: } C = 0.61 * \frac{\sqrt{\frac{2 * 1.204}{7088845.108}}}{1.204 * 0.001134} = 0.26 \left[ \frac{\sqrt{\frac{kg/m^3}{1/m^4}}}{\frac{kg}{m^3} \cdot m^2} \right]$$

Considering equation (C.1) the fractional uncertainty of  $U_{sg}$  can be written as:

$$\frac{E(U_{sg})}{U_{sg}} = C \cdot \left( \frac{0.5 \cdot e(\Delta P_{cell})}{\Delta P_{cell}} + \frac{0.5 \cdot e(P_{inlet})}{P_{inlet}} + \frac{e(P_{inlet})}{P_{inlet}} \right) \quad (C.2)$$

where:

$e(\Delta P_{cell})$  is the error in reading the DP cell;  $e(\Delta P_{cell}) = \pm 0.5 \text{ PSI} = \pm 0.034473 \text{ bar}$

$e(P_{inlet})$  is the error in reading the inlet air pressure gauge;  $e(P_{inlet}) = \pm 0.1 \text{ bar}$

By substituting the value of these two errors in equation C.2, the fractional uncertainty of  $U_{sg}$  is obtained:

$$\frac{E(U_{sg})}{17.5} = 0.26 \cdot \left( \frac{0.5 \cdot 0.034473}{0.0724} + \frac{0.5 \cdot 0.1}{1.6} + \frac{0.1}{1.6} \right) = 0.0862 = 8.62\% \quad (C.3)$$

Therefore, the uncertainty of  $U_{sg}$  is:

$$E(U_{sg}) = \pm 0.0862 \cdot 17.5 \text{ m/s} = \pm 1.5 \text{ m/s} \quad (C.4)$$

Thus, is can be written:

$$U_{sg} = (17.5 \pm 1.5) \text{ m/s} \quad (\text{C.5})$$

*Error analysis on the superficial liquid velocity:*

The liquid superficial velocity is obtained by reading the number in the liquid rotameter. The two rotameters used for the inlet liquid flow rate measurement were calibrated before the experiments.

The error in reading the two liquid rotameter is,  $E(\text{Rot}) = 0.5$  Unit. This error gives an uncertainty in the liquid superficial velocity of:

$$E(U_{sl}) = \pm 0.000479 \text{ m/s} \quad (\text{C.6})$$

$$U_{sl} = (0.0115 \pm 0.000479) \text{ m/s} \quad (\text{C.7})$$

The fraction uncertainty is, therefore:

$$\frac{E(U_{sl})}{U_{sl}} = \frac{0.000479}{0.0115} = 0.041 = 4.1\% \quad (\text{C.8})$$

*Error analysis on the liquid film flow rate:*

The mass flow rate of the liquid film taken out through the window is determined dividing 0.4litres of liquid film by the time in which this volume is collected.

$$\omega_l = \frac{Q}{t} = \frac{0.4}{t} \quad (\text{C.9})$$

For this analysis a combination of two errors has to be considered:

Error in measuring rise in the liquid volume in the separator tank:  $\pm 0.02$  l

Error in reading the stop clock:  $\pm 0.5$  s

The combined fractional uncertainty of  $\omega_1$  is given by:

$$\frac{E(\omega_1)}{\omega_1} = \frac{e(Q)}{Q} + \frac{e(t)}{t} \quad (\text{C.10})$$

In this section it will be considered the time measured to take the liquid film off the main section of the vertical Venturi with the valve fully opened:

$$t \cong 120s$$

Thus, the fractional uncertainty of the partial liquid taken off through the window is:

$$\frac{E(\omega_1)}{0.003} = \frac{0.02}{0.4} + \frac{0.5}{120} = 0.054 = 5.4\% \quad (\text{C.11})$$

which gives:

$$E(\omega_1) = (0.054 * 0.003) / s = 0.000162 / s \quad (\text{C.12})$$

$$\omega_1 = (0.003 \pm 0.000162) / s \quad (\text{C.13})$$

## Appendix D

### Signal Processing

(Taken from a report of Dr. Hans van Maanen)

#### D.1 Fourier Transformation

##### D.1.1 Main theorem of Fourier

The Fourier Transform (or analysis) is a cornerstone of the current signal analysis, although other techniques are being developed which might have a big impact on LDA (Laser Doppler Anemometry). The main theorem of Fourier is that any (physical) signal can be written as an infinite sum of sine and cosine waves. This opens the possibility to analyze the signal in all its constituent frequencies and to determine each contribution. This process can be reversed (and it is called Inverse Fourier Transformation) under certain conditions. It is common practice to talk about a function in *time* or *frequency* domain. Mathematically speaking it contains identical information in both domains.

The main theorem of Fourier is:

Any signal of finite length that contains only a finite number of discontinuities and which can be integrated in its absolute value, can be written as an infinite sum of sine and cosine functions.

Example for the interval  $(-\pi, \pi)$ :

$$f(t) = \frac{1}{2}a_0 + \sum_{n=1}^{\infty} [a_n \cos(nt) + b_n \sin(nt)] \quad (\text{D.1})$$

in which:

$$a_n = \frac{1}{\pi} \int_{-\pi}^{\pi} f(t) \cos(nt) dt \quad (\text{D.2})$$

and

$$b_n = \frac{1}{\pi} \int_{-\pi}^{\pi} f(t) \sin(nt) dt \quad (\text{D.3})$$

### D.1.2 Spectral leakage.

When there is a periodic signal with a cycle time which is not exactly equal to an integer multiple of time interval over which the signal is defined (and that is always the case) the periodic continuation will create a step at the interval boundaries; compare fig. 1 and 2 with fig. 3 and 4. In case the signal consists of a pure sinusoidal wave, the spectrum should have only one single peak as is shown in fig. 5. However, if the signal does not fit precisely in the time interval, the periodic continuation leads to all kinds of additional components in the spectrum that would not be expected at first sight. This phenomenon is called "leakage" because energy leaks from the original input frequency to other frequencies and it is a big nuisance for the interpretation of spectra. As this phenomenon appears in virtually all situations, it is essential to apply the so-called "windowing" functions. But before discussing that in more detail it is essential to introduce the notion of "spectral resolution".

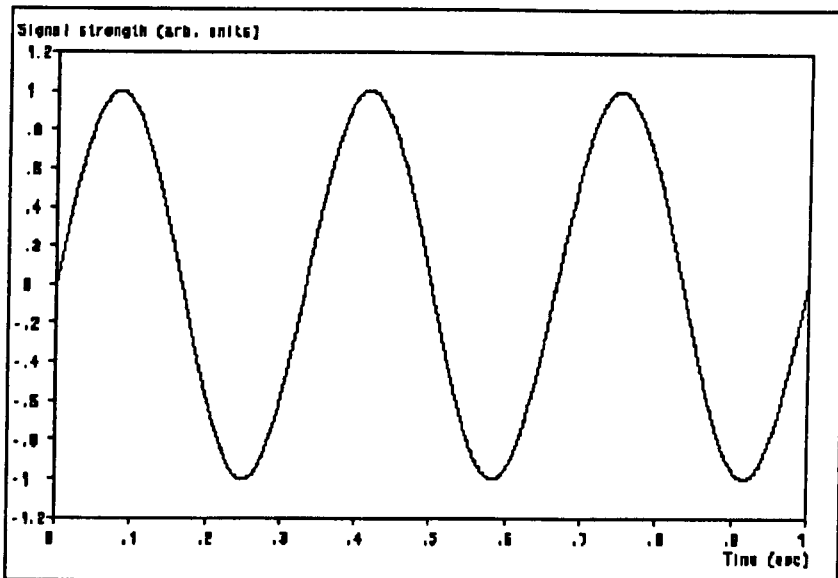


**Figure D.1:** If the interval  $[0,1]$  seconds is considered as the basic interval it can happen that an integer number of cycles fits into this interval.

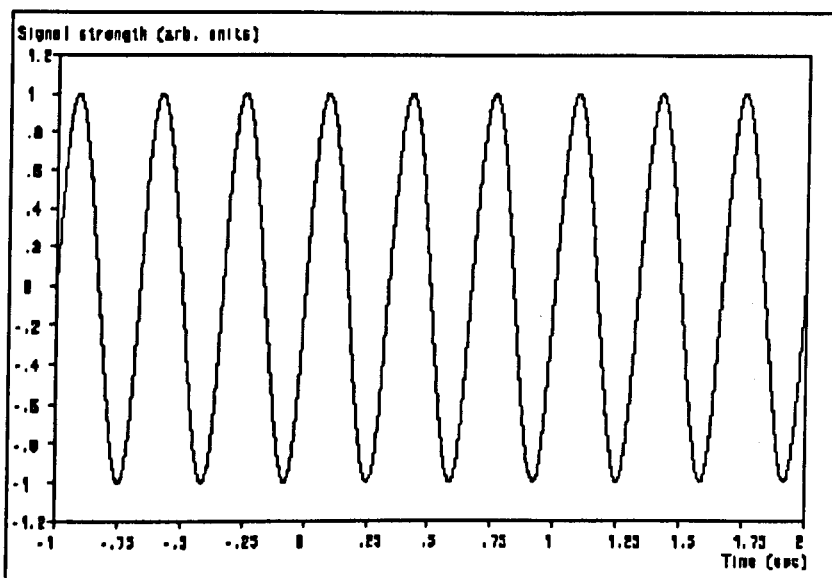


**Figure D.2:** Periodic continuation of this signal does not cause any trouble.

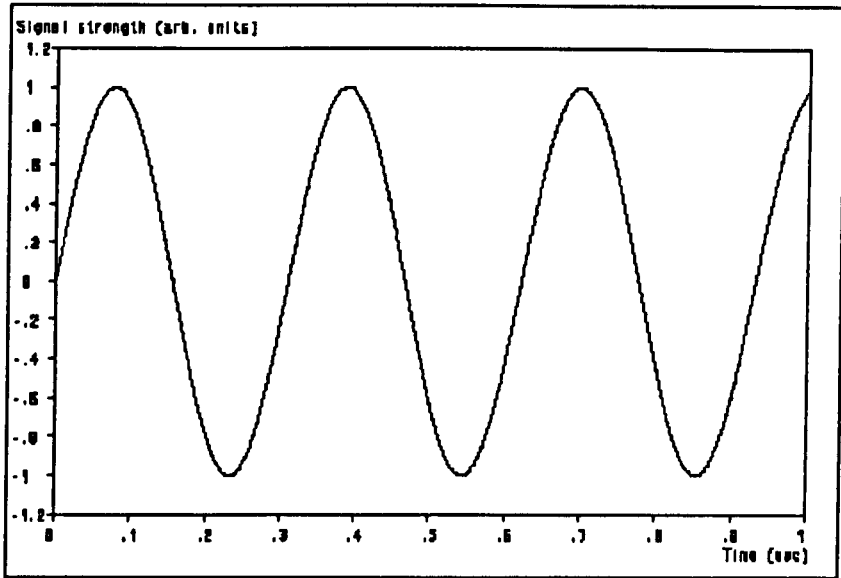


Figure D.3: But usually this is not the case.....

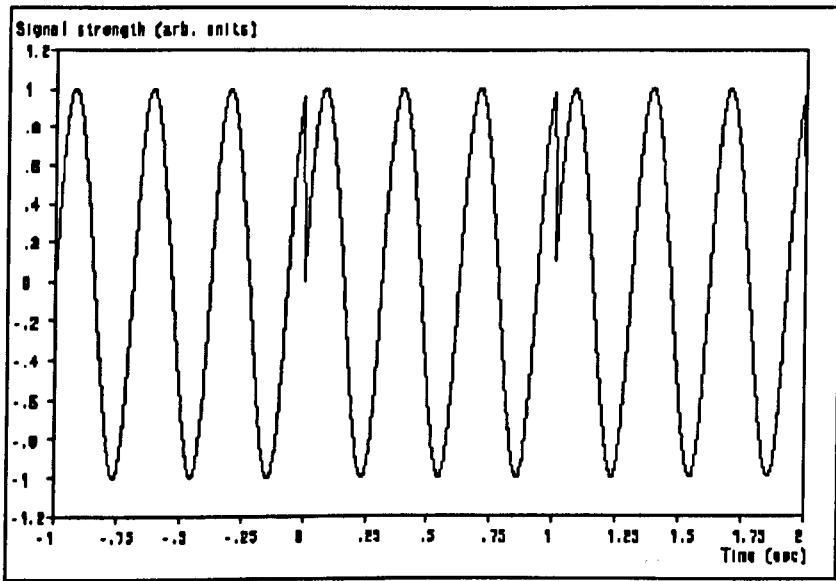
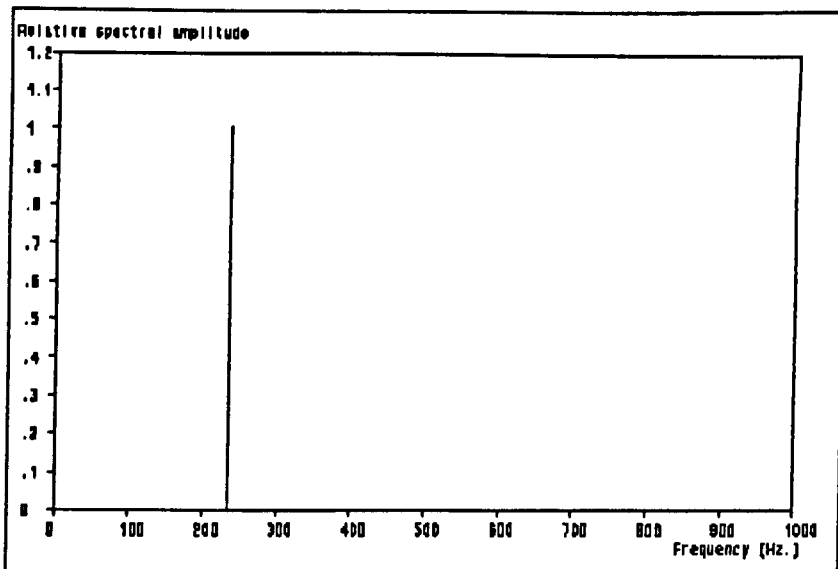
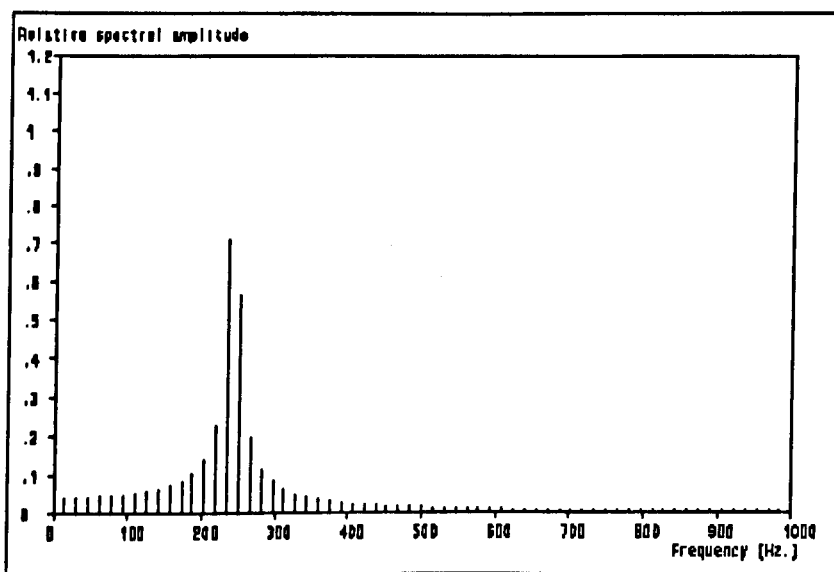


Figure D.4: ... and the periodic continuation of the signal is equipped with some weird jumps at the interval boundaries at 0 and 1 sec.



**Figure D.5:** If an integer number of cycles fits precisely into the transformation window, the spectrum consists of one single line.



**Figure D.6:** But if it does not fit so nicely "leakage" is the result. This is caused by the jumps at the boundaries of the continued signal, which represents different frequencies.

### D.1.3 Spectral resolution.

When there is a signal available over a finite time interval, it is convenient to determine its Fourier Transform as a **Fourier series** of which the subsequent components have a frequency difference equal to  $1/(\text{intervallength})$ . For example, when the time interval has a length of 1 sec., the difference between two successive components is 1 Hz. When the length of the time interval is 0.1 sec. the difference is 10 Hz. It is common to state that the spectral resolution of the spectrum is equal to this difference. Another example: with a signal of 1000 Hz available on an interval of 100 ms, the resolution is 10 Hz and 100 cycles of the signal are available. As a rule of thumb is, therefore, often used:

$$\frac{\Delta f}{F} = \frac{1}{N} \quad (\text{D.5})$$

in which:

$\Delta f$  = spectral resolution Hz

$F$  = frequency Hz

$N$  = number of cycles

The equation given above can be also written as:

$$\Delta f \cdot \Delta t = 1 \quad (\text{D.6})$$

with:

$$\Delta t = \frac{N}{F} \quad (\text{D.7})$$

### D.1.3 Spectral distortion.

When a Fourier transformation is applied to a signal, the "DC" contribution to it can lead to useless results. As the frequency 0 also has a certain spectral width (see above), a DC component also introduces a contribution at higher frequencies. But if the decay of the (turbulent) velocity fluctuations in the spectrum is faster than the decay of the leakage of the DC component, the actual spectrum is completely masked. This results in complete nonsense spectra as can be seen from fig. 7. Therefore, it is best to subtract the DC component beforehand. When a Fourier transformation is applied to an Auto Correlation Function to get a Power Spectrum of a signal (see section D.1.5), it is convenient to estimate the DC contribution from the tail of the correlation function<sup>1</sup> and remove it before the Fourier transformation. A first improvement can be done by applying a windowing function (see section D.1.4) in the spectrum as is shown in fig.8. But only the removal of the DC contribution solves the problem, as can be seen from fig. 9.

If the limiting values of the signal at the left and right hand side of the interval are not equal (and with stochastic signals this will always be the case) the signal can be thought as if it were superimposed on a sawtooth function, the slope of which is determined by the difference between the values at the left and right hand boundaries of the time interval and its length. This is illustrated in fig. 10 to 12. This sawtooth function plays a role because of the periodic repetition of the signal thanks to the Fourier series, as discussed above. But this sawtooth has a spectrum, which decays relatively slowly because of its discontinuity. Also, it is slower than the spectrum of dissipating turbulence. Because of this the spectrum will be distorted (or modified), which can easily lead to an incorrect interpretation. It is therefore required to remove this slope before the calculation of the Fourier transform. However, dependent on the

---

<sup>1</sup> Because the correlation coefficient for stochastic signals goes to zero for large time shifts, the DC contribution can be estimated from the limiting value when the time shift goes to "infinity". However, it is also wise to subtract the DC contribution from the signal before calculation of the ACF as the DC contribution is only a burden that even could lead to round-off errors in the numerical computation of the ACF.

algorithm chosen, a DC component could be introduced again. It is advised to remove this potential DC contribution too. The artifacts introduced by this sawtooth contribution are illustrated in fig.13; after removal of this the spectrum definitely has a different shape, especially at higher frequencies, as can be seen from fig. 14.

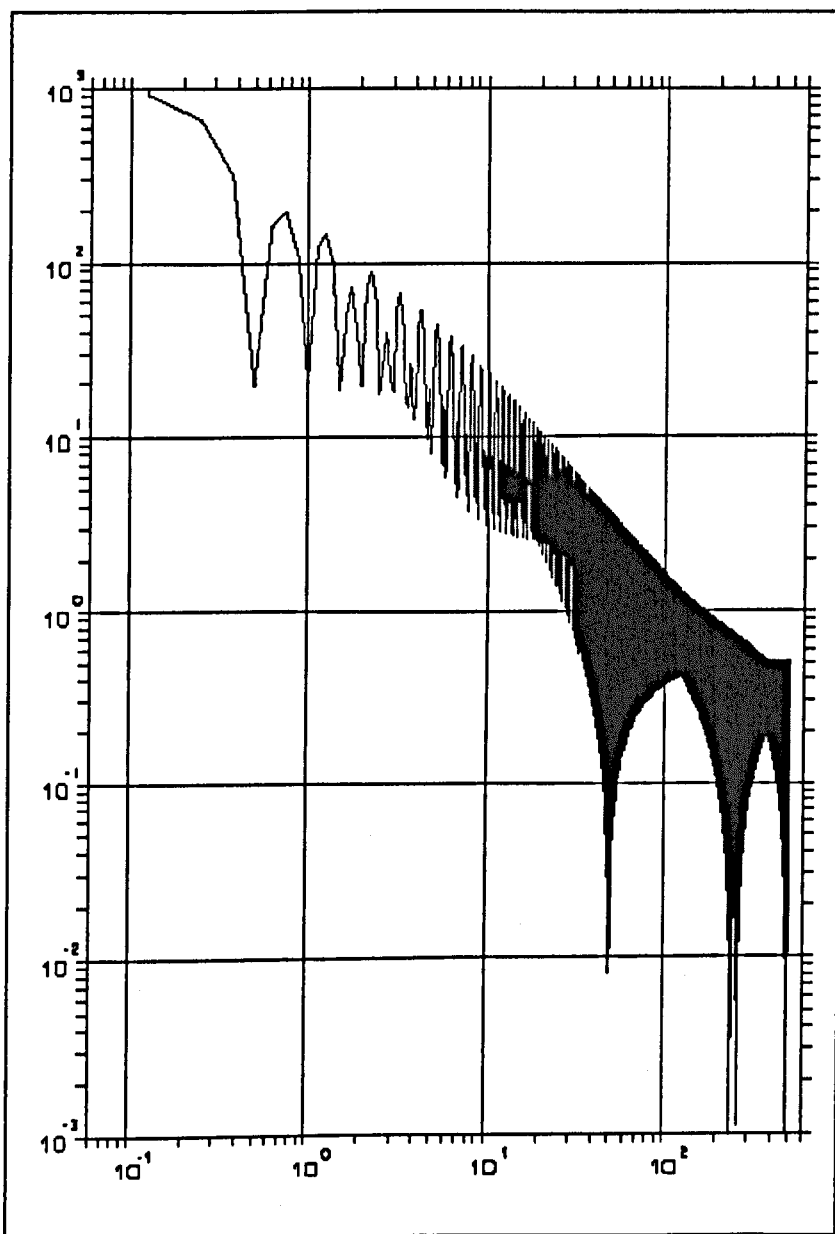


Figure D.7: Interpolated spectrum with a DC contribution, without windowing.

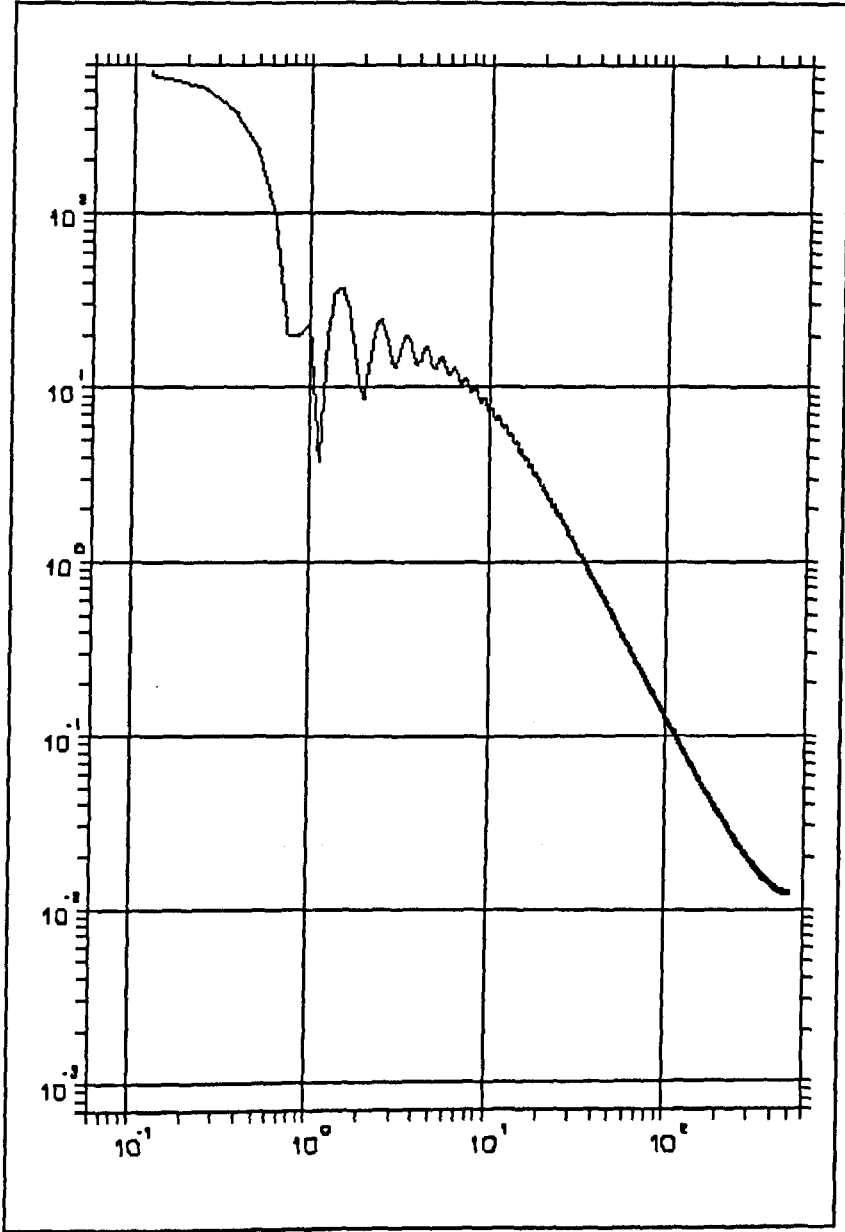


Figure D.8: Interpolated spectrum with a DC contribution and windowing.

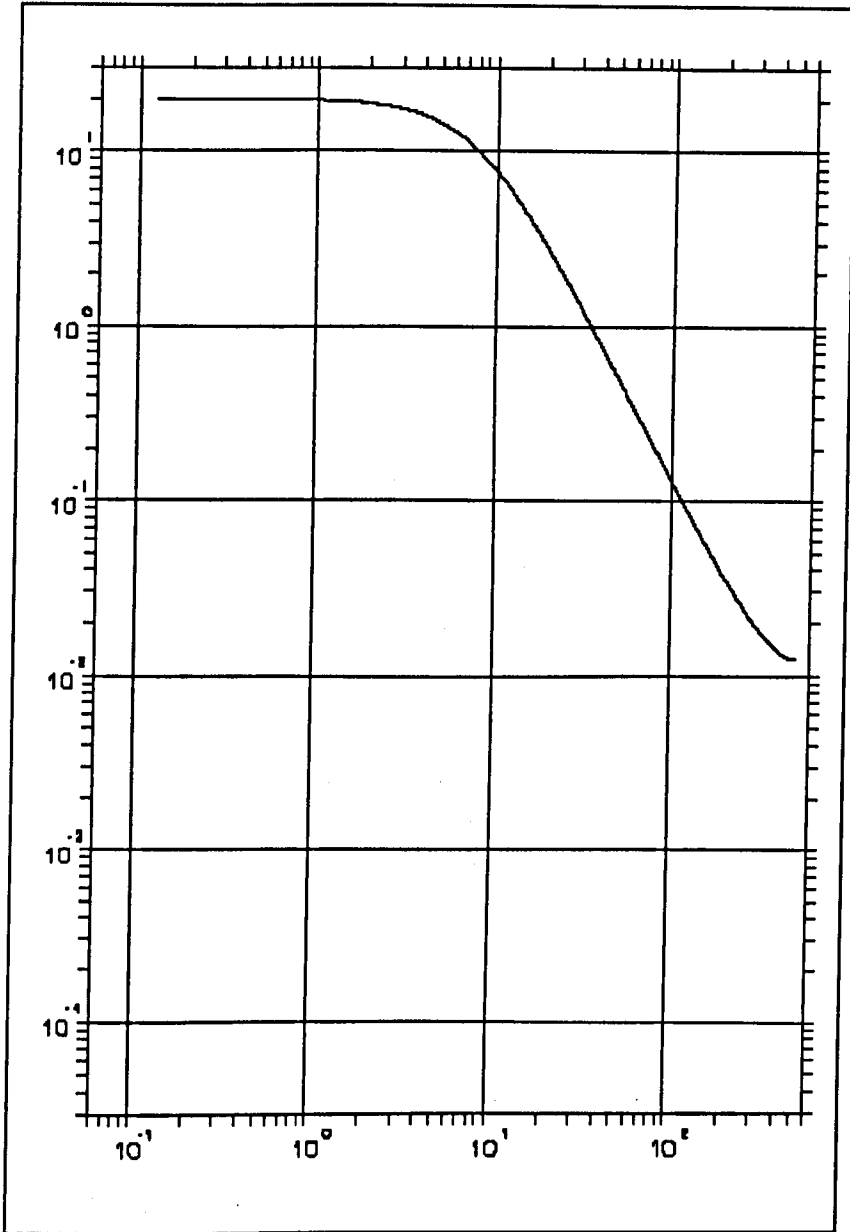


Figure D.9: Interpolated spectrum after removal of the DC contribution.

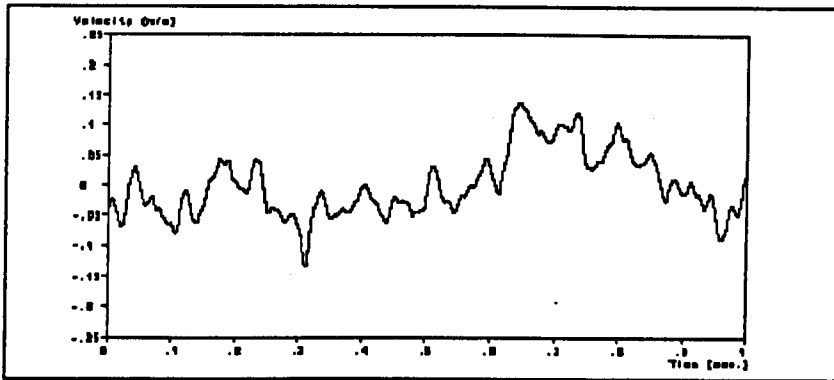


Figure D.10: The original signal can be regarded as.....

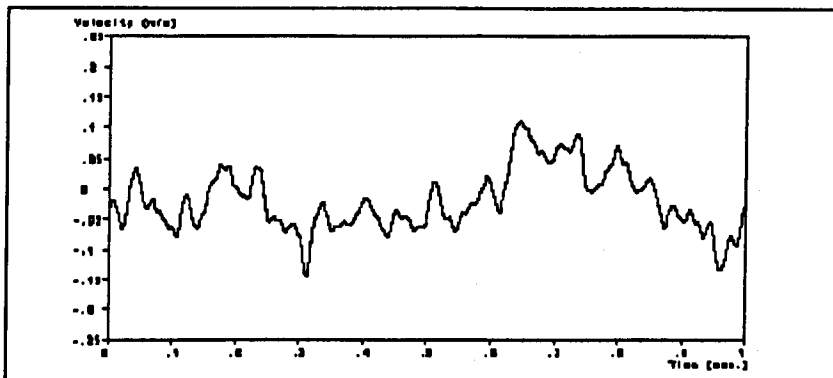


Figure D.11: ....a combination of the fluctuations and.....

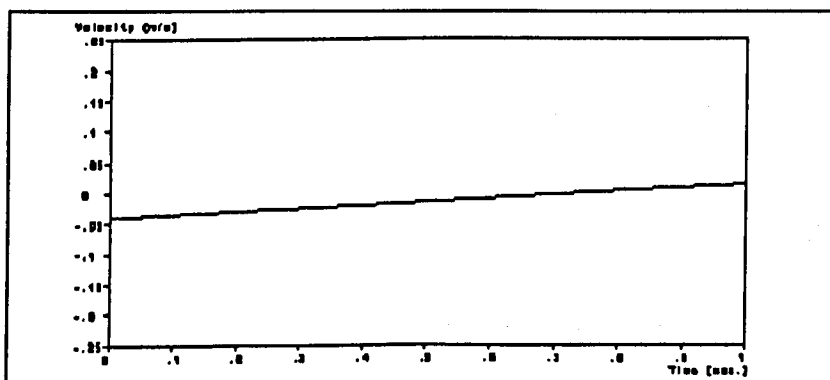
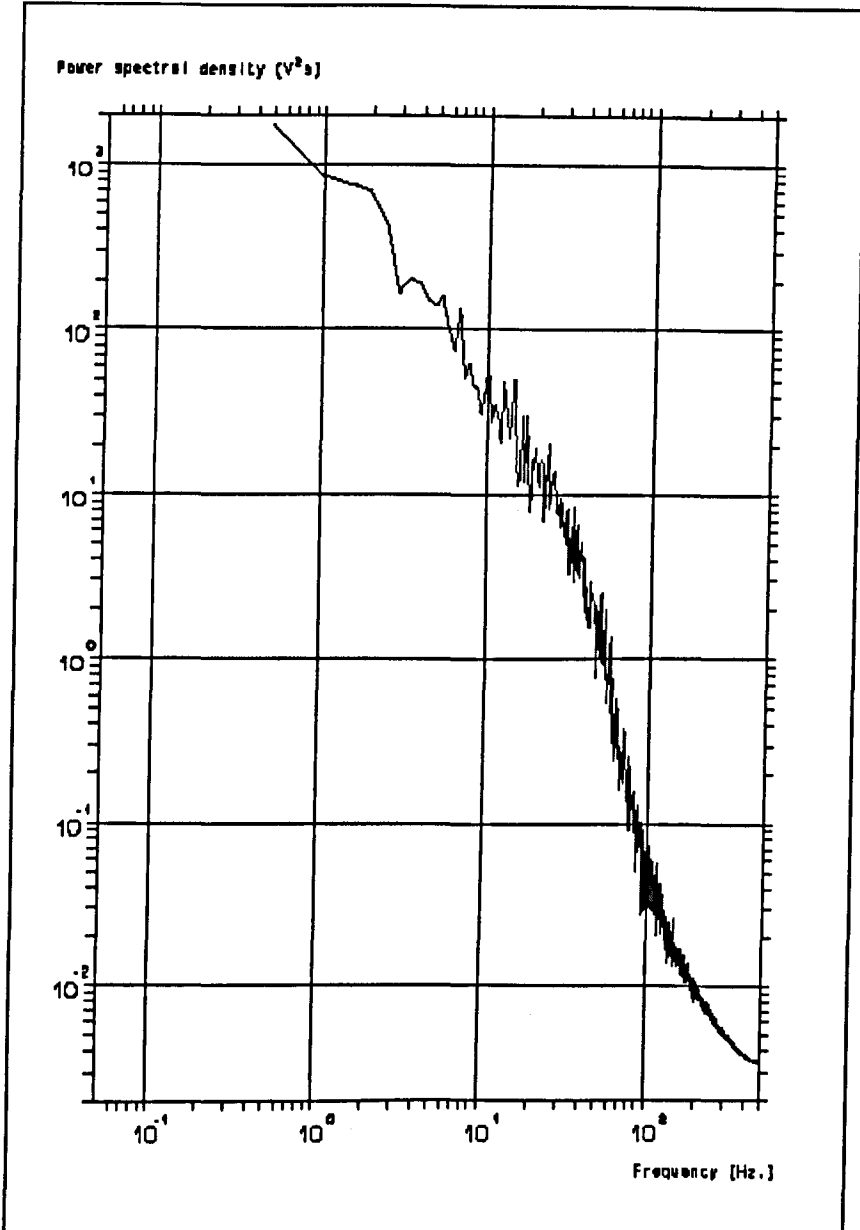


Figure D.12: ....the slope, which leads to discontinuities at the interval boundaries.



**Figure D.13:** Spectrum obtained as the average of 9 independent estimators without removal of the trend (sawtooth function).

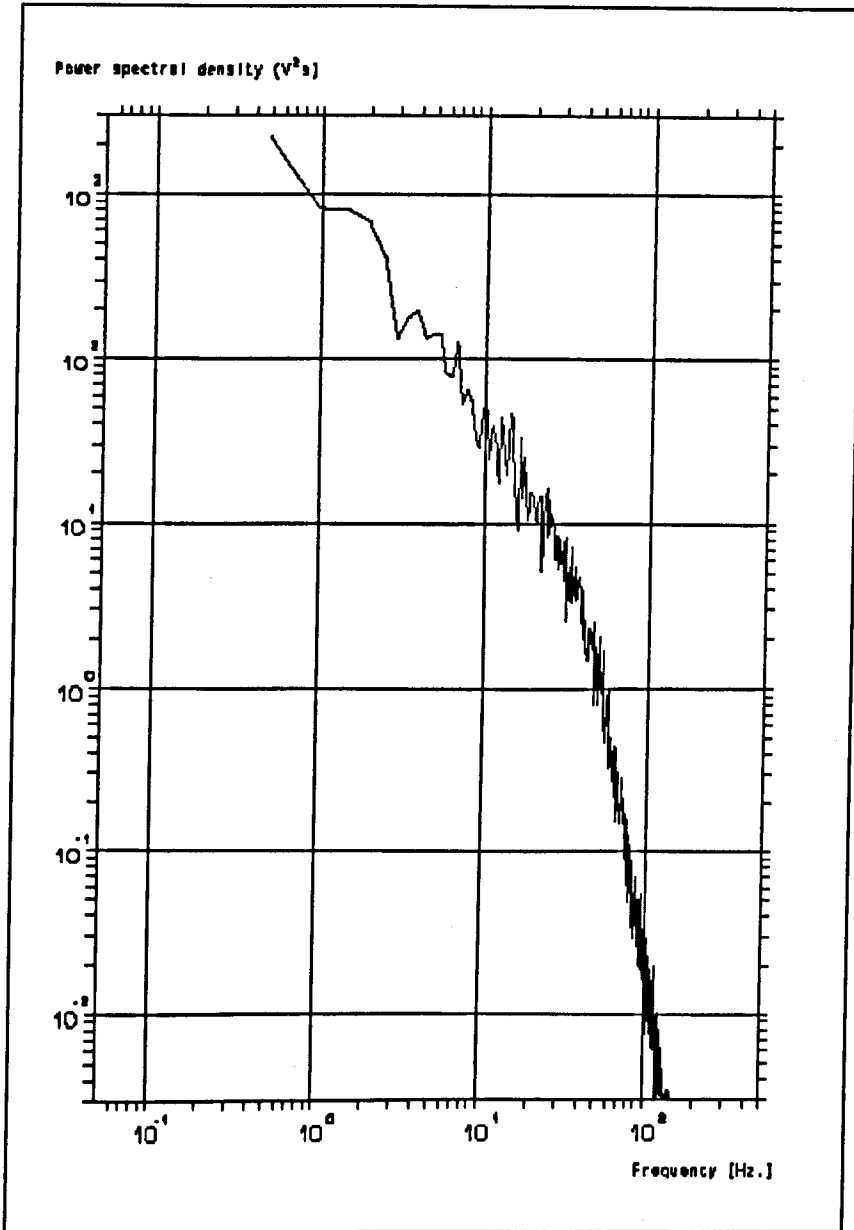


Figure D.14: Spectrum obtained as the average of 9 independent estimators after removal of the trend (sawtooth function).

### D.1.4 Windowing.

Windowing functions are functions with which the actual signal (in time domain) is multiplied to suppress the leakage problem. The leakage problem finds its cause in the usual condition that the signal has a different value at the left and right hand boundaries of the time interval. The windowing functions solve that problem by going to zero at those boundaries. However, the spectral resolution  $\Delta f$  is reduced<sup>2</sup> too. In fact, a combination of a windowing function with the actual signal leads to the *convolution* of the original spectrum with the Fourier Transform of the windowing function:

$$F_w(\omega) = \int_{-\infty}^{\infty} F(\Omega) \cdot W(\omega - \Omega) d\Omega = F(\omega) * W(\omega) \quad (\text{D.8})$$

When  $F(\omega)$  is the spectrum of the signal and  $W(\omega)$  is the spectrum of the windowing function then the spectrum obtained is  $F(\omega) * W(\omega)$ , in which  $*$  is the symbol for convolution.

In the course of history numerous windowing functions have been invented and applied as well.

Below there are listed some properties, which a windowing function should have:

1. Zero or at least small at the boundaries.
2. One in the middle of the time interval.
3. Continuous.
4. Monotonously decaying towards the boundaries.
5. Symmetrical.

---

<sup>2</sup> Meaning in this case that  $\Delta f$  is increased

6. The derivative in the middle should be zero.
7. Differentiable.
8. Have a high value (close to one) in as large a part of the time interval as possible.

Other important considerations are:

- The higher the spectral resolution (smaller  $\Delta f$ ), the more leakage occurs.
- The Gauss curve is the most optimum choice because the Fourier Transform of a Gauss is a Gaussian function. This is also true for filtering.

A number of known windowing functions and their spectra are presented in fig.15 to 26 and these illustrate nicely the statements above. That these windowing functions do suppress leakage is clearly shown in fig. 27.

It is common sense to look for a windowing function that fits best for a specific problem. The damping of the sidelobes in the spectrum is of prime importance in a number of cases, e.g. when periodic components are present in the flow, which is under investigation. If the leakage from the generated peaks in the spectrum is not sufficiently suppressed, it is no longer possible to retrieve the contribution from the random turbulence. This is nicely illustrated in fig. 28, where a complete spectrum has been generated with just one single sinusoid (one single frequency). Fig. 29 shows that windowing can improve the situation and fig. 30 shows that with an appropriate choice of the windowing both the contributions of the periodic components as well as those of the random turbulence can clearly be distinguished. Windowing is therefore essential to obtain interpretable results.

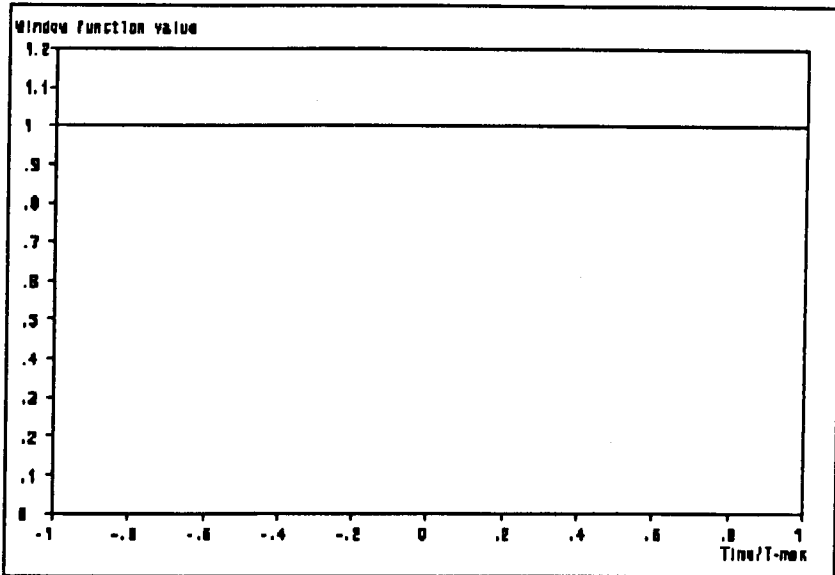


Figure D.15: The simplest windowing function is the constant 1.

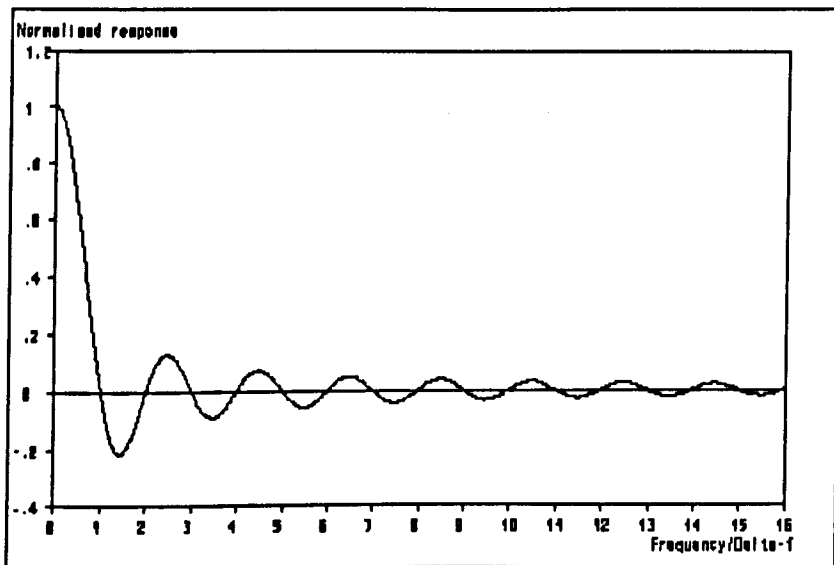


Figure D.16: Spectrum of the rectangular windowing function.

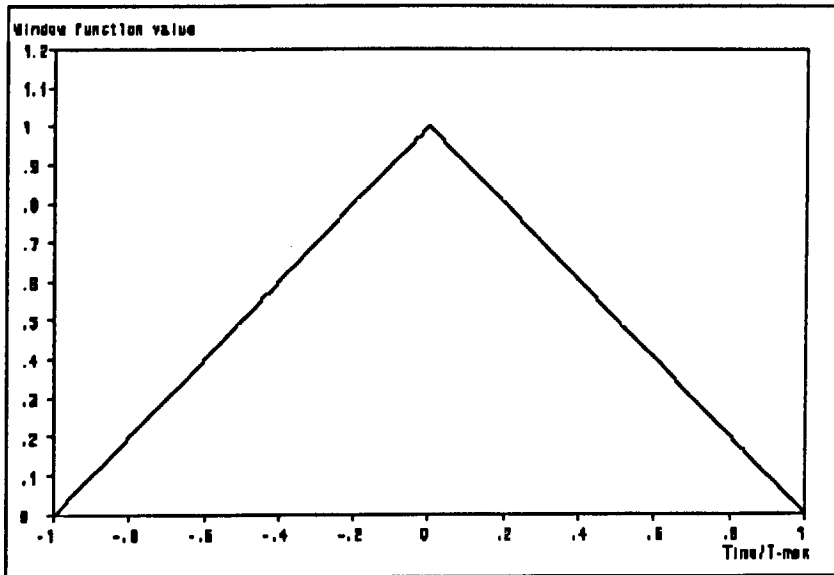


Figure D.17: One of the simplest windowing functions: the triangle.

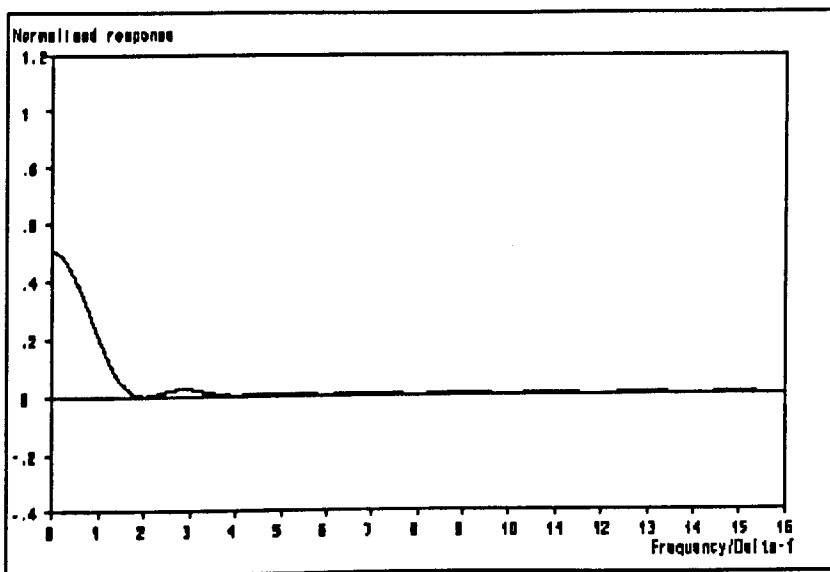


Figure D.18: Spectrum of the triangular windowing function.

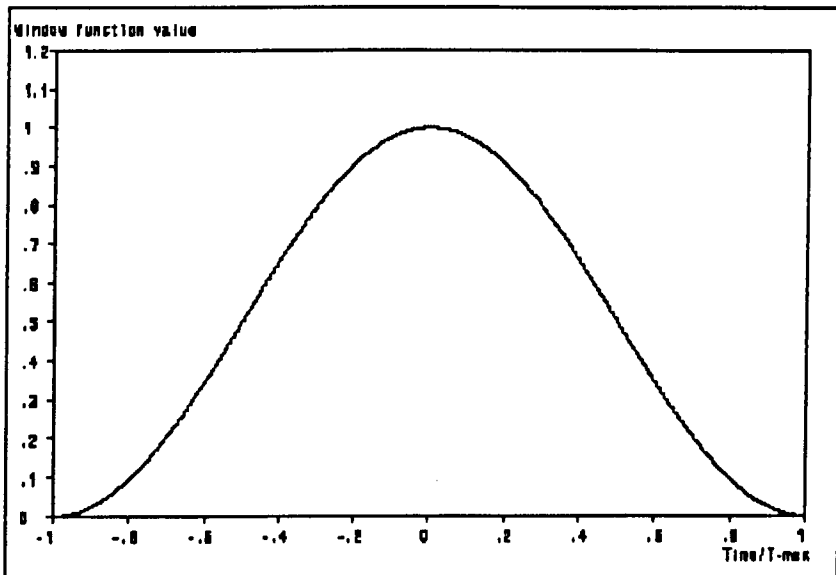


Figure D.19: An often applied windowing function:  $0.5 + 0.5 * \text{COSINE}$ .

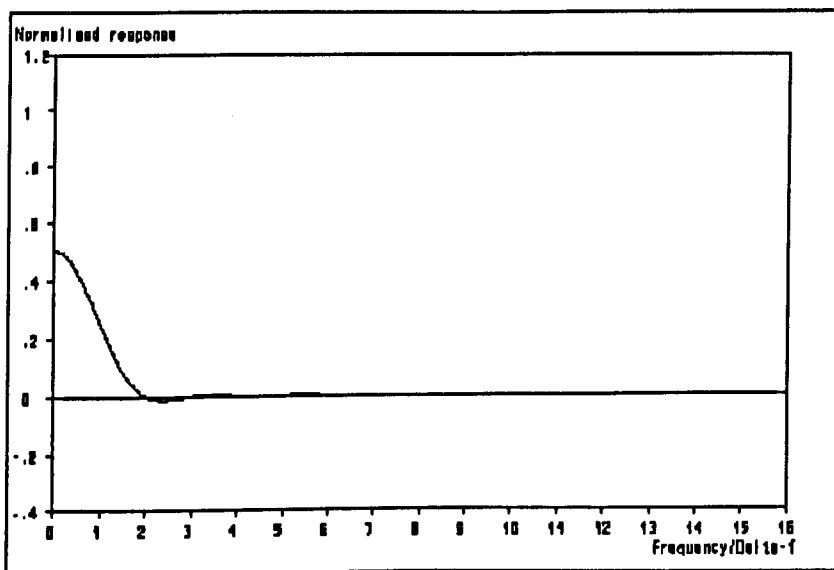


Figure D.20: Spectrum of the shifted cosine windowing function.

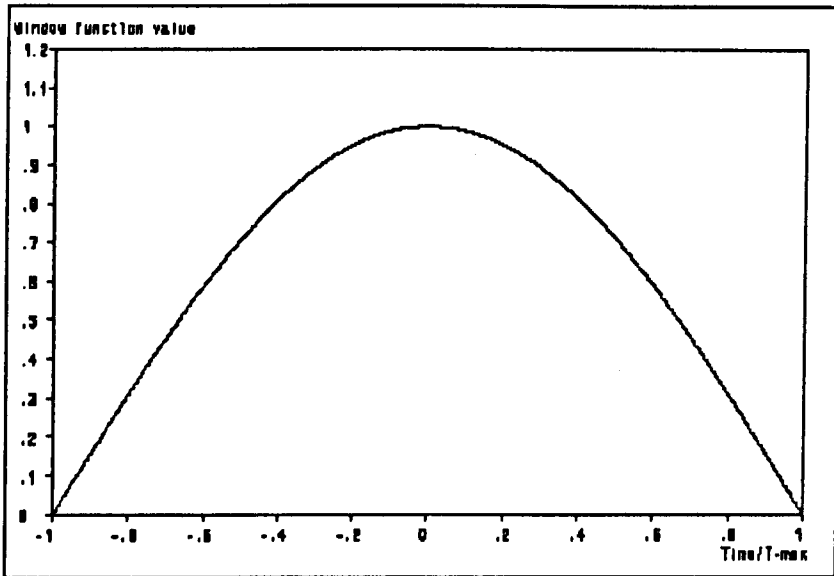


Figure D.21: Half a cosine is a suitable one as well, but it has stronger sidelobes.

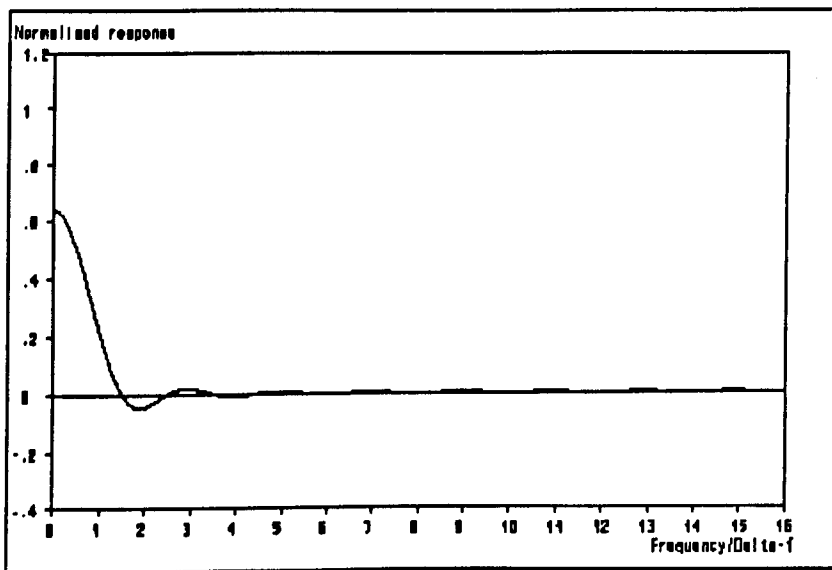


Figure D.22: Spectrum of the half-cosine windowing function.

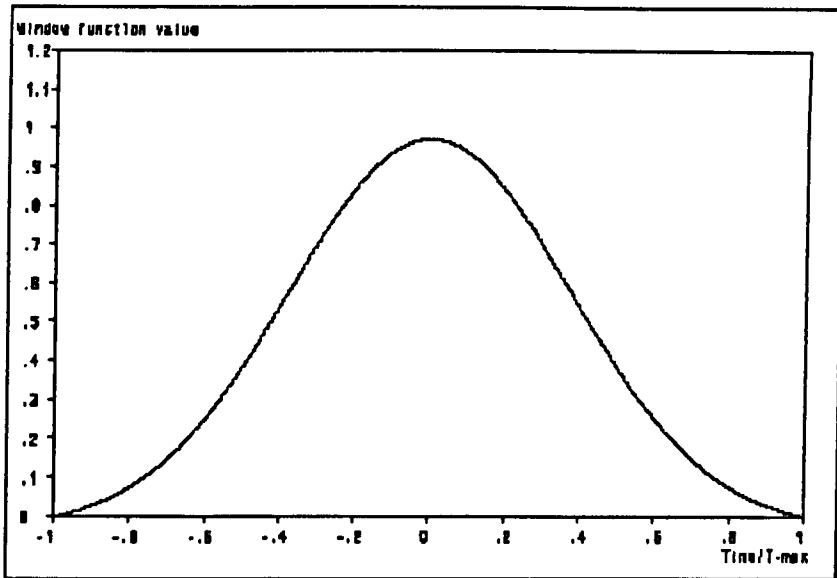


Figure D.23: A shifted and scaled Gaussian function is often applied as well.

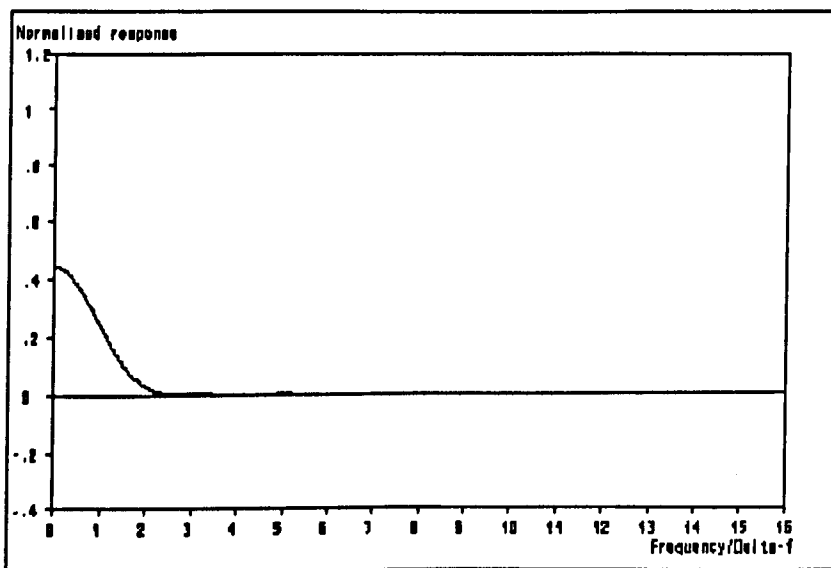


Figure D.24: Spectrum of the shifted and scaled Gaussian windowing function

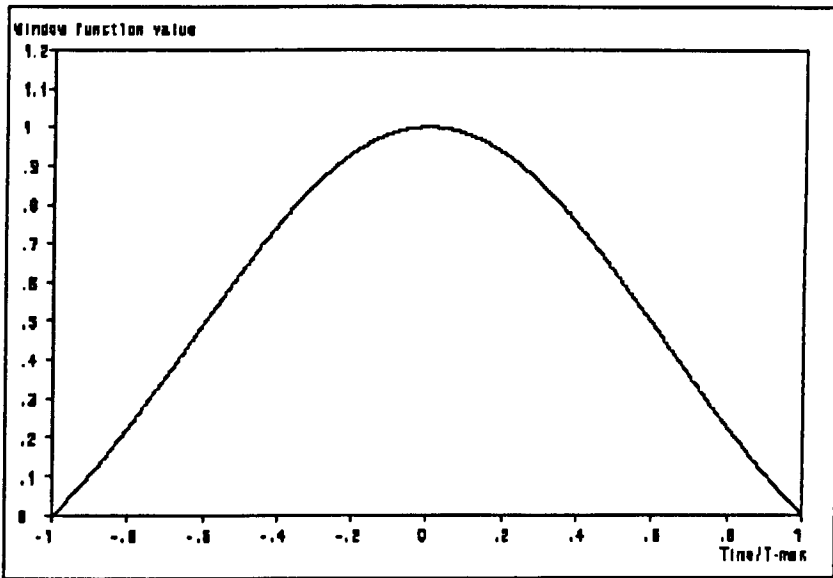


Figure D.25: A combination of a half-cosine and a part of the Gauss curve yields an effective windowing function.

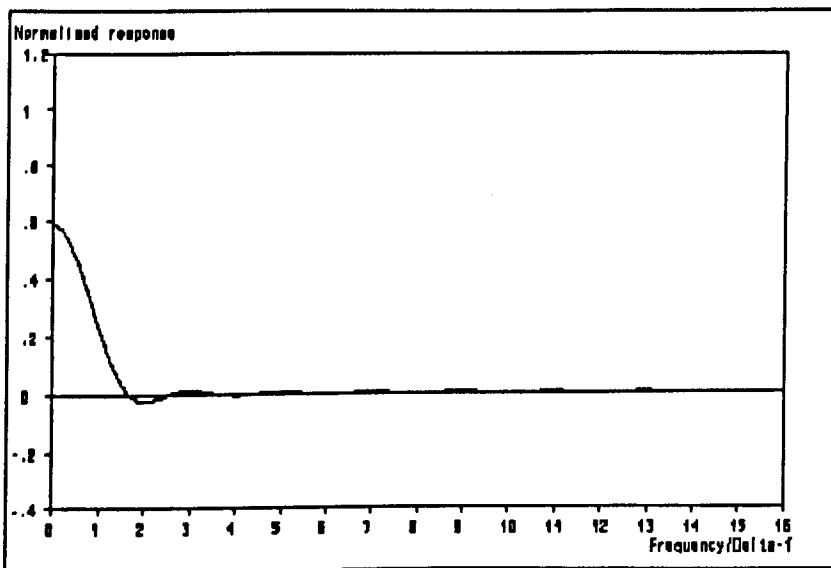


Figure D.26: Spectrum of the combined half-cosine/Gauss windowing function.

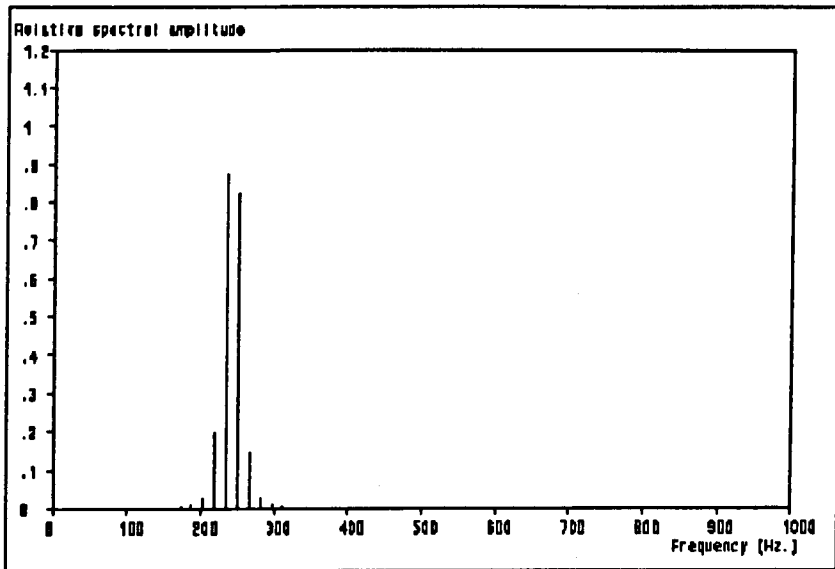
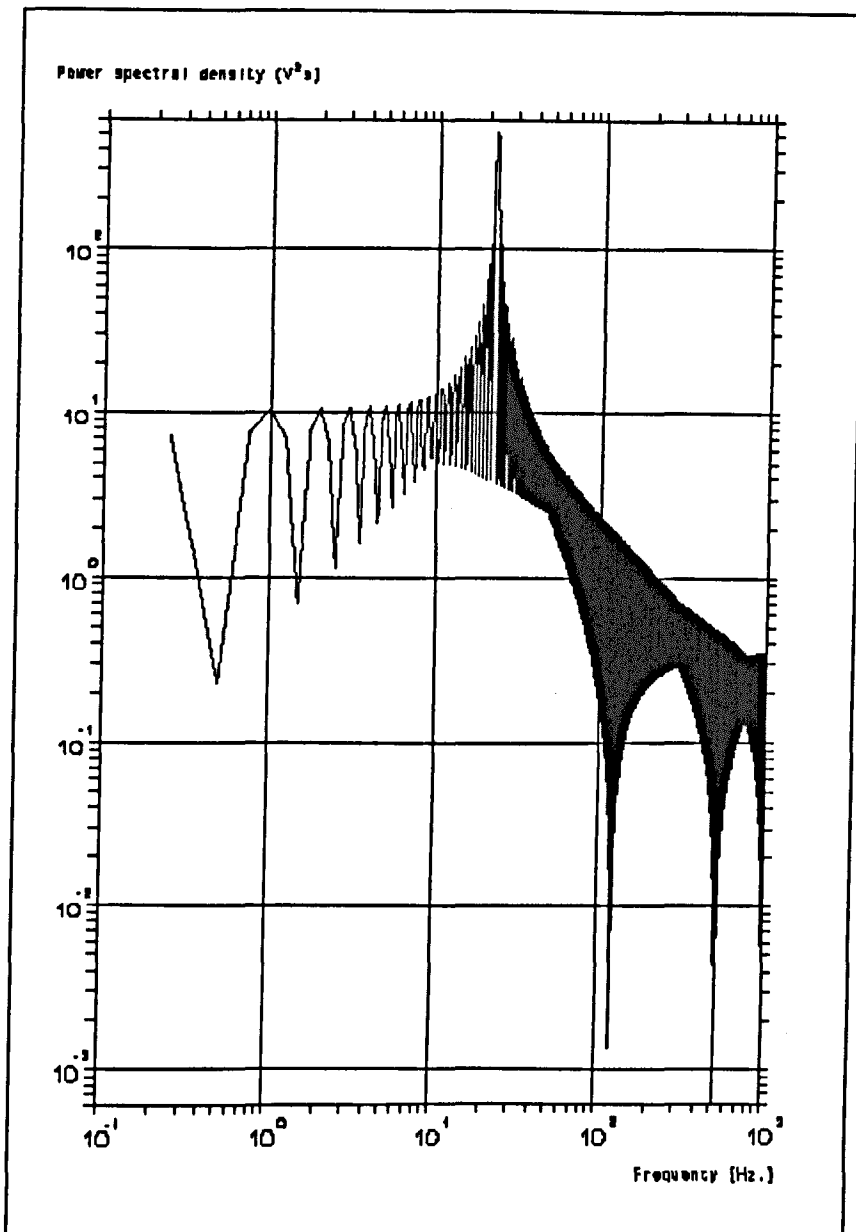


Figure D.27: "Windowing" suppresses leakage significantly.



**Figure D.28:** Leakage prohibits the observation of the contribution of the turbulent velocity fluctuations to the Power Spectrum. This spectrum is made with just one single sinusoid.

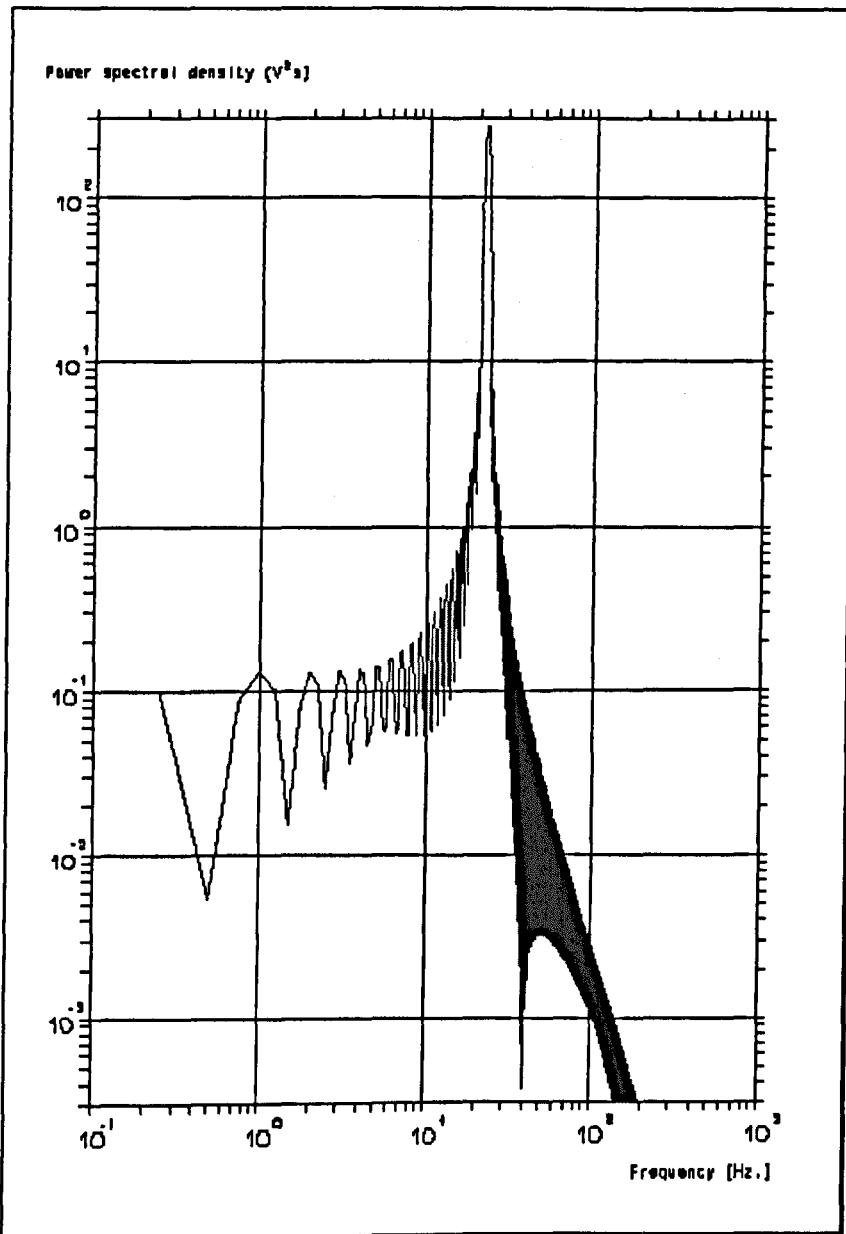
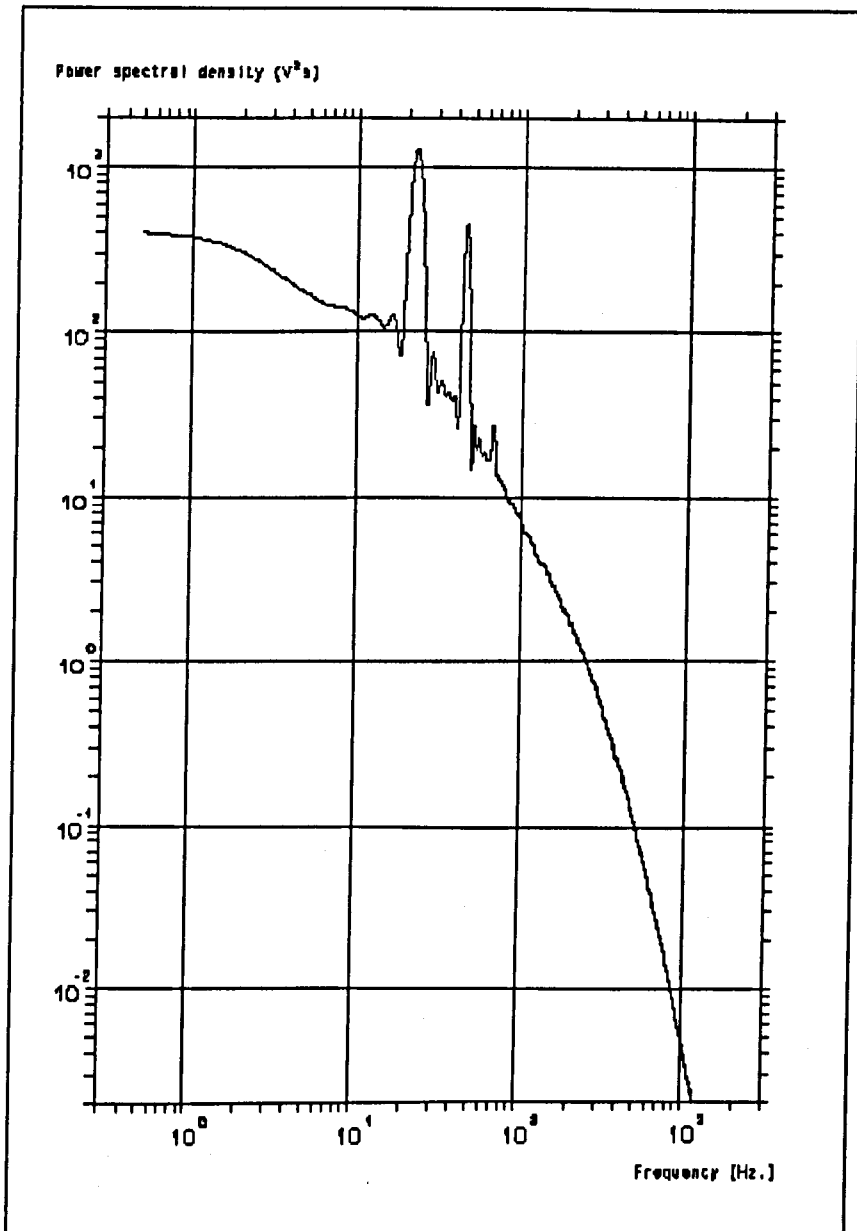


Figure D.29: Windowing can reduce these influences significantly, compare with fig.D.28.



**Figure D.30:** With an appropriate choice of the windowing function both the contributions from the periodic components and the random turbulence can be observed.

### D.1.6 Covariance and correlation functions.

An important class of functions in signal analysis is the covariance and the correlation functions. A distinction between covariance and correlation will be introduced. The essential difference between the two is that the correlation functions are dimensionless, whereas the covariance functions still have a dimension like  $m^2/s^2$ .

A very important property of this class of functions is that they are able to realize a significant data-reduction without elimination of the essential information, contained in the input signal(s). This can be understood by looking at them in more detail.

The auto covariance function of a signal  $f(t)$  is defined as:

$$R_{ff}(\tau) = \lim_{T \rightarrow \infty} \left( \frac{1}{T} \right) \int_0^T f(t) \cdot f(t + \tau) dt \quad (D.9)$$

The auto correlation function is the auto covariance function divided by the mean square value of the signal.

The cross covariance function of the functions  $f(t)$  and  $g(t)$  is defined as:

$$R_{fg}(\tau) = \lim_{T \rightarrow \infty} \left( \frac{1}{T} \right) \int_0^T f(t) \cdot g(t + \tau) dt \quad (D.10)$$

The cross correlation function is the cross covariance function, divided by the product of the RMS values of  $f(t)$  and  $g(t)$ . Note that in case  $f(t) = g(t)$ , the cross covariance and cross correlation function are identical to the auto covariance and auto correlation functions. The auto covariance and auto correlation function can therefore be regarded as a special case of the cross covariance and the cross correlation functions.

Next to the temporal covariance and correlation functions, also spatial correlation functions are used extensively in turbulence research. These are defined as:

$$R_{ff}(\Delta x) = \frac{\lim_{T \rightarrow \infty} \left( \frac{1}{T} \right) \int_0^T f(x, t) \cdot f(x + \Delta x, t) dt}{RMS[f(x, t)] \cdot RMS[f(x + \Delta x, t)]} \quad (D.11)$$

The fundamental advantage of the spatial correlation functions over the temporal correlation functions is that no assumptions need to be made about the “translation” from time to space (Taylor hypothesis) and are therefore more general valid. The disadvantages are that two LDA’s with a very accurate alignment, a very stable flow system and a lot of persistence are necessary.

Important properties of the auto covariance function are:

1.  $R_{ff}(0)$  is equal to mean square value of  $f(t)$ :
2. The phase is eliminated
3.  $R_{ff}(\tau) = R_{ff}(-\tau)$
4. When the signal is stochastic, random, non-periodic, the ACF becomes zero after a certain time shift. This is attractive for data-reduction and implicit averaging.
5. Calculation of the ACF is “one way street”: it is not possible to reconstruct the original signal from the ACF.
6. The Fourier transform of the ACF is the power spectrum of the signal.
7. The calculation time is proportional to the product of the length of the signal and the ACF. As the latter parameter is fixed, the calculation time of the ACF for signals of long duration is superior to the fast Fourier transformation (FFT), because the calculation time of the FFT is proportional to  $N^2 \log(N)$ , in which  $N$  is the number of data-points in the signal.

### D.1.5 Auto Covariance Function and Power Spectrum.

The Fourier transform of the Auto Covariance Function is the Power Spectrum of the signal. Here will not be a proof of this in a mathematically rigid sense. Therefore, the basic equation of the Fourier analysis will be introduced:

$$f(t) = \frac{1}{2}a_0 + \sum_{n=1}^{\infty} [a_n \cos(n \cdot t) + b_n \sin(n \cdot t)] \quad (\text{D.12})$$

Considering the average value ( $a_0$ ) negligible and taking the sine and cosine contributions together the previous equation becomes:

$$f(t) = \sum_{n=1}^{\infty} c_n \cos(n \cdot t + \varphi_n) \quad (\text{D.13})$$

This is allowed if  $a_n = c_n \text{COS}(\varphi_n)$  and  $b_n = -c_n \text{SIN}(\varphi_n)$ . Please note that  $c_n^2 = a_n^2 + b_n^2$  and that  $\text{ATN}(\varphi_n) = b_n / a_n$ .

The equation of the Auto Covariance Function:

$$R_{ff}(\tau) = \overline{f(t) \cdot f(t + \tau)} \quad (\text{D.14})$$

applied to equation (D.13) gives:

$$R_{ff}(\tau) = \left[ \sum_{n=1}^{\infty} c_n \cos(n \cdot t + \varphi_n) \right] \cdot \left[ \sum_{n=1}^{\infty} c_n \cos(n \cdot (t + \tau) + \varphi_n) \right] \quad (\text{D.15})$$

Moreover,

$$\overline{\cos(n \cdot t) \cdot \cos(m \cdot t)} = \frac{1}{2} \delta_{nm} \quad (\text{D.16})$$

where  $\delta$  is the Kronecker symbol, which is negligible compared to the diagonal terms; therefore:

$$R_{ff}(\tau) = \overline{\sum_{n=1}^{\infty} c_n \cos(n \cdot t + \varphi_n) \cdot c_n \cos(n \cdot (t + \tau) + \varphi_n)} \quad (\text{D.17})$$

which basically is a number of Auto Covariance Functions of cosine functions. In one of the previous chapters it has been shown that the phase is eliminated in an Auto Covariance Function and thus the following result is obtained:

$$R_{ff}(\tau) = \sum_{n=1}^{\infty} \frac{1}{2} c_n^2 \cos(n \cdot \tau) \quad (\text{D.18})$$

which is a Fourier Series of power terms. In other words: the Auto Covariance Function can be written as the inverse Fourier Transform of the Power Spectrum. But because the Fourier Transform is reversible, the Power Spectrum is the Fourier Transform of the Auto Covariance Function.

### D.1.6 Spectra of periodically sampled signals.

Normally, an analog signal is sampled with a specific time  $t$  (seconds) and a frequency  $f$  (Hz), which give a total number of samples  $N = f \times t$  ( $N$  is determined by the sampling frequency and the length of the measurement time interval). Consequently, the Fourier series is truncated at  $N/2$  (which give us  $N/2 + 1$  values for the  $a_n$  and  $N/2 - 1$  values for the  $b_n$ )<sup>3</sup>.

---

<sup>3</sup> The Fourier Transform in its elementary form is a one-to-one projection from the time domain to the frequency domain. With a limited number of samples this means that the transformation can be written

Thus, a periodically sampled signal does not only have a lower limit in its spectral composition ( $1/\Delta T$ ), but also an upper limit ( $1/(2\Delta t)$ ,  $\Delta t=1/f$ ), in which  $\Delta T$  is the length of the measurement time interval is and  $\Delta t$  is the time in between to successive samples. The most well-known consequence of this all is the risk of aliasing, as it is stated in the Shannon/Nyquist sampling theorem:

*When we want to describe a signal by sampling it with a fixed frequency, this can be achieved provided that this signal does not contain spectral components above half this sampling frequency.*

Frequencies which are above half this sampling frequency appear as "ghost signals" with a frequency which is as much below half the sampling frequency as the original frequency was above it (aliases). This half of the sampling frequency is therefore often referred to as the folding or Nyquist frequency. Aliasing needs to be avoided at all costs, because information, which has been corrupted by aliasing, cannot be corrected anymore and therefore needs to be treated as trash. The correct use of antialiasing filters is therefore essential.

#### **D.1.7 Optimisation of the measurement times.**

It has been highlighted that there is a severe lack of knowledge on the time, required to do an experiment. Many researchers tend to use too short measurement times. However, there is a great difference between a collection of numbers acquired in a short time and results on which firm conclusions about the flow can be based. The experimenters tend to look at relatively simple parameters like the average velocity and the RMS value of the velocity fluctuations to decide when the experiment can be terminated. However, it looks as if the variance in such parameters decays pretty rapidly, but that does not mean that it is sufficient for more complicated parameters such as higher moments and turbulence power spectra. For the determination of the

---

as a set of  $N$  equations with  $N$  unknowns. Of course, no more than  $N$  independent solutions can be obtained.

turbulence power spectrum, the information is presented in a large number of bins of frequency. To get the same value of the variance in each bin compared to the RMS value, this requires a longer time record. Such parameters are more vulnerable for deviations than an average velocity.

The analysis becomes more complicated as soon as a flow becomes intermittent. The most well-known example of an intermittent flow is the free jet. At its boundaries the flow has a strongly intermittent character where the fast moving fluid from the jet and the stationary fluid move in and out of the measurement volume. When the average value and the RMS value of the fluctuations or even higher moments of the distribution need to be measured, a very long recording time has to be considered: the integral time scale is very long due to the intermittent character of the flow, compared to stationary flows. Moreover, before planning any experiments and the recording time it is important to take the properties of the flow into account. It is also relevant that the flow (system) is stable during this measurement time.

## List of Figures

### Chapter 1

<b>Figure 1.2.1:</b> Principle of the tracer technique	9
--	---

### Chapter 2

<b>Figure 2.1.1:</b> Flow patterns in vertical upward flow	13
<b>Figure 2.1.2:</b> Flow Patterns in horizontal two-phase flow	15
<b>Figure 2.1.3:</b> Vertical annular flow	17
<b>Figure 2.2.1:</b> Two-phase flow pattern transitions, $Y=0$	21
<b>Figure 2.3.1:</b> Mechanism of droplet entrainment. Figure taken from Azzopardi (1997)	31
<b>Figure 2.3.2:</b> Schematic representation of the variation of film flow	35
<b>Figure 2.4.1:</b> Momentum balance on an element of annular vertical upward flow	38
<b>Figure 2.4.2:</b> Interests in pressure drop in Venturi	43
<b>Figure 2.4.3:</b> Example of the three main mechanisms of pressure drops in Venturi	49
<b>Figure 2.5.1:</b> Variation of film thickness with inclination angle. Figure taken from Paz <i>et al.</i> (1984)	55
<b>Figure 2.6.1:</b> Signal flow diagram	60
<b>Figure 2.6.2:</b> Film thickness trace with average value and probability distribution	62

### Chapter 3

<b>Figure 3.1.1:</b> Geometrical characteristic of Venturi. Units in mm	67
<b>Figure 3.1.2:</b> Inclination flow facility	68
<b>Figure 3.1.3:</b> Inclination flow facility	69
<b>Figure 3.1.4:</b> Schematic arrangement of inclination flow facility	70
<b>Figure 3.2.1:</b> Arrangement for pressure drop measurements	72
<b>Figure 3.3.1:</b> Main test section with flush-mounted probes	74
<b>Figure 3.3.2:</b> Throat test section with flush-mounted probes	74
<b>Figure 3.3.3:</b> Sketch of the arrangement for data collection	75
<b>Figure 3.3.4:</b> Main test section cylinder. Unit in mm	76
<b>Figure 3.3.5:</b> Throat test section cylinder. Unit in mm	76

<b>Figure 3.3.7:</b> Calibration curve for flush mounted probes in the main test section showing signal plateau. Conductivity = 612 $\mu\text{S}/\text{cm}$	77
<b>Figure 3.3.8:</b> Calibration curve for flush mounted probes in the throat test section showing signal plateau. Conductivity = 612 $\mu\text{S}/\text{cm}$	78
<b>Figure 3.3.9:</b> Wire probe test section for film thickness measurement at the bottom of pipe	79
<b>Figure 3.3.10:</b> Calibration lines for the three pairs of probes for a conductivity of 612 $\mu\text{S}/\text{cm}$	80
<b>Figure 3.4.1:</b> Partial take-off device for the main pipe	83
<b>Figure 3.4.2:</b> Internal cylinder equipped used for the pipe. Unit in mm	83
<b>Figure 3.4.3:</b> Partial take-off device for the throat	84
<b>Figure 3.4.4:</b> Internal cylinder used for the throat. Unit in mm	84
 <b>Chapter 4</b>	
<b>Figure 4.1:</b> Take-off characteristic of the porous sinter wall	90
<b>Figure 4.1.1:</b> Liquid flow rate variation with the angle of inclination in the main section. Gas mass flowrate=0.04 kg/s, liquid mass flowrate=0.0079 kg/s	92
<b>Figure 4.1.2:</b> Liquid flow rate variation with the angle of inclination in the main section. Gas mass flowrate=0.04 kg/s, liquid mass flowrate=0.0131 kg/s	92
<b>Figure 4.1.3:</b> Liquid flow rate variation with gas mass flowrate in the main section. Liquid mass flowrate=0.0131 kg/s, angle of inclination=0°	94
<b>Figure 4.1.4:</b> Liquid flow rate variation with gas mass flowrate in the main section. Liquid mass flowrate=0.0131 kg/s, angle of inclination=20°	95
<b>Figure 4.1.5:</b> Liquid flow rate variation with gas mass flowrate in the main section. Liquid mass flowrate=0.0131 kg/s, angle of inclination=45°	95
<b>Figure 4.1.6:</b> Liquid flow rate variation with gas mass flowrate in the main section. Liquid mass flowrate=0.0131 kg/s, angle of inclination=70°	96
<b>Figure 4.1.7:</b> Liquid flow rate variation with gas mass flowrate in the main section. Liquid mass flowrate=0.0131 kg/s, angle of inclination=85°	96
<b>Figure 4.1.8:</b> Liquid flow rate variation with liquid mass flowrate in the main section. Gas mass flowrate=0.04 kg/s, angle of inclination=0°	97

<b>Figure 4.1.9:</b> Liquid flow rate variation with liquid mass flowrate in the main section. Gas mass flowrate=0.04 kg/s, angle of inclination=20°	98
<b>Figure 4.1.10:</b> Liquid flow rate variation with liquid mass flowrate in the main section. Gas mass flowrate=0.04 kg/s, angle of inclination=45°	98
<b>Figure 4.1.11:</b> Liquid flow rate variation with liquid mass flowrate in the main section. Gas mass flowrate=0.04 kg/s, angle of inclination=70°	99
<b>Figure 4.1.12:</b> Liquid flow rate variation with liquid mass flowrate in the main section. Gas mass flowrate=0.04 kg/s, angle of inclination=85°	99
<b>Figure 4.1.13:</b> Entrained fraction variation with the angle of inclination and gas mass flowrate in the main section. Liquid mass flowrate=0.0079 kg/s	101
<b>Figure 4.1.14:</b> Entrained fraction variation with the angle of inclination and gas mass flowrate in the main section. Liquid mass flowrate=0.0131 kg/s	101
<b>Figure 4.1.15:</b> Entrained fraction variation with gas mass flowrate and pipe inclination in the main section. Liquid mass flowrate=0.0079 kg/s	104
<b>Figure 4.1.16:</b> Entrained fraction variation with gas mass flowrate and pipe inclination in the main section. Liquid mass flowrate=0.0131 kg/s	104
<b>Figure 4.1.17:</b> Entrained fraction variation with liquid mass flowrate in the main section. Gas mass flowrate=0.03 kg/s	106
<b>Figure 4.1.18:</b> Entrained fraction variation with liquid mass flowrate in the main section. Gas mass flowrate=0.04 kg/s	106
<b>Figure 4.2.1:</b> Liquid flow rate variation with the angle of inclination in the throat section. Gas mass flowrate=0.04 kg/s, liquid mass flowrate=0.0079 kg/s	108
<b>Figure 4.2.2:</b> Liquid flow rate variation with the angle of inclination in the throat section. Gas mass flowrate=0.04 kg/s, liquid mass flowrate=0.0131 kg/s	108
<b>Figure 4.2.3:</b> Liquid flow rate variation with gas mass flowrate in the throat section. Liquid mass flowrate=0.0131 kg/s, angle of inclination=0°	109
<b>Figure 4.2.4:</b> Liquid flow rate variation with gas mass flowrate in the throat section. Liquid mass flowrate=0.0131 kg/s, angle of inclination=45°	110
<b>Figure 4.2.5:</b> Liquid flow rate variation with gas mass flowrate in the throat section. Liquid mass flowrate=0.0131 kg/s, angle of inclination=85°	110
<b>Figure 4.2.6:</b> Liquid flow rate variation with liquid mass flowrate in the throat section. Gas mass flowrate=0.04 kg/s, angle of inclination=0°	111

<b>Figure 4.2.7:</b> Liquid flow rate variation with liquid mass flowrate in the throat section. Gas mass flowrate=0.04 kg/s, angle of inclination=45°	112
<b>Figure 4.2.8:</b> Liquid flow rate variation with liquid mass flowrate in the throat section. Gas mass flowrate=0.04 kg/s, angle of inclination=85°	112
<b>Figure 4.2.9:</b> Entrained fraction variation with inclination in the throat section. Liquid mass flowrate=0.0079 kg/s	113
<b>Figure 4.2.10:</b> Entrained fraction variation with inclination in the throat section. Liquid mass flowrate=0.0131 kg/s	114
<b>Figure 4.2.11:</b> Entrained fraction variation with gas mass flowrate in the throat section. Liquid mass flowrate=0.0079 kg/s	115
<b>Figure 4.2.12:</b> Entrained fraction variation with gas mass flowrate in the throat section. Liquid mass flowrate=0.0131 kg/s	115
<b>Figure 4.2.13:</b> Entrained fraction variation with liquid mass flowrate in the throat section. Gas mass flowrate=0.03 kg/s	116
<b>Figure 4.2.14:</b> Entrained fraction variation with liquid mass flowrate in the throat section. Gas mass flowrate=0.04 kg/s	117
<b>Figure 4.2.15:</b> Entrained fraction variation with the gas mass flux. Angle of incl.=0°	117
<b>Figure 4.2.16:</b> Entrained fraction variation with the liquid mass flux. Angle of incl.=0°	118
<b>Figure 4.2.17:</b> Entrained fraction variation with the gas mass flux. Angle of inclination=0°. The liquid mass fluxes of the present data are 7 kg/s and 11.5 kg/(s*m <sup>2</sup> ). The other data are taken from Ribeiro, Bott & Jepson (1995) [i.d.=32mm]	118
<b>Figure 4.2.18:</b> Entrained fraction variation with the liquid mass flux. Angle of inclination=0°. The liquid mass fluxes of the present data are 7 kg/s and 11.5 kg/(s*m <sup>2</sup> ). The other data are taken from Ribeiro, Bott & Jepson (1995) [i.d.=32mm]	119
<b>Figure 4.2.19:</b> Entrained fraction variation with inclination. Gas velocity=15-17 m/s. Liquid mass fluxes of the present data of 7 and 11.5 kg/(s*m <sup>2</sup> ). The other data are taken from Azzopardi <i>et al.</i> (1995)	119

## Chapter 5

<b>Figure 5.1.1:</b> Film thickness signal in the main section. Gas mass flowrate=0.04 kg/s, liquid mass flowrate=0.0131 kg/s, angle of inclination=45°, wires B	122
--	-----

<b>Figure 5.1.2:</b> PDF of film thickness in the main section. Gas mass flowrate=0.04 kg/s, liquid mass flowrate=0.0131 kg/s, angle of inclination=45°, wires B	122
<b>Figure 5.1.3:</b> Liquid film thickness distribution in the main section. Gas mass flowrate=0.04 kg/s, liquid mass flowrate=0.0079 kg/s	124
<b>Figure 5.1.4:</b> Liquid film thickness distribution in the main section. Gas mass flowrate=0.04 kg/s, liquid gas mass flowrate=0.0131 kg/s	124
<b>Figure 5.1.5:</b> Liquid film thickness distribution in the main section. Gas mass flowrate=0.04 kg/s, liquid mass flowrate=0.0317 kg/s	124
<b>Figure 5.1.6:</b> Liquid film thickness distribution. Gas mass flowrate=0.04 kg/s, liquid mass flowrate=0.0131 kg/s, angle of inclination=45°	126
<b>Figure 5.1.7:</b> Liquid film thickness variation with angle of inclination. Gas mass flowrate=0.04 kg/s, liquid mass flowrate=0.0079 kg/s	126
<b>Figure 5.1.8:</b> Liquid film thickness variation with angle of inclination. Gas mass flowrate=0.04 kg/s, liquid mass flowrate=0.0131 kg/s	127
<b>Figure 5.1.9:</b> Liquid film thickness variation with angle of inclination. Gas mass flowrate=0.04 kg/s, liquid mass flowrate=0.0317 kg/s	127
<b>Figure 5.1.10:</b> Liquid film thickness variation with angle of inclination. Gas mass flowrate=0.04 kg/s, liquid mass flowrate=0.0527 kg/s	128
<b>Figure 5.1.11:</b> Liquid film thickness variation with angle of inclination. Gas mass flowrate=0.04 kg/s, liquid mass flowrate=0.0899 kg/s	128
<b>Figure 5.1.12:</b> Liquid film thickness variation with liquid mass flowrate. Gas mass flowrate=0.04 kg/s, angle of inclination=0°	130
<b>Figure 5.1.13:</b> Liquid film thickness variation with liquid mass flowrate. Gas mass flowrate=0.04 kg/s, angle of inclination=30°	131
<b>Figure 5.1.14:</b> Liquid film thickness variation with liquid mass flowrate. Gas mass flowrate=0.04 kg/s, angle of inclination=45°	131
<b>Figure 5.1.15:</b> Liquid film thickness variation with liquid mass flowrate. Gas mass flowrate=0.04 kg/s, angle of inclination=60°	132
<b>Figure 5.1.16:</b> Liquid film thickness variation with liquid mass flowrate. Gas mass flowrate=0.04 kg/s, angle of inclination=85°	132

- Figure 5.1.17:** Variation of film thickness at the bottom with liquid superficial velocity. Angle of inclination= $60^\circ$ . Gas superficial velocity of the present data: 10.8 and 17.6 m/s. The other data are taken from Paz & Shoham (1994) 133
- Figure 5.1.18:** Liquid film thickness variation with gas mass flowrate. Liquid mass flowrate=0.0079 kg/s, angle of inclination= $0^\circ$  134
- Figure 5.1.19:** Liquid film thickness variation with gas mass flowrate. Liquid mass flowrate=0.0131 kg/s, angle of inclination= $0^\circ$  134
- Figure 5.1.20:** Liquid film thickness variation with gas mass flowrate. Liquid mass flowrate=0.0317 kg/s, angle of inclination= $0^\circ$  135
- Figure 5.1.21:** Liquid film thickness variation with gas mass flowrate. Liquid mass flowrate=0.0527 kg/s, angle of inclination= $0^\circ$  135
- Figure 5.1.22:** Liquid film thickness variation with gas mass flowrate. Liquid mass flowrate=0.0899 kg/s, angle of inclination= $0^\circ$  136
- Figure 5.1.23:** On the right variation of film thickness with time and on the left probability density function of film thickness. Gas mass flowrate=0.04 kg/s, liquid mass flowrate=0.0131 kg/s and angle of inclination= $0^\circ$  138
- Figure 5.1.24:** On the right variation of film thickness with time and on the left probability density function of film thickness. Gas mass flowrate=0.04 kg/s, liquid mass flowrate=0.0131 kg/s and angle of inclination= $30^\circ$  139
- Figure 5.1.25:** On the right variation of film thickness with time and on the left probability density function of film thickness. Gas mass flowrate=0.04 kg/s, liquid mass flowrate=0.0131 kg/s and angle of inclination= $45^\circ$  140
- Figure 5.1.26:** On the right variation of film thickness with time and on the left probability density function of film thickness. Gas mass flowrate=0.04 kg/s, liquid mass flowrate=0.0131 kg/s and angle of inclination= $60^\circ$  141
- Figure 5.1.27:** On the right variation of film thickness with time and on the left probability density function of film thickness. Gas mass flowrate=0.04 kg/s, liquid mass flowrate=0.0131 kg/s and angle of inclination= $85^\circ$  142
- Figure 5.1.28:** On the right, variation with time of film thickness measured by wires B. On the left, probability density function of film thickness. Gas mass flowrate=0.04 kg/s, liquid mass flowrate=0.0131 kg/s 146

- Figure 5.1.29:** On the right, variation with time of film thickness measured by wires C. On the left, probability density function of film thickness. Gas mass flowrate=0.04 kg/s, liquid mass flowrate=0.0131 kg/s 147
- Figure 5.1.30:** On the right, variation with time of film thickness measured by probes 3(2). On the left, probability density function of film thickness. Gas mass flowrate=0.04 Kg/s, liquid mass flowrate=0.0131 kg/s 148
- Figure 5.1.31:** On the right, variation with time of film thickness measured by probes 4(2). On the left, probability density function of film thickness. Gas mass flowrate=0.04 Kg/s, liquid mass flowrate=0.0131 kg/s 148
- Figure 5.1.32:** On the right, variation with time of film thickness measured by probes 5(2). On the left, probability density function of film thickness. Gas mass flowrate=0.04 Kg/s, liquid mass flowrate of 0.0131 kg/s 149
- Figure 5.1.33:** On the right variation of film thickness with time and on the left probability density function of film thickness. Gas mass flowrate=0.03 kg/s, liquid mass flowrate=0.0131 kg/s and angle of inclination=0° 151
- Figure 5.1.34:** On the right variation of film thickness with time and on the left probability density function of film thickness. Gas mass flowrate=0.03 kg/s, liquid mass flowrate=0.0131 kg/s and angle of inclination=30° 152
- Figure 5.1.35:** On the right variation of film thickness with time and on the left probability density function of film thickness. Gas mass flowrate=0.03 kg/s, liquid mass flowrate=0.0131 kg/s and angle of inclination=45° 153
- Figure 5.1.36:** On the right variation of film thickness with time and on the left probability density function of film thickness. Gas mass flowrate=0.03 kg/s, liquid mass flowrate=0.0131 kg/s and angle of inclination=60° 154
- Figure 5.1.37:** On the right variation of film thickness with time and on the left probability density function of film thickness. Gas mass flowrate=0.03 kg/s, liquid mass flowrate=0.0131 kg/s and angle of inclination=85° 154
- Figure 5.1.38:** On the right, variation with time of film thickness measured by wires B. On the left, probability density function of film thickness. Gas mass flowrate=0.03 kg/s, liquid mass flowrate=0.0131 kg/s 157

- Figure 5.1.39:** On the right, variation with time of film thickness measured by wires C. On the left, probability density function of film thickness. Gas mass flowrate=0.03 kg/s, liquid mass flowrate=0.0131 kg/s 158
- Figure 5.1.40:** On the right, variation with time of film thickness measured by probes 3(2). On the left, probability density function of film thickness. Gas mass flowrate=0.03 kg/s, liquid mass flowrate=0.0131 kg/s 159
- Figure 5.1.41:** On the right, variation with time of film thickness measured by probes 4(2). On the left, probability density function of film thickness. Gas mass flowrate=0.03 kg/s, liquid mass flowrate=0.0131 kg/s 159
- Figure 5.1.42:** On the right, variation with time of film thickness measured by probes 5(2). On the left, probability density function of film thickness. Gas mass flowrate=0.03 kg/s, liquid mass flowrate=0.0131 kg/s 160
- Figure 5.1.43:** Power spectrum density at the bottom. Gas mass flowrate=0.04 kg/s, liquid mass flowrate=0.0131 kg/s, angle of inclination=45° 161
- Figure 5.1.44:** Effect of liquid mass flowrate on power spectrum density at the bottom (wires B). Gas mass flowrate=0.04 kg/s, liquid mass flowrate=0.0131 kg/s, angle of inclination=0° 162
- Figure 5.1.45:** Effect of inclination on power spectrum density along the lower part of the pipe. Gas mass flowrate=0.04 kg/s, liquid mass flowrate=0.0131 kg/s 164
- Figure 5.1.46:** Frequency variation with liquid mass flowrate. Gas mass flowrate=0.04 kg/s 164
- Figure 5.1.47:** Frequency variation with angle of inclination. Gas mass flowrate=0.04 kg/s 165
- Figure 5.1.48:** Liquid based Strouhal number plotted against Lockhart-Martinelli parameter 165
- Figure 5.1.49:** Liquid based Strouhal number plotted against Lockhart-Martinelli parameter 166
- Figure 5.1.50:** Variation of RMS with liquid mass flowrate. Gas mass flowrate=0.04 kg/s, angle of inclination=0° 168
- Figure 5.1.51:** Variation of standard deviation RMS with angle of inclination. Gas mass flowrate=0.04 kg/s, liquid mass flowrate=0.0079 kg/s 169

- Figure 5.1.52:** Profile of  $1/s$  plotted against  $\cos\theta$ . Gas mass flowrate=0.04 kg/s, liquid mass flowrate=0.0131 kg/s, angle of inclination= $0^\circ$  170
- Figure 5.1.53:** Profile of  $1/s$  plotted against  $\cos\theta$ . Gas mass flowrate=0.03 kg/s, liquid mass flowrate=0.0131 kg/s, angle of inclination= $0^\circ$  171
- Figure 5.2.1:** Effect of inclination on liquid film thickness distribution in the throat section. Gas mass flowrate=0.04 kg/s, liquid mass flowrate=0.0079 kg/s 173
- Figure 5.2.2:** Effect of inclination on liquid film thickness distribution in the throat section. Gas mass flowrate=0.04 kg/s, liquid mass flowrate=0.0131 kg/s 173
- Figure 5.2.3:** Effect of inclination on liquid film thickness distribution in the throat section. Gas mass flowrate=0.04 kg/s, liquid mass flowrate=0.0317 kg/s 173
- Figure 5.2.4:** Liquid film thickness distribution. Gas mass flowrate=0.04 kg/s, liquid mass flowrate=0.0131 kg/s, angle of inclination= $45^\circ$  174
- Figure 5.2.5:** Liquid film thickness variation with angle of inclination. Gas mass flowrate=0.04 kg/s, liquid mass flowrate=0.0079 kg/s 174
- Figure 5.2.6:** Liquid film thickness variation with angle of inclination. Gas mass flowrate=0.04 kg/s, liquid mass flowrate=0.0131 kg/s 175
- Figure 5.2.7:** Liquid film thickness variation with angle of inclination. Gas mass flowrate=0.04 kg/s, liquid mass flowrate=0.0317 kg/s 175
- Figure 5.2.8:** Liquid film thickness variation with angle of inclination. Gas mass flowrate=0.04 kg/s, liquid mass flowrate=0.0527 kg/s 176
- Figure 5.2.9:** Liquid film thickness variation with angle of inclination. Gas mass flowrate=0.04 kg/s, liquid mass flowrate=0.0899 kg/s 176
- Figure 5.2.10:** Liquid film thickness variation with liquid mass flowrate. Gas mass flowrate=0.04 kg/s, angle of inclination= $0^\circ$  177
- Figure 5.2.11:** Liquid film thickness variation with liquid mass flowrate. Gas mass flowrate=0.04 kg/s, angle of inclination= $30^\circ$  178
- Figure 5.2.12:** Liquid film thickness variation with liquid mass flowrate. Gas mass flowrate=0.04 kg/s, angle of inclination= $45^\circ$  178
- Figure 5.2.13:** Liquid film thickness variation with liquid mass flowrate. Gas mass flowrate=0.04 kg/s, angle of inclination= $60^\circ$  179
- Figure 5.2.14:** Liquid film thickness variation with liquid mass flowrate. Gas mass flowrate=0.04 kg/s, angle of inclination= $85^\circ$  179

- Figure 5.2.15:** Liquid film thickness variation with gas mass flowrate. Liquid mass flowrate=0.0079 kg/s, angle of inclination=0° 180
- Figure 5.2.16:** Liquid film thickness variation with gas mass flowrate. Liquid mass flowrate=0.0131 kg/s, angle of inclination=0° 181
- Figure 5.2.17:** Liquid film thickness variation with gas mass flowrate. Liquid mass flowrate=0.0317 kg/s, angle of inclination=0° 181
- Figure 5.2.18:** Liquid film thickness variation with gas mass flowrate. Liquid mass flowrate=0.0527 kg/s, angle of inclination=0° 182
- Figure 5.2.19:** On the right, variation with time of film thickness. On the left, probability density function of film thickness. Gas mass flowrate=0.04 kg/s, liquid mass flowrate=0.0131 kg/s, angle of inclination=0° 183
- Figure 5.2.20:** On the right, variation with time of film thickness. On the left, probability density function of film thickness. Gas mass flowrate=0.04 kg/s, liquid mass flowrate=0.0131 kg/s, angle of inclination=30° 184
- Figure 5.2.21:** On the right, variation with time of film thickness. On the left, probability density function of film thickness. Gas mass flowrate=0.04 kg/s, liquid mass flowrate=0.0131 kg/s, angle of inclination=45° 184
- Figure 5.2.22:** On the right, variation with time of film thickness. On the left, probability density function of film thickness. Gas mass flowrate=0.04 kg/s, liquid mass flowrate=0.0131 kg/s, angle of inclination=60° 185
- Figure 5.2.23:** On the right, variation with time of film thickness. On the left, probability density function of film thickness. Gas mass flowrate=0.04 kg/s, liquid mass flowrate=0.0131 kg/s, angle of inclination=85° 185
- Figure 5.2.24:** On the right, variation with time of film thickness measured by wires 1(2). On the left, probability density function of film thickness. Air flowrate of 0.04 kg/s, water flowrate of 0.0131 kg/s 188
- Figure 5.2.25:** On the right, variation with time of film thickness measured by wires 4(1). On the left, probability density function of film thickness. Air flowrate of 0.04 kg/s, water flowrate of 0.0131 kg/s 189
- Figure 5.2.26:** On the right, variation with time of film thickness measured by wires 3(1). On the left, probability density function of film thickness. Air flowrate of 0.04 kg/s, water flowrate of 0.0131 kg/s 190

- Figure 5.2.27:** On the right, variation with time of film thickness measured by wires 3(2). On the left, probability density function of film thickness. Air flowrate of 0.04 kg/s, water flowrate of 0.0131 kg/s 191
- Figure 5.2.28:** On the right, variation with time of film thickness. On the left, probability density function of film thickness. Gas mass flowrate=0.03 kg/s, liquid mass flowrate=0.0131 kg/s, angle of inclination=0° 192
- Figure 5.2.29:** On the right, variation with time of film thickness. On the left, probability density function of film thickness. Gas mass flowrate=0.03 kg/s, liquid mass flowrate=0.0131 kg/s, angle of inclination=30° 193
- Figure 5.2.30:** On the right, variation with time of film thickness. On the left, probability density function of film thickness. Gas mass flowrate=0.03 kg/s, liquid mass flowrate=0.0131 kg/s, angle of inclination=45° 193
- Figure 5.2.31:** On the right, variation with time of film thickness. On the left, probability density function of film thickness. Gas mass flowrate=0.03 kg/s, liquid mass flowrate=0.0131 kg/s, angle of inclination=60° 194
- Figure 5.2.32:** On the right, variation with time of film thickness. On the left, probability density function of film thickness. Gas mass flowrate=0.03 kg/s, liquid mass flowrate=0.0131 kg/s, angle of inclination=85° 194
- Figure 5.2.33:** On the right, variation with time of film thickness measured by probes 1(2). On the left, probability density function of film thickness. Gas mass flowrate=0.03 kg/s, liquid mass flowrate=0.0131 kg/s 196
- Figure 5.2.34:** On the right, variation with time of film thickness measured by probes 4(1). On the left, probability density function of film thickness. Gas mass flowrate=0.03 kg/s, liquid mass flowrate=0.0131 kg/s 197
- Figure 5.2.35:** On the right, variation with time of film thickness measured by probes 3(2). On the left, probability density function of film thickness. Gas mass flowrate=0.03 kg/s, liquid mass flowrate=0.0131 kg/s 198
- Figure 5.2.36:** On the right, variation with time of film thickness measured by probes 3(1). On the left, probability density function of film thickness. Gas mass flowrate=0.03 kg/s, liquid mass flowrate=0.0131 kg/s 199
- Figure 5.2.37:** Power spectrum density at the lower part of the throat section. Gas mass flowrate=0.04 kg/s, liquid mass flowrate=0.0131 kg/s, angle of inclination=45° 200

- Figure 5.2.38:** Effect of liquid mass flowrate on power spectrum density of film thickness measured by probes 1(1). Gas mass flowrate=0.04 kg/s, liquid mass flowrate=0.0131 kg/s, angle of inclination=0° 201
- Figure 5.2.39:** Effect of inclination on power spectrum density along the lower part of the throat. Gas mass flowrate=0.04 kg/s, liquid mass flowrate=0.0131 kg/s 203
- Figure 5.2.40:** Frequency variation with liquid mass flowrate. Gas mass flowrate=0.04 kg/s 203
- Figure 5.2.41:** Frequency variation with angle of inclination. Gas mass flowrate=0.04 kg/s 204
- Figure 5.2.42:** Liquid based Strouhal number plotted against Lockhart-Martinelli parameter in the throat section 204
- Figure 5.2.43:** Variation of RMS with liquid mass flowrate. Gas mass flowrate=0.04 kg/s, angle of inclination=60° 206
- Figure 5.2.44:** Variation of standard deviation RMS with angle of inclination. Gas mass flowrate=0.04 kg/s, liquid mass flowrate=0.0079 kg/s 206
- Figure 5.2.45:** Profile of  $1/s$  plotted against  $\cos\theta$  in the throat section. Gas mass flowrate=0.04 kg/s, liquid mass flowrate=0.0131 kg/s, angle of inclination=0° 207
- Figure 5.2.46:** Profile of  $1/s$  plotted against  $\cos\theta$  in the throat section. Gas mass flowrate=0.03 kg/s, liquid mass flowrate=0.0131 kg/s, angle of inclination=0 208
- Figure 5.2.47:** Liquid film thickness distributions in the throat. Gas mass flowrate=0.04 kg/s, angle of inclination=2° downwards 209
- Figure 5.2.48:** Liquid film thickness distributions in the throat. Gas mass flowrate=0.04 kg/s, angle of inclination=2° upwards 209
- Figure 5.2.49:** Liquid film thickness variation with angle of inclination. Gas mass flowrate=0.04 kg/s, liquid mass flowrate=0.0131 kg/s 210
- Figure 5.2.50:** Liquid film thickness variation with gas mass flowrate. Liquid mass flowrate=0.0131 kg/s, angle of inclination=2 downwards 210
- Figure 5.2.51:** Liquid film thickness variation with gas mass flowrate. Liquid mass flowrate=0.0131 kg/s, angle of inclination=2 upwards 211
- Figure 5.3.1:** Comparison between experimental data and the model of Fukano and Ousaka (1988). Gas mass flowrate = 0.04 kg/s, angle of inclination = 0° 214

<b>Figure 5.3.2:</b> Comparison between experimental data and the model of Fukano and Ousaka (1988). Gas mass flowrate = 0.03 kg/s, angle of inclination = 0°	214
<b>Chapter 6</b>	
<b>Figure 6.1.1:</b> Positions of pressure tapings	218
<b>Figure 6.1.2:</b> Effect Pressure drop along Venturi. Gas mass flowrate=0.04 kg/s, angle of inclination=0°	219
<b>Figure 6.1.3:</b> Pressure drop along Venturi. Gas mass flowrate=0.04 kg/s, angle of inclination=2° upwards	220
<b>Figure 6.1.4:</b> Pressure drop along Venturi. Gas mass flowrate=0.04 kg/s, angle of inclination=2° downwards	220
<b>Figure 6.1.5:</b> Pressure drop along Venturi. Gas mass flowrate=0.04 kg/s, angle of inclination=85°	221
<b>Figure 6.1.6:</b> Effect of angle of inclination on pressure drop. Gas mass flowrate=0.04 kg/s, liquid mass flowrate=0.0079 kg/s	221
<b>Figure 6.1.7:</b> Effect of angle of inclination on pressure drop. Gas mass flowrate=0.04 kg/s, liquid mass flowrate=0.0187 kg/s	222
<b>Figure 6.1.8:</b> Effect of angle of inclination on pressure drop. Gas mass flowrate=0.04 kg/s, liquid mass flowrate=0.0317 kg/s	222
<b>Figure 6.1.9:</b> Effect of angle of inclination on pressure drop. Gas mass flowrate=0.04 kg/s, liquid mass flowrate=0.0527 kg/s	223
<b>Figure 6.1.10:</b> Effect of liquid mass flowrate on total pressure drop in Venturi. Gas mass flowrate=0.04 kg/s	224
<b>Figure 6.1.11:</b> Effect of liquid mass flowrate on pressure recovery in the diffuser. Gas mass flowrate=0.04 kg/s	224
<b>Figure 6.1.12:</b> Effect of liquid mass flowrate on pressure drop variations with inclination. Gas mass flowrate=0.0189 kg/s. Data taken from Azzopardi <i>et al.</i> (1989), Venturi A	228
<b>Figure 6.1.13:</b> Effect of Venturi geometrical characteristics on pressure difference at the throat for different flow conditions. Data taken from Azzopardi <i>et al.</i> (1989), Venturi A and D	229

<b>Figure 6.2.1:</b> Comparison between experimental data and model of Azzopardi & Co-workers. Gas mass flowrate=0.04 kg/s, angle of inclination=0°	231
<b>Figure 6.2.2:</b> Comparison between experimental data and model of Azzopardi & Co-workers. Gas mass flowrate=0.04 kg/s, angle of inclination=85°	231
<b>Figure 6.2.3:</b> Comparison between experimental and predicted pressure drop. Gas mass flowrate=0.04 kg/s, angle of inclination=0°	232
<b>Figure 6.2.4:</b> Comparison between experimental and predicted variation of total pressure drop with liquid mass flowrate. Gas mass flowrate=0.04 kg/s, angle of inclination=0°	233
<b>Figure 6.2.5:</b> Comparison between experimental and predicted variation of total pressure drop with liquid mass flowrate. Gas mass flowrate=0.04 kg/s, angle of inclination=85°	233
<b>Figure 6.2.6:</b> Comparison between experimental and predicted variation of pressure recovery with liquid mass flowrate. Gas mass flowrate=0.04 kg/s, angle of inclination=0°	234
<b>Figure 6.2.7:</b> Comparison between experimental and predicted variation of pressure recovery with liquid mass flowrate. Gas mass flowrate=0.04 kg/s, angle of inclination=85°	234

## Appendix A

<b>Figure A.1:</b> Wetted approach Venturi scrubber	244
---	-----

## Appendix B.1

<b>Figure B.1:</b> Simple momentum balance on an element of duct with separated flow	245
--	-----

## Appendix D

<b>Figure D.1:</b> When we take the interval [0,1] seconds as the basic interval it can -by pure accident happen that an integer number of cycles fits into this interval.	256
<b>Figure D.2:</b> Periodic continuation of this signal does not cause any trouble	256
<b>Figure D.3:</b> But usually this is not the case.....	257
<b>Figure D.4:</b> ... and the periodic continuation of the signal is equipped with some weird jumps at the interval boundaries at 0 and 1 sec.	257
<b>Figure D.5:</b> If an integer number of cycles fits precisely into the transformation window, the spectrum consists of one single line.	258
<b>Figure D.6:</b> But if it does not fit so nicely "leakage" is the result. This is caused by the jumps at the boundaries of the continued signal, which represents different frequencies.	258

<b>Figure D.7:</b> Interpolated spectrum with a DC contribution, without windowing.	261
<b>Figure D.8:</b> Interpolated spectrum with a DC contribution and windowing.	262
<b>Figure D.9:</b> Interpolated spectrum after removal of the DC contribution.	263
<b>Figure D.10:</b> The original signal can be regarded as.....	264
<b>Figure D.11:</b> ....a combination of the fluctuations and.....	264
<b>Figure D.12:</b> ....the slope, which leads to discontinuities at the interval boundaries.	264
<b>Figure D.13:</b> Spectrum obtained as the average of 9 independent estimators without removal of the trend (sawtooth function).	265
<b>Figure D.14:</b> Spectrum obtained as the average of 9 independent estimators after removal of the trend (sawtooth function).	266
<b>Figure D.15:</b> The simplest windowing function is the constant 1.	269
<b>Figure D.16:</b> Spectrum of the rectangular windowing function.	269
<b>Figure D.17:</b> One of the simplest windowing functions: the triangle.	270
<b>Figure D.18:</b> Spectrum of the triangular windowing function.	270
<b>Figure D.19:</b> An often applied windowing function: $0.5 + 0.5 * \text{COSINE}$ .	271
<b>Figure D.20:</b> Spectrum of the shifted cosine windowing function.	271
<b>Figure D.21:</b> Half a cosine is a suitable one as well, but it has stronger sidelobes.	272
<b>Figure D.22:</b> Spectrum of the half-cosine windowing function.	272
<b>Figure D.23:</b> A shifted and scaled Gaussian function is often applied as well.	273
<b>Figure D.24:</b> Spectrum of the shifted and scaled Gaussian windowing function	273
<b>Figure D.25:</b> A combination of a half-cosine and a part of the Gauss curve yields an effective windowing function.	274
<b>Figure D.26:</b> Spectrum of the combined half-cosine/Gauss windowing function.	274
<b>Figure D.27:</b> "Windowing" suppresses leakage significantly.	275
<b>Figure D.28:</b> Leakage prohibits the observation of the contribution of the turbulent velocity fluctuations to the Power Spectrum. This spectrum is made with just one single sinusoid.	276
<b>Figure D.29:</b> Windowing can reduce these influences significantly, compare with fig.D.28.	277
<b>Figure D.30:</b> With an appropriate choice of the windowing function both the contributions from the periodic components and the random turbulence can be observed.	278

## List of Tables

### Chapter 3

<b>Table 3.3.1:</b> Film thickness obtained with the cylinders into the two test sections	76
---	----

### Chapter 4

<b>Table 4.1:</b> Positions of the porous sintered wall unit window	89
---	----

### Chapter 5

<b>Table 5.1:</b> Gas mass flowrates and gas velocities	121
<b>Table 5.2:</b> Liquid mass flowrates and liquid velocities	121
<b>Table 5.1.1:</b> Characteristics of the liquid film at different inclinations, gas mass flowrate=0.04 kg/s, liquid mass flowrate=0.0131 kg/s	144
<b>Table 5.1.2:</b> Characteristics of liquid film at different inclinations, gas mass flowrate=0.03 kg/s, liquid mass flowrate=0.0131 kg/s	156
<b>Table 5.2.1:</b> Characteristics of the liquid film at different inclinations, gas mass flowrate=0.04 kg/s, liquid mass flowrate=0.0131 kg/s	186
<b>Table 5.2.2:</b> Characteristics of liquid film at different inclinations, gas mass flowrate=0.03 kg/s, liquid mass flowrate=0.0131 kg/s	195

### Appendix A

<b>Table A.1:</b> Advantages and disadvantages of wet scrubbers (Muir, 1992)	243
--	-----

## Nomenclature

### Symbols

$a$	Length of the window	m
$a_n$	coefficient of Fourier transform	[signal]
$A$	Pipe cross sectional area	$m^2$
$b$	Perimeter between the fins	m
$b_n$	coefficient of Fourier transform	[signal]
$c$	Capacitance	F
$c_i$	Tracer concentration in the injected solution	$mol/m^3$
$c_p$	Tracer concentration in the pipeline	$mol/m^3$
$C$	Droplet Concentration	$kg/m^3$
$C_D$	Drag coefficient between gas and drop	
$d$	Throat inside diameter	m
$D$	Pipe inside diameter	m
$E$	Entrained fraction	
$f$	Moody friction factor	
$f(t)$	signal	[signal]
$F$	Frequency	Hz
$F_s$	Sampling frequency	Hz
$F_n$	Nyquist frequency	Hz
$F_w(t)$	Fourier transform of the windowing function	[signal]
$F(\omega)$	Spectrum of the signal	[signal] <sup>2</sup>
$g$	Acceleration due to gravity	m/s
$k$	Circumferential transport coefficient	mm
$k_D$	Deposition coefficient	m/s

$K_{\text{mass}}$	Constant of mass transfer	$\text{m}^2/\text{s}^2$
$l_t$	Length of throat	m
L/G	Liquid to gas ratio	litres/ $\text{m}^3$
m	Mass flux	$\text{kg}/\text{m}^2\text{s}$
M	Mass flow rate	kg/s
p	pipe cross sectional perimeter	
P	Pressure	Pa
Q	Volumetric flow rate	$\text{m}^3/\text{s}$
$Q_i$	Injection volumetric flowrate of tracer solution	$\text{m}^3/\text{s}$
r	Pipe inside radius	m
R	Resistance	$\Omega$
$R_A$	Rate of atomization	$\text{kg}/\text{m}^2\text{s}$
$R_D$	Rate of deposition	$\text{kg}/\text{m}^2\text{s}$
Re	Reynolds number	
$R_{ff}(\tau)$	Auto covariance function	[signal]
$R_{fg}(\tau)$	Cross correlation function	[signal]
RMS	Root-mean-squared value of the signal (standard deviation)	[signal]
s	Liquid film thickness	m
St	Strouhal number	$\text{Hz}\cdot\text{s}$
t	Time	s
T	Signal period	s
U	Fluid velocity	m/s
$\bar{U}$	Mean velocity	m/s
$U_R$	Slip ratio	
$W(\omega)$	Spectrum of the windowing function	[signal] <sup>2</sup>
x	Distance in the axial direction	m
$x_g$	Gas quality	
X	Lockhart Martinelli parameter	
$X_R$	Reactance	$\Omega$
y	Distance in the radial direction	m

Z Impedance

$\Omega$

## Greek Symbols

$\alpha$	Inclination of the pipe	Deg
$\beta$	Half angle of the convergent	Deg
$\gamma$	Rate of momentum transport	kg*m/s <sup>2</sup>
$\Gamma_x$	Flow rate per unit width of surface	kg/m*s
$\delta$	Half angle of the diffuser	Deg
$\varepsilon_g$	Void fraction	
$\theta$	Circumferential coordinate angle	Deg
$\mu$	Dynamic viscosity	kg/ms
$\rho$	Density	kg/s
$\sigma$	Surface tension	N/m
$\tau$	Shear Stress	N/m <sup>2</sup>
$\tau_i$	Interfacial shear stress	N/m <sup>2</sup>
$\tau_0$	Wall shear stress	N/m <sup>2</sup>
$\nu$	Cinematic viscosity	m <sup>2</sup> /s
$\phi$	Two phase multiplier	
$\omega_1$	Off-taken liquid rate at the intercept (y=0)	kg/s

## Subscripts

A	Atomization
<i>acc</i>	<i>Accelerational</i>
D	Deposition
dep	Deposition
drop	Drops
drop,f	Drops at the end of throat

ent	Entrainment
eq	Equivalent taking into account film thickness
<i>fric</i>	Frictional
<i>g</i>	Gas
gd	Gas relative to the gas-liquid mixture
gH	Gas in the homogeneous model
<i>grav</i>	Gravitational
H	Homogeneous
<i>i</i>	Inlet of the venturi
it	Difference between the inlet and the throat of the Venturi
<i>l</i>	Liquid
ld	Liquid relative to the gas-liquid mixture
LE	Liquid Entrained
LF	Liquid film
LFF	Liquid film between the fins
LFC	Critical liquid film
mass	Mass transfer
MP	Multi phase
<i>sg</i>	Superficial gas
<i>sl</i>	Superficial liquid
SP	Single phase
TP	Two phase
<i>x</i>	Axial direction

### Greek Subscripts

$\theta$	Circumferential direction
----------	---------------------------

## BIBLIOGRAPHY

- Abolfadl, M.A., (1984), "Analysis of annular two-phase flow with liquid entrainment", *Ph.D. Thesis*, Thayer School of Engineering, Dartmouth College, U.S.A.
- Adelberg, M., (1967), "Breakup rate and penetration of a liquid jet in a gas stream", *A.I.A.A. J.*, Vol. 5, No. 8, pp. 1408-1415.
- Allen, R.W.K. and Van Santen, A., (1996), "Designing for pressure drop in Venturi scrubbers: the importance of dry pressure drop", *Chem. Eng. Journal*, Vol. 61, pp. 203-211.
- Alves, G.E., (1954), "Co-current liquid-gas flow in a pipeline contactor", *Chemical and Process Engineering*, Vol. 50, pp. 449-456.
- Alves, I.N., Caetano, E., Minami, K. And Shoham, O., (1991), "Modeling annular flow behavior for gas wells", *SPEPE*, pp. 435-440.
- Andritsos, N., (1986), "Effect of pipe diameter and liquid viscosity on horizontal stratified flow", *Ph.D. Thesis*, Univ. of Illinois, Urbana.
- Andritsos, N. and Hanratty, T. J., (1987), "Influence of interfacial waves in stratified gas-liquid flows, *AIChE Journal*, Vol. 33, 444-454
- Andritsos, N. (1992), "Statistical analysis of waves in horizontal stratified flow", *Int. J. Multiphase Flow*, Vol. 18, 456-473.
- Arnold, C.R. and Hewitt, G.F., (1967), "Further Developments in the Photography of Two-Phase Gas-Liquid Flow", *J. Photographic Sc.*, Vol. 15, pp. 97-114.

- Asali, J.C., Hanratty, T.J. and Andreussi, P., (1985), "Interfacial drag and film height for vertical annular flow", *AIChE Journal*, Vol. 31, No. 6, pp. 895-902.
- Azzopardi, B.J. and Whalley, P.B., (1980), "Artificial waves in annular two-phase flow", ASME Winter Annual Meeting, Chicago, Published in *Basic Mechanisms in Two-Phase Flow and Heat-Transfer*, pp. 1-8.
- Azzopardi, B.J., Taylor, S. and Gibbons, D.B., (1983), "Annular two-phase flow in large diameter pipes", *bzt. Conf. on Physical Modelling of Multi-Phase Flow*, April 19-21, Coventry. pp. 267-282.
- Azzopardi, B.J. and Govan, A.H., (1984), "The modelling of Venturi scrubbers", *Filtration & Separation*, May / June, pp. 196-200.
- Azzopardi, B.J. and Govan, A.H., (1985), "Annular two-phase flow in Venturis", European Two-Phase Flow Group Meeting, Marchwood Eng. Lab., June 4-7.
- Azzopardi, B.J., Memory, S.B. and Smith, P. (1989), "Data from an experimental study of annular flow in a Venturi", AERE R13352, Thermal Hydraulics Division, Harwell Laboratory.
- Azzopardi, B.J., Teixeira, S.F.C.F., Govan, A.H. and Bott, T.R., (1991), "An improved model for pressure drop in Venturi scrubbers", *Trans. I. Chem. E.*, Vol. 69, Part B, pp. 237-245.
- Azzopardi, B.J., (1993), "Liquid distribution in Venturi scrubbers – The importance of liquid films on channel walls", *Chem. Eng. Sci.*, Vol. 48, No. 15, pp. 2807-2813.
- Azzopardi, B.J., (1997), "Drops in annular two-phase flow", *Int. J. Multiphase Flow*, Vol. 23, Suppl., pp. 1-53.

Azzopardi, B.J., Zaidi, S.H. and Jepson, D.M., (1997), "Entrained fraction in inclined annular gas-liquid flow", *Proceedings of the ASME Fluids Engineering Division*, Vol. 244, pp. 69-76.

Barnea, D., Shoham, O. and Taitel, Y. (1980), Flow pattern characterization in two phase flow by electrical conductance probe, *International Journal of Multiphase Flow*, Vol. 6, pp. 387-397.

Barnea, D., Shoham, O., Taitel, Y. and Dukler, A., (1980), "Flow pattern transition for gas-liquid flow in horizontal and inclined pipes", *International Journal of Multiphase Flow*, Vol. 6, pp. 217-225.

Barnea, D., Shoham, O. and Taitel, Y., (1982a), "Flow pattern transition for vertical downward two phase flow", *Chem. Engng Sci.*, Vol. 37, pp. 741-746.

Barnea, D., Shoham, O. and Taitel, Y., (1982b), "Flow pattern transition for downward inclined two phase flow; horizontal to vertical", *Chem. Engng Sci.*, Vol. 37, pp. 735-740.

Barnea, D., Shoman, O. and Taitel, Y., (1985), "Gas-liquid flow in inclined tubes: flow pattern transitions for upward flow", *Chem. Eng. Sci.*, Vol. 40, pp. 131-136.

Baroczy, C.J., (1963), "Correlation of liquid fraction in two-phase flow with application to liquid metals", 6<sup>th</sup> National Heat Transfer Conference, *AIChE Journal*, Preprint No. 26. (from Azzopardi and Hills (1999)).

Beggs, H.D. and Brill, J.P., (1973), "A study of two-phase flow in inclined pipes", *J. Petroleum Technology*, Vol. 25, pp. 607-617.

Behie, S.W. and Beeckmans J.M., (1974), "Effects of water injection arrangement on the performance of a Venturi scrubber", *J. of the Air Pollution Control Association*, Vol. 24, No. 10, pp. 943-945,.

Bertodano, M.A.L., Jan, C.S. and Beus, S.G., (1997), "Annular flow entrainment rate experiment in a small vertical pipe", *Nucl. Engng. And Design*, Vol. 178, pp. 61-70.

Bessem, J.M. and van Maanen, H.R.E., (1994), "Optimization of digital storage of random analogue data", *Meas. Sci. Technology*, Vol. 5, pp. 1331-1338.

Boll, R.H., (1973), "Particle collection and pressure drop in Venturi scrubbers", *Ind. Eng. Chem. Fundam.*, Vol. 12, No. 1, pp. 40-50.

Brink, J.A. and Contant, C.E., (1958), "Experiments on an industrial Venturi scrubber", *Industrial and Engineering Chemistry*, Vol. 50, No. 8, pp. 1157-1160.

Brown, D.J., Jensen, A. and Whalley, P.B., (1975), "Non-equilibrium effects in heated and unheated annular two-phase flow", ASME paper No. 75-WA/HT-7. (from Govan (1990)).

Butterworth, D., (1969), "Note of fully-developed, horizontal, annular two-phase flow", *Chemical Engineering Science*, Vol. 24, pp. 1832-1834.

Butterworth, D., (1972), "Air-water annular flow in a horizontal tube", *Progress in Heat and Mass Transfer* (G. Hestroni Ed.), Vol. 6, pp. 235-251.

Butterworth, D. and Pulling, D.J., (1973), "Film flow and film thickness measurements for horizontal, annular, air-water flow", Report AERE-R 7576, U.K.A.E.A., Harwell, Oxon.

Caetano, E.F., (1985), "Upward vertical two phase flow through an annulus", *Ph.D. Thesis*, University of Tulsa, Tulsa, OK.

Calvert, S., (1970), "Venturi and other atomizing scrubbers: Efficiency and pressure drop", *AIChE Journal*, Vol. 16, No. 3, pp. 392-396.

Calvert, S., (1977), *Scrubbing*, in: A.C. STERN (ed.), *Air Pollution*, 3rd ed., Vol. IV, Chapter 6. Academic Press, New York,.

Chisholm, D., (1973), "An equation for velocity ratio in two-phase flow", N.E.L., Report No. 535.

Chisholm, D., (1977), "Two phase flow through sharp-edged orifices", Research note, *Journal of mechanical engineering science*.

Conte, G., (2000), "An experimental study for the characterization for gas/liquid flow splitting at T-junctions", *Ph.D. Thesis*, University of Nottingham, UK.

Costigan, G. and Whalley, P.B., (1997), "Slug flow regime identification from dynamic void fraction measurements in vertical air-water flows", *International Journal of Multiphase Flow*, Vol. 23, pp. 263-282.

Cousins, L.B. and Hewitt, G.F., (1968a), "Liquid phase mass transfer in annular two-phase flow: Droplet deposition and liquid entrainment", ,United Kingdom Atomic Energy Authority, Harwell, Report No. AERE-R 5657.

Cousins, L.B. and Hewitt, G.F., (1968b), "Liquid phase mass transfer in annular two-phase flow: Radial liquid mixing", U.K.A.E.A., Report No. AERE-R 5693.

Dallman, J.C., (1978), "Investigation of separated flow model in annular gas-liquid two phase flows", *Ph.D. Thesis*, University of Illinois, Urbana, IL.

De Leeuw, H., (1994), "Wet gas flow measurement using a combination of Venturi meter and a tracer technique", In proceedings of the north sea flow measurement workshop, Peebles, Scotland, October.

De Leeuw, H., (1997), "Venturi meter performance in wet gas flow", In proceedings of multiphase '97 conference, Cannes, France, June.

De Leeuw, H., (1997), "Liquid correction of Venturi meter readings in wet-gas flow", In proceedings of the north sea flow measurement workshop, Kristiansand, Norway, October.

Dukler, A.E., (1960), "Fluid mechanics and heat transfer in vertical falling film systems", *Chem. Eng. Prog.*, Vol. 56, No. 30, pp. 1-10.

Fernandez-Alonso, D., (2000), "Experimental study of hydrodynamics in laboratory-scale Venturi scrubbers with two different types of liquid injection", *Ph.D. Thesis*, University of Nottingham, UK.

Fisher, S.A. and Pearce, D.L., (1978), "A theoretical model for describing horizontal annular flows", Int. Sem. Heat Mass Transfer, Two phase flow in energy and chem. systems, Dubrovnik, Yugoslavia, Paper No. 3.3-5.

Friedel, L., (1979), "Improved friction pressure drop calculations for horizontal and vertical two-phase pipe flow", European Two-Phase Flow Group Meeting. (from Azzopardi and Hills (1999)).

Fukano, T., Ousaka, A., Morimoto, T. and Sekoguchi, K., (1983), "Air-annular two-phase flow in a horizontal tube", 2<sup>nd</sup> Report, *Bull. JSME*, 26, 1387-1395.

Fukano, T. and Ousaka, A., (1989), "Prediction of the circumferential distribution of the film thickness in horizontal and near-horizontal gas-liquid annular flows", *Int. J. Multiphase Flow*, Vol. 15, No. 3, pp. 403-419.

Govan, A.H., (1990) "Modelling of vertical annular and dispersed two-phase flows", *Ph.D. thesis*, Imperial College, London

Haller, H., Muschelknautz, E. and Schultz, T., (1989), "Venturi scrubber calculation and optimization", *Chemical Engineering and Technology*, Vol. 12, pp. 188-195.

- Hanratty, T.J. and Asali, J.C., (1983), "Entrainment measurements and their use in design equations", Report to the Design Inst. for Multiphase Processing, University of Illinois, Urbana, IL.
- Hassan, A.R. and Kabir, C.S., (1988), "A study of multiphase flow behavior in vertical wells", *SPEPE*, pp. 263-272; *Trans.*, AIME, Vol. 285.
- Hawkes, N.J., (1996), "Wispy-annular flow", *Ph.D. Thesis*, Imperial College of Science, Technology and Medicine, London.
- Henstock, W.H. and Hanratty, T.J., (1976), "The interfacial drag and the height of the wall layer in annular flows", *AIChE J.*, Vol. 22, No. 6, pp. 990-1000.
- Hesketh, H.E., (1974), "Atomization and cloud behaviour in Venturi scrubbers", U.S. – U.S.S.R. Symposium. Control of fine particulate emissions, San Francisco, January 15-18.
- Hewitt, G.F., (1961), "Analysis of annular two phase flow: application of the Dukler analysis to vertical upward flow in a tube", U.K.A.E.A., Harwell, Report No. AERE-R 3680.
- Hewitt, G. F. and Nicholls, B., (1969), "Film thickness measurements in annular two-phase flow using a fluorescence spectrometer technique, Report AERE-R4506, UKAEA.
- Hewitt, G.F. and Hall-Taylor, N.S., (1970), "Annular two-phase flow", Pergamon Press, Oxford.
- Hewitt, G.F. and Whalley, P.B., (1980), "Advanced optical instrumentation methods", *Int. J. Multiphase Flow*, Vol. 6, pp. 139-156.

Hewitt, G.F. and Govan, A.H., (1990), "Phenomenological modelling of non-equilibrium flows with phase change", *Int. J. Heat and Mass Transfer*, Vol. 33, No. 2, pp. 229-242.

Hills, J.H., (1997), "The critical liquid flow rates for wave and droplet formation in annular gas-liquid flow", *Experimental Heat Transfer, Fluid Mechanics and Thermodynamics*, pp. 1241-1246.

Hollands, K.G.T. and Goel, K.C., (1975), "A general method for predicting pressure loss in Venturi scrubbers", *Ind. Eng. Chem. Fundam.*, Vol. 14, No. 1, pp. 16-22.

Holowach, M.J., Hockreiter, L.E. and Cheung, F.B., (2002), "A model of droplet entrainment in heated annular flow", *Int. J. Heat and Fluid Flow*, Vol. 23, pp. 807-822.

Holt, A.J., (1996), "Two-phase pressure drop and void fraction in narrow channels", *Ph.D. Thesis*, University of Nottingham, UK.

Hurlburt, E.T. and Newell, T.A., (2000), "Prediction of the circumferential film thickness distribution in horizontal annular gas-liquid flow", *Journal of Fluids Engineering, Transaction of the ASME*, Vol. 122, pp. 396-402.

Hutchinson, P. and Whalley, P.B., (1973), "A possible characterisation of entrainment in annular flow", *Chem. Engng. Sci.*, Vol. 28, pp. 974-975.

Ilobi, M.I. and Ikoku, C.U., (1981), "Minimum gas flow rate for continuous liquid removal in gas wells", Paper SPE 10170 presented at the SPE Annual Technical Conference and Exhibition, San Antonio.

Ishii, M. and Grolmes, M.A., (1975), "Inception criteria for droplet entrainment in two-phase concurrent flow", *AIChE J.*, Vol. 21, pp. 308-318.

James, P.W., Hewitt, G.F. and Whalley, P.B., (1980), "Droplet motion in two phase flow", Proc. ANS/ASME/NRC Int. Topical Meeting on Nuclear Reactor Thermal-Hydraulics, Vol. 2, pp. 1484-1503.

Jayanti S., (1990), "Contribution to the study of non-axisymmetric flows", *Ph.D. Thesis*, Imperial College of Science, Technology and Medicine, UK.

Jepson, W.P., (1988), "Liquid film thickness variation in horizontal annular flow in large diameter pipes", AERE-R1 2991.

Jepson, D.M., (1992), "Vertical annular flow", *Ph.D. Thesis*, University of Oxford, Oxford, United Kingdom.

Johnstone, H.F., Field, R.B. and Tassler, M.C., (1954), "Gas absorption and aerosol collection in Venturi scrubbers", *Ind. Eng. Chem.*, Vol. 45, pp. 1601-1608.

Kataoka, I. and Ishii, M., (1982), "Mechanism and correlation of droplet entrainment and deposition in annular two-phase flow", *NUREG CR-2885*, Vol. ANL-82-44.

Koehler, J.L.M., Feldman, H.A. and Leith, D., (1987), "Gas-borne liquid flow rate in a Venturi scrubber with two different liquid injection arrangements", *Aerosol Science & Technology*, Vol. 7, pp. 15-29.

Lapple, C.E. and Kamack, H.J., (1955), "Performance of wet dust scrubbers", *Chem. Eng. Progress*, Vol. 51, No. 3, pp. 110-121.

Laurinat, J.E., (1982), "Studies of the effects of pipes size on horizontal annular two-phase flows", *Ph.D. Thesis*, University of Illinois, Urbana, IL.

Laurinat, J.E., Hanratty, T.J. and Dallman, J.C., (1984), "Pressure drop and film height measurements for annular gas-liquid flow", *Int. J. Multiphase Flow*, Vol. 10, No. 3, pp. 341-356.

- Laurinat, J.E., Hanratty, T.J. and Jepson, W.P., (1985), "Film thickness distribution for gas-liquid annular flow in horizontal pipe", *Physico-Chemical Hydrodynamics*, Vol. 6, No. 1/2, pp. 179-195.
- Leith, D., Martin, K.P. and Cooper, D.W., (1985), "Liquid utilisation in a Venturi scrubber", *Filtration & Separation*, May / June, pp. 191-195.
- Lin, T.F., Jones, O.C., Lahey, Jr, R.T., Block, Jr, R.C. and Murase, M., (1985), "Film thickness measurements and modelling in horizontal annular flows", *PCH PhysicoChemical Hydrodynamics*, Vol. 6, No. ½, pp. 197-206.
- Lockart, R.W. and Martinelli, R.C., (1949), "Proposed correlations for isothermal two-phase flow in pipes", *Chemical Engineering Progress*, Vol. 49, pp. 39-48.
- Luninski, Y., Barnea, D. and Taitel, Y., (1983), "Film thickness in horizontal annular flow", *Can. J. Ch. E.*, Vol. 61, pp. 621-626.
- Mayinger, F. and Neumann, M., (1978), "Dust collection in Venturi scrubbers", *Ger. Chem. Eng.*, Vol. 1, pp. 289-293.
- Mayinger, F. and Lehner, M., (1995), "Operating results and aerosol deposition of a Venturi scrubber in self-priming operation", *Chemical Engineering and Processing*, Vol. 34, pp. 283-288.
- McManus, H.N., Jr., (1961), "Local liquid distribution and pressure drops in annular two phase flow", A.S.M.E.-E.I.C Hydraulic Conference, Montreal, Canada, Paper 61- HYD-20.
- Mishima, Y. and Ishii, M., (1984), "Flow regime transition criteria for two phase flow in vertical tubes", *Int. J. Heat Mass Transfer*, Vol. 75, No. 5, pp. 723-736.

Muir, D.M. and Kuye, A.O., (1986), "Effect of droplet size, polydispersity and degree of liquid entrainment on Venturi scrubber performance", *4<sup>th</sup> World Filtration Congress*, Ostend, Belgium, April 22-25.

Mukerjee, H. and Brill, J.P., (1985), "Empirical equations to predict flow patterns in two-phase inclined flow", *Int. J. Multiphase Flow*, Vol. 17, pp. 455-468.

Muller-Steinhagen, H. and Heck, K., (1986), "A simple fraction pressure drop correlation for two-phase flow in pipes", *Chemical Engineering Processes*, Vol. 20, pp. 297-308.

Murdock, J.W., (1962), "Two phase flow measurements with orifices", *Journal of Basic Engineering*.

Nedderman, R.M. and Shearer, C.J., (1963), "The motion and frequency of large disturbance waves in annular two-phase flow of air-water mixtures", *Chem. Engng Sci.*, Vol. 18, pp. 661-670.

Nencini, R. M. and Andreussi, P., (1983), "Study of the behaviour of large disturbance waves in annular two-phase flow", *Can. J. Chem. Engng.*, 60, 459-466.

Nigmatulin R.I., Nigmatulin B.I., Khodzhaev, YA.D. and Kroshilin, V.E., (1996), "Entrainment and deposition rates in a dispersed-film flow", *Int. J. Multiphase Flow*, Vol. 22, No. 1, pp. 19-30.

Nukiyama, S. and Tanasawa, Y., (1938), "An experiment on the atomisation of liquid by means air stream", *Transactions of the Society of Mechanical Engineers (Japan)*, Vol. 4, pp. 86-93.

Okawa, T., Kataoka, I., Kitahara, T., Yoshida, K. and Matsumoto, T., (2000), "Mechanistic correlation of entrainment fraction in equilibrium annular flow", *Second*

Japanese-European Two-Phase Flow Group Meeting, Tsukuba, Japan, September 25-29.

Oliemans, R.V.A., Pots, B.F.M and Trompe, N., (1986), "Modelling of annular dispersed two phase flow in vertical pipes", *Int. J. Multiphase Flow*, Vol. 12, No. 5, pp. 711-732.

Ousaka, A. and Kariyasaki, A., (1992), "Distribution of entrainment flow rate for air-water annular two-phase flow in a horizontal tube", *JSME International Journal, Series II*, Vol. 35., No. 3, pp. 354-360.

Owen, D.G., (1986), "An equilibrium and theoretical analysis of equilibrium annular flows", *Ph.D. Thesis*, University of Birmingham, UK.

Owen, D.G. and Hewitt, G.F., (1987), "An improved annular two-phase flow model", *Proc. 3<sup>rd</sup> Int. Conf. on Multiphase Flow*, The Hague, Paper C1.

Paras, S.V. and Karabelas, A.J., (1991), "Droplet entrainment and deposition in horizontal annular flow", *Int. J. Multiphase Flow*, Vol. 17, No. 4, pp. 455-468.

Paras, S.V., Vlachos, N.A. and Karabelas, A.J., (1994), "Liquid layer characteristics in stratified-atomization flow", *Int. J. Multiphase Flow*, Vol. 20, No. 5, pp. 939-956.

Paz, R.J. and Shoham, O., (1994), "Film thickness distribution for annular flow in directional wells: horizontal to vertical", SPE 28541, pp. 257- 272.

Pearce, D. L., (1979), "Film waves in horizontal annular flow: space-time correlator experiments", CEGB Report No. RD/L/N 111/79, Central Electricity Research Laboratories.

- Premoli, A., Francesco, D. and Prine, A., (1970), "An empirical correlation for evaluating two-phase mixture density under adiabatic conditions", European Two-Phase Flow Group Meeting. ( from Azzopardi and Hills (1999)).
- Pulley, R.A., (1997), "Modelling the performance of Venturi scrubbers", *Chem. Eng. Journal*, Vol. 67, pp. 9-18.
- Quandt, E.R., (1965), "Measurements of some basic parameters in two-phase annular flow", *AIChE Journal*, Vol. 11, pp. 311-318. (from Azzopardi (1997))
- Rea, S., (1998), "Stratified flow at T-junctions", *Ph. D. Thesis*, University of Nottingham, Nottingham, England.
- Ribeiro, A.M., Bott T.R., Jepson D.M., (1995), "Drop size and entrainment measurements in horizontal flow", *Two-phase Flow Modelling and Experimentation*", G. P. Celata and R. K. Shah Editors, 1995 Edizioni ETS.
- Rudnick, S.N., Koehler, J.L.M., Martin, K.P., Leith, D. and Cooper, D.W., (1986), "Particle collection efficiency in a Venturi scrubber: comparison of experiments with theory", *Environ. Sci. Technol.*, Vol. 20, No. 3, pp. 237-242.
- Sawai, T., Yamauchi, S. and Nakanishi, S., (1989), "Behaviour of disturbance waves under hydrodynamic non-equilibrium conditions", *Int. J. Multiphase Flow*, Vol. 15, pp. 341-356.
- Schadel, S.A., Leman, G.W., Binder, J.L. and Hanratty, T.J., (1990), "Rates of atomization and deposition in vertical annular flow", *Int. J. Multiphase Flow*, Vol. 16, No. 3, pp.363-374.
- Sekoguchi, K., Ousaka, A., Fukano, T. and Morimoto, T., (1982), "Air-annular two-phase flow in a horizontal tube", 1<sup>st</sup> Report, *Bull. JSME*, 25, 1559-1566.

Sekoguchi, K. and Takeishi, M. (1989), "Interfacial structures in upward huge wave flow and annular flow regimes", *Int. J. Multiphase Flow*, Vol. 15, pp. 295-305.

Semrau, K.T., Marynowski, C.W., Lunde, K.E. and Lapple, C.E., (1958), "Influence of power input on efficiency of dust scrubbers", *Industrial and Engineering Chemistry*, Vol. 50, No. 11, pp. 1615-1620.

Spedding, P.L. and Nguyen, V.T., (1980), "Regime maps for air water two phase flow", *Chem. Eng. Sci.*, Vol. 35, pp. 779-793.

Spedding, P.L., Chen, J.J.J. and Nguyen, V.T., (1982), "Pressure drop in two phase gas-liquid flow in inclined pipes", *Int. J. Multiphase Flow*, Vol. 8, pp. 407-431.

Srichai, S., (1994), "High pressure two-phase separated flow", *Ph.D. Thesis*, Imperial College of Science, Technology and Medicine, London.

Sun, H. and Azzopardi, B.J., (2003), "Modelling gas-liquid flow in Venturi scrubbers at high pressure", *Trans. IChemE*, Vol. 81, Part B.

Taitel, Y. and Dukler, A.E., (1976), "A model for predicting flow regime transitions in horizontal and near horizontal gas-liquid flow", *AIChE Journal*, Vol. 22, pp. 47-55.

Taitel\_Y, Bornea, D and Dukler, AE (1980), "Modelling flow pattern transitions for steady upward gas-liquid flow in vertical tubes", *AIChE Journal*, 26, 345-354.

Teixeira, S.F.C.F., (1989), "A model for the hydrodynamics of Venturis applicable to scrubbers", *Ph.D. Thesis*, University of Birmingham, UK.

Turner, R. G., Hubbard, M.G. and Dukler, A.E., (1969), "Analysis and prediction of minimum flow rate for the continuous removal of liquids from gas wells", *JPT*, pp. 1475- 1482; *Trans.*, AIME, Vol. 246.

Van Maanen, H.R.E., (1999), "Cost Reduction for wet-gas measurement using the tracer-Venturi combination", In proceedings of the workshop Practical developments in gas flow metering, East Kilbride, Scotland, paper 2, June 24.

Van Werver, M., van Maanen, H.R.E, Ooms, G. and Azzopardi, B.J., (2003), "Modelling wet-gas annular/dispersed flow through a Venturi", *AIChE Journal*, Vol. 49, No. 6, pp. 1383-1391.

Viswanathan, S., Gnyp, A.W. and St. Pierre, C.C., (1985), "Annular flow pressure drop model for Pease-Anthony type Venturi scrubbers", *AIChE Journal*, Vol. 31, No. 12, pp. 1947-1958.

Viswanathan, S., Gnyp, A.W. and St. Pierre, C.C., (1997), "Estimating film flow rate in a Venturi scrubber", *Particulate Sci. & Tech.*, Vol. 15, pp. 65-76.

Wallis, G.B., (1969), "One dimensional two-phase flow", McGraw-Hill.

Watson, M.J. and Hewitt G.F., (1999), "Pressure effects on the slug to churn transition", *International Journal of Multiphase Flow*, Vol: 25, pp. 1225-1241.

Whalley, P.B. and Hewitt, G.F., (1978), "The correlation of liquid entrainment fraction and entrainment rate in annular two-phase flow", United Kingdom Atomic Energy Authority, Harwell, Report No. AERE-R 9187.

Whalley, P.B., (1980), "Annular flow entrainment data bank", Unpublished report, AERE, Harwell

Williams, L.R., (1990), "Effects of the pipe diameter on horizontal annular two phase flow", *Ph.D. Thesis*, University of Illinois, Urbana, IL.

Woodmansee, D.E. and Hanratty, T.J., (1969), "Mechanism for the Removal of Droplets from a Liquid Surface by a Parallel Air Flow", *Chem. Eng. Sci.*, Vol. 24, pp. 299.

Yao, S.C. and Sylvester, N.D., (1987), "A mechanistic model for two phase annular mist flow in vertical pipes", *AIChE J.*, Vol. 33, pp. 1008-1012.

Yung, S.C., Barbarika, H.F. and Calvert, S., (1977), "Pressure loss in Venturi scrubbers", *J.A.P.C.A.*, Vol. 27, No. 4, pp. 348-350.

Yung, S.C., Parker, R., Duncan, M., Le, T. and Calvert, S., (1981), "Performance of Gas-atomized spray scrubbers at high pressure", U.S., D.O.E., Report MC/19167-1150.

Yung, S.C., Calvert, S. and Duncan, M., (1984), "Performance of Gas-atomized spray scrubbers at high pressure", *Journal of the Air Control Association*, Vol. 34, pp. 736-743.